Technische Universität München
TUM School of Engineering and Design

Energy Evaluation of Dynamically Operated Reverse Osmosis Systems

Alexander Präbst

Vollständiger Abdruck der von der TUM School of Engineering and Design der Technischen Universität München zur Erlangung eines

DOKTORS DER INGENIEURWISSENSCHAFTEN (DR.-ING.)

genehmigten Dissertation.

Vorsitz:
Prof. Dr.-Ing. Hartmut Spliethoff
Prüfende der Dissertation:
Prof. Dr.-Ing. Thomas Sattelmayer
Prof. Philip Davis, Ph.D.

Die Dissertation wurde am **02.10.2023** bei der Technischen Universität München eingereicht und durch die TUM School of Engineering and Design am **06.02.2024** angenommen.

Acknowledgements

This thesis emerged during my time as research associate at the Institute of Thermodynamics at the Technical University of Munich. The research project was funded by the German Federal Ministry of Education and Research (BMBF) and the Israeli Ministry of Science and Technology (MOST) as part of the joint German-Israeli research program for water technology (02WA1299). My sincere thanks go to all sponsors and industrial partners for their support.

First of all, I would like to thank Prof. Dr.-Ing. Thomas Sattelmayer for the opportunity to carry out this work under his supervision. I want to thank him for his patience and for his support, which have contributed significantly to the success of this work. It was an honor for me to be part of the institute as a research assistant. I would like to sincerely thank Prof. Philip Davies, Ph.D. for being the second reviewer and for his interest and enthusiasm in my work. I wish him and his research work all the best. Last but not least, I also want to thank Prof. Dr.-Ing. Hartmut Spliethoff as examination chairman.

My special thanks go to my students for their input and their always friendly cooperation. I also would like to thank the employees in our electrical and mechanical workshop and especially Thomas Schleussner and Jens Hümmer for their support in the development of the various test benches. Furthermore, I am grateful to the secretariat led by Helga Basset, Sigrid Schulz-Reichwald and Brigitte Hirsch for their support in all organizational, administrative and financial matters.

I came across the topic of seawater desalination through Dr.-Ing. Markus Spinnler, who unfortunately passed away on the 20th of December 2023. I would especially like to thank him for his friendship, his support and his persistent great optimism whenever I doubted myself or my work. I wish you, wherever you may be, and your family all the best and much strength for this difficult time. I am very grateful to have met you and to have learned professionally and personally from you.

The beauty of scientific work is the scientific discourse, without which this

work would not have been possible. First and foremost, I would like to thank Florian Kiefer, especially for his friendship during and after my time at the institute, but also for his knowledge, his ideas and his always profound and critical questioning, which have contributed significantly to the success of the work. Special thanks also go to Bernd Heithorst, Paul Christ, Hannes Dietz, Mayamen Naser Reda, Andreas Kastl, Alexander Kroiß, Jürgen Kranz and Konrad Költzsch for their support, discussions, and friendship.

Finally, I want to thank my family for their support and confidence. I am incredibly grateful for the patience, support and faith my wife Anna, my daughter Greta and my son Emil have shown in me. Without you, I wouldn't be sitting here writing these lines. I dedicate this work to you.

Gaimersheim, 2024

Alexander Präbst

Kurzfassung

Die Wasserentsalzung durch Umkehrosmose ist energieintensiv und die Verringerung des Energiebedarfs ist eines der Hauptthemen aktueller Forschung. Ein Nachteil von Membranverfahren ist die Bildung einer Konzentrationsgrenzschicht an der Membran, die zu einem Anstieg des zu überwindenden osmotischen Drucks führt. Der Einsatz pulsierender Strömungen kann diese Konzentrationsgrenzschicht stören. Ziel dieser Arbeit ist es, den Einfluss pulsierender Strömungen auf den Stoffübergang und den Energiebedarf von Umkehrosmoseanlagen zu untersuchen. Um den Energiebedarf pulsierender Strömungen im Vergleich zu konventionell betriebenen Umkehrosmosesystemen zu bewerten, müssen drei Faktoren untersucht werden: Dämpfung, Druckverlust und Stoffübergang.

Die ersten beiden Parameter wurden experimentell bestimmt. Mit Hilfe von Strömungssimulationen (Computational Fluid Dynamics) wurden die Phänomene zur Verbesserung des Stoffübergangs mit Hilfe der Proper Orthogonal Decomposition identifiziert. Des weiteren wurde eine Korrelation zwischen Sherwood-Zahl und Anregungsfrequenz, Amplitude, durchschnittliche Reynoldszahl und Permeatfluss entwickelt. Diese Korrelation wurde für ein quasi-2D Simulationstool für Spiralwickelmodule verwendet, um die Erkenntnisse auf die Systemebene zu übertragen.

Ein zentrales Ergebnis dieser Arbeit ist, dass pulsierende Strömungen in Spiralwickelmodulen den Stoffübergang durch Störungen der Konzentrationsgrenzschicht deutlich verbessern. Die Verbesserung steigt mit Amplitude und Frequenz. Allerdings steigen auch Dämpfungsraten und Druckverluste. Diese Tendenzen haben entgegengesetzte Auswirkungen auf den spezifischen Energiebedarf. Daher müssen optimale dynamische Parameter gefunden werden. Bei Brackwassersystemen konnte der erhöhte Stoffübergang den zusätzlichen Energiebedarf nicht kompensieren. Für Meerwasserentsalzungsanlagen wurde eine optimale Womersley Zahl von 7 ermittelt. Dies führte zu einer Verringerung des Energiebedarfs um bis zu -9%. Für beide Systeme wurde eine Verringerung des Permeatsalzgehalts um bis zu -16% für Brackwasser- und -22% für Meerwasseranlagen ermittelt. Pulsierende Strömungen sind da-

her eine potentielle Möglichkeit, Umkehrosmosesysteme zu verbessern.

Abstract

Water desalination by Reverse Osmosis is energy intensive and the reduction of its energy demand is one of the main topics in current research. A disadvantage of membrane processes is the formation of a concentration boundary layer at the membrane, resulting in an increased osmotic pressure that needs to be overcome. Applying pulsating flows is a possible approach to disturb this boundary layer. The purpose of this work is to investigate the impact of pulsating flows on the mass transfer in spacer-filled channels and thus on the energy demand of Reverse Osmosis systems. To evaluate the energy demand of applying pulsating flows compared to conventionally operated Reverse Osmosis systems, three main issues have to be investigated: damping, pressure loss and mass transfer across the membrane.

The first two parameters were experimentally determined. Computational Fluid Dynamics simulations were used to identify the predominant phenomena for mass transfer enhancement by using Proper Orthogonal Decomposition. A correlation between the Sherwood number and excitation frequency, amplitude ratio, average Reynolds number, and permeate flux was developed. This correlation was used for a developed quasi-2D simulation tool for spiral-wound modules to transfer the findings to an entire Reverse Osmosis system.

A key finding of this work is that pulsating flows in spiral-wound modules can significantly improve the mass transfer due to strong perturbations of the concentration boundary layer. The enhancement increases with the amplitude and excitation frequency applied. However, damping rates and pressure losses also increase. These tendencies have opposite impacts on the specific energy demand. Therefore, optimum dynamic parameters needed to be found. For brackish water systems, the increased mass transfer could not compensate the additional energy demand. For seawater desalination systems, an optimum Womersley number of 7 was determined. This resulted in a maximum reduction in energy demand of -9%. For both systems, a maximum permeate salinity decrease of -16% for brackish water and of -22% for seawater systems was determined. Therefore, pulsating flows can be considered as a potential way to improve the performance of Reverse Osmosis systems.

Contents

List of Figures

List of Tables

Nomenclature

Latin Characters

A_{mem}	[m s^{-1} Pa^{-1}]	Water permeability coefficient
A	[m^2]	Area
$A_{\mathrm{v,sp}}$	[m^2]	Volume specific area
A_{orif}	[kg^{-1} m^{-1}]	Parameter for determination of dynamic mass flow rate
a	[-]	Position
AR	[-]	Amplitude ratio
B_{mem}	[m s^{-1}]	Salt permeability coefficient
B_{orif}	[m^{-1}]	Parameter for determination of dynamic mass flow rate
C_{c}	[-]	Contraction factor
C_{orif}	[m^{-1} s^{-1}]	Parameter for determination of dynamic mass flow rate
C_{π}	[-]	Factor for osmotic pressure calculation
c	[kg m^{-3}]	Concentration
$c_{0,1,2,3}$	[-]	Parameter for the analytical solution
d	[m]	Diameter
d_{h}	[m]	Hydraulic diameter
E	[J]	Energy
E_{Φ}	[-]	Relative kinetic energy of POD Mode
El_{f}	[N m^{-2}]	Fluid elasticity
EMT	[−]	Enhanced mass transfer based on permeate flux
$\mathrm{EMT}_{\mathrm{ECP}}$	[−]	Enhanced mass transfer based on salt mass fraction
$\mathrm{EMT}_{\mathrm{Sh}}$	[−]	Enhanced mass transfer based on Sherwood number
$\mathrm{EMT}_{\Delta\pi}$	[-]	Enhanced mass transfer based on osmotic pressure
f	[Hz]	Frequency
G	[J]	Gibbs energy

GCI	[-]	Grid convergence index
H	[m]	Channel height
i	[-]	Order of POD mode
$\overline{i}$	[-]	Placeholder for average value i
$\mathbf{I}$	[-]	Unit tensor
J'	[m^2 N^{-1}]	Real part of the complex creep function
J''	[m^2 N^{-1}]	Imaginary part of the complex creep function
j	[kg m^{-2} s^{-1}]	Mass flux
J_0	[-]	Bessel function of the first kind
k	[-]	Time step
L	[m]	Length between two filaments
$L_{1,2}$	[m]	Filament clearances
l	[m]	Length
m	[kg]	Mass
$\dot{m}$	[kg s^{-1}]	Mass flow rate
$\mathbf{n}$	[-]	Normal vector
n	[-]	nth part,number
n_{cells}	[-]	Number of cells
NDP	[Pa]	Net driving pressure
p	[Pa]	Pressure
P_{n}	[Pa kg^{-1} m^2]	Specific pressure gradient
pH	[-]	pH value
r	[m]	Radius
R	[J K^{-1} mol^{-1}]	Gas constant
q	[-]	Iteration step
$\mathbb{R}$	[-]	Ratio between number of cells
$\mathbf{R}$	[-]	Correlation matrix
$\mathbf{R}_{\text{ij}}$	[-]	Correlation matrix component
RR	[-]	Recovery rate
S	[J K^{-1}]	Entropy
s	[m]	Flow path
SEC	[kWh m^{-3}]	Specific energy consumption
t	[s]	Time
T	[K]	Temperature

TMP	[Pa]	Transmembrane pressure
u, v	[m s^{-1}]	Velocity in x,y direction
$\mathbf{u}$	[m s^{-1}]	Velocity vector
u_{wave}	[m s^{-1}]	Wave propagation speed
v_{sv}	[m^3 kg^{-1}]	Specific volume of the solvent
v_{P}	[m^3 m^{-2} s]	Permeate volume flux across the membrane
V	[m^3]	Volume
$\dot{V}$	[m^3 s^{-1}]	Volume flow rate
w	[mol mol^{-1}]	Mole fraction
x	[m]	Coordinate parallel to the membrane
y	[m]	Coordinate normal to the membrane
z	[m]	Normal coordinate within the membrane

Greek Symbols

α	[m^{-1}]	Damping rate
$\alpha_{1,2}$	[-]	Coriolis coefficients
α_{dis}	[-]	Discharge coefficient
$\alpha_{\text{mem,p}}$	[-]	Membrane permeability pressure constant
$\alpha_{\text{mem,T}}$	[-]	Membrane permeability temperature constant
β	[m s^{-1}]	Mass transfer coefficient
$\beta_{\text{mem,t}}$	[-]	Salt permeability temperature constant
$\Delta\bar{i}$	[-]	Difference of variable $\bar{i}$
δ	[m]	Thickness
δ_1	[°]	Flow attack angle
δ_2	[°]	Mesh angle
ϵ	[-]	Porosity, void fraction
ϵ	[s^{-1}]	Strain rate tensor
η	[-]	Efficiency, relative error
Γ	[m^2 s^{-2}]	Mutual diffusion coefficient salt-water
γ_{sv}	[-]	Solvent activity
λ	[-]	Eigenwert
λ_{wave}	[m]	Wave length

Λ	[s^{-1}]	Vorticity
Λ	[s^{-1}]	Vorticity vector
μ	[J mol^{-1}]	Chemical potential
ν	[m^2 s^{-1}]	Kinematic viscosity
ω	[rad s^{-1}]	Angular frequency
Ω	[s^{-1} m^{-2}]	Vorticity flux
ϖ	[-]	Amplitude
ϖ_x	[m]	Local amplitude in x direction
ϖ_y	[m]	Local amplitude in y direction
Φ	[-]	Mode
ϕ	[-]	Osmotic coefficient
φ	[°]	Phase shift
π	[Pa]	Osmotic pressure
Π	[-]	Dimension
Ψ	[m^{-1}]	Fluctuating part of the mass fraction
ψ	[m s^{-1}]	Time coefficient
ψ_p	[-]	Pressure ratio
ρ	[kg m^{-3}]	Density
σ	[kg m^2 s^{-1}]	Cauchy stress tensor
τ	[kg m^2 s^{-1}]	Shear stress
τ_{ws}	[Pa]	Wall shear stress
τ^*_{ws}	[Pa m^{-1}]	Normalized wall shear stress
τ_{PS}	[-]	Tortuosity of the porous structure
θ^*	[-]	Dimensionless amplitude
ξ	[kg kg^{-1}]	Salt mass fraction
ζ	[-]	Friction coefficient

Subscripts

$(...)_\infty$	Ambient
$(...)_{\mathrm{AL}}$	Active layer
$(...)_{\mathrm{analyt}}$	Analytical
$(...)_{\mathrm{b}}$	Bulk

$(...)_{BL}$	Boundary layer
$(...)_{ch}$	Channel
$(...)_{cutoff}$	Cutoff
$(...)_{D}$	Draw
$(...)_{diff}$	Diffusive
$(...)_{dir}$	Direct
$(...)_{f}$	Feed
$(...)_{ECP}$	External concentration polarization
$(...)_{ECP\backslash ICP}$	External without internal concentration polarization
$(...)_{ECP+ICP}$	External and internal concentration polarization
$(...)_{eff}$	Effective
$(...)_{el}$	Element
$(...)_{env}$	Envelope
$(...)_{ex}$	Excitation
$(...)_{exp}$	Experiment
$(...)_{F}$	Feed
$(...)_{fil}$	Filament
$(...)_{f}$	Fluid
$(...)_{FO}$	Forward Osmosis
$(...)_{h}$	Hydraulic
$(...)_{i}$	Current component index
$(...)_{ICP}$	Internal concentration polarization
$(...)_{Inlet}$	Inlet
$(...)_{max}$	Maximum
$(...)_{meas}$	Measured
$(...)_{mem}$	Membrane
$(...)_{min}$	Minimum
$(...)_{mod}$	Module
$(...)_{n}$	Number
$(...)_{orif}$	Orifice
$(...)_{outlet}$	Outlet
$(...)_{part}$	Particle
$(...)_{PIV}$	Particle Image Velocimetry
$(...)_{P}$	Permeate

$(...)_{\text{pipe}}$	Pipe
$(...)_{\text{PS}}$	Porous structure
$(...)_{\text{p}}$	Pressure
$(...)_{\text{puls}}$	Pulsation
$(...)_{\text{PGD}}$	Pulsation generation device
$(...)_{\text{puls-stst}}$	Difference between pulsation and steady-state case
$(...)_{\text{ref}}$	Reference
$(...)_{\text{rel}}$	Relative
$(...)_{\text{res}}$	Resonance
$(...)_{\text{resp}}$	Response
$(...)_{\text{R}}$	Retentate
$(...)_{\text{RO}}$	Reverse Osmosis
$(...)_{\text{s}}$	Salt
$(...)_{\xi}$	Salt mass fraction
$(...)_{\text{sim}}$	Simulation
$(...)_{\text{sys}}$	System
$(...)_{\text{sensor}}$	Sensor
$(...)_{\text{sv}}$	Solvent
$(...)_{\text{sp}}$	Spacer
$(...)_{\text{stst}}$	Steady-state
$(...)_{\text{submerged}}$	Submerged
$(...)_{\text{sys}}$	System
$(...)_{\text{T}}$	Temperature
$(...)_{\text{tube}}$	Tube
$(...)_{u}$	Velocity
$(...)_{\text{w}}$	Water
$(...)_{\text{ws}}$	Wall shear
$(...)_{\text{wave}}$	Wave
$(...)_{\text{zig-zag}}$	Zig-zag

Dimensionless Numbers

He	Helmholtz number
Pe	Peclet number
Re	Reynolds number
Sc	Schmidt number
Sh	Sherwood number
Sr	Strouhal number
Wo	Womersley number

Abbreviations

AC	Alternating current
ACF	Active carbon filter
AL	Active layer
AR	Amplitude ratio
B	Balance
BT	Buffer tank
BW	Brackish Water
CFD	Computational Fluid Dynamics
CP	Concentration polarization
CS	Conductivity sensor
DC	Direct current
DPS	Differential pressure sensor
DRS	Dry run sensor
DT	Draw tank
ECP	External concentration polarization
ERD	Energy recovery device
EXP	Experimental
F	Filter
FFT	Fast Fourier transformation
FLT	Flush tank
FM	Flow meter

FO	Forward Osmosis
FOTC	Forward Osmosis test cell
FT	Feed tank
FV	Flotation valve
GP	Gear pump
HPP	High pressure pump
HX	Heat exchanger
ICP	Internal concentration polarization
LPP	Low pressure pump
MM	Manometer
NV	Needle valve
PD	Pulsation dampener
PGD	Pulsation generation device
PIV	Particle Image Velocimetry
PL	Porous layer
PRV	Pressure regulation valve
PS	Porous structure
RO	Reverse Osmosis
RR	Recovery rate
SEC	Specific energy consumption
SIM	Simulation
SL	Support layer
SV	Solenoid valve
SW	Seawater
TS	Temperature sensor
V	Valve

Operators

$\nabla(\cdot)$	Gradient
$< (\cdot) >$	Space-/volume-averaged, integrated
$\overline{(\cdot)}$	Time-averaged, averaged

1 Introduction

Water desalination is an energy-intensive technology and the reduction of its energy demand is one of the key issues in the development and design of all desalination processes [1]. Therefore, great effort has been and is still being made to improve the energy efficiency [2]. The market dominating and most energy-efficient seawater desalination technology is Reverse Osmosis (RO). The large amount of energy is required to overcome the osmotic pressure by the hydraulic pressure to drive the diffusion process of the permeate across the membrane. The formation of a concentration boundary layer at the membrane leads to an increased osmotic pressure and thus to a higher specific energy consumption (SEC). The present work addresses this problem by disturbing the concentration boundary layer through applying pulsating feed flows.

1.1 Background and Motivation

Modern seawater RO (SWRO) plants operate with a SEC of about 3.5 kWh per m^3 permeate [3, 4]. Researchers work on reducing the energy demand by improving the permeability of RO membranes [4]. But according to Werber et al. [5], recent membranes are already close to an optimum. An increase in permeability is always accompanied with a higher salt passage, which deteriorates the product water quality. The salt passage increases among others due to a higher accumulation of salt due to the increased permeate fluxes. This results in a large concentration gradient across the membrane. Therefore, the optimization of membranes must go in hand with an optimization of the mass transfer at the membrane [6, 7].

According to preliminary studies [8], the use of pulsating flows can improve the mass transfer in RO modules. In order to evaluate the energy requirements

of dynamically operated RO systems in comparison to conventional operation modes, general aspects of the energy requirement for RO systems are explained in the following.

1.1.1 Energy Requirement of Reverse Osmosis Systems

A common RO system consists of a high pressure pump (HPP), membrane modules and optionally an energy recovery device (ERD), cf. Figure 1.1. The ERD can be a turbine or pressure exchanger, whereas the latter is known to be the most efficient option for desalination systems. The RO units are typically multi-stage systems optionally including booster pumps to keep the recovery rate for each stage constant. The SEC including the energy demand of the booster pumps minus the recovered energy can be calculated as

$$\mathrm{SEC} = \underbrace{\frac{p_\mathrm{F}}{\mathrm{RR}\,\eta_\mathrm{pump}}}_{\text{HPP}} + \underbrace{\sum_{i=2}^{n} \frac{\dot{V}_{\mathrm{F,i}}}{\dot{V}_\mathrm{P}} (p_{\mathrm{F,i}} - p_{\mathrm{F,i-1}})}_{\text{Booster pumps}} - \underbrace{\frac{1-\mathrm{RR}}{\mathrm{RR}} p_\mathrm{R}\,\eta_\mathrm{ERD}}_{\text{ERD}}, \tag{1.1}$$

with the recovery rate RR, which relates the permeate with the feed volume flow rate

$$\mathrm{RR} = \frac{\dot{V}_\mathrm{P}}{\dot{V}_\mathrm{F}}. \tag{1.2}$$

In the following, the ERD is considered as black box with a constant efficiency of $\eta_\mathrm{ERD} = 95\,\%$, which is a common value for such devices [9]. Figure 1.2 shows

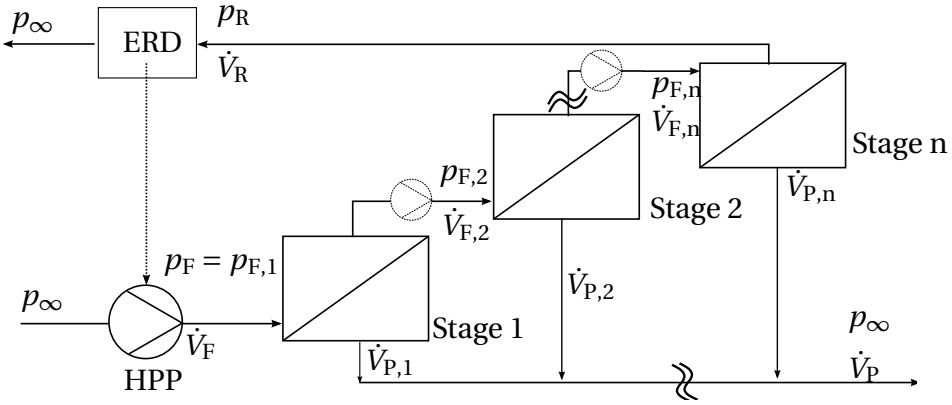

Figure 1.1: Simplified RO plant for desalination.

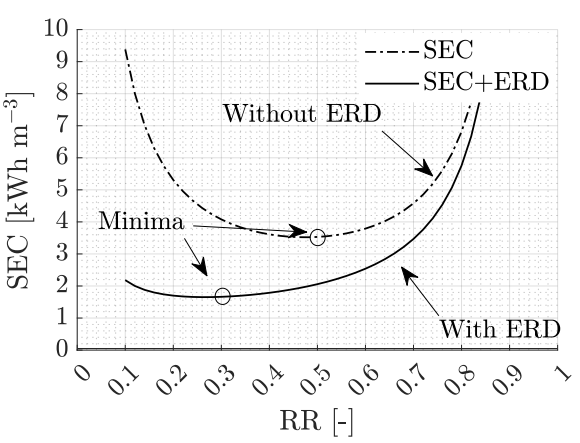

(a) SWRO: $\xi_F = 0.035$.

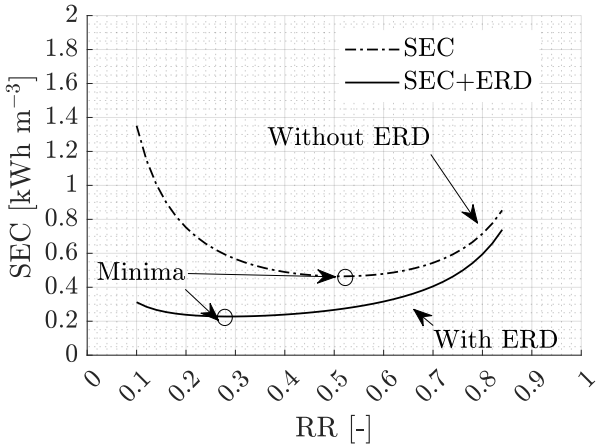

(b) BWRO: $\xi_F = 0.005$.

Figure 1.2: SEC of an ideal single-stage RO system with and without ERD; $\eta_{ERD} = 95$ %; $\eta_{pump} = 95$ %; $T_F = 298.15$ K; $A_{mem} = 7 \cdot 10^{-12}$ m Pa^{-1} s^{-1} and $B_{mem} = 3.8 \cdot 10^{-8}$ m s^{-1}.

the results gained for an ideal single-stage system. A brackish water (BW) RO (BWRO) system and SWRO system are compared, whereas concentration polarization effects are neglected. The system works at the thermodynamic limit, which means a zero net driving pressure NDP at the end of the module [10, 11]

$$\text{NDP} = (p_F - p_P) - (\pi_F - \pi_P) = \text{TMP} - (\pi_F - \pi_F) = 0, \tag{1.3}$$

with the trans-membrane pressure TMP defined as the hydraulic pressure difference between feed and permeate side and the osmotic pressure π, which is explained in Section 2.1 in detail. The SEC shows a minimum due to the competing effects of an increasing permeate output and a rising osmotic pressure for increasing feed concentrations at higher recovery rates. The minimum energy is needed at RR $\simeq$ 50 % without an ERD. With an ERD, the minimum lies at RR $\simeq$ 30 %. This minimum results from the higher energy recovery for lower recovery rates. On the basis of Figure 1.2, it can be explained why BWRO systems are operated without an ERD. The reduction of energy demand using an ERD is only 0.2 kWh m^{-3}. Due to this low improvement and to save investment and maintenance costs of the ERD, BWRO systems usually operate without an ERD.

1.1.2 Ultra-Permeable Membranes and the Need of Mass Transfer Improvement

Considering the influence of the improved membrane permeability on the mass transport across the membrane, the study of McGovern et al. [6] for a single-stage RO system is used. Based on the solution-diffusion model and a stagnant film model, both of which are described in Section 2.3, the water flux j_w at a given recovery rate for an ideal membrane, i.e. no salt passage, can be expressed by [6]

$$j_\mathrm{w} = A_\mathrm{mem}\left(p_\mathrm{F} - \frac{\pi_\mathrm{F}}{1-\mathrm{RR}} e^{\frac{j_\mathrm{w}\mathrm{RR}}{\beta}}\right), \tag{1.4}$$

with A_mem as membrane permeability, π_F as osmotic pressure of the feed and β as mass transfer coefficient. The results are obtained with a basic mass transfer coefficient of $\beta_\mathrm{ref} = 5 \cdot 10^{-5}$ m s^{-1}, which represents a mass transfer efficiency for state-of-the-art RO modules and a recovery rate of RR = 50 %.

Figure 1.3 shows the SEC over an increasing membrane permeability A_mem for different mass transfer enhancements, which are represented by the ratio $\frac{\beta}{\beta_\mathrm{ref}}$. It can be seen that the SEC asymptotically decreases by increasing the membrane permeability towards a minimum depending on the mass transfer coefficient. In this asymptotic region, mass transfer towards the membrane becomes more and more process limiting. Considering state-of-the-art membranes with a permeability of up to $A_\mathrm{mem} = 1 \cdot 10^{-6}$ m s^{-1} bar^{-1} [5], the SEC is already close to the asymptotic minimum. The only way to decrease the SEC is to optimize the mass transfer at the membrane, i.e. increasing β by pulsating flows.

Hence, as mentioned above, the improvement of the RO process should include not only improvements of the membrane, but also optimization of mass transfer towards the membrane. Passive techniques like eddy promoters, so called feed spacers, are already installed in state-of-the-art spiral-wound modules to reach mass transfer coefficients of around $\beta_\mathrm{ref} = 5 \cdot 10^{-5}$ m s^{-1}. But to further increase the mass transfer, an additional active technique has to be used. The combination of both is classified as a compound enhancement technique [12]. In literature, there are contradictory statements on the potential of pulsating flows as active technique for enhancing heat and mass

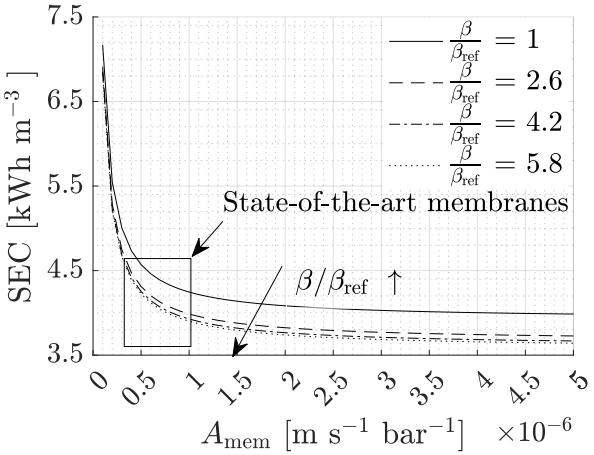

Figure 1.3: SEC plotted over increasing membrane permeabilities A_{mem} for different relative mass transfer coefficients $\frac{\beta}{\beta_{\mathrm{ref}}}$ with $\beta_{\mathrm{ref}} = 5 \cdot 10^{-5}$ m s^{-1}; adapted from [5].

transfer. According to Benavides [13], the contradicting conclusions can be summarized as follows: Pulsations enhance [14, 15, 16], deteriorate [17], do not affect [18] or can enhance heat and mass transfer depending on the flow conditions [19].

In addition to potentially improving mass transfer, pulsating feed flows can decrease the fouling potential in RO systems [20]. Generally, it is well known that oscillatory flows influence the dispersion of particles or contaminants [21, 22]. The appearance of periodic peaks of wall shear stress in a time-periodic internal flow can lead to the removal and prevention of deposits [23]. Zamani et al. [24] studied different strategies to increase the wall shear stress at the membrane and to enhance membrane processes regarding fouling. Additionally, they reviewed different active techniques regarding additional energy requirements. For pulsating flows, they did not find data for a wide range of scenarios.

Considering the influence of pulsating flows on membrane systems, different researchers studied pulsating flows in tubular or empty membrane channels. Kennedy [25] validated a model for hollow fiber modules developed by Ilias and Govind [26] and indicated that pulsations at 1 Hz increase the permeate production by 68 %. Baikov et al. [27] theoretically and experimentally in-

vestigated pulsating flows in flat membrane channels and found an optimum frequency of 3 Hz. Ali et al. [28] found a permeate flux increase of 42 % and a salt passage reduction of 20 % in a tubular RO membrane under pulsating flows at 1 Hz. Thomas et al. [29] numerically studied pulsatile flows in tubular RO membranes and did not observe a performance enhancement, but even a deterioration. Jaffrin et al. [30] observed a permeate flux increase of 45 % and Bertram [31] obtained an increase of 60 % with only a minor increase in energy demand. Gupta et al. [32] performed an experimental study on Ultra- and Microfiltration using a pulsating piston cylinder apparatus and gained a permeate flux increase of 45 %.

Pulsating flows in spacer-filled channels were also investigated. Abbas et al. [35] noted in their studies that at 1 Hz the permeate flux could be increased by 60 to 80 %. Liang et al. [33] and Garcia-Picazo et al. [34] numerically and experimentally investigated two different methods of enhancing mass transfer: oscillating membrane walls and oscillating flows in zig-zag spacer channels. They used an experimental test rig and 2D Computational Fluid Dynamics (CFD). A linear stabilization analysis was performed to identify a critical frequency, where large enhancements can be expected. The largest enhancement of 20 % was identified at 15 Hz by induced vortex shedding. Already small relative velocity amplitudes of 0.01 lead to vortex shedding and an increased mixing. These studies were performed within the entrance length of the module and cannot be transferred to the complete RO module. Rodrigues et al. [36] experimentally studied frequencies of 10 Hz and 50 Hz at different Reynolds numbers in spacer-filled channels and observed a mass transfer enhancement of up to 50 % at a pressure loss increase of only 10 %. Besides membrane systems, pulsations and oscillations were investigated in baffled tubes used in many chemical processes. Ni et al. [37] reviewed various studies and summarized that pulsations can lead to a heat and mass transfer enhancement by 20 to 30 times.

A lack of knowledge could be identified in the numerical and experimental investigation of the influence of pulsating flows in different spacer-filled channels on the mass transport enhancement phenomena within a wide range of different amplitudes and frequencies. Another important aspect that has not

yet been addressed in literature are the advantages of this improvement in mass transfer for the overall RO system and its impact on energy demand. This work closes this gap by analyzing pulsating flows for a wide range of different dynamic conditions using different experiments and simulations, which will be presented in the following.

1.2 Thesis Outline

The main goals of this work are to analyze the phenomena enhancing the mass transfer across the membrane and to evaluate the energetic advantages of RO systems operated with pulsating flows. The strategy for achieving these objectives is depicted in Figure 1.4.

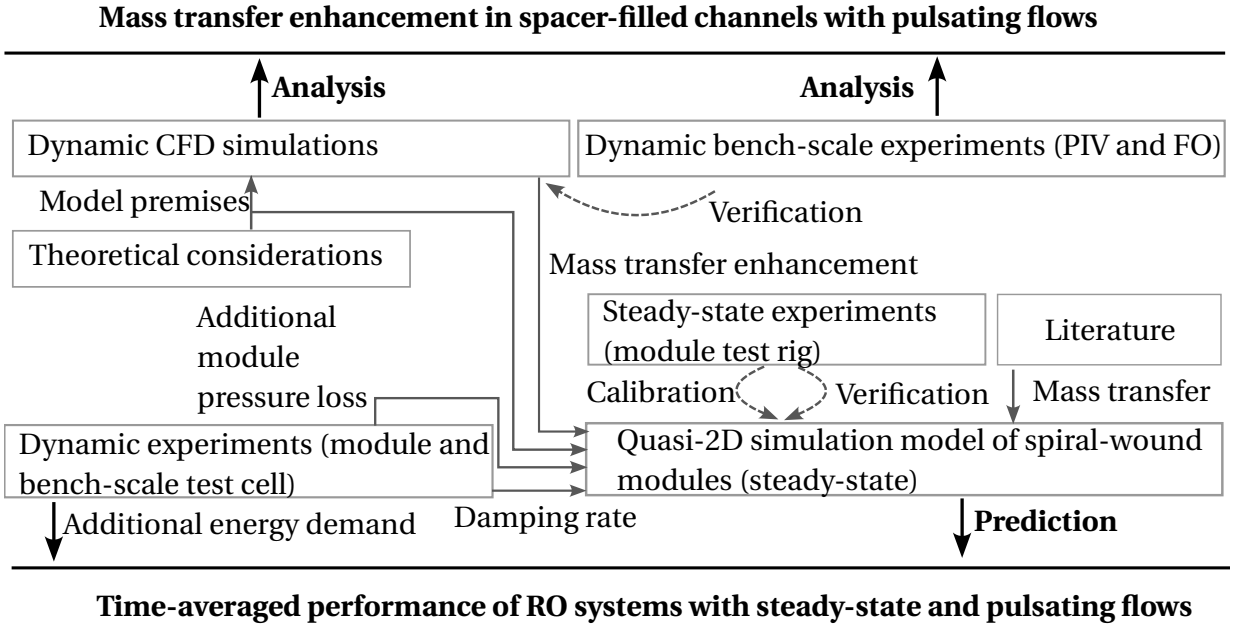

Figure 1.4: Objectives and methodological approach of this work.

A CFD model was developed to analyze the influence of dynamic flows on the mass transfer in spacer-filled channels. The model assumptions were verified against theoretical considerations as well as Particle Image Velocimetry (PIV) measurements and experiments with a laboratory scale Forward Osmo-

sis (FO) test rig. For the dynamic experiments, a pulsation generator (PGD) was used to provide pulsating flows in a wide range of amplitude ratios and frequencies. To evaluate the time-averaged performance of RO systems with pulsating flows, a steady-state quasi-2D simulation model of spiral-wound modules was developed. The results from experiments and CFD simulations delivered time-averaged input parameters for the quasi-2D model. The system model was verified by experiments of the RO Module test rig. The present work is structured as follows:

1. Chapter 2 will summarize the basic thermodynamic fundamentals of desalination and salt and water transport across the membrane. The phenomenon of concentration polarization will be presented. The dynamic mass transport across the membrane due to pressure changes and periodic flows will be analyzed theoretically. These findings form the basis for the simulation models and further analyses.

2. In Chapter 3, the experimental methods will be introduced. Two different setups will be presented: a bench-scale FO test rig and an RO module test rig. Moreover, the PIV setup will be described. This will be followed by the determination of the amplitude ratio of pulsating flows generated with the PGD.

3. Chapter 4 will focus on the CFD and system simulation model developed in this work. Both models will be verified with test results from the experimental test rigs.

4. In Chapter 5, the impact of pulsating flows on flow and mass transport in spacer-filled channels will be studied using the data of the lab-scale test rig and CFD simulations. The flow as well as mass transport dynamics will be analyzed using the method of Proper Orthogonal Decomposition (POD).

5. In Chapter 6, the damping of pulsating flows and the additional pressure losses will be determined. Additionally, time-averaged Sherwood numbers at different amplitude ratios and frequencies will be analyzed. These findings will be transferred to the quasi-2D model to evaluate the performance enhancement in RO systems by applying pulsating feed flows.

2 Fundamentals and Basic Analysis

The present chapter is devoted to the fundamentals of the desalination of aqueous sodium chloride solutions using dense membranes, to the phenomenon of concentration polarization and its interplay with periodic changes of flow velocities or pressures. The thermodynamics of desalination and fundamental properties of salt solutions will be introduced in Section 2.1. The membrane structure and the basic transport mechanisms inside the different membrane layers for Forward Osmosis (FO) and Reverse Osmosis (RO) processes will be described in Section 2.2 and 2.3. The fundamentals of concentration polarization and mass transfer in spacer-filled channels will be introduced in Section 2.4 and 2.5. The chapter will close with the analysis of the dynamic mass transport inside the active layer (AL), porous structure (PS) and the external and internal concentration polarization (ECP and ICP) layer in Sections 2.6.

2.1 Thermodynamics of Desalination of Salt Solutions

As stated in Chapter 1, the main drawback of desalination processes is the large amount of energy required for the separation of pure water from an aqueous saline solution. The process without the presence of an electric field can be mathematically described by the change in Gibbs energy dG [38, 39] with

$$\mathrm{d}G = V\mathrm{d}p - S\mathrm{d}T + \sum_i \left(\mu_\mathrm{i}\mathrm{d}n_i\right). \tag{2.1}$$

At mechanical and thermal equilibrium (dp = dT = 0), the change of Gibbs energy dG only depends on the change in composition and therefore, on the chemical potential μ_i. The chemical potential of a liquid solvent can be calculated with the reference to the chemical potential of the pure component

$\mu_{\mathrm{sv,ref}}(T,p)$ as

$$\mu_{\mathrm{sv}} = \mu_{\mathrm{sv,ref}}(T,p) + \mathrm{R}T \ln \gamma_{\mathrm{sv}}(T,p). \tag{2.2}$$

The chemical potential depends on temperature, pressure and solvent concentration. While it decreases for larger concentrations, it increases for higher pressures and temperatures. For determination of the activity of aqueous salt solutions, the osmotic coefficient ϕ of the solvent is introduced, which represents a more sensitive measure of the deviation to the ideal behavior [39],

$$\phi \equiv \frac{\ln \gamma_{\mathrm{sv}}}{\ln w_{\mathrm{sv}}}. \tag{2.3}$$

In the present work, the extended equations by Clarke and Glew [40, 41] are used to calculate ϕ and the osmotic pressure, which is defined as

$$\pi = -\frac{\mathrm{R}T}{v_{\mathrm{sv}}} \ln \gamma_{\mathrm{sv}}. \tag{2.4}$$

When pure water is separated from an aqueous salt solution at constant pressure and temperature with an ideal membrane that allows only water to pass, the process of FO occurs, in which water flows from the low-concentrated solution to the high-concentrated solution due to the higher chemical potential of the low-concentrated solution. The water flows as long as a pressure difference establish, where both solutions are in chemical equilibrium. This pressure difference is defined as the osmotic pressure. If the hydrostatic pressure on the high-concentrated side overcomes the osmotic pressure difference, water flows from the high to the low-concentrated side. This process is called RO.

2.2 Membrane Structure and Transport Mechanisms

In the work at hand, different steady-state and dynamic experiments and simulations will be compared. Therefore, it is important to know, which parameters influence the mass transfer across the membrane to avoid a misinterpretation of the results.

Figure 2.1 shows a typical RO membrane structure. Membranes that are predominantly used in osmotic separation processes are asymmetric. They consist of two to three layers including an AL, which separates the salt from the water, as well as a support layer (SL) and porous layer (PL), which give the membrane its stability. The SL and PL can be seen as a PS. The AL, which is made of cellulose acetate or polyamide, has a thickness up to around 300 nm [42], which allows a low permeability resistance at a high salt rejection. The surface has a microscopic roughness due to the polymerization process in the order of magnitude of 10^2 nm [43]. The summarized thickness of the SL and PL can be up to around 300 μm [42]. The membranes are hydrophilic, which is achieved by negatively charged functional groups [44].

The simplest mechanism of separation within the AL is geometric rejection [43]. Solutes larger than the free volume void, cf. Figure 2.1, are rejected. Water molecules are much smaller than the salt molecules and can pass. Nevertheless, there exist network holes, which can be larger than the radii of salt molecules and would intuitively lead to a high salt breakthrough. But additional to the steric hindrance, the separation is caused by electrostatic repulsion and dielectric exclusion [45]. Having contact to an aqueous solution, polymeric membranes have a surface charge balanced by the counter-ions in the solution due to charge neutrality leading to an electric double layer [46]. The surface charge can vary with the pH value. Co-ions are rejected while counter-ions would be attracted and would quickly pass through the AL. Due to the charge neutrality, the permeability of the counter-ions (cations Na^+) is as low as that of the co-ions (anions Cl^-) [44]. The dielectric exclusion is caused by interactions of ions in the solution and the AL, which have different dielectric constants [45]. These interactions cause image forces, which are formally caused by image charges located at an equivalent dissociated interface to the real charge. This represents an additional energetic barrier for the solvation of the ions [45].

This brief summary shows that it is important to keep the feed concentration, membrane parameters and feed pH-values constant when comparing different measurements or simulations.

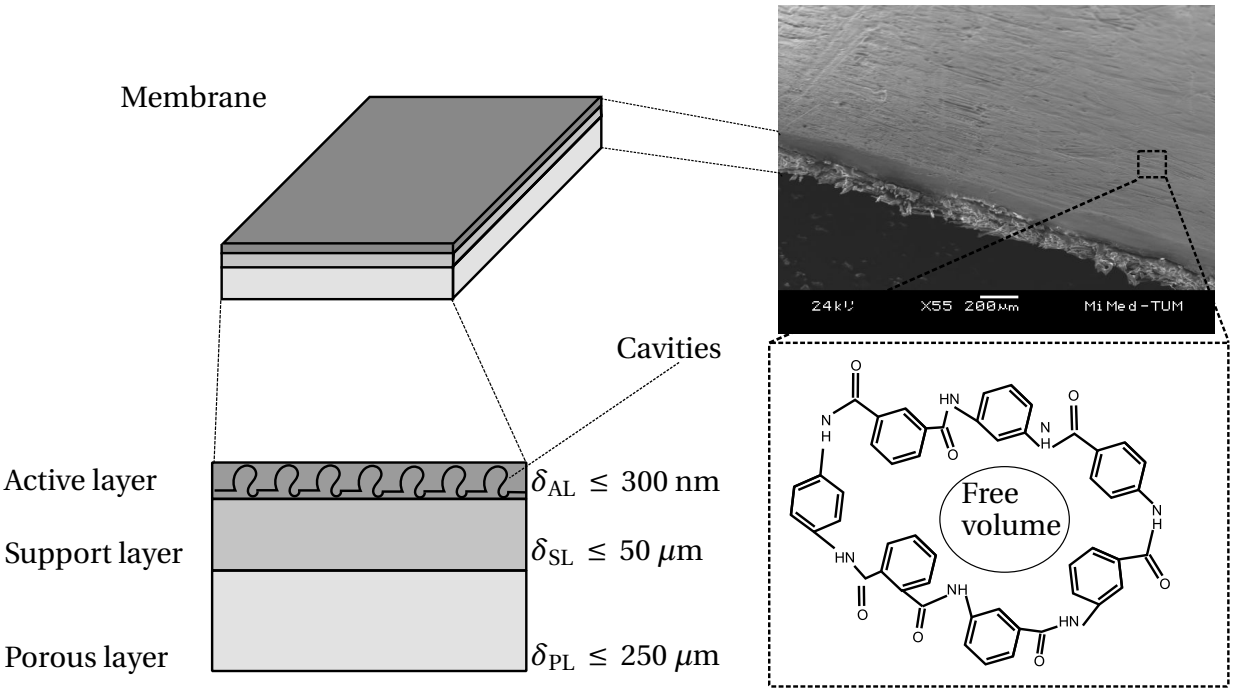

Figure 2.1: RO membrane at microscopic scale, adapted from [47, 48].

2.3 Water and Salt Transport in Reverse and Forward Osmosis Processes

In the work at hand, RO and FO processes are used for studying the dynamic mass transport across the membrane. Therefore, both osmotic processes are explained based on the solution-diffusion model [49] in the present section. The classical solution-diffusion model is based on the following assumptions [49, 50]:

- The AL is considered to be dense and the transport of water or salt molecules through the AL takes place solely through diffusion.
- The AL is seen as a very thin immobile smooth sheet without pores, which is resistant against pressure gradients.
- The permeability coefficients of the AL are constant.
- Exponential functions are linearized.

- Water and salt fluxes within the AL are decoupled.
- At the AL surface, chemical equilibrium prevails between the solution inside and outside the AL.

As only sodium chloride is considered in the present work, the index s is used for the salt. Figure 2.2 shows the resulting profiles of the hydrostratic pressure p, the salt mass fraction ξ and the chemical potential of the solvent μ_{sv} for the RO and FO process based on the solution-diffusion model. The profiles are presented within the respective high- (RO: feed, FO: draw) and low-concentrated solutions (RO: permeate, FO: feed), as well as within the membrane. The membrane is simplified with only two layers AL and PS, which combines the SL and PL, cf. Figure 2.1.

Main aspects of the RO process (Figure 2.2a):

- Pressure: As stated in Section 2.1, the hydrostatic pressure of the feed has to overcome the osmotic pressure difference across the AL in order to initiate the RO process. According to the solution-diffusion model, the pressure within the AL corresponds to the feed pressure despite the compactness of the AL [49].
- Chemical potential: At the AL surface, chemical equilibrium prevails [49]. Due to the elevated pressure on the feed side, the chemical potential of the feed exceeds that of the permeate.
- Water and salt flux: Due to the difference in the chemical potential across the AL, water is transported from the high- to the low-concentrated solution, represented by j_{w}. The salt is transported, represented by j_{s}, due to the negative concentration gradient across the AL in the same direction as the water flux.
- Salt mass fraction: The formation of the resulting concentration profiles, which are dependent on j_{P} and on the diffusive salt transport, represented by $\Gamma \frac{\partial \xi}{\partial y,z}$, are called concentration polarization. This is explained in more detail in Section 2.4. In osmotic processes, two types of concentration polarization are distinguished. The ECP describes the estab-

lishing concentration gradient within the boundary layer of the high-concentrated solution at the AL ($\xi_{F,b} \rightarrow \xi_{F,AL}$) or of the low-concentrated solution at the PS ($\xi_{P,PS} \rightarrow \xi_{P,b}$). The increased salt concentration at the surface of the AL results in an increased osmotic pressure, along with an increased salt flux attributed to a higher salt gradient across the AL. The ICP is defined as the establishing concentration profile within the PS ($\xi_{PS,AL} \rightarrow \xi_{PS,P}$). The ICP arises from the permeation of water and salt through the PS, resulting in the accumulation of salt within the PS and the formation of a polarized layer within the PS at the AL [51]. Directly at the AL surface, the jump of the concentration is due to the change from a two-phase (salt-water) to a three-phase system (salt-water-AL).

In general, the resulting profiles of p, ξ and μ_{sv} are qualitatively similar to the RO process with the following differences.

Main aspects of the FO process (Figure 2.2b):

- Pressure: The pressure is equal in both solutions and the membrane.
- Chemical potential: The difference in the chemical potential as driving potential across the AL is established by the difference in salt concentration of each side.
- Water and salt flux: The water flows from the low- to the high-concentrated solution. The salt flux is contrary due to the negative concentration gradient across the membrane.
- Salt mass fraction: For the considered membrane orientation (AL → draw solution), the draw solution is diluted towards the AL due to the water transport from the feed to the draw. Compared to the RO process, the ICP is more pronounced, which results from the contrary salt and water flux [51]. Both the water flux towards the draw side and salt flux from the draw to the feed side concentrates the feed solution. Moreover, the ICP in the PS is not significantly affected by the convective conditions in the channel of the low-concentrated solution. This also contributes to the

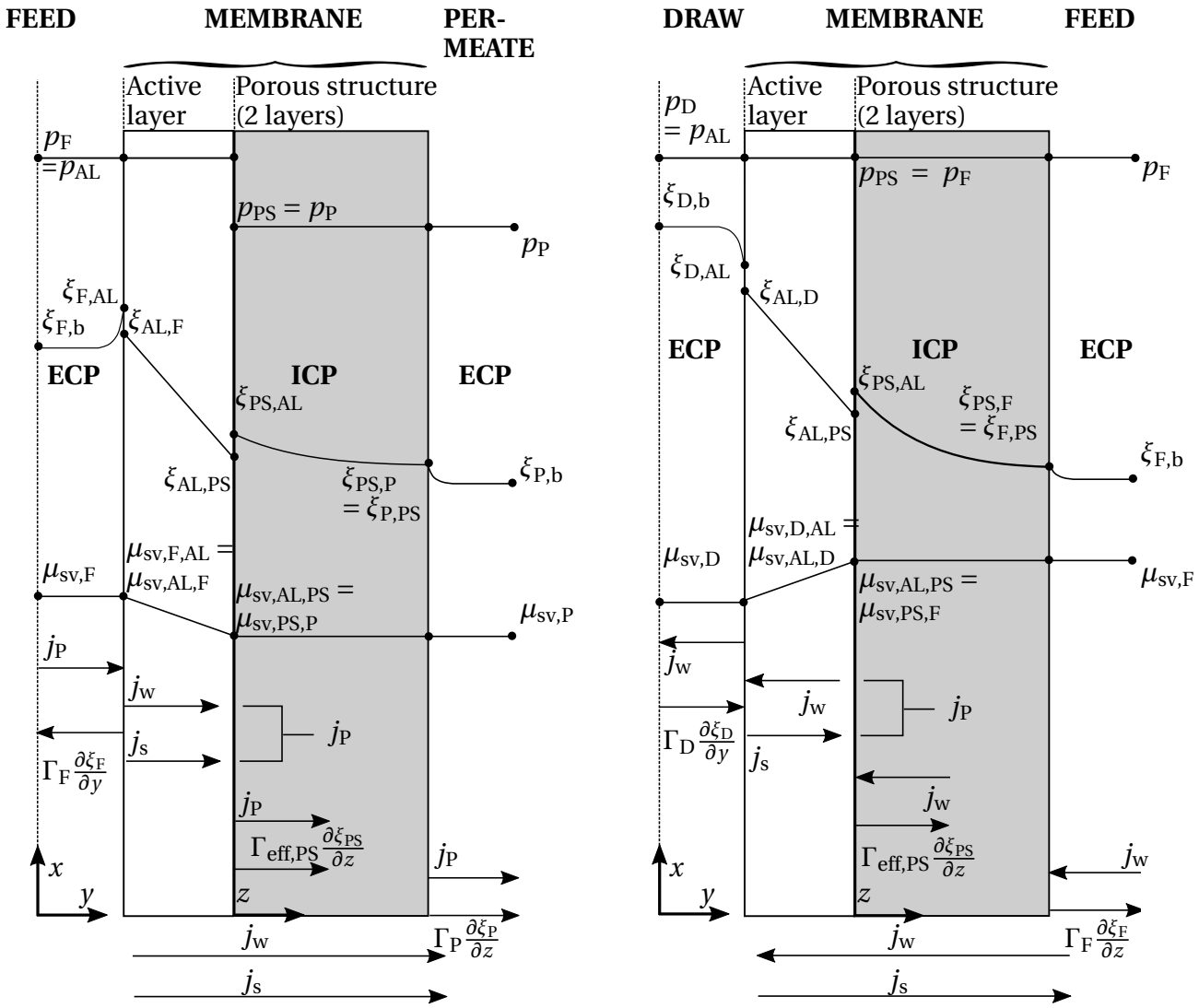

(a) Reverse Osmosis. **(b)** Forward Osmosis.

Figure 2.2: Profiles of pressure p, salt mass fraction ξ and chemical potential μ_{sv} for the RO and FO process from the solutions (subscripts F, D and P) to the membrane (subscripts AL and PS).

formation of a large concentration gradient. In FO, the ICP has a greater impact on the amount of water flux than the ECP at both solution sides [51].

As described before, these profiles are based on the assumptions of the

solution-diffusion model. The equations to calculate the water and salt flux j_w and j_s across the AL are given without derivation, but are extensively described in [49]. For common seawater desalination applications, the water and salt transport across the AL can be well described with the solution-diffusion model with [49]

$$j_w = A_{mem}\, \rho_{F,AL} \left((p_F - p_P) - (\pi_{F,AL} - \pi_{PS,AL}) \right) \tag{2.5}$$

and

$$j_s = B_{mem}\, \rho_{F,AL} \left(\xi_{F,AL} - \xi_{PS,AL} \right). \tag{2.6}$$

A_{mem} and B_{mem} are the water and salt permeability of the AL. The permeate flux j_P is the sum of the salt and water flux within the membrane and can be calculated with

$$j_P = j_s + j_w. \tag{2.7}$$

A_{mem} and B_{mem} are functions of the pH value, salt mass fraction, temperature and pressure. For comparative experiments regarding the mass transfer at the membrane, these boundary conditions have to be the same.

2.4 Fundamentals of Concentration Polarization in Osmotic Processes

As written before, the concentration polarization between bulk and membrane is formed by the equilibrium of the convective and diffusive salt transport at the interface of the AL or PS and the solutions, which is called ECP. Within the PS, a concentration gradient also establish, which is called ICP. In the work at hand, FO and RO processes are used to study the dynamic mass transport across the membrane. In the present section, the basic equations for the ECP and ICP are presented for the RO process at the feed side, but also applies for the FO process. The equations can be easily derived by replacing the subscript F with D and P with F, respectively.

ECP: Governing equations
The steady-state convection-diffusion equation for the salt transport within

the boundary layer on the feed side can be derived according to Melin et al. [49] and Bitter [52] as

$$\frac{\partial}{\partial y}\left(\xi_{\mathrm{F}} j_{\mathrm{P}}\right) - \frac{\partial}{\partial y}\left(\rho_{\mathrm{F}} \Gamma_{\mathrm{F}} \frac{\partial \xi_{\mathrm{F}}}{\partial y}\right) = 0. \tag{2.8}$$

The boundary layer is commonly described by the film model, which assumes that the mass transport takes places in a thin layer close to the membrane surface [53]. Assuming constant material and physical properties, Equation (2.8) can be analytically solved and reformulated to calculate the ECP using Equations (2.5) and (2.6) to

$$\xi_{\mathrm{F}}(y)\, j_{\mathrm{P}} + j_{\mathrm{s}} - \rho_{\mathrm{F}} \Gamma_{\mathrm{F}} \frac{\mathrm{d}\xi_{\mathrm{F}}(y)}{\mathrm{d}y} = 0. \tag{2.9}$$

Using the boundary conditions

$$\xi_{\mathrm{F}}(y)\Big|_{y = \delta_{\mathrm{ECP}}} = \xi_{\mathrm{F,AL}} \quad \text{and} \quad \frac{\mathrm{d}\xi_{\mathrm{F}}(y)}{\mathrm{d}y}\Big|_{y = 0} = 0,$$

Equation (2.9) can be integrated over the boundary layer thickness δ_{ECP}. The salt mass fraction at the AL $\xi_{\mathrm{F,AL}}$ can then be calculated with [49]

$$\xi_{\mathrm{F,AL}} = \xi_{\mathrm{PS,AL}}\left(1 - e^{\frac{j_{\mathrm{P}}}{\rho_{\mathrm{F}} \beta}}\right) + \xi_{\mathrm{F,b}}\, e^{\frac{j_{\mathrm{P}}}{\rho_{\mathrm{F}} \beta}}, \tag{2.10}$$

with the mass transfer coefficient β. Analogous to the heat transfer problem, β can be derived for a mass transfer problem without a convective flux in y direction ($j_{\mathrm{P}} = 0$) with [53]

$$\beta = -\frac{\Gamma_{\mathrm{F}} \left.\frac{\mathrm{d}\xi_{\mathrm{F}}(y)}{\mathrm{d}y}\right|_{y=0}}{(\xi_{\mathrm{F,AL}} - \xi_{\mathrm{F,b}})}. \tag{2.11}$$

This holds true since, according to Fick's law, the concentration gradient at the static surface is proportional to the salt concentration or mass fraction difference at the membrane ($\xi_{\mathrm{F,AL}} - \xi_{\mathrm{PS,AL}}$) [53]. Using β, the Sherwood number Sh can be calculated with [53]

$$\mathrm{Sh} = \frac{\beta d_{\mathrm{h}}}{\Gamma_{\mathrm{F}}}. \tag{2.12}$$

Sh varies with changing permeate fluxes since $\xi_{\mathrm{F,AL}}$ and therefore β depend on $|j_{\mathrm{P}}|$, cf. Equation (2.10). This change can also be expressed via a Stefan-correction [53]. Therefore, Sh is not only a function of the Reynolds number Re and Schmidt number Sc but also of $|j_{\mathrm{P}}|$:

$$\mathrm{Sh} = f(\mathrm{Re}, \mathrm{Sc}, |j_{\mathrm{P}}|). \tag{2.13}$$

ICP: Governing equations

To calculate the ICP, the salt transport equation within the PS with an effective diffusion coefficient $\Gamma_{\mathrm{eff,PS}}$,

$$\xi_{\mathrm{PS}}(z)\, j_{\mathrm{P}} + j_{\mathrm{s}} - \rho_{\mathrm{PS}} \Gamma_{\mathrm{eff,PS}} \frac{\mathrm{d}\xi_{\mathrm{PS}}(z)}{\mathrm{d}z} = 0, \tag{2.14}$$

has to be solved [54]. The diffusion coefficient has to be modified due to the PS, which represents an additional hindrance, and can be calculated with [54]

$$\Gamma_{\mathrm{eff,PS}} = \Gamma_{\mathrm{PS}} \frac{\epsilon_{\mathrm{PS}}}{\tau_{\mathrm{PS}}^2}. \tag{2.15}$$

ϵ_{PS} is the porosity and τ_{PS} is the tortuosity of the PS. Neglecting the ECP at the permeate side, Equation (2.14) can be solved analogously to before with the boundary conditions

$$\xi_{\mathrm{PS}}(z)\Big|_{z\,=\,0} = \xi_{\mathrm{PS,AL}} \quad \text{and} \quad \frac{\mathrm{d}\xi_{\mathrm{PS}}(z)}{\mathrm{d}z}\Big|_{z\,=\,\delta_{\mathrm{PS}}} = 0.$$

After the integration of Equation (2.14) along δ_{PS}, the result for the salt mass fraction $\xi_{\mathrm{PS,AL}}$ is [54]

$$\xi_{\mathrm{PS,AL}} = \frac{j_{\mathrm{s}}}{j_{\mathrm{P}}} \left(e^{-\frac{j_{\mathrm{P}} \delta_{\mathrm{PS}}}{\rho_{\mathrm{P}} \Gamma_{\mathrm{eff,PS}}}} - 1 \right) + \xi_{\mathrm{P}} e^{-\frac{j_{\mathrm{P}} \delta_{\mathrm{PS}}}{\rho_{\mathrm{P}} \Gamma_{\mathrm{eff,PS}}}}. \tag{2.16}$$

Analysis of the ECP at the high-concentrated side for RO and FO processes

Based on the presented equations, Figure 2.3 exemplary shows the ratio of the salt mass fraction at the AL and bulk $\xi_{\mathrm{F,AL}}/\xi_{\mathrm{F,b}}$ and Sh for increasing $|j_{\mathrm{P}}|$ and β in the range of $\beta = 2.1 \ldots 8.1 \cdot 10^{-5}$ m s^{-1}, common for RO systems. In Figure 2.3a, it can be seen that $\xi_{\mathrm{F,AL}}/\xi_{\mathrm{F,b}}$ increases with increasing $|j_{\mathrm{P}}|$ due to the larger accumulation of salt at the membrane. The lower β the stronger is the

dependence on $|j_P|$. In Figure 2.3b, it can be seen that Sh linearly increases for increasing $|j_P|$. The slope remains constant for different β. Nevertheless, Sh changes more significantly with increasing β than with $|j_P|$. These both figures show that for comparative measurements of different mass transfer efficiencies, not only physical properties, but also $|j_P|$ should be kept constant, especially when comparing $\xi_{F,AL}$.

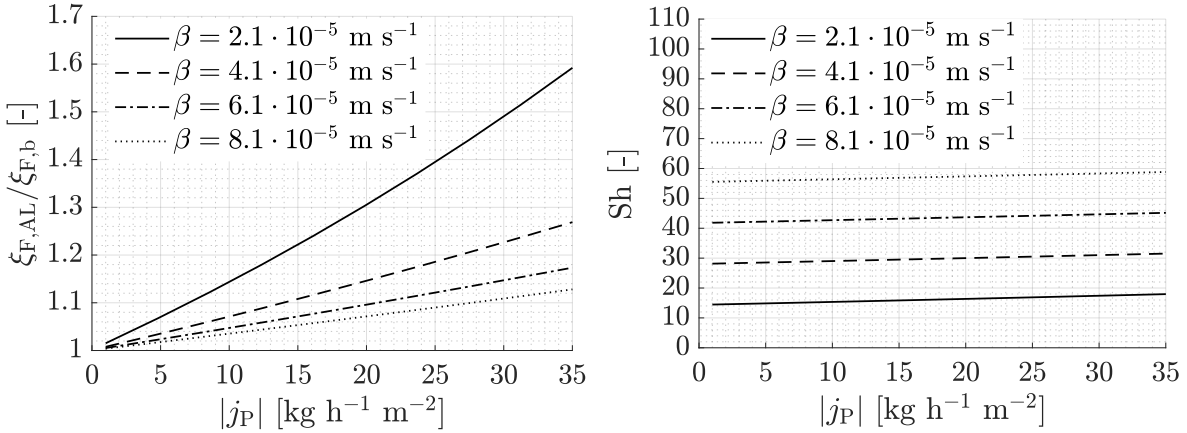

(a) Ratio of the salt mass fraction at the AL and bulk $\xi_{F,AL}/\xi_{F,b}$.

(b) Sherwood number Sh.

Figure 2.3: Dependence of $\xi_{F,AL}/\xi_{F,b}$ and Sh on $|j_P|$ and β; boundary conditions: $\xi_P = 0.0001$, $\xi_F = 0.035$, $T_F = 298.15$ K.

In addition to comparative experiments on steady-state and dynamic mass transfer, FO experiments with the presented membrane orientation (AL → draw solution) are used to analyze the mass transfer enhancement of pulsating flows in spacer-filled channels and provide verification data for the CFD model. Therefore, the transferability has to be proven. This is done by comparing the ratio of the salt mass fraction at the membrane and bulk at the high-concentrated side of the RO and FO process, respectively, cf. Figure 2.4. The figure shows $\xi_{F,AL}/\xi_{F,b}$ and $\xi_{D,b}/\xi_{D,AL}$ plotted for changing $|j_w|$ and β. The calculations were performed with Equations (2.10) and (2.16). In Figure 2.4, it can be seen that for all considered $|j_w|$ and β, the difference in $\xi_{F,AL}/\xi_{F,b}$ and $\xi_{D,b}/\xi_{D,AL}$ is only minor. This holds true, even for the large salt flux difference in the FO and RO process in the range of $\frac{|j_{s,FO}|}{|j_{s,RO}|} = 10 \ldots 12.1$. This means that the

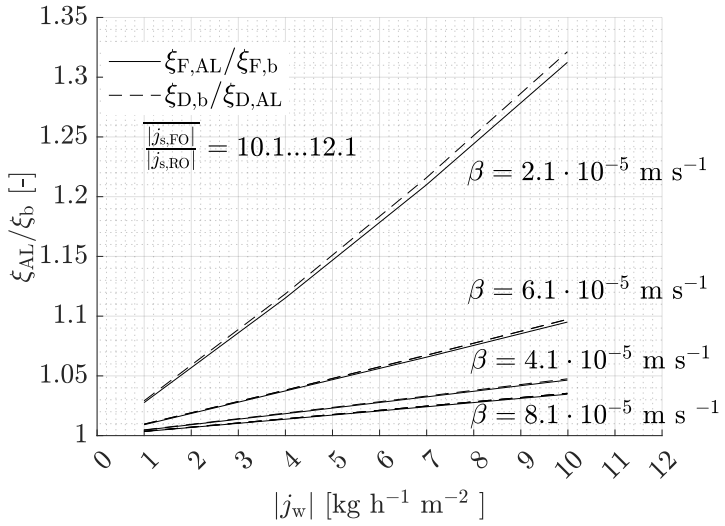

Figure 2.4: Comparison of $\xi_{F,AL}/\xi_{F,b}$ and $\xi_{D,b}/\xi_{D,AL}$ for different $|j_w|$ and β; boundary conditions: $\xi_{P,F} = 0.001$, $\xi_D = 0.15$, $\xi_F = 0.035$, $T_F = T_D = 298.15$ K.

concentration boundary layer at the high-concentrated side for FO and RO processes are similar for comparable mass transfer and water flux conditions. The only difference is that in RO processes the solution concentrates from the high concentration side, while in FO processes it dilutes towards the AL side, which means that $\xi_{F,AL}/\xi_{F,b}$ and $\xi_{D,b}/\xi_{D,AL}$ are reciprocally equal. It is therefore assumed that the behavior of the ECP at the high-concentrated side of RO and FO processes is similar. Mass transfer enhancement techniques should therefore lead to the same quantitative and qualitative result. Due to this similarity, it is legitimate to directly transfer the results from FO experiments regarding the mass transfer enhancement to RO processes and vice versa. This applies to the boundary conditions considered and given membrane orientations, but is independent on β or $|j_w|$.

2.5 Mass Transfer Enhancement in Spacer-Filled Channels

Feed spacers, also known as eddy promoters, are incorporated to enhance mass transfer across the membrane within the feed channel, see Figure 2.5. These spacers also have the task to mechanically stabilize the feed channel.

The feed spacers are characterized by specific parameters, see Figure 2.5. Figure 2.5a shows a reconstructed spacer geometry, which is used in CFD simulations. The mesh angle δ_2 defines the angle between two attached filaments. The mesh clearances L_1 and L_2 represent the distances between two filaments. These characteristics vary depending on the RO application. Larger spacer diameters as well as longer mesh lengths lead to a lower fouling propensity but also to a lower mass transfer effectiveness. The flow attack angle δ_1 also plays a crucial role. In common spiral-wound modules, this angle is 45°, which is the best compromise regarding mass transfer, pressure drop and fouling propensity [55]. This value is also used for the experiments of the work at hand. Figure 2.5b shows a photograph of a real spacer geometry used in the experiments. It can be seen that the spacer filament's diameters are very heterogenous due to the production process. The mesh clearances are $L_1 = L_2 = 4$ mm and the mesh angle $\delta_2 = 90°$. Comparing real and reconstructed spacers for simulations, Horstmeyer et al. [56] found that even small geometric inaccuracies can lead to a different local mass transfer characteristics across the membrane, whereas the averaged characteristics stay similar.

By improving the averaged mass transfer across the membrane, spacers increase the pressure drop along the module. Furthermore, flow stagnation zones appear, characterized by a locally increased fouling propensity and salt concentration. Due to the high pressure drop, RO systems are operated under laminar flow conditions [55, 57, 58]. The Reynolds number decrease along the module depending on the recovery rate. Koutsou et al. [58] observed that at Reynolds numbers of $Re > 40$ the flow can show small periodic and aperiodic dynamic structures with small amplitudes. The formation of steady vortices, velocity oscillations and laminar vortex shedding can occur. Nevertheless, the influence of these flow dynamics on the mass transport across the membrane can be regarded as minimal [57]. Vortex structures and 3D effects start to be

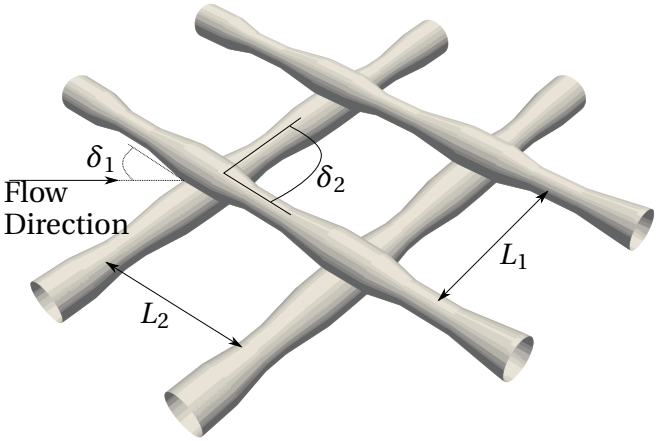

(a) Reconstructed spacer including characteristic parameters: flow attack angle δ_1, mesh angle δ_2 and filament clearances $L_{1,2}$; adapted from [59].

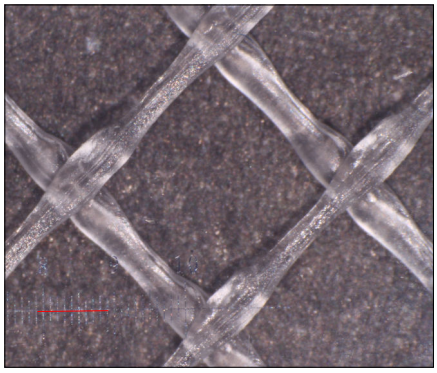

(b) Image of feed spacer from DOW spiral-wound module; $L_1 = L_2 = 4$mm, $\delta_2 = 90°$; adapted from [59].

Figure 2.5: Images of a real and reconstructed feed spacer filament for CFD simulations.

significant at Reynolds numbers of Re > 800 [55]. According to Koutsou et al. [58], Reynolds numbers of Re > 500 are rarely reached in small and medium RO applications.

Schock and Miquel [60] developed practical correlations for the Sherwood number in spiral-wound modules. They found that the mean Sherwood number Sh correlates to Sherwood number correlations in turbulent channels. The resulting equation for RO modules is:

$$\mathrm{Sh} = 0.065\,\mathrm{Re}^{0.875}\mathrm{Sc}^{0.25}. \tag{2.17}$$

This equation is used for the further investigations in this work. The Reynolds number Re for the spacer filled channel is

$$\overline{\mathrm{Re}} = \frac{\langle \overline{\mathbf{u}}_\mathrm{F} \rangle d_\mathrm{h}}{\nu_\mathrm{F}}, \tag{2.18}$$

with the hydraulic diameter d_h defined as [60]

$$d_\mathrm{h} = \frac{4\epsilon}{2H^{-1} + (1-\epsilon)A_{\mathrm{v,sp}}}. \tag{2.19}$$

$A_{v,sp}$ is the volume specific area, H the channel height and ϵ the volume fraction.

Longitudinal vortices can enhance the local mixing and therefore heat or mass transfer by several hundred percent [61]. Winglet type eddy promoters showed the best compromise between pressure loss and heat transfer enhancement. Due to the similarity of the scalar heat and salt mass transfer in osmotic membrane systems, these findings can be transferred to the mass transfer in RO or FO processes. The strength of vortices inside a computational domain can be quantified by the absolute vorticity flux Ω defined by

$$\Omega = \frac{\int |\Lambda| \mathrm{d}A}{A}. \tag{2.20}$$

Here, Ω is the integral of the vorticity Λ over the flow cross section A. Chang et al. [62] and Habchi et al. [63] showed that an increased heat transfer qualitatively correlates with a high vorticity flux Ω. According to Lemenand et al. [64], not only the value that can be interpreted as vortex intensity, but also the location of the vortex structure is an important factor. A high vorticity strength does not automatically lead to a high local heat transfer coefficient. Nevertheless, it is an important value to quantify the averaged intensity of vortices or secondary flows, which indicates a strong mixing.

Due to the resulting complex local flow structures in spacer filled channels, mass transfer varies strongly within a mesh filament. In the stagnation zones, mass transfer is strongly dominated by diffusion, while in other regions it is strongly dominated by convective forces.

2.6 Dynamic Mass Transport in Osmotic Membrane Processes

Considering Equations (2.5), (2.6), (2.14) and (2.16), the water and salt flux across the membrane are influenced by flow conditions, concentrations at the AL, pressure and temperature. The focus of this section is the theoretical analysis of the dynamic mass transport across the membrane due to significant periodic changes in pressure or flow conditions.

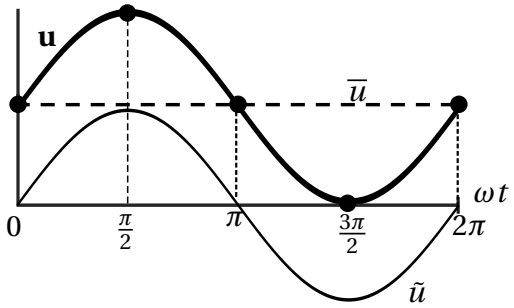

Figure 2.6: Steady-state value $\overline{u}$, periodic part $\tilde{u}$ and summarized velocity u during one pulsation cycle from ωt =0 to $\omega t = 2\pi$.

Generally, unsteadiness in dynamic flow problems can be divided into two categories [65, 66]: aperiodic (broadband, turbulent, white noise, jumps) and periodic (pulsating, oscillating) flows. The terms for describing pulsating flows used in the literature are sometimes contrary. In this work, the definition adopted from Telionis [67] and Cardenas [68] is used. Pulsating flows are characterized by a composition of a mean component $\overline{\mathbf{u}}(\mathbf{x})$, a time dependent oscillating velocity component $\tilde{\mathbf{u}}(\mathbf{x},\mathbf{t})$ and a broadband aperiodic component $\mathbf{u}'(\mathbf{x}, t)$ [67]:

$$\mathbf{u}(\mathbf{x}, t) \;=\; \overline{\mathbf{u}}(\mathbf{x}) \;+\; \tilde{\mathbf{u}}(\mathbf{x}, t) \;+\; \mathbf{u}'(\mathbf{x}, t). \tag{2.21}$$

For laminar flows, $\mathbf{u}'(\mathbf{x}, t)$ vanishes. An oscillating flow is a sub-branch of pulsating flows with vanishing mean part $\overline{\mathbf{u}}(\mathbf{x})$ [67]. The decomposition can be done analogously for the pressure field $p(\mathbf{x}, t)$ or salt mass fraction field $\xi(\mathbf{x}, t)$. The pulsation period can be divided into three phases, cf. Figure 2.6. Figure 2.6 shows the mean value $\overline{u}$, the fluctuating part $\tilde{u}$ and the summarized velocity u during one pulsation period from ωt =0 to ωt =2π. The first acceleration phase is from ωt =0 to $\omega t = \pi/2$, where the highest average velocity is reached. The deceleration phase is between $\omega t = \pi/2$ and $\omega t = 3/2\pi$, before the initial mean velocity is reached again at $\omega t = 2\pi$.

Three parameters characterize periodic flows: Reynolds number, amplitude and frequency [69]. The amplitude can be represented with the amplitude ratio AR

$$\mathrm{AR} \;=\; \frac{1/V \int_V \varpi_u(\mathbf{x}, t)\mathrm{d}V}{1/V \int_V \overline{\mathbf{u}}(\mathbf{x}, t)\mathrm{d}V} \;=\; \frac{\langle \mathbf{u}(t) - \overline{\mathbf{u}} \rangle_{\max}}{\langle \overline{\mathbf{u}} \rangle}, \tag{2.22}$$

which compares the amplitude ϖ_u of the volume-averaged unsteady velocity to the volume- and time-averaged velocity. The velocity u can be replaced by any other value i. In this case, AR is indicated with a corresponding index i in the work at hand.

Using the amplitude ratio and frequency, another characteristic variable for heat and mass transfer in dynamic flows can be identified:

$$\varpi_x = \frac{\mathrm{AR}\,\langle\overline{u}\rangle}{f}. \tag{2.23}$$

ϖ_x is the local amplitude. It measures the length over which a fluid element is maximally displaced during one half of the pulsation cycle [70]. For sinusoidal flows, which are mainly analyzed in this work, the local amplitude can be easily calculated with AR. Kurzweg [71] showed that the diffusivity correlates to this parameter and the Womersley number. The Womersley number Wo,

$$\mathrm{Wo} = d_\mathrm{h}\sqrt{\frac{\omega}{\nu}} = \sqrt{2\,\pi\,\overline{\mathrm{Re}}\cdot\mathrm{Sr}}, \tag{2.24}$$

which compares the dynamic inertial to viscous forces, is the dimensionless frequency. It can be calculated with $\overline{\mathrm{Re}}$, cf. Equation (2.18), and Sr. Sr is the Strouhal number and is defined as

$$\mathrm{Sr} = \frac{f\,d_\mathrm{h}}{\langle|\overline{u}|\rangle}. \tag{2.25}$$

To describe the averaged mass transfer at the membrane in periodic flows, the mass transfer coefficient β is integrated over one time period $\omega t = 0 \ldots 2\pi$

$$\overline{\beta} = \frac{1}{2\pi}\int_0^{2\pi}\frac{\Gamma\left.\frac{\mathrm{d}\xi}{\mathrm{d}y}\right|_{y=0}}{\xi_\mathrm{AL}-\xi_\mathrm{b}}\mathrm{d}\omega t. \tag{2.26}$$

The averaged coefficient is used to calculate the averaged Sherwood number

$$\overline{\mathrm{Sh}} = \frac{\overline{\beta}d_\mathrm{h}}{\Gamma}. \tag{2.27}$$

These dimensionless values are used for the further analyses and to compare the steady-state with the dynamic mass transport.

Having now the basic tools and definitions to describe dynamic flows and mass transport, the present section continues with the fundamental analysis of the mass transport dynamics in the boundary layers as well as within the membrane.

2.6.1 Analysis of the Dynamic Mass Transfer in Reverse Osmosis Processes due to Pressure Changes

The dynamic conjugate mass transfer problem consists of the mass transport within the boundary layers at the high- and low-concentrated side, within the AL and within the PS. For an efficient simulation approach, it is crucial to know, which transport resistance dominates the dynamic transport process. In this subsection, the dynamic mass transport for the complete problem is studied. It is the aim of this analysis to identify the time-limiting dynamic process of the conjugate mass transfer problem for a large periodic change in pressure and therefore in permeate flux. The problem is discussed for the RO process.

The analysis is performed with following assumptions and boundary conditions:

- According to preliminary studies [8], the dynamic mass transport inside the AL and the permeate channel can be neglected. The steady-state diffusion across the AL is described by Equations (2.5) and (2.6) with $A_{\mathrm{mem}} = 7 \cdot 10^{-12}$ m s^{-1} Pa^{-1} and $B_{\mathrm{mem}} = 4 \cdot 10^{-8}$ m s^{-1}.
- The bulk feed salt mass fraction is $\xi_{\mathrm{F,b}} = 0.035$.
- The ECP at the permeate side is neglected.
- The problem is considered only as 1D normal to the membrane. Gradients parallel to the membrane are neglected.
- The PS has a thickness of $\delta_{\mathrm{PS}} = 250$ µm.
- The film model is applied. The Sherwood number is constantly set to Sh = 18, which results in a mass transfer coefficient of $\beta = 2 \cdot 10^{-5}$ m s^{-1}.

- To produce a periodic variation of the mass transfer, the pressure sinusoidally changes with an amplitude of 8.5 bar. The pressure pulsations are applied with Equation (2.5).
- The produced flow perturbations normal to the membrane do not influence the main flow ($\tilde{j}_\mathrm{P} << \overline{u}_\mathrm{F}$).

Governing equations and solution procedure

Neglecting the dynamic mass transport across the AL, the 1D mass transfer problem, cf. Figure 2.2a, can be described by the partial differential equations of the transport within the ECP layer at the feed side

$$\frac{\partial \xi_\mathrm{F}}{\partial t} + j_\mathrm{P}\frac{\partial \xi_\mathrm{F}}{\partial y} = -\Gamma_\mathrm{F}\frac{\partial^2 \xi_\mathrm{F}}{\partial y^2}. \tag{2.28}$$

The mass transport within the ICP layer within the PS is described by

$$\frac{\partial \xi_\mathrm{PS}}{\partial t} + j_\mathrm{P}\frac{\partial \xi_\mathrm{PS}}{\partial z} = -\Gamma_\mathrm{eff,PS}\frac{\partial^2 \xi_\mathrm{PS}}{\partial z^2}. \tag{2.29}$$

Both transport equations are discretized using the finite volume method with 40 elements each and numerically solved using the non-linear system solver `fsolve` from MATLAB [72]. The mass transport of the ECP and ICP layer is coupled using the mass balance across the AL,

$$\xi_\mathrm{PS,AL} = \frac{j_\mathrm{s}}{j_\mathrm{s} + j_\mathrm{w}} = \frac{j_\mathrm{s}}{j_\mathrm{P}}. \tag{2.30}$$

j_w and j_s are calculated using Equations (2.5) and (2.6). These equations are solved within an iterative routine in MATLAB [72].

To identify the time-dominating mass transport, two simulation approaches including and neglecting the dynamic mass transport inside the PS are compared, represented by the indices ECP\ICP and ECP+ICP, respectively:

- ECP\ICP: In this model approach, only the dynamic mass transport within the boundary layer on the feed side, cf. Equation (2.28), is calculated. The salt mass fraction within the PS at the AL equals the bulk permeate salt mass fraction ($\xi_\mathrm{P} = \xi_\mathrm{PS,AL}$).

- ECP+ICP: Here, both dynamic transport equations (2.28) and (2.29) with the coupling term (2.30) are solved.

Results

The responses of the permeate flux, feed and permeate salt mass fractions due to periodic pressure changes are used as indicators. Figure 2.7 shows the results of the calculations calculated for a range of excitation Womersley numbers of Wo = 1 ... 19. Figure 2.7a shows the applied pressure signal plotted over ωt. It is a sinusoidal function with an amplitude of ϖ_p = 8.5 bar. This amplitude was chosen to maximize the periodic permeate flux in the range from 0 to $j_{\mathrm{P,max}}$. This periodic change of the permeate flux in turn can be interpreted as small velocity pulsations normal to the membrane.

Before comparing the dynamic behavior of both approaches, the averaged relative difference $\Delta\overline{i}_{\mathrm{rel,ECP-ICP}}$ of both simulation approaches, with $\overline{i} = \overline{j}_{\mathrm{P}}, \overline{j}_{\mathrm{s}}, \overline{\xi}_{\mathrm{F,AL}}, \overline{\xi}_{\mathrm{P}}$, is compared. It is calculated with

$$\Delta\overline{i}_{\mathrm{rel,ECP-ICP}} = \frac{|\overline{i}_{\mathrm{ECP\backslash ICP}} - \overline{i}_{\mathrm{ECP+ICP}}|}{|\overline{i}_{\mathrm{ECP+ICP}}|}. \tag{2.31}$$

Considering the difference in the average permeate flux $\Delta\overline{j}_{\mathrm{P,rel,ECP-ICP}}$, it increases with increasing Wo and stagnates for Wo > 9 at $\Delta\overline{j}_{\mathrm{P,rel,ECP-ICP}} = 2\%$. The relative difference for the average salt mass fraction at the membrane $\Delta\overline{\xi}_{\mathrm{F,AL,rel,ECP-ICP}}$ linearly increases with increasing Wo and also reaches $\Delta\overline{\xi}_{\mathrm{F,AL,rel,ECP-ICP}} = 2\%$ at Wo = 19. Considering the difference in the average salt flux $\Delta\overline{j}_{\mathrm{s,rel,ECP-ICP}}$ and permeate salt mass fraction $\Delta\overline{\xi}_{\mathrm{P,rel,ECP-ICP}}$, the relative difference stays below $\Delta\overline{\xi}_{\mathrm{P,rel,ECP-ICP}} < 0.3\%$. These values are neglected in the following considerations due to the low relative difference of both approaches.

Figure 2.7c shows the permeate flux relative to the temporal maximum flux $j_{\mathrm{P}}/j_{\mathrm{P,max}}$ for both simulation approaches. It can be seen that the amplitudes decrease from 0.5 to 0.2 for larger frequencies. For all considered Wo, both approaches qualitatively show a similar dynamic behavior with only small quantitative deviations. A small phase shift can be identified for increasing Wo.

In Figure 2.7d, the salt mass fraction at the membrane relative to the temporal

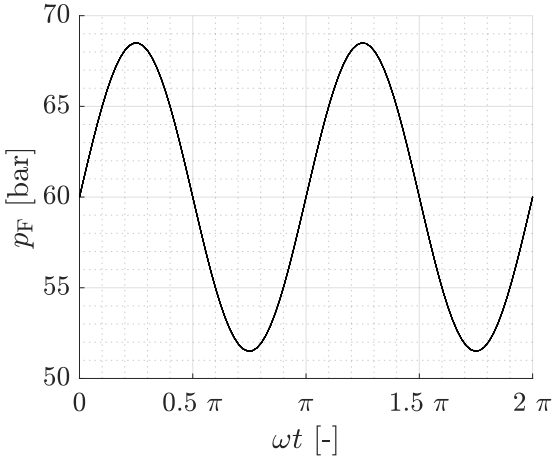

(a) Pressure signal.

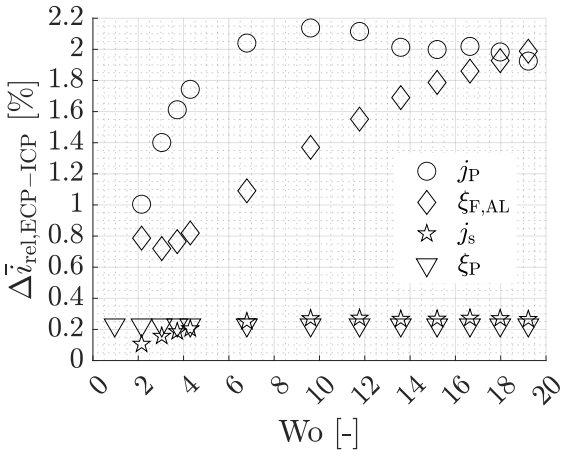

(b) Averaged relative difference between both simulation approaches.

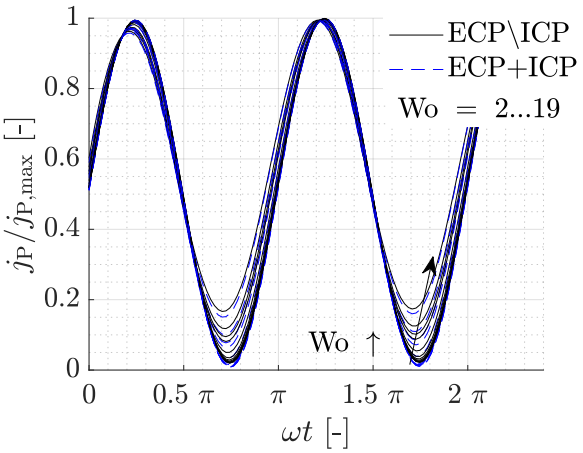

(c) Time-dependent relative permeate flux.

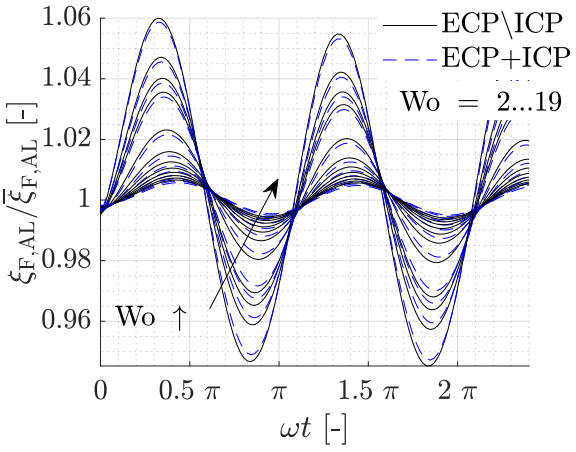

(d) Time-dependent relative feed concentration at the membrane.

Figure 2.7: Comparison of the dynamic mass transfer across the membrane with (ECP+ICP) and without (ECP\ICP) consideration of the dynamic mass transport within the PS.

maximum $\xi_{F,AL}/\xi_{F,AL,max}$ can be seen. Analogous to the considerations of the difference in j_P, both approaches are similar. The amplitude decreases with increasing Wo from 0.06 to 0.02 including a small phase shift.

In general, both approaches show only minor qualitative and quantitative dif-

ferences in their averaged key values and dynamic responses. This is based on the fast mass transport through the PS and the weak dynamic response of $\xi_{F,AL}$. Since $\xi_{F,AL}$ not only depends on j_P, but also on diffusive forces inside the boundary layer at the feed side, the amplitude is smaller. This results in a smaller changing salt mass fraction gradient across the membrane and therefore to small changes of $\xi_{F,AL}$ and $\xi_{PS,AL}$. Moreover, the high selectivity of the membrane results in a very small difference of $\xi_{PS,AL}$ and ξ_P and therefore in a minor impact on the driving forces of j_w and j_s. The dynamic mass transport within the PS therefore has generally a minor influence on the overall mass transport across the membrane. Under these conditions, the mass transport resistance within the PS can be assumed as non-significant and quasi-steady-state, which leads to the dynamic similarity of both simulation approaches (ECP\ICP and ECP+ICP). Due to this similarity, even under these extreme dynamic conditions, it can be concluded that for the problems considered in this work, the dominating limiting dynamic process is the mass transport in the boundary layer at the feed side.

2.6.2 Interaction of Pulsating Flows with the Concentration Boundary Layer in Empty Channels

After identifying the dominant mass transport process, the analytical solution for pulsating flows including a membrane in an empty channel is presented in the following. It is used to explain basic aspects of pulsating flows regarding flow dynamics, mass transfer enhancement, mass transfer dynamics and pressure losses. Moreover, it provides the basis for the interpretation of the results presented in Chapter 5. To provide a convenient reading, the complete derivation of the governing equations is given in Appendices A and B. Only the RO process and the feed side are considered.

The analysis is performed using the following assumptions:

- The configuration can be seen in Figure 2.8. The channel has a height of 1.25 mm, which corresponds to the hydraulic diameter of the spacer-filled channels used in this work. The coordinate system has the basis in

the center of the channel and the axis coordinate y, which ranges from 0 to H. H is defined as half the height. x is the axial direction, parallel to the membrane, and y normal to the membrane.

- The flow is incompressible and hydrodynamically developed.
- Salt water with a bulk salt mass fraction of $\xi_{F,b} = 0.035$ is considered as feed solution.
- The osmotic pressure is a linear function of the salt mass fraction with the proportional factor C_π [49].
- Transport and thermo-physical properties are constant. This lead to constant Schmidt number of Sc = 600.
- The time- and volume-averaged velocity $\langle \overline{u}_F \rangle$ is set to $\langle \overline{u}_F \rangle = 0.1$ m s^{-1}, which corresponds to a Reynolds number of $\overline{\mathrm{Re}} = 136.8$ and Peclet number of up to Pe > 10^4. The velocity normal to the membrane due to the permeate flux does not affect the tangential velocity profile ($|\overline{u}_F| >> |v_w|$).
- The film model assumptions according to Section 2.4 are valid.
- The membrane is ideal ($B_{mem} = 0 \leftrightarrow \xi_P = 0$).
- According to Section 2.6.1, mass transport dynamics within the AL and PS of the membrane are neglected.

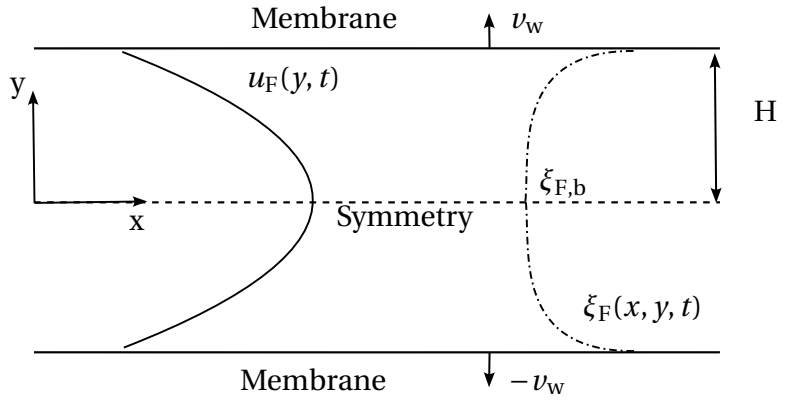

Figure 2.8: Channel Configuration.

Governing equations

Using these given premises, the momentum balance in the feed channel reduces to

$$\frac{\partial u_\mathrm{F}}{\partial t} = -\frac{1}{\rho_\mathrm{F}}\frac{\partial p_\mathrm{F}}{\partial x} + \nu_\mathrm{F}\frac{\partial^2 u_\mathrm{F}}{\partial y^2}. \tag{2.32}$$

The salt mass balance is given by

$$\frac{\partial \xi_\mathrm{F}}{\partial t} + u_\mathrm{F}\frac{\partial \xi_\mathrm{F}}{\partial x} = \frac{\partial}{\partial y}\left(\Gamma_\mathrm{F}\frac{\partial \xi_\mathrm{F}}{\partial y}\right). \tag{2.33}$$

The analytical solutions for pulsating flows in empty channels, which can be represented by a Fourier type velocity

$$u_\mathrm{F}(y,t) = \overline{u}_\mathrm{F}(y) + \sum_{n=1}^{\infty} u_{\mathrm{F,n}} e^{i\omega n t} \tag{2.34}$$

and pressure gradients

$$-\frac{1}{\rho_\mathrm{F}}\left(\frac{\partial p_\mathrm{F}}{\partial x}\right) = P_\mathrm{F} = \overline{P}_\mathrm{F} + \sum_{n=1}^{\infty} P_{\mathrm{F,n}} e^{i\omega n t}, \tag{2.35}$$

were developed by Haddad et al. [23] based on different studies [73, 74, 75, 76]. The solution for the velocity is

$$\begin{aligned} u_\mathrm{F}(y,t) = \frac{3}{2}\overline{u}_\mathrm{F}\Bigg(&\left(1-\frac{y^2}{H^2}\right) \\ &- \Re\left\{\sum_{n=1}^{\infty} i\frac{P_{\mathrm{F,n}}\nu_\mathrm{F}}{\overline{P}_\mathrm{F}\omega n H^2}\left(1-\frac{\cosh\left(y\sqrt{\frac{i\omega n}{\nu_\mathrm{F}}}\right)}{\cosh\left(\mathrm{H}\sqrt{\frac{i\omega n}{\nu_\mathrm{F}}}\right)}\right)e^{i\omega n t}\right\}\Bigg). \end{aligned} \tag{2.36}$$

For the mass transport problem, according to [73], a solution for ξ_F can be found in the form of

$$\xi_\mathrm{F}(x,y,t) = \xi_\mathrm{F}(x,y) + \sum_{n=1}^{\infty} \Re\left\{\frac{\partial \overline{\xi}_\mathrm{F}}{\partial x}\Psi_\mathrm{n}(y) e^{i\omega n t}\right\}, \tag{2.37}$$

with $\frac{\partial \overline{\xi}_\mathrm{F}}{\partial x}$ =const. This gradient is approximated with the salt mass fractions at the end $\overline{\xi}_\mathrm{R}$ and beginning of one module $\overline{\xi}_\mathrm{F}$,

$$\frac{\partial \overline{\xi}_\mathrm{F}}{\partial x} \cong \frac{\overline{\xi}_\mathrm{R} - \overline{\xi}_\mathrm{F}}{l_\mathrm{mod}} = \frac{\mathrm{RR}}{1-\mathrm{RR}}\frac{\overline{\xi}_\mathrm{F}}{l_\mathrm{mod}}. \tag{2.38}$$

For common module recovery rates in RO systems of RR = 0.15, a module length of $l_{\mathrm{mod}} = 1$ m, and a mean feed salt mass fraction of $\overline{\xi}_{\mathrm{F}} = 0.035$, the gradient has a value of 0.0062 m^{-1}.

Analogous to the solution presented in [73], the solution for the local component $\Psi_{\mathrm{n}}(y)$ is

$$\begin{aligned}\Psi_{\mathrm{n}}(y) &= c_2 \sinh\left(y\sqrt{\frac{i\omega n}{\Gamma_{\mathrm{F}}}}\right) + c_3 \cosh\left(y\sqrt{\frac{i\omega n}{\Gamma_{\mathrm{F}}}}\right) \\ &+ \frac{p_{\mathrm{F,n}}}{i^2\omega^2 n^2}\left(\frac{\mathrm{Sc}}{\mathrm{Sc}-1}\frac{\cosh\left(y\sqrt{\frac{i\omega n}{\nu_{\mathrm{F}}}}\right)}{\cosh\left(H\sqrt{\frac{i\omega n}{\nu_{\mathrm{F}}}}\right)} - 1\right),\end{aligned} \tag{2.39}$$

with $c_2 = 0$ and

$$\begin{aligned}c_3 = &\frac{-p_{\mathrm{F,n}}}{i^2\omega^2 n^2(\mathrm{Sc}-1)\cosh\left(H\sqrt{\frac{i\omega n}{\Gamma_{\mathrm{F}}}}\right)} \\ &\frac{\left(\rho_{\mathrm{F}}\overline{\xi}_{\mathrm{F}}A_{\mathrm{mem}}C_\pi - \overline{j}_{\mathrm{P}} + \rho_{\mathrm{F}}\sqrt{i\omega n\nu_{\mathrm{F}}}\tanh\left(H\sqrt{\frac{i\omega n}{\nu_{\mathrm{F}}}}\right)\right)}{\left(\rho_{\mathrm{F}}\overline{\xi}_{\mathrm{F}}A_{\mathrm{mem}}C_\pi - \overline{j}_{\mathrm{P}} + \rho_{\mathrm{F}}\sqrt{i\omega n\Gamma_{\mathrm{F}}}\tanh\left(H\sqrt{\frac{i\omega n}{\Gamma_{\mathrm{F}}}}\right)\right)}.\end{aligned} \tag{2.40}$$

These equations are employed to examine the dynamic interplay between the salt mass fraction, velocity fields, and mass transfer at the membrane. To achieve this objective, indicators such as the phase shift of the salt mass fraction at the membrane $\varphi_u(\xi_{\mathrm{F,AL}})$ relative to $\langle u_{\mathrm{F}}(t)\rangle$, cf. Figure 2.9a, the ratio of the amplitude ratios of $\xi_{\mathrm{F,AL}}(t)$ and $\langle u_{\mathrm{F}}(t)\rangle$, cf. Figure 2.9b and the change in the Sherwood number between pulsating and steady-state cases $\overline{\mathrm{Sh}}_{\mathrm{puls}}/\overline{\mathrm{Sh}}_{\mathrm{stst}} - 1$, cf. Figure 2.9c, are analyzed.

Influence of axial pulsating flows on the salt mass fraction

In Figure 2.9a, it can be seen that $\varphi_u(\xi_{\mathrm{F,AL}})$ asymptotically decreases to $\varphi_u(\xi_{\mathrm{F,AL}}) = \frac{\pi}{2}$ for Wo = 0.4...13.9. For Wo ≥ 13.9, $\varphi_u(\xi_{\mathrm{F,AL}})$ remains constant. A similar behavior can be observed for $\mathrm{AR}_\xi/\mathrm{AR}$, cf. Figure 2.9b. The ratio asymptotically decreases for increasing Wo from $\mathrm{AR}_\xi/\mathrm{AR} = 0.13$ at Wo = 0.3 to $\mathrm{AR}_\xi/\mathrm{AR} = 0$ for Wo > 2. This is independent of AR. Considering the phase shift observations, it can be assumed that the dynamic response of pulsating flows on the concentration boundary layer does not change significantly for

Wo > 4.4. Moreover, for Wo > 2, the amplitude of $\xi_{\mathrm{F,AL}}(t)$ tends towards 0 and a quasi-steady-state profile can be assumed. This behavior is also independent of AR. Hence, large axial perturbations in the flow do not necessarily result in significant perturbations within the concentration boundary layer. This is based on the fact that $\frac{\partial \bar{\xi}_{\mathrm{F}}}{\partial x}$ is much smaller compared to the gradient normal to the membrane. Perturbations in the salt mass fraction resulting from pulsations are strongly dependent on both the magnitude of the gradient aligned with these pulsations and on Wo. Therefore, to produce significant pulsation-induced disturbances, it is necessary that the pulsation has to be aligned parallel to the prevailing salinity gradient.

Influence of axial pulsations on the mass transfer

Besides $\mathrm{AR}_\xi/\mathrm{AR}$, $\overline{\mathrm{Sh}}_{\mathrm{puls}}/\overline{\mathrm{Sh}}_{\mathrm{stst}}$ also decreases for increasing Wo for constant local amplitudes ϖ_x = const., cf. Figure 2.9c. This decrease results from a decrease in transported salt for a fixed time-averaged mass flow rate, based on an enhanced axial mass transport in the negative x direction for increasing excitation frequencies and local amplitudes [21, 22]. This increase opposes the concentration of the feed and consequently results in a decrease when compared to the steady-state flow. Using analogous assumptions, Watson [73], Brereton and Jalil [77], Hemida [15] and Blythman [78] theoretically studied mass and heat transfer enhancement of oscillatory and pulsating flows. The studies showed that the heat transfer reduces due to the enhanced axial diffusion in pulsating flows for a constant heat flux or wall temperature. The magnitude is dependent on the product of the fluctuating velocity and temperature $\tilde{u}\tilde{T}$, Wo and AR.

Enhanced axial diffusion is also observed in spacer-filled channels when operated with pulsating flows. However, the findings concerning local mass transfer across the membrane cannot be directly extrapolated from the empty channel. In preliminary studies, it could be shown that pulsating flows can increase the local Sherwood number [8]. The use of pulsating flows in spacer-filled channels leads to a more complex response of flow dynamics. In addition to the generation of vortex structures, the induced disturbances occur in both tangential and normal directions relative to the membrane [8, 33, 34].

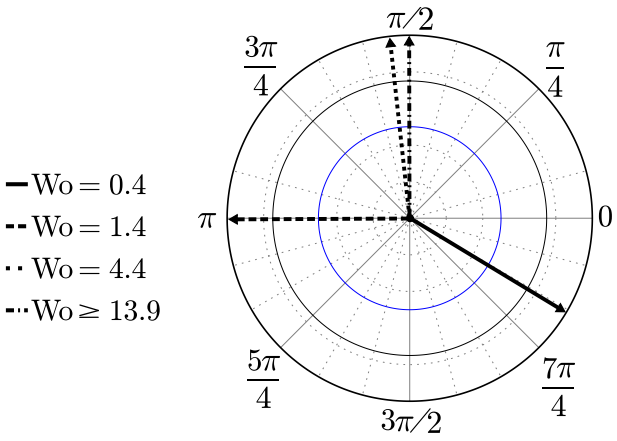

(a) Phase shift $\varphi_u(\xi_{\mathrm{F,AL}})$ between $\xi_{\mathrm{F,AL}}$ and $u_{\mathrm{F}}(t)$ plotted for different Wo at AR= 1, adapted from [80].

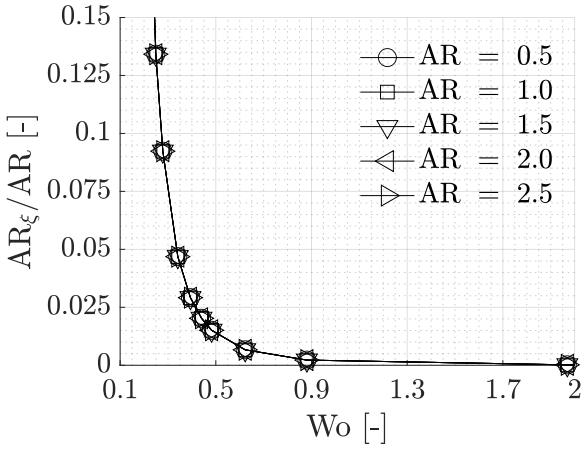

(b) Amplitude ratio of salt mass fraction and velocity $\mathrm{AR}_\xi/\mathrm{AR}$ plotted over Wo.

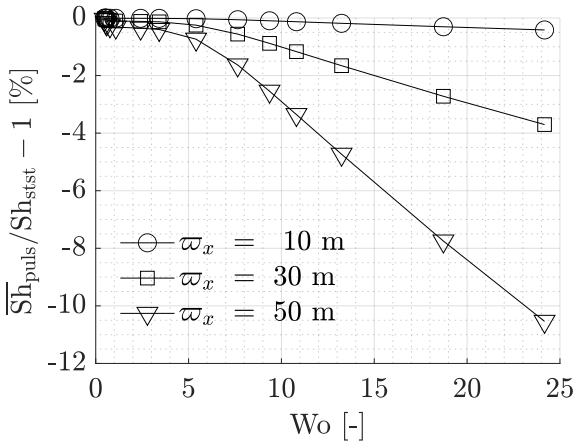

(c) Change of $\overline{\mathrm{Sh}}_{\mathrm{puls}}/\overline{\mathrm{Sh}}_{\mathrm{ststst}}$ plotted over Wo for different ϖ_x.

Figure 2.9: Influence of pulsating flows on dynamic mass transfer in empty RO channels at $\overline{\mathrm{Re}} = 136.8$.

Influence of pulsations normal to the membrane on the mass transfer

The potential for mass transfer enhancement due to pulsations normal to the membrane is demonstrated in Figure 2.10. These results are based on the simulations described in Subsection 2.6.1. Here, $\mathrm{EMT}_{\mathrm{F,ECP}}$ and the change of the time- and volume-averaged local relative salt mass fraction gradient calcu-

lated with

$$\left\langle \frac{\mathrm{d}\Delta\overline{\xi}_{\mathrm{F,rel,puls-stst}}}{\mathrm{d}y} \right\rangle = \frac{\left\langle \frac{\mathrm{d}\overline{\xi}_{\mathrm{F,puls}}}{\mathrm{d}y} \right\rangle}{\left\langle \frac{\mathrm{d}\overline{\xi}_{\mathrm{F,stst}}}{\mathrm{d}y} \right\rangle} \tag{2.41}$$

is plotted over Wo. The latter value represents the averaged gradient along the boundary layer height referenced by the steady state value. As the Sherwood number remains constant in the case of normal perturbation, the outcome is expressed as the relative enhancement of the ECP, calculated with

$$\mathrm{EMT}_{\mathrm{F,ECP}} = \frac{\overline{\xi}_{\mathrm{F,AL,puls}} - \xi_{\mathrm{F,AL,stst}}}{\xi_{\mathrm{F,AL,stst}}}. \tag{2.42}$$

It can be seen that $\mathrm{EMT}_{\mathrm{F,ECP}}$ asymptotically decreases for increasing Wo. Comparing the local average gradient for different Wo, it can be seen that the time- and volume-averaged local relative salt mass fraction gradient also asymptotically decreases for increasing Wo. This is in accordance with the considerations before. As mentioned earlier, pulsations result in enhanced diffusion along the primary pulsation direction. The pulsations normal to the membrane increase therefore the back transport of the salt from the AL to the bulk. Although the perturbations are minor, even small fluctuations can significantly change the mean values in heat and mass transfer problems due to nonlinear convective terms in the transport equations [53]. The results are also in accordance to Reverberi et al. [79]. They experimentally and numerically studied pressure pulsations with an amplitude of 10 bar, which induce pulsations normal to the membrane by periodically changing the permeate flux. They observed an increase in their time-averaged permeate flux with increasing excitation frequencies.

Conclusion

This brief analysis shows that the perturbations caused by pulsating flows must have certain directional properties to improve mass transfer compared to steady-state. This is one of the reasons why different studies come to opposite conclusions regarding the improvement of mass transfer by pulsating flows [13]. The locally produced perturbations in spacer-filled channels caused by pulsating flows are vortical, parallel and normal to the membrane. This leads to a strongly heterogeneous local mass transfer behaviour [8].

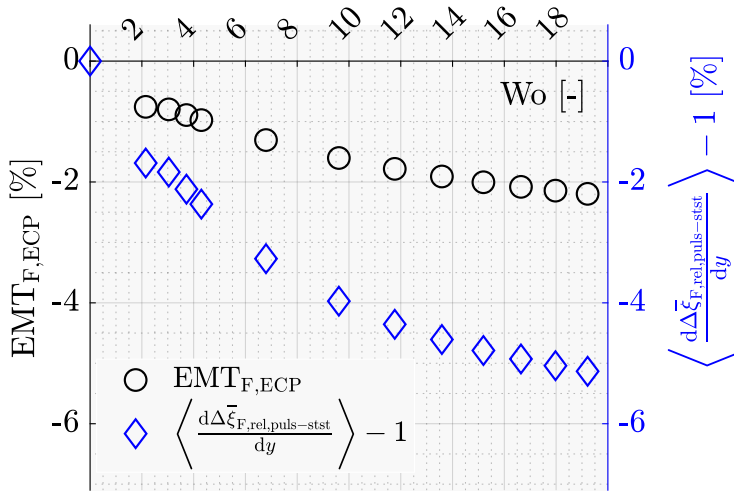

Figure 2.10: Relative change of enhanced mass transfer and the time- and volume-averaged local relative salt mass fraction gradient plotted over Wo for pulsations normal to the membrane, cf. Subsection 2.6.1.

Therefore, the evaluation of the mass transfer enhancement in spacer-filled channels needs a more detailed analysis, which will be presented in Chapter 5. The fundamental transport phenomena discussed in this section provide a basis for interpreting the results in the following chapters.

2.6.3 Increased Energy Demand of Pulsating Flows

To benefit from the mass transfer enhancement, the reduction of the energy requirement due to a lower salt concentration at the membrane has to overcome the pressure loss increase and overall energy consumption of the pump. In this section, the increased pressure loss due to pulsating flows is considered, based on the analytical solution for channels, cf. Section 2.6.2. Figure 2.11 shows the relative time-averaged pressure gradient $\overline{\nabla p}_{\mathrm{F,puls}}/\nabla p_{\mathrm{F,stst}}$ for different pulsation conditions and the ratio of the viscous and inertial acting forces. The analysis is done for an averaged Reynolds number of $\overline{\mathrm{Re}} = 136.8$. Considering the energy requirement of pulsating flows com-

pared to the steady-state operation, it can be generally seen in Figure 2.11a that the pressure gradient increases with higher frequencies as well as higher amplitude ratios. The increase is strongly non-linear for all cases considered. The higher the amplitude ratios are, the stronger is the increase for increasing Womersley numbers, especially for Wo > 10.

The additional energy requirement results from higher viscous as well as inertial forces [20, 80]. According to [80], the pressure gradient is the sum of the velocity gradient $\rho_{\mathrm{F}} \frac{\partial u_{\mathrm{F}}}{\partial t}$ and a normalized wall shear stress $\tau^*_{\mathrm{F,ws}}$, which can be derived by the integration of Equation (2.32) over the cross-section. $\tau^*_{\mathrm{F,ws}}$ is calculated according to [23] and [80] with

$$\tau^*_{\mathrm{F,ws}} = \frac{4}{d_{\mathrm{h}}} \overline{\tau}_{\mathrm{F,ws}} \left(1 - \Re \left\{ \sum_{n=1}^{\infty} \frac{\sqrt{i\nu_{\mathrm{F}}} P_{\mathrm{F,n}}}{\overline{P}_{\mathrm{F,n}} H \sqrt{\omega n}} \left[\frac{\mathrm{J}_{1/2}\left(\sqrt[3]{i} H \sqrt{\omega n / \nu_{\mathrm{F}}} \right)}{\mathrm{J}_{-1/2}\left(\sqrt[3]{i} H \sqrt{\omega n / \nu_{\mathrm{F}}} \right)} \right] e^{i\omega n t} \right\} \right). \tag{2.43}$$

Figure 2.11b shows the evolution of the maximum inertial forces $\left\langle \rho_{\mathrm{F}} \frac{\partial u_{\mathrm{F}}}{\partial t} \right\rangle_{\max}$ and normalized wall shear stress $\tau^*_{\mathrm{F,ws,max}}$ during one pulsation period to the maximum occurring pressure gradient $|\nabla p_{\mathrm{F,max}}|$ for a constant amplitude ratio of the mass flow rate of $\mathrm{AR}_{\dot{m}} = 1$. For Wo > 2, the inertial forces dominate the pressure loss. The reciprocal behavior can be seen for the viscous forces $\tau^*_{\mathrm{F,ws,max}}$. For Wo = 2, both forces are in equilibrium. This analysis shows that the operating parameters have to be carefully chosen. Based on preliminary studies [8], it is expected that the mass transfer enhancement is significantly increased for AR > 0.5 and Wo > 5.6. But higher amplitudes and frequencies lead to a significant higher energy consumption. For Wo > 2, the inertial forces dominate. Therefore, optimum operation parameters have to be chosen, where the additional energy consumption does not over exceed the beneficial effects of an enhanced mass transfer.

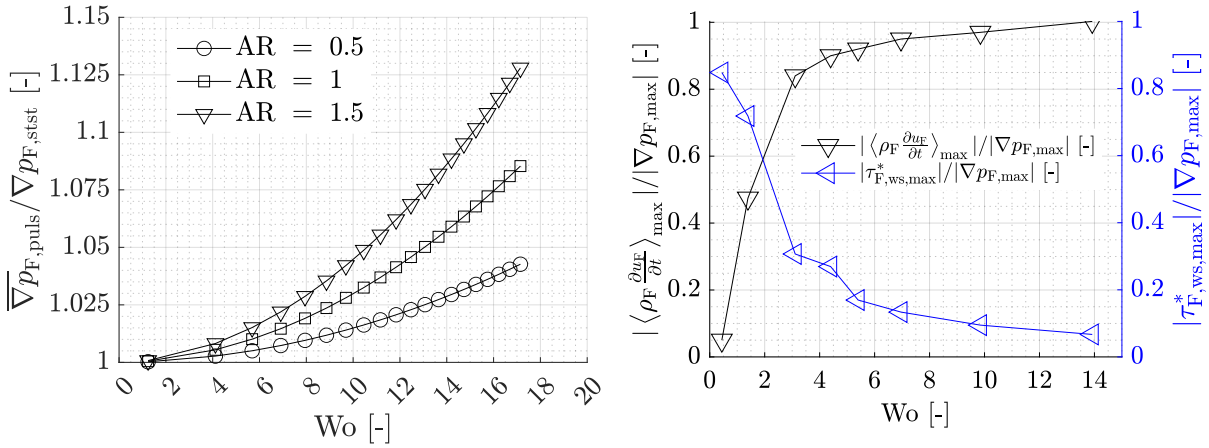

(a) Relative time-averaged pressure gradient for various amplitude ratios.

(b) Ratio of acting forces for an amplitude ratio of 1, adapted from [80].

Figure 2.11: Relative time-averaged pressure gradient $\overline{\nabla p}_{F,puls}/\nabla p_{F,stst}$ and ratios of the maximum inertial forces $\left\langle \rho_F \frac{\partial u_F}{\partial t} \right\rangle_{max}$ and viscous forces $\tau^*_{F,ws,max}$ to the maximum pressure gradient $|\nabla p_{F,max}|$ plotted over Wo.

2.7 Summary of Fundamentals and Basic Analysis

Following conclusions can be drawn from the different analyses in this chapter:

- The fundamental aspects of desalination of aqueous solutions and the phenomenon of concentration polarization were presented. For comparative experiments considering the mass transfer, the pH values, temperature and average water flux have to be the same.
- Due to the similarity of the mass transfer in FO and RO processes, it is legitimate to directly transfer the results from FO experiments regarding the mass transfer enhancement to RO processes and vice versa at the same permeate flux, pH value and flow boundary conditions.
- The dynamic mass transport in the boundary layer on the feed side is the

time-limiting process in RO processes. The mass transport within the AL and PS can be seen as quasi-steady-state due to the large selectivity and slightly changing concentration gradients across the membrane.

- For axial perturbations and Wo > 5, the dynamic response of the salt mass fraction does not significantly change.
- For perturbations parallel to the membrane and increasing Wo, the change of the salt mass fraction significantly decreases and a quasi-steady-state profile can be assumed.
- Perturbations only parallel to the membrane lead to a decrease of the Sherwood number, while already small perturbations normal to the membrane lead to an enhancement of the mass transfer. These normal pulsations lead to an increased back transport of the salt from the membrane to the bulk. In spacer-filled channels, the flow is more complex and need a more detailed analysis.
- Regarding the energy demand of pulsating flows, viscous stresses dominate the energy demand for Womersley numbers of Wo < 2. For Wo > 2, the inertial forces dominate the pressure loss and therefore the needed additional energy demand. The general energy demand non-linearly increases with higher frequencies and amplitude ratios.

These fundamental aspects help to understand the analyses in more complex flows and build the basis for the needed considerations for the evaluation of the mass transfer and energy demand of pulsating flows in RO systems. The work at hand continues with the experimental and numerical methods.

3 Experimental Setup

In the present chapter, two experimental setups will be introduced: a small-scale Reverse Osmosis (RO) unit (cf. Section 3.1) and a bench-scale Forward Osmosis (FO) test rig (cf. Section 3.2). In Section 3.3, the Particle Image Velocimetry (PIV) measurement setup to investigate the flow pattern in spacer-filled channels is introduced. With the PIV data, the measurements to determine the amplitude ratio in pulsating flows will be verified in Section 3.4.

3.1 Small-Scale Reverse Osmosis Unit

A modified brackish water RO system (product name TBL001) from the company TRUNZ Water Systems located in Steinach, Switzerland was used for the experiments. The system can also be found in preliminary studies [59]. The system consisted, as common for RO systems, of two main parts: the pump system (feed and high pressure pump) and the RO modules.

Pump system
The feed pump (low pressure pump, LPP) was a submersible positive displacement helical screw pump with an integrated micro controller for solar applications. The high pressure pump (HPP) was a positive displacement rotary vane pump for pressures up to 20 bar and at least 1.4 bar inlet pressure. Both pumps were driven by a DC motor, which was chosen to minimize electrical conversion losses.

RO modules
The feed water was desalinated in a spiral-wound module (product name TML10D) from the company Toray [81]. It consisted of 5 envelopes with an effective membrane area of $A = 7\ \mathrm{m}^2$ and a low-fouling membrane, containing a spacer with a thickness of $d_{\mathrm{fil}} = 0.86$ mm installed in a pressure vessel. The module had a diameter of $d_{\mathrm{mod}} = 101$ mm and a length of $l_{\mathrm{mod}} = 1.02$ m.

Piping and Instrumentation Diagram (P & ID)
Figure C.1 shows the P & ID of the module test rig. Since it can be found in [59, 82] and is a standard concept, it is placed in the appendix. The complete measurement equipment is summarized in Appendix C.1.

Measurement procedure
A measurement period of 5 min was used after reaching the target pressure and temperature for the steady-state experiments. The temperature required approximately 15 min to reach steady-state. The pressure was reached after a few seconds. The measurement time period allowed an averaging with an adequate amount of data. Two different NaCl feed salt concentrations were used: $\xi_{\mathrm{F}} = 2\ \mathrm{g\,kg^{-1}}$ and $\xi_{\mathrm{F}} = 4\ \mathrm{g\,kg^{-1}}$. These feed solutions were prepared using pure sodium chloride and RO permeate produced by the RO unit with softened water as feed. The pH value was measured with a Mettler Toledo Seven Excellence device and showed a constant behavior. Therefore, the possibility of pH variations influencing the experimental results can be excluded. Details of the measurement procedure can also be found in [82, 83, 84].

3.2 Bench-Scale Forward Osmosis System

The bench-scale FO test rig, which can also be found in part in preliminary studies [20, 59], was used to experimentally investigate the potential for improving mass transfer by pulsating flows. As stated in Section 2.2, the water flux in the FO process is established by the osmotic pressure but not by a hydraulic pressure difference. The low pressure level minimized pressure shocks, which allowed the use of low-pressure measuring devices in the pulsating circuit, allowing for highly accurate measurements of the differential pressures.

The basic mass transfer phenomena in FO and RO systems are identical (cf. Section 2.2), therefore, the findings regarding mass transfer enhancement in pulsating flows are transferable between FO and RO systems, and vice versa.

P & ID

Figure C.2 shows the P & ID of the bench-scale test rig. Analogous to before, the P & ID is included in the appendix. Instead of one hydraulic circuit like in the RO system, the FO system consists of two hydraulic circuits. The pulsations are generated in the draw solution circuit. A damping system downstream of the test cell was installed to completely damp the pulsations. A comprehensive overview of the measurement equipment is provided in Appendix C.2.

Membranes

Different membrane types were used for the FO experiments: RO brackish water membranes from TORAY [81] and seawater membranes from DOW [85]. They were stored in distilled water at room temperature and used within 4 weeks. RO membranes are mechanically more stable than FO membranes, why RO membranes were chosen for the pulsation experiments although the internal concentration polarization (ICP) is more pronounced for RO membranes due to the larger thickness of the porous structure (PS).

Measurement procedure

For each experiment, a new membrane was used to avoid any influence of fouling. To ensure that deviations in a specific membrane sample did not influence the results, the experiments were reproduced with different membrane sheets. Before starting the experiments, the system was operated with deionized water for at least one hour and then two hours with the desired draw and feed salt concentration. After this start-up procedure the experiments were performed. The duration of each experiment's measurement period ranged from 15 to 20 minutes. To have a high water flux across the membrane, a salt mass fraction of $\xi_D = 0.17$ was used for the draw solution. The solution was prepared with softened water. The feed side was operated with softened water with an average salt mass fraction of $\xi_F = 0.002$, and renewed before each experiment. The pH value was regularly measured with the Mettler Toledo Seven Excellence device. A constant pH value of around pH = 7.5 was

observed for each experiment. Before and after each dynamic experiment, a steady-state experiment was performed. The data of the dynamic measurements were compared to the average of the steady experiment before and after each dynamic experiment.

FO test cell
The feed and draw circuits were coupled via the FO test cell (FOTC) shown in Figure 3.1. The FOTC can also be found in [59]. It was made of acrylic glass, which allowed to observe the membrane during the experiments. The effective membrane area was square with a side length of 100 mm. Inside the draw channel, a 34 mil spacer was installed with a height of approximately 0.9 mm, see also Figure 2.5b. A flow straightener guaranteed a uniform flow distribution over the width of the draw channel. Inside the feed channel, a spacer with a height of 0.3 mm was used. The feed and draw solution flow were arranged in cross flow configuration as it is established in RO modules. The measurements showed that over the length of the cell the concentration increase or decrease in the main flow direction could be neglected due to the low permeate fluxes of $j_P < 6\ \mathrm{kg\ m^{-2}\ h^{-1}}$. Two screws at the top of the cell allowed complete deaeration of the draw channel, which was important since air bubbles would act as pulsation dampers [86]. The test cell was sealed using two o-rings on the draw and feed side. The AL of the membrane was always oriented to the draw and therefore the pulsating side. The pressure on the draw side was consistently maintained at a higher level than that on the feed side. This ensured that any potential mass transfer enhancement resulting from pulsating flows was solely attributed to the reduction of the external concentration polarization (ECP) on the draw side, without influence from possible leakages.

3.3 Particle Image Velocimetry Test Section Design

2D digital Particle Image Velocimetry (PIV) measurements were conducted to verify the CFD simulation approach and to calibrate the orifice measurement system. PIV is a technique to non-invasively analyze velocity fields inside a certain fluid domain [87]. Particles with a density similar to that of the fluid are mixed into the flow. These particles are illuminated with a laser beam and

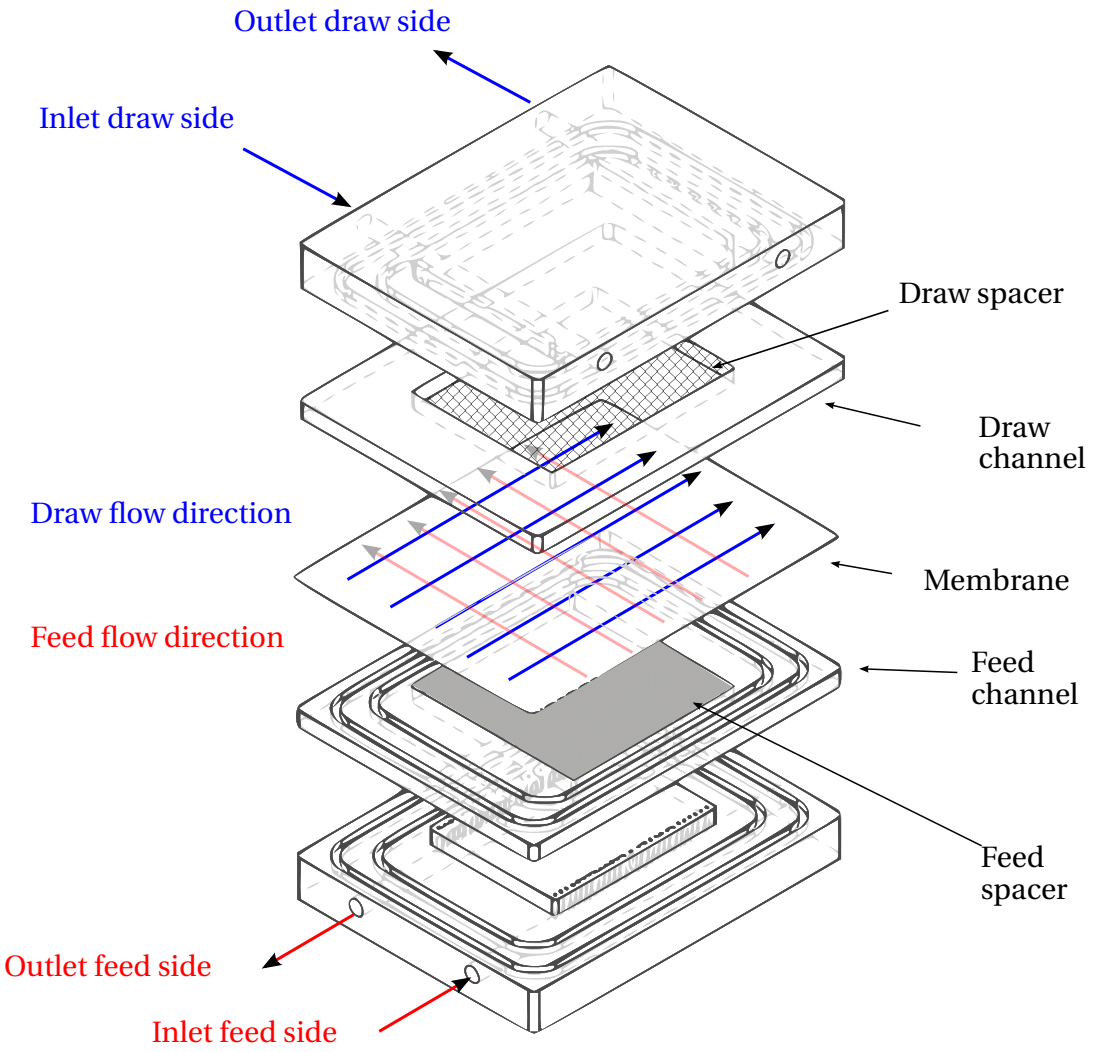

Figure 3.1: Bench-scale test cell with flow configuration of draw and feed side.

a camera detects the mie-scattering from the particles. A detailed description of the technique can be found e.g. in [87].

Instead of a pulsed laser, a continuous-wave-laser (Coherent Genesis CX488-4000) was used, since the flow velocities were very low ($u < 0.2\ \mathrm{m\ s^{-1}}$). The shutter speed of the high speed camera (Photron APX) was fast enough to resolve the particle trajectories. To generate the laser sheet normal to the average flow direction, a system of convex and concave lenses was used. Round, white polyamide particles with an average diameter of 5 µm supplied by the company ILA were used as seeding particles. The particles had a density of

1016 kg m^{-3}. The particle concentration was set to 60 g m^{-3}. The trajectories were evaluated with the open-source tool PIVlab 1.4 [88].

Two test cells, which can also be found in [59], with filaments arranged according to the zig-zag and submerged configuration, cf. Figure 4.1, were used. The zig-zag configuration test cell can be seen in Figure 3.2. The test cells were made of polycarbonate with two acrylic windows on the top and on the side. To increase the accuracy of the PIV experiments, the test cells were scaled in size by the factor 20 compared to common RO channels. The channel height was 20 mm. The spacer filaments had a diameter of 10 mm to maintain the ratio of height to spacer diameter of 2. To fulfill Reynolds' similarity law, the volume flow rates were adapted to obtain a Reynolds number of $\overline{\mathrm{Re}} = 100$. Similar values of the Womersley number could not be adjusted since these would lead to frequencies of $f_{\mathrm{ex}} < 0.01$ Hz. Therefore, it was decided to use the same excitation frequencies, which resulted in higher Wo to verify the dynamic flow simulations. According to Section 2.6.2, the dynamic response of the salt mass fraction does not significantly change for Wo > 5. The channel width was 160 mm, which allowed to assume 2D flow in the middle of the channel. A flow straightener at the inlet of the test cells guaranteed a uniform flow, although this also acted as pulsation damper.

3.4 Generation and Measurement of Pulsating Flows

The pulsations generated by the pulsation generation device (PGD) used in this work did not provide knowledge on the time-dependent mass flow rate and therefore on the amplitude ratio AR a priori. For the analysis of pulsating flows or the comparison between simulation and experiments, these values need to be known. No standardized measurement technique is available, but essentially needed for the detailed investigation of mass transfer enhancement. Continuous measurement devices as hot-film probes, LDA or PIV [89] with a highly dynamic response were ruled out due to the limited space inside the pipes and the complex flow profiles. This would cause a high measurement error. The use of invasive particles would influence the membrane performance by deposition.

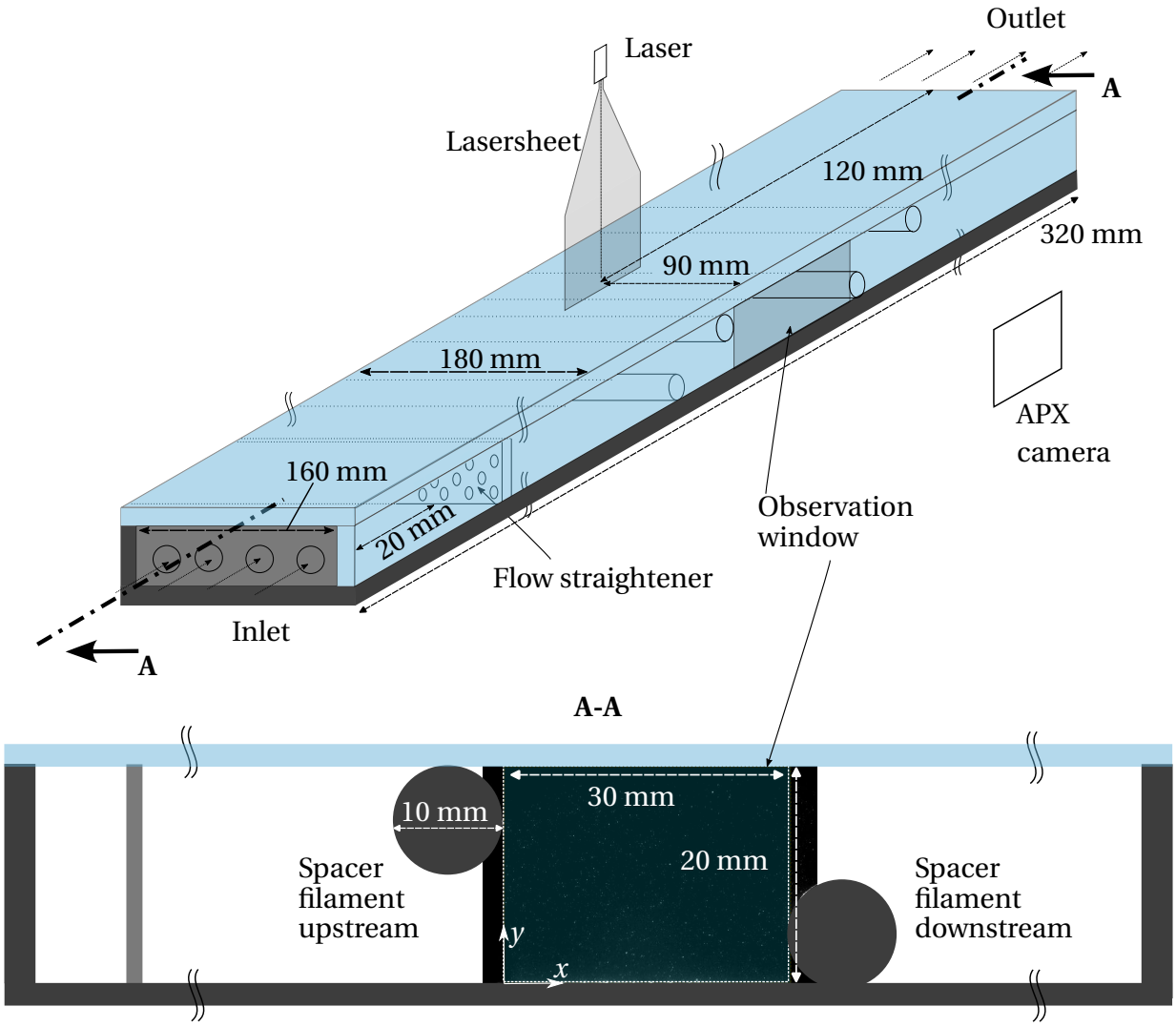

Figure 3.2: PIV setup of the zig-zag test cell for investigation of pulsating flows in spacer filled channels.

Therefore, it was decided to use a non-invasive method. The studies of Doblhoff-Dier et al. [90] were used as a basis. Dolbhoff-Dier et al. [90] determined the average mass flow rate using the linearized form of the orifice equations specified in the ISO/TR 3313 standard [91]. They found that their procedure yielded satisfactory results for determining the time-averaged mass flow rate, as long as the local amplitude remained $\varpi_x < 1$ m. However, the amplitude ratio was not verified. There have also been several studies on measuring

pulsating or oscillating flows using orifices [92, 93]. The investigations were primarily conducted with low amplitude ratios compared to the average velocities and low frequencies. As described in preliminary studies [8], the mass transfer enhancement of pulsating flows is significant for AR> 0.2 depending on Wo. Hence, the amplitudes considered in this work are of the same order of magnitude as the average velocities. To account for this, a modified measurement technique incorporating PIV measurements for calibration purposes is developed. The PGD and the measurement procedure are described in detail in the following subsections.

3.4.1 Pulsation Generation Device and Measurement Setup

In literature, most of the work on pulsating flows can be found in the areas of blood flows, heat transfer and cleaning enhancement. Membrane pumps [94], solenoid valves [36, 95] and choke and stroke mechanisms [96] are common ways to obtain periodic flows [97]. Nevertheless, they are technically feasible only for low frequencies. Moreover, the lubrication with oil would influence the performance of a membrane. These techniques have a low flexibility considering wave form, frequency and amplitude. Durst et al. [98, 99, 100] developed a complex air mass flow rate control system based on a controlled ball valve, which is able to produce different types of pulsation forms (sine, rectangular or triangular). Eichinger [101] and Spiazzi [102] employed a rotating-disk device to investigate hydraulic resistances in pipes and the fouling behavior in tubular membrane modules subjected to flow pulsations.

Design of the PGD

Because of its flexibility, a siren-type PGD was chosen to meet the requirements of studying pulsatile flows in osmotic membrane systems with respect to varying frequency and amplitude ratios over a wide range [59]. The PGD was designed based on preliminary studies [8] and Spiazzi et al. [102]. Results gained with the PGD can be found in preliminary studies [20, 59]. The design can be seen in Figure 3.3. More details and design calculations can be found in [103]. The materials and technical properties can be found in Appendix C.3.

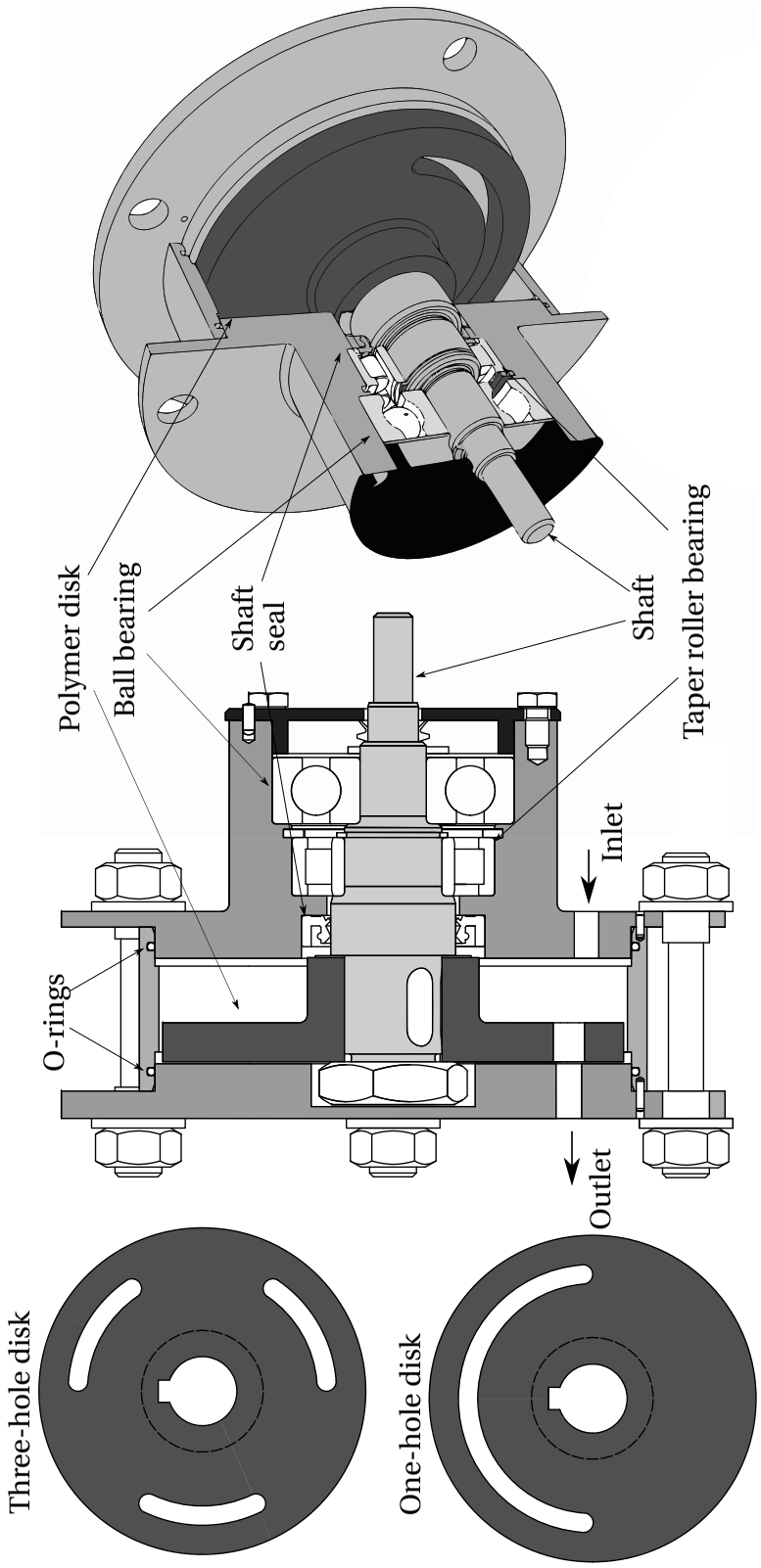

Figure 3.3: Sketch of the PGD and two different rotating disks; adapted from [103].

The main components of the PGD were a shaft and a rotating disk. The system was lubricated with grease and sealed with a shaft seal capable of withstanding pressures of up to 16 bar. The shaft rotated using an AC motor controlled via an inverter. Due to the rotation, the outlet was periodically opened and closed.

The rotating disks used here differed from typical siren constructions for acoustic excitation, see for example Kathan [104]. This distinction arises from the different research objectives; here, the focus is on generating large velocity pulsations rather than specific acoustic pressure fluctuations for very large frequencies. In contrast to the construction of Kathan [104], one or only few holes were uniformly distributed over the disks. With this design, achieving a continuous sinusoidal opening and closing of the outlet was not feasible. This design resulted in more pronounced excitation of broadband pressure fluctuations due to the abrupt opening and closing, but was needed to ensure proper sealing and to achieve higher amplitudes in the velocity by a fast generation and releasing of the elevated pressure to accelerate the fluid. Amplitude ratios between AR=0.7 and AR=1.4, depending on volume flow rate and frequency, could be achieved.

Measurement setup
The PGD was installed in the measurement setup as shown in Figure 3.4. An orifice produced by DOSCH Messaparate GmbH was used. Downstream of the orifice, another straight tube ensured that the flow field was fully developed in the PIV section. The observation window of the PIV section had a size of 20 x 21 mm. The pipe was made of acrylic glass and had a wall thickness of 1.5 mm. To minimize reflections and refraction due to a strong change of the refractive index on the pipe wall, a cube filled with water was installed around the pipe.

To guarantee that secondary flows do not influence the PIV results, the length between orifice and PIV section has to be greater than the flow development length. Ray et al. [105] developed an equation for the maximum development length $(L/D)_{\max}$ in a pipe when applying pulsating flows. The ratio $(L/D)_{\max}$ decreases with the excitation frequency and increases for higher amplitude ratios and volume flow rates. The largest development length is $(L/D)_{\max} = 51.5$

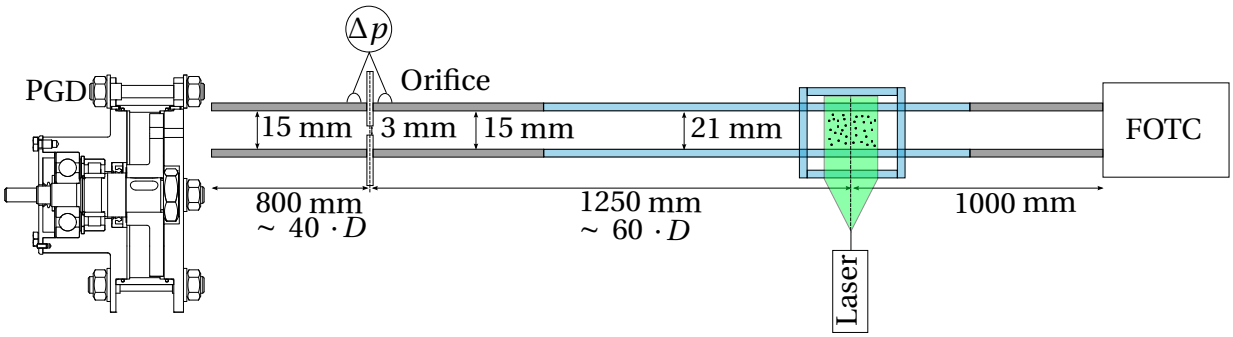

Figure 3.4: Setup for measurement of the amplitude ratio AR in pulsating flows.

at $\dot{V} = 60\,\mathrm{l\,h^{-1}}$, $f_{ex} = 1$ Hz and $AR = 1.4$. The experiments were performed at volume flow rates of $\dot{V} = 30$ ... 50 l/h, amplitude ratios of up to AR= 1.4 and $f_{ex} \geq 1$, where the flow can be assumed as fully hydraulically developed, when entering the PIV section.

The pressure drop Δp_{orif} over the orifice was measured directly at the in- and outlet of the orifice. The pressure transducer was positioned below the orifice. This guaranteed that the pipe to the sensor was completely filled with water to avoid damping of the signal due to air inclusions. To accurately measure the dynamic pressure response, the system should fulfill two aspects. First, the resonance frequency f_{res} of the pressure sensor including the tubing has to be much higher than the expected frequencies. This can be approximated using the equations of Bajsic et al. [106]

$$f_{res} = \frac{1}{2\pi} \cdot u_{wave} \cdot \sqrt{\frac{A_{tube}}{V_{eff} \cdot l_{tube}}}, \tag{3.1}$$

with u_{wave} as the wave propagation velocity and V_{eff} as the effective volume of the measurement section

$$V_{eff} = V_{sensor} + \frac{l_{tube} \cdot A_{tube}}{2}. \tag{3.2}$$

The second aspect is the response time of the system to overcome a low-pass filtering of the signal [90]. The response time can be approximated by

$$t_{resp} = \frac{A_{sensor}}{4 \cdot \pi \nu}. \tag{3.3}$$

Inserting the kinematic viscosity ν of water at 25°C and a wave propagation velocity of u_{wave} = 900 ms^{-1} (water at T =25 °C in polymer tube) the resonance frequency results in f_{res} =634.28 Hz and the response time has a scale of t_{resp} =2.25 s. This large time scale results from the area of the pressure sensors and the high density of water. To reduce this time, smaller diameters should be used, which was not possible due to the hydraulic connections of the sensor and orifice. Therefore, PIV measurements were used to calibrate the measurement procedure.

Generated pulsation forms

A range of pulsation forms for different frequencies and amplitude ratios can be seen in Figure 3.5. These values were generated from PIV data using the pipe PIV configuration, cf. Figure 3.4. The volume flow rate is calculated using integrated velocity gained from the PIV measurements with

$$\dot{V} = \int_{A_{\text{pipe}}} \overline{u}(r)\mathrm{d}A. \tag{3.4}$$

The Fourier analysis is represented by the normalized amplitude θ^*.

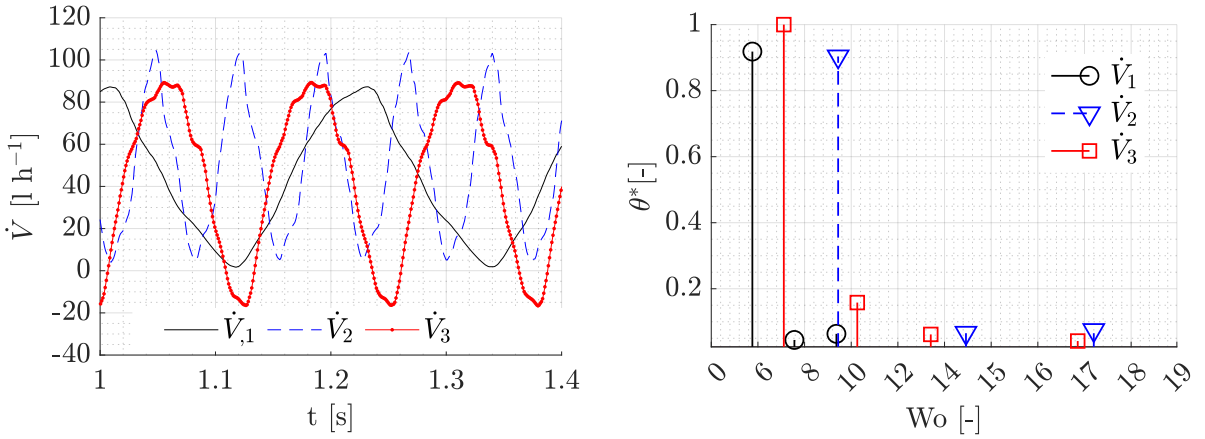

(a) Time series of different volume flow rates for different frequencies occuring in the FO bench-scale test rig.

(b) FFT of different volume flow rates for different Womersley numbers occuring in the FO bench-scale test rig.

Figure 3.5: Forms of occurring pulsating flows in the FO bench-scale test rig.

The normalized amplitude θ^*

$$\theta^* = \frac{\omega}{\omega_{\max}} \tag{3.5}$$

of the signal is plotted over the occurring frequencies. It can be seen that the pulsating flows are not ideally sinusoidal but are similar in terms of their frequency spectrum. Despite the sharp-edged holes in the rotating disks in the PGD, the pulsations were attenuated due to the large inertia of the water and damping of the entire system.

3.4.2 Flow Patterns and Governing Equations for the Evaluation of the Volume Flow Rate

The approximations in the Norm ISO/TR 3313 [91] to calculate dynamic flows in orifices are based on Bernoulli's law and a quasi-steady-state flow field, which can be seen in Figure 3.6a. It is assumed that the basic flow pattern remains stable, which is valid for steady-state flows and flows with low perturbation amplitudes.

Flow patterns in orifices using steady-state and pulsating flow rates
The gray shaded area represents the area of stream lines constricted by the orifice and the resulting flow separation zones. Upstream of the orifice, the fluid flows through the complete cross-sectional area of the pipe A_1 and is then narrowed due to the orifice. At position 2 all streamlines are parallel. A_2 is the cross-section at the position, where the streamlines show the strongest constriction and therefore smallest cross-section. Separation zones up- and downstream of the orifice occur. For pulsating flows, a CFD simulation was performed to qualitatively compare the flow pattern at steady-state and pulsating flow rates with an amplitude ratio of AR = 1.2. The 2D case was simulated using `OpenFOAM 3.0.x` with the standard k-ω-SST model. The computational domain reproduced the geometry of the orifice of the test rig. Figure 3.6b shows the stream lines and flow pattern for pulsating flows. The elasticity of the pipe is neglected. Compared to the steady-state flow pattern shown in Figure 3.6a, it can be seen that the effective cross-sections up- and downstream of the orifice strongly change over time. Periodic symmetrical

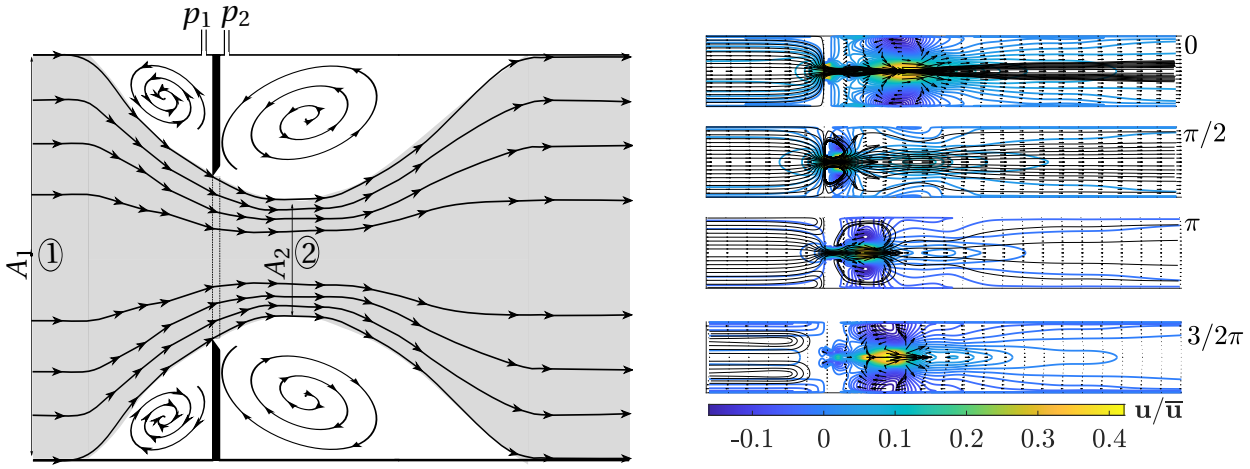

(a) Flow through an orifice with initial crosssection A_1 and constricted crosssection A_2; reproduced from [90].

(b) Flow pattern of a sinusoidal pulsating flow in an orifice with AR = 1.2 and f_{ex} = 15 Hz for $\omega t = 0, \pi/2, \pi, 3/2\pi$.

Figure 3.6: Steady-state and pulsating flow through an orifice.

vortices occur during the acceleration phase due to the strong velocity gradients produced directly at the outlet of the constriction. These structures vanish when the average velocity decreases. This highlights the importance of considering the variations in the flow pattern's cross-section during different phases. It also indicates that the assumptions made in the ISO/TR 3313 standard [91] are not entirely applicable to pulsating flows with large amplitude ratios.

The studies of Dobrowolski [92], who investigated time-dependent flows in orifices, are used as a basis. The unsteady problem can be represented using the Navier Stokes equations and Bernoulli's approximation [92]. Here, the flow can be calculated on a flow path s neglecting viscous and gravitational forces with

$$\frac{\partial u}{\partial t} + u \cdot \frac{\partial u}{\partial s} = -\frac{1}{\rho}\frac{\partial p}{\partial s}. \tag{3.6}$$

Assuming that the flow cross-sections are time-dependent, the mass flow rate through the orifice can be calculated with

$$\dot{m}(t) = u(s,t) \cdot A(s,t) \cdot \rho. \tag{3.7}$$

Integrating Equation (3.7) along the streamline from 1 to 2, cf. Figure 3.6a, Equation (3.6) leads to [92]

$$\begin{aligned}\Delta p_{\mathrm{orif}}(t) \;=\; & \underbrace{\left(\frac{1}{2\rho\alpha_{\mathrm{dis}}^2 A_1^2}\right)\overline{\dot{m}}^2}_{\text{steady-state}} \;+\; \underbrace{\left(\frac{1}{\psi_p}\int_{s_1}^{s_2}\frac{\mathrm{d}s'}{A(s,t)}\right)\frac{\mathrm{d}\dot{m}(t)}{\mathrm{d}t}}_{\text{local change of cross-section}} \\ & - \underbrace{\left(\frac{1}{\psi_p}\int_{s_1}^{s_2}\frac{1}{A^2(s,t)}\frac{\partial A(s,t)}{\partial t}\mathrm{d}s'\right)\dot{m}(t)}_{\text{temp. change of cross-section}},\end{aligned} \tag{3.8}$$

with the discharge coefficient α_{dis}

$$\alpha_{\mathrm{dis}} \;=\; \frac{C_{\mathrm{c}}\sqrt{\psi_p}}{\sqrt{\alpha_2 \;+\; \zeta - \alpha_1\left(\frac{d_{\mathrm{orif}}}{d_{\mathrm{pipe}}}\right)^2 C_{\mathrm{c}}^2}}. \tag{3.9}$$

Here, C_{c} is the contraction coefficient, α_1 and α_2 are the Coriolis coefficients, ζ is the loss coefficient, and ψ_p is the ratio between the pressure in the middle of the orifice and the measured pressure,

$$\psi_p \;=\; \frac{\Delta p_{\mathrm{orif}}}{\Delta p_{\mathrm{meas}}}. \tag{3.10}$$

The first term on the right hand side of Equation (3.8) describes the steady-state value. The second term describes the local change of the cross-section over the flow path and the third part the change of the cross-sectional area over time. All three terms exhibit strong changes at varying frequencies and amplitude ratios, thus necessitating their experimental or numerical determination.

The change of the discharge coefficient α_{dis} for different Reynolds numbers depends on the diameter ratio $d_{\mathrm{orif}}/d_{\mathrm{pipe}}$ of the orifice. α_{dis} can be assumed as $\alpha_{\mathrm{dis}} = 1$ for $\mathrm{Sr} >> 1$ in the linear regime [107]. For the non-linear regime ($\mathrm{Sr} << 1$), the discharge coefficient is $\alpha_{\mathrm{dis}} < 1$ [107] and can be approximated as $\alpha_{\mathrm{dis}} = 0.6$ [90]. Since the system of orifice, water and elastic pipes is acoustically compact ($\mathrm{He} = \mathrm{L}/\lambda_{\mathrm{wave}} << 1$), the flow can be considered as incompressible [107].

The time-varying pre-factors in Equation (3.8) are not known a priori, but are eliminated by following approximation. For evaluating Equation (3.8), the pre-factors of the mass flow rate $\dot{m}(t)$ are substituted by the time-averaged parameters A_{orif}, B_{orif} and C_{orif}. This leads to the following equation, which is used for the evaluation of the mass flow rate

$$\begin{aligned}\Delta p_{\text{orif}}(t) \;=\; & A_{\text{orif}}(\overline{\dot{m}})\;\dot{m}^2(t)\;\text{sign}(\dot{m}(t)) \;+\; B_{\text{orif}}(f,\text{AR})\;\frac{\mathrm{d}\dot{m}(t)}{\mathrm{d}t} \\ & -\; C_{\text{orif}}(f,\text{AR})\dot{m}(t).\end{aligned} \tag{3.11}$$

Doblhoff-Dier [90] used also averaged values, but neglect the influence of the changing cross-section over time, captured in the parameter C_{orif}. Finally, the parameters A_{orif}, B_{orif} and C_{orif} were calibrated using the PIV measurements, which is described in the following section.

3.4.3 Calibration and Verification of the Measurement Procedure

In the present subsection, the determination of the parameters A_{orif}, B_{orif} and C_{orif} from Equation (3.11) is explained. Before that, the procedure of the pressure measurement is described and the PIV measurement data are compared to the analytical solution.

Pressure measurements
Pressure oscillations arise within the PGD due to the abrupt opening or closing by the rotating disks. The pressure waves are reflected from the pipe walls and the hydraulic components. The oscillations depend on the Eigenfrequencies of the system as well as the excitation frequency and flow rates. However, these parasitic pressure oscillations do not contribute to the kinetic energy input into the system [93]. The pressure signal consists of the excitation frequency and an integer multiple of it [108]. Compared to the flow signal, the pressure signal has a wider bandwidth, which is due to the high inertia of the flow. Phase averaging by auto-correlation is applied to evaluate the pressure signal relevant to the calculation of Equation 3.11. Subsequently, the signal is filtered above the excitation frequency, using a low-pass filter. Based on the findings from various studies described before and the pressure signals calculated, using the PIV measurements and the analytical solution for pulsating

flows in pipes (cf. Appendix A), the cutoff frequency of the low-pass filter of the pressure signal was set to $f_{\text{cutoff}} = 5\ f_{\text{ex}}$.

Verification of the PIV measurements of the velocity profiles within the pipe
Figure 3.7 shows the PIV data and the calculations using the analytical solution, cf. Equation (A.16). In Figure 3.7a, the results are shown for $f_{\text{ex}} = 7$ Hz and AR = 1.3. Figure 3.7b shows the measurement data for $f_{\text{ex}} = 17$ Hz and AR = 0.55. The results are shown at $\omega t = 0,\ 0.5\pi,\ \pi,\ 1.5\pi$, cf. Figure 2.6. Comparing the PIV signal to the analytical solution of pulsating flows in pipes for both pulsation conditions, it can be seen that the sharp velocity profiles near the walls do not agree well. Due to reflections and the low concentration of the PIV particles, the velocity profile cannot be measured precisely at the wall. However, the averaged velocity profiles are in good agreement. The averaged relative error regarding the average volume flow rate is below 4.3 %. Therefore, the PIV measurements are considered sufficient for the further considerations, since only the averaged values are used.

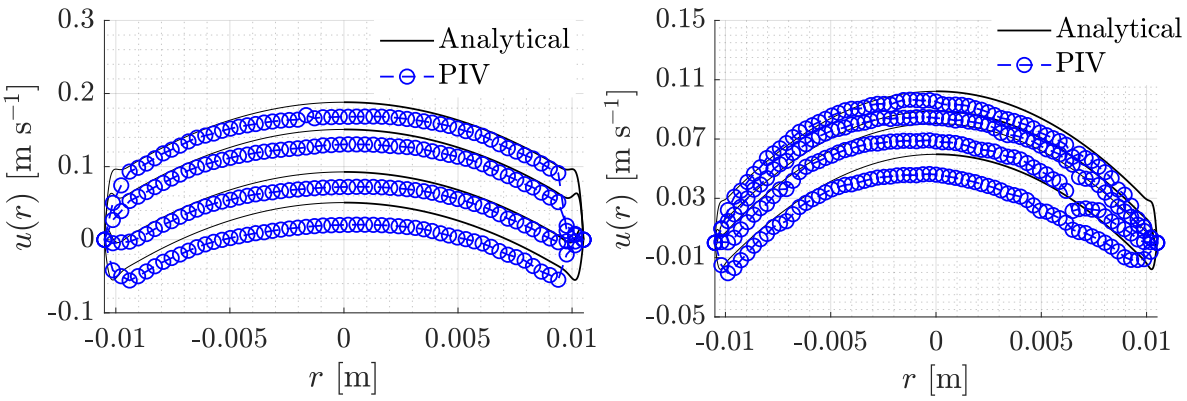

(a) $f_{\text{ex}} = 7$ Hz, AR=1.3, $\overline{\dot{V}} = 40\,\text{l}\,\text{h}^{-1}$. **(b)** $f_{\text{ex}} = 17$ Hz, AR=0.55, $\overline{\dot{V}} = 60\,\text{l}\,\text{h}^{-1}$.

Figure 3.7: Comparison of the PIV measurement data and the analytical solution for $\omega t = 0, \frac{\pi}{2}, \pi, \frac{3\pi}{2}$.

Calibration of the orifice parameters
Similar to Doblhoff-Dier [90] the parameter A_{orif} is determined using steady-state experiments, cf. Figure C.3 in Appendix C.3. Parameters B_{orif} and C_{orif} are determined using an optimization algorithm. Equation (3.8) was solved us-

ing MATLAB's Runge Kutta solver. The optimization problem was solved using MATLAB's implemented routine `fmincon` [72]. The variable η_{PIV}, determined by

$$\eta_{\mathrm{PIV}} = \left(\frac{(\overline{\dot{m}}_{\mathrm{meas}} - \overline{\dot{m}}_{\mathrm{calc}})^2}{\overline{\dot{m}}_{\mathrm{meas}}^2} + \frac{(f_{\mathrm{meas}} - f_{\mathrm{calc}})^2}{f_{\mathrm{meas}}^2} + \frac{(\mathrm{AR}_{\mathrm{meas}} - \mathrm{AR}_{\mathrm{calc}})^2}{\mathrm{AR}_{\mathrm{meas}}^2} \right), \tag{3.12}$$

which represents the relative error between the calculated and measured values, is minimized. In this minimization routine, the parameters $\overline{\dot{m}}_{\mathrm{meas}}$, f_{meas} and $\mathrm{AR}_{\mathrm{meas}}$, obtained through measurements with the PIV setup, are selected as target parameters.

Verification of the measurement and evaluation procedure

Figure 3.8 shows the relative error $\eta_{\mathrm{rel,AR}}$ plotted over the Strouhal number calculated with the orifice's diameter and velocity $\mathrm{Sr}_{\mathrm{orif}}$. This relative error compares the amplitude ratio $\mathrm{AR}_{\mathrm{orif}}$ calculated with Equation (3.11) and $\mathrm{AR}_{\mathrm{meas}}$ determined with the data gained with the PIV experiments:

$$\eta_{\mathrm{rel,AR}} = \frac{|\mathrm{AR}_{\mathrm{orif}} - \mathrm{AR}_{\mathrm{PIV}}|}{\mathrm{AR}_{\mathrm{PIV}}}. \tag{3.13}$$

$\mathrm{Sr}_{\mathrm{orif}}$ is calculated with

$$\mathrm{Sr}_{\mathrm{orif}} = \frac{f d_{\mathrm{orif}}}{\overline{u}_{\mathrm{orif}}}. \tag{3.14}$$

In the following, two different evaluation procedures are compared: the routine of Doblhoff-Dier [90] using only the averaged mass flow rate as optimization variable (cf. Figure 3.8a) and the procedure described before (cf. Figure 3.8b). Using the procedure of Doblhoff-Dier [90], the relative error lies in the range of $\eta_{\mathrm{rel,AR}} = 10$ % to $\eta_{\mathrm{rel,AR}} = 160$ % for the operation window of the FO test rig. Using the procedure developed in the present work, the amplitude ratio can be calculated with a relative error between $\eta_{\mathrm{rel,AR}} = 10$ % to $\eta_{\mathrm{rel,AR}} = 90$ %. The relative error is increasing for higher $\mathrm{Sr}_{\mathrm{orif}}$. The error could be therefore reduced due to calibration with the PIV results, but increases for increasing $\mathrm{Sr}_{\mathrm{orif}}$. For $\mathrm{Sr}_{\mathrm{orif}} > 0.028$, the relative error reaches values of $\eta_{\mathrm{rel,AR}} = 90$ %. The increase can be explained by the larger and non-linearly increasing disturbing pressure oscillations in the measured signal and the large response time, cf. Equation (3.3). Another error potential are the simplifications and averaging of the parameters B_{orif} and C_{orif} in Equation (3.8). Calculations showed that

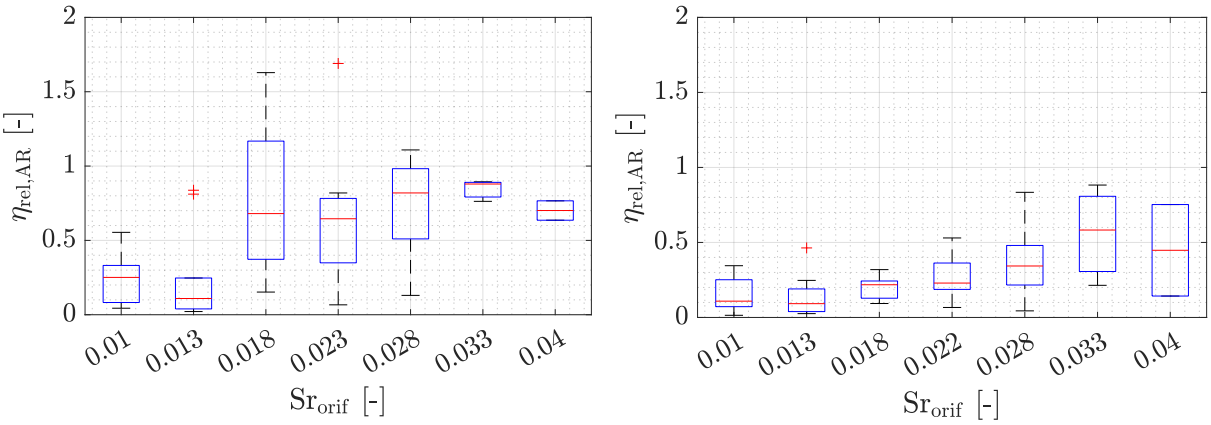

(a) Measurement procedure according to [90].

(b) Measurement procedure used in the work at hand.

Figure 3.8: Relative measurement error $\eta_{rel,AR}$ plotted over Sr_{orif}.

these parameters fluctuate over time, depending on amplitude, frequency and average mass flow rate. The larger the frequency, the larger are the pressure fluctuations. The described method to determine the amplitude ratio is used for the experiments with the FO test rig for $Sr_{orif} < 0.028$ to have a compromise between a minimized relative error and a noticeable mass transfer enhancement, since larger excitation frequencies are expected to lead to a larger enhancement. The error is therefore $\eta_{rel,AR} \leq 50\%$ within the 75th percentile.

3.5 Summary of the Experimental Methods

In the present chapter, the experimental methods have been presented. The chapter can be summarized as follows:

- The small-scale RO test rig and the FO bench-scale test rig were presented. In addition, two PIV setups were explained. The first PIV setup was used to analyze pulsating flows in spacer-filled channels. For this purpose, Reynolds similar test cells for the submerged and zig-zag spacer configuration were used. The second PIV setup was used to verify and

calibrate the measurement of the amplitude ratio AR using an orifice.

- To produce pulsating flows over a wide range of Wo and AR, a siren-based PGD was used.
- Since the amplitude ratio is not known a priori, a measurement procedure was established. The calculation is based on Bernoulli's law. While both methods are based on the same law, in contrast to the Doblhoff-Dier calculation method [90], the newly developed approach considers evolving flow fields, resulting in a lower relative measurement error.
- The calibration of the measurement procedure was performed using PIV data. A comparison with the analytical solution of pulsating flows in pipes showed that the velocity profiles near to the pipe wall cannot be measured precisely, but the result is well representing the average flow rate.
- Compared to the PIV results, the amplitude ratio could be determined with an average error of $\eta_{\mathrm{rel,AR}} < 50$ % within the 75th percentile for Strouhal numbers of $\mathrm{Sr}_{\mathrm{orif}} < 0.028$.

After introducing the experimental methods, the simulation tools will be described in the next chapter.

4 Numerical Methods

In this chapter, the numerical methods used in this work are presented. Two simulation models were developed to perform a comprehensive analysis of the dynamic mass transfer in Reverse Osmosis (RO) processes. Section 4.1 will present the Computational Fluid Dynamics (CFD) model used to simulate the fluid flow and salt mass transport in spacer-filled channels. The chapter will conclude with the explanation of the quasi-2D system simulation model in Section 4.2.

4.1 Computational Fluid Dynamics

In the present section, the governing equations, the computational domain, and the numerical schemes for the CFD model are introduced.

4.1.1 Governing Equations

The system of equations to describe the laminar flow in membrane channels (cf. Section 2.4) consists of the continuity equation of the feed flow

$$\nabla \cdot \mathbf{u}_\mathrm{F} \;=\; 0 \tag{4.1}$$

and the momentum equation

$$\frac{\partial \mathbf{u}_\mathrm{F}}{\partial t} + \nabla \cdot (\mathbf{u}_\mathrm{F} \otimes \mathbf{u}_\mathrm{F}) = -\nabla p_\mathrm{F} + 2\nu_\mathrm{F} \nabla \cdot \boldsymbol{\varepsilon}(\mathbf{u}_\mathrm{F}), \tag{4.2}$$

presuming a constant density ρ_F. The rate-of-deformation tensor $\boldsymbol{\varepsilon}(\mathbf{u}_\mathrm{F})$ is

$$\boldsymbol{\varepsilon}(\mathbf{u}_\mathrm{F}) \;=\; \frac{1}{2}\left(\nabla \mathbf{u}_\mathrm{F} + (\nabla \mathbf{u}_\mathrm{F})^T\right). \tag{4.3}$$

The salt transport is described via the convection-diffusion equation of the salt mass fraction ξ_F

$$\frac{\partial \xi_F}{\partial t} + \nabla \cdot (\mathbf{u}_F \xi_F) \;=\; \nabla \cdot (\Gamma_F(\xi_F) \nabla \xi_F), \tag{4.4}$$

assuming a concentration dependent diffusion coefficient $\Gamma_F(\xi_F)$. Given the low salt mass fraction in RO (usually $\xi_F \leq 0.1$), the effects arising from the enthalpy of mixing are disregarded, rendering the RO process an isothermal process.

4.1.2 Computational Domain and Meshing

The 3D spacer geometry is approximated using 2D geometries with the same characteristic lengths. While 3D effects, such as helix-vortical structures, can occur in flows with realistic spacers, a 2D approach is adopted to separately analyze the phenomena of pulsating flows and their impact on the mass transfer at the membrane. This allows a focused analysis and significantly reduces the computational effort. Geometrical uncertainties such as channel height, spacer-membrane attachment and blockage through particles or local deviations also exist for 3D simulations. To consider all dominant phenomena, the zig-zag as well as submerged configuration, see Figure 4.1, are used. These two configurations represent the dominant filament configurations along the mean flow direction for 3D spacers with a flow attack angle of 45°. The filament diameter is set to d = 0.5 mm. The height H of the simulated domains is H = 2d, the ratio of length to filament diameter is L/d = 8. These values represent typical configurations for CFD simulations in RO modules [55]. Due to the periodicity of the spacer filaments, a unit cell approach is chosen to efficiently simulate the flow and mass transport. The computational domain is reduced to two filaments, also for the submerged spacer configuration, which is a trade-off between low computational effort, meshing and reduced influence of the boundaries.

The mesh is generated using the `OpenFOAM` tools `blockMesh` and `snappyHexMesh`. A grid convergence study for each geometry was conducted to ensure mesh-independent results, cf. Appendix E.

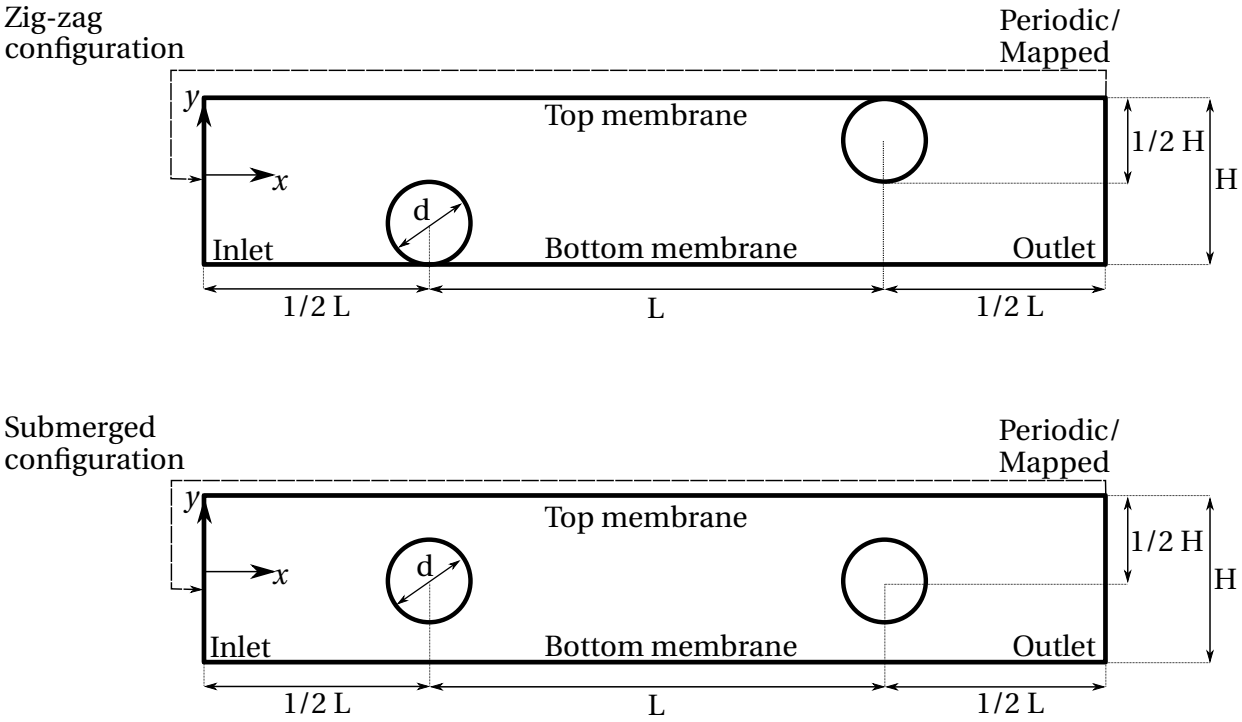

Figure 4.1: 2D computational domains.

4.1.3 Computational Setup for the Unit Cell Approach

The open source C++ library `OpenFOAM 3.x` is used to solve the steady and transient CFD problems. The implemented solvers are based on preliminary studies [8] and `OpenFOAM's` solver `simpleFoam` for the steady-state and `pimpleFoam` for the transient simulation. Both solvers are extended by the salt balance, see Equation (4.4), and thermophysical properties containing the density, the kinematic viscosity and the diffusion coefficient $\Gamma_F(\xi_F)$, which is a function of the salt mass fraction.

Second order schemes are chosen for discretization. The time discretization scheme Crank-Nicholson and the QUICK scheme for the divergence terms of the scalar transport equation are used. The local gradient terms are discretized using a linear central scheme. The linear central scheme is also used for the pressure and velocity divergence terms. Details about the basics of the different schemes can be found in [109].

To ensure a stable flow inside the periodic computational domain, a momen-

tum source term was implemented. The standard source term for steady-state flows `meanVelocityForce` is extended for periodic pressure gradients, which can be represented by a Fourier series. The volume averaged velocity for the periodic case is

$$\langle \mathbf{u}_{\mathrm{F}}(t) \rangle \;=\; \langle \overline{\mathbf{u}}_{\mathrm{F}} \rangle + \Re \left\{ \sum_{n=1}^{\infty} \langle u_{\mathrm{F,n}} \rangle e^{i\omega n t} \right\}. \tag{4.5}$$

This velocity represents the actual volume averaged velocity at time step k

$$\left\langle \mathbf{u}_{\mathrm{F,k}} \right\rangle \;=\; \frac{1}{V} \sum_{a} \mathbf{u}_{\mathrm{F,a,k}} V_{\mathrm{a}}. \tag{4.6}$$

$\mathbf{u}_{\mathrm{F,a,k}}$ represents the velocity at position a at time step k. The increment of the pressure gradient $\left\langle \nabla p_{\mathrm{F,k}} \right\rangle$ is calculated to adjust the velocity

$$\begin{aligned} \left\langle \nabla p_{\mathrm{F,k}} \right\rangle \;=\; & \frac{1}{V} \sum_{\mathrm{a}} \mathbf{I}^{-1} \\ & \left(\rho_{\mathrm{F,a,k}} \frac{\partial (\mathbf{u}_{\mathrm{F,a,k+1}} - \mathbf{u}_{\mathrm{F,a,k}})}{\partial t} + \nabla \cdot \left(\mathbf{u}_{\mathrm{F,a,k+1}} - \mathbf{u}_{\mathrm{F,a,k}} \right) + \Delta \left(\mathbf{u}_{\mathrm{F,a,k+1}} - \mathbf{u}_{\mathrm{F,a,k}} \right) \right) V_{\mathrm{a}}. \end{aligned} \tag{4.7}$$

The pressure term is used as source term to manipulate the calculated velocity field according to Equation (4.2). This manipulation ensures a specific transient flow inside the computational domain with periodic inlet and outlet conditions.

The mass fraction profile at the outlet is mapped onto the inlet boundary. The profile is normalized and set using the average value $\overline{\xi}_{\mathrm{F}}$ with [41]

$$\xi_{\mathrm{F}}(x,y)|_{x=x_{\mathrm{inlet}}} \;=\; \frac{\xi_{\mathrm{F}}(x,y)|_{x=x_{\mathrm{outlet}}}}{\left(\frac{\int_{A_{\mathrm{inlet}}} \xi_{\mathrm{F}}(x,y)|_{x=x_{\mathrm{outlet}}} \mathrm{d}A}{A_{\mathrm{inlet}}} \right)} \overline{\xi}_{\mathrm{F}}. \tag{4.8}$$

The outlet boundary values are sampled, manipulated according to Equation (4.8) and written on the inlet boundary. At the outlet boundary, a zero gradient condition is imposed. The error made by this approach can be neglected for dominantly convective flows with high Peclet numbers with an order of magnitude of 10^5, which is the case for RO processes.

The dynamic flow simulations were seen as converged when the difference of the averaged velocity profiles at $\omega t = 0$ and $\omega t = 2\pi$ were below 2%. Aperiodic

structures were not identified for the considered pulsating conditions. During the salt transport simulations, the permeate flux as well maximum and minimum salt mass fractions are logged. The simulation is regarded as converged when the change of the mean permeate flux and of the applied pressure across the membrane is below 5%.

4.1.4 Membrane Boundary Conditions

The membrane boundary conditions were implemented based on preliminary studies [8]. The mass transport across the membrane is modeled with the following assumptions:

- Dynamic mass transport inside the AL and PS are neglected, according to [8] and to Section 2.6.1.
- Dynamic flow and mass transport inside the permeate channel are neglected and a homogeneous mixing in the permeate channel is assumed.
- At the membrane, a no-slip boundary condition is prescribed.
- The steady-state diffusion across the AL is described by the solution-diffusion model and by the water and salt flux calculated with Equations (2.5) and (2.6).
- The salt and water mass transport through the membrane is only 1D normal to the membrane surface. Tangential gradients are neglected.
- Only the volume-averaged value is used for the permeate concentration.
- A water permeability of $A_{\mathrm{mem}} = 9.7 \cdot 10^{-12}$ m s^{-1} Pa^{-1} and salt permeability of $B_{\mathrm{mem}} = 1 \cdot 10^{-7}$ m s^{-1} are assumed.

The mass transport at the membrane is calculated with a Neumann boundary condition

$$\xi_{\mathrm{F,AL}}\, j_{\mathrm{P}} + \Gamma_{\mathrm{F}} \nabla(\rho_{\mathrm{F,AL}} \xi_{\mathrm{F,AL}}) = \langle \xi_{\mathrm{P}} \rangle\, j_{\mathrm{P}}. \tag{4.9}$$

The local permeate flux j_P is calculated according to Equation (2.5)

$$j_P = \rho_{F,AL} A_{mem}((p_F - p_P) - (\pi_{F,AL} - \langle \pi_P \rangle)). \tag{4.10}$$

The local salt flux j_s is calculated according to Equation (2.6)

$$j_s = \rho_F B_{mem}(\xi_{F,AL} - \langle \xi_P \rangle). \tag{4.11}$$

The averaged permeate salt mass fraction $\langle \xi_P \rangle$ is determined by an integration over the membrane boundary of width B and length of the unit cell 2L with [8]

$$\langle \xi_P \rangle = \frac{B}{A_m} \int_0^{2L} \frac{j_s}{j_w + j_s} dx. \tag{4.12}$$

Finally, the velocity normal to the membrane is calculated with

$$\mathbf{u}_{mem} = \mathbf{n} \cdot \frac{j_w + j_s}{\rho_{F,AL}}. \tag{4.13}$$

Equations (4.9) to (4.13) are iteratively solved until the residuum of the permeate salt concentration is below 10^{-4}.

The mass transfer to the membrane surface can be characterized by the Sherwood number. Its value does not only depend on the hydrodynamic conditions but also on the permeate flux across the membrane, which is a function of the pressure difference, cf. Section 2.4. Therefore, it is important to use the same permeate flux conditions when comparing simulations and experiments. To ensure this, a routine to adjust the average permeate flux across the membrane was implemented in the model. The average flux across the membrane is given by integration along the membrane with the width B and length L

$$\langle \bar{j}_P \rangle = \frac{B}{A_m} \int_0^{2L} \bar{j}_P(x) dx = \text{const.} \tag{4.14}$$

To adjust the desired averaged flux across the membrane, the local flux $\bar{j}_P(\mathbf{x})$ at the lower membrane boundary is adjusted analogously to the mapping procedure using Equation (4.8) replacing the salt mass fraction with the permeate flux. The averaged pressure is calculated with

$$\langle p_F \rangle = \frac{\langle \bar{j}_P \rangle}{A_{mem}} - \frac{1}{A_m} \int_0^x p_F(x) dx' + \frac{1}{A_m} \int_0^x \pi_{F,AL}(x) dx' - \langle \pi_P \rangle, \tag{4.15}$$

and set as system pressure to calculate the permeate flux across the bottom and top membrane (cf. Figure 4.1) according to Equation (4.10). This ensured a physical reasonable scenario. The difference of the permeate flux between the top and bottom membrane was smaller than 3 %. These equations are combined with Equations (4.9) to (4.13).

4.1.5 Comparison of CFD Approach with Steady-State Literature Data

Two cases were selected to validate the membrane boundary modeling approach using literature data for steady-state operation of RO processes. The permeate flux is used as verification parameter because it is the most important directly measurable parameter in the experiments. Data from Alexiadis et al. [110] for brackish water conditions and data from Xie et al. [111] for seawater operation conditions are taken for the comparison.

Brackish water conditions
Alexiadis et al. [110] considered an empty channel. The boundary conditions for the brackish water case can be seen in Table 4.1. In contrast to simulations

Table 4.1: Boundary conditions for the comparison with experimental data from Alexiadis et al. [110].

Variable	Values	Unit
$\xi_{\mathrm{F,Inlet}}$	0.002	-
T_{F}	298.15	K
p_{F}	8.89 − 13.98	bar
A_{mem}	$9.72 \cdot 10^{-7} \pm 0.3 \cdot 10^{-7}$	$\frac{\mathrm{m}}{\mathrm{bar\,s}}$
$u_{\mathrm{F,Inlet}}$	0.15	$\frac{\mathrm{m}}{\mathrm{s}}$

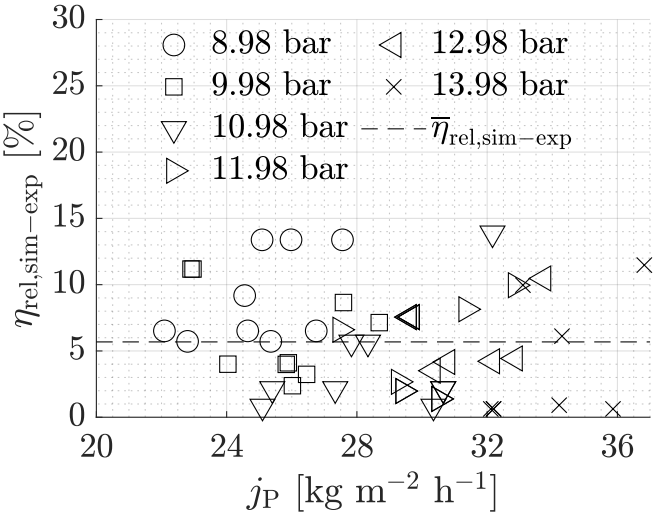

Figure 4.2: Comparison of the CFD results with experimental data from Alexiadis et al. [110], adapted from [8].

conducted by Alexiadis et al. [110], only the flow field and salt mass transport in the feed channel are calculated here. A summary of the gained results is given in Figure 4.2. The relative error between the experimental results of Alexiadis and the simulation is in the range from $\eta_{\text{rel,sim-exp}} = 0.08\ \%...14.80\ \%$. Based on the experimental results, the permeate flux shows a high variability even under similar boundary conditions. The average relative error between simulations and experiments is $\overline{\eta}_{\text{rel,sim-exp}} = 5.2\%$.

Seawater conditions

Xie et al. [111] investigated an empty and a sinusoidal channel. The boundary conditions for the SWRO case are listed in Table 4.2. In Figure 4.3, the simulation results are plotted against the experimental results for different permeate fluxes across the membrane j_{p}. The permeate flux for the sinusoidal geometries is consistently overestimated on average, similar to the simulation results of Xie et al. [111]. On average, the flux is predicted with an relative error of $\overline{\eta}_{\text{rel,sim-exp}}$ =10.3 %. Both comparisons show deviations in the permeate

Table 4.2: Boundary conditions for the comparison with experimental data from [111].

Variable	Values	Unit
$\xi_{\text{F,Inlet}}$	0.023, 0.029, 0.035	-
T_{F}	293.15	K
p_{F}	55 - 69	$\frac{\text{kg}}{\text{h}}$
A_{mem}	$5.24 \cdot 10^{-7}$	$\frac{\text{m}}{\text{bar s}}$
$u_{\text{F,Inlet}}$	0.148	$\frac{\text{m}}{\text{s}}$

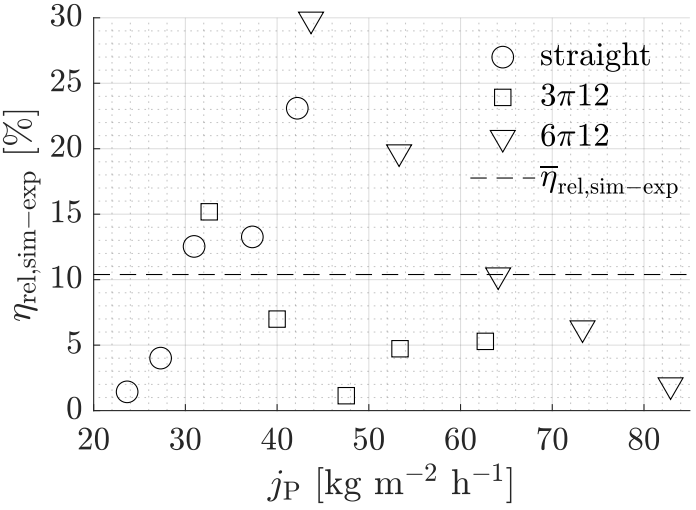

Figure 4.3: Comparison of the CFD results with experimental data from Xie et al. [111], adapted from [8].

flux, which may result, for example, from experimental uncertainties in the determination of membrane parameters or permeate flux. Another reason for the differences are the simplified modeling approaches like the simulation of

the feed without considering the permeate channel and the constant membrane parameters for different concentration and pressure conditions. Nevertheless, both comparisons show that the simulation approach described in Section 4.1 can predict the permeate flux with an averaged relative error below $\overline{\eta}_{\mathrm{rel,sim-exp}}$ =10.3 % for a wide range of boundary conditions, even with the described simplifications. The proposed simulation approach is therefore a good compromise between computational effort and accuracy and will be used for the further analyses.

4.2 Quasi-2D Modeling of the Steady-State RO Process in Spiral-Wound Modules

To transfer the results from the detailed analyses of the bench-scale experiments and CFD simulations to an RO system, a steady-state quasi-2D model was implemented into MATLAB [72]. The model resolves the field variables in the primary flow direction but calculates these variables at the membrane without resolving the entire profile normal to the membrane. For that, the tool uses the resulting relations and parameters gained with the experiments and CFD simulations. As starting point, the work of Borgmann [112] was used. It was partially re-implemented to make the model consistent as well as less computational expensive. In Subsection 4.2.1, the module geometry and model assumptions will be presented. Based on this, the governing equations will be introduced in Subsection 4.2.2. In Subsection 4.2.3, the verification of the model will be presented. At the end of this section, the coupling with the findings regarding pulsating flows gained with the dynamic CFD simulation and experiments will be described in Subsection 4.2.4.

4.2.1 Module Geometry and Modeling Approach

The module geometry is depicted in Figure 4.4. A spiral-wound module consists of envelopes including two membranes glued together and one permeate channel separated by feed spacers. These envelopes are wound into a module.

The feed flows axially through the modules, while the permeate flows spirally towards the center of the module, where it is collected in a tube. This results in a cross-flow operation mode. From a modeling point of view, this would lead to a 3D simulation approach. Due to the high salt rejection and a high permeate flux through the membrane, differences in the permeate concentration can be neglected and an averaged value is assumed.

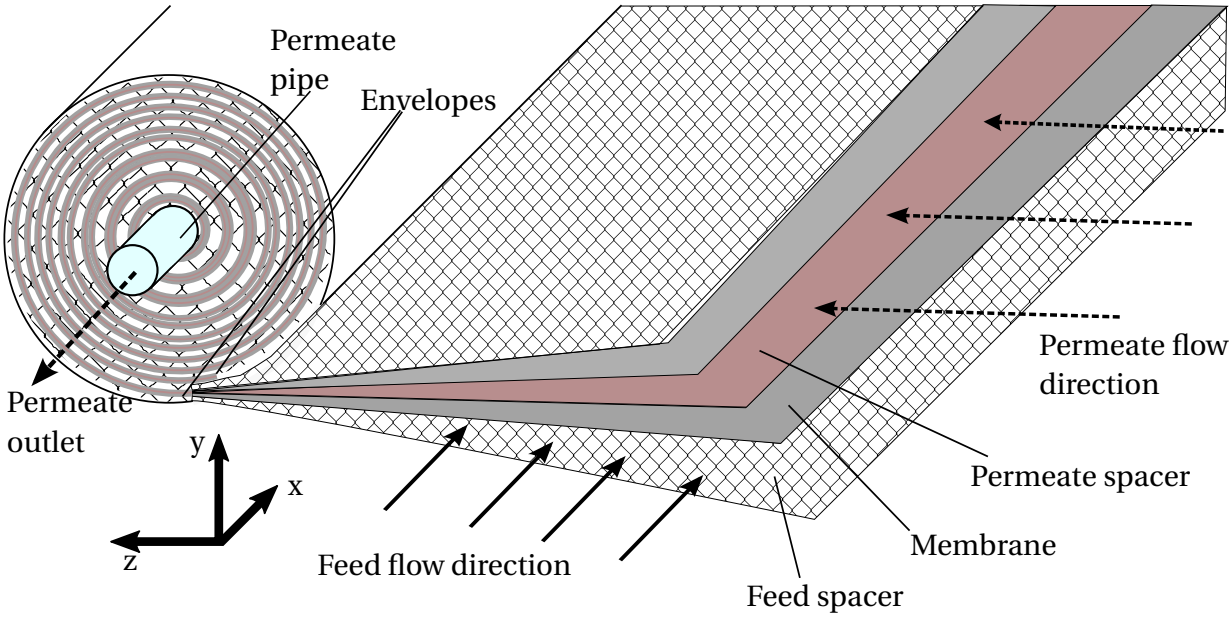

Figure 4.4: Sketch of a spiral-wound module.

Based on the description above, the following assumptions and simplifications are made to model the mass transport in a spiral-wound module:

- The flow is incompressible.
- The model only resolves the salt transport equation along the main feed flow direction of the feed channel x .
- The state variables (i.e. pressure, temperature, and concentration) and hydrodynamic properties are equally distributed across the flow direction in all membrane envelopes. Therefore, only one feed channel is calculated with a top and bottom membrane.
- The influence of the curvature is neglected.

- Concentration polarization in the permeate channel is neglected.

- Effects related to the entrance length on the steady-state Sherwood number are disregarded.

4.2.2 Governing Equations and Solution Procedure

The main governing equation is the steady-state salt transport equation along the module

$$u_{\mathrm{F}} \frac{\partial \xi_{\mathrm{F}}}{\partial x} = \Gamma_{\mathrm{F}} \frac{\partial^2 \xi_{\mathrm{F}}}{\partial x^2} - \frac{j_{\mathrm{P}}(x)}{\rho_{\mathrm{F}}} \xi_{\mathrm{P,AL}}. \tag{4.16}$$

This equation is discretized into 20 elements using the finite volume method in the main feed flow direction x. Due to the high values of the Peclet number of Pe> 10^6 the upwind discretization scheme is chosen for its stability. A Dirichlet at the inlet and a Neumann boundary condition with a zero gradient at the outlet are chosen as boundaries. The resulting equations are solved using `fsolve` from MATLAB [72]. The pressure loss gradient is calculated using a fit from the measurements.

To calculate the velocity, a steady-state mass balance is solved in each finite volume. j_{P} is determined with Equations (2.5), (2.6) and (2.7). The salt mass fraction at the membrane in the feed channel $\xi_{\mathrm{F,AL}}$ is calculated with Equation (2.10). As the model only resolves the salt mass fraction in x and calculate $\xi_{\mathrm{F,AL}}$ without resolving the entire profile in y, the model is called quasi-2D. Since the permeate concentration is also not known a priori, these equations are solved using an iterative subroutine, which is graphically shown in Figure 4.5. First, the mass balances are solved using an estimation of ξ_{P}. The salt mass fraction at the membrane $\xi_{\mathrm{F,AL}}$ is calculated using the film model, cf. Section 2.4. The Sherwood number is determined with the correlation of Schock and Miquel [60], cf. Equation (2.17). Using the Sherwood number, the mass transfer coefficient β is calculated to solve $\xi_{\mathrm{F,AL}}$ using Equation (2.10). The permeate concentration is solved with

$$\xi_{\mathrm{P}} = \frac{j_{\mathrm{s}}}{j_{\mathrm{s}} + j_{\mathrm{w}}} \tag{4.17}$$

Finally, the new permeate concentration and the residuum $res_{\xi_P,q}$

$$res_{\xi_P} = \frac{\langle \xi_{P,q} - \xi_{P,q-1} \rangle}{\langle \xi_{P,q-1} \rangle} < 1 \cdot 10^{-3} \tag{4.18}$$

are calculated. The iterative subroutine is seen as solved if the relative change of the permeate concentration ξ_P is smaller than $1 \cdot 10^{-3}$.

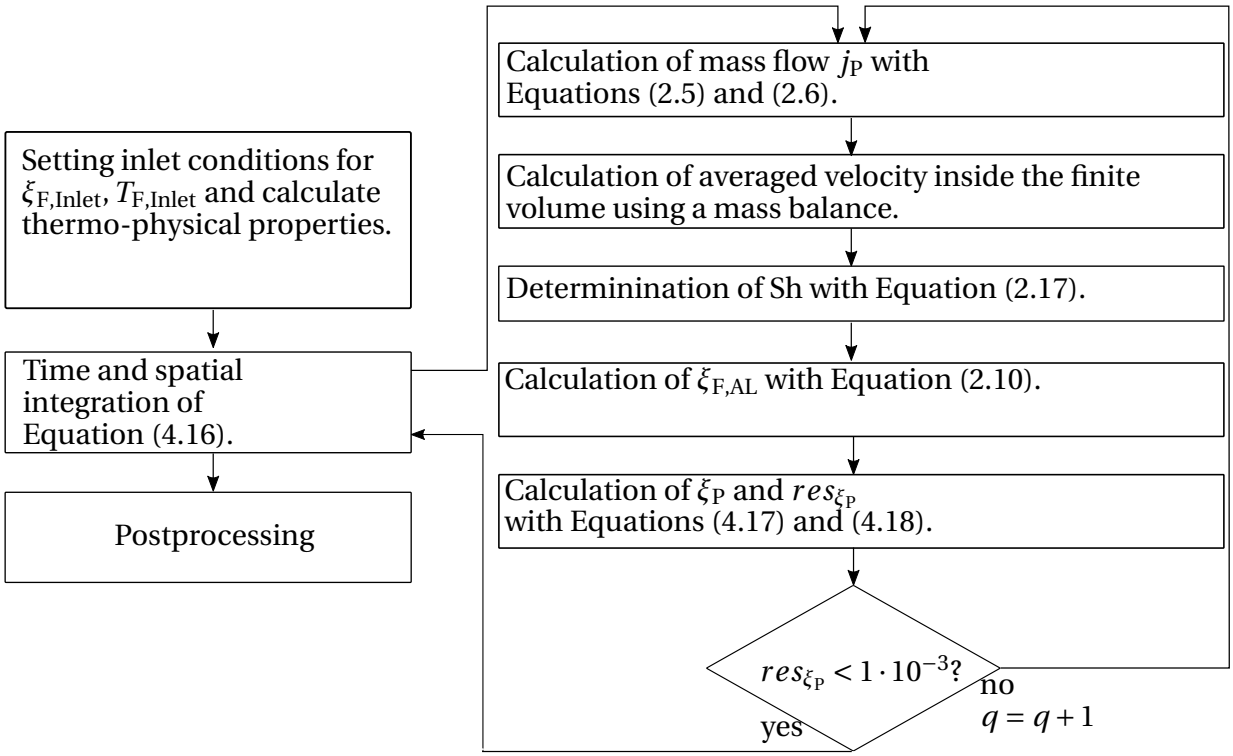

Figure 4.5: Solution strategy for the quasi-2D modeling approach of the RO module.

Input parameters

To calibrate the simulation model, only four parameters have to be determined experimentally: the Sherwood number to calculate the mass transfer coefficient β, the pressure loss gradient ∇p along the module in mean flow direction and the membrane parameters A_{mem} and B_{mem}, cf. Equations (2.5) and (2.6). These four input variables are listed in Table 4.3. A_{mem}, B_{mem} and $\nabla p_{mod,ststs}$ are determined with experimental steady-state data of the RO module and FO test-rig, cf. Section 3.1 and 3.2. Sh is calculated using Equation

Table 4.3: Input parameters (steady-state) for the quasi-2D simulation model.

Input parameter	Variable	Unit	Source of determination
Water permeability	A_{mem}	$[\frac{\mathrm{m}}{\mathrm{bar\,s}}]$	RO Module test rig, cf. Section 3.1
Salt permeability	B_{mem}	$[\frac{\mathrm{m}}{\mathrm{s}}]$	RO Module test rig, cf. Section 3.1
Sherwood number	Sh	[-]	Schock and Miquel [60]
Module pressure loss gradient	$\nabla p_{\mathrm{mod,stst}}$	[Pa]	RO Module test rig, cf. Section 3.1 and FO test rig, cf. Section 3.2

(2.17) [60]. The last two input variables are also needed for the pulsating case. How the model is used to predict the performance of pulsating flows will be described in Subsection 4.2.4.

4.2.3 Verification of the Quasi-2D Model

The model parameters A_{mem} and B_{mem} are calibrated using different experiments gained with the RO module test rig, cf. Section 3.1. The results can be seen in Appendix F. To verify the basic assumptions, the model is verified with the experimental data from RO module test rig, cf. Section 3.1. Here, the pressure loss measured with RO module test rig was used, which can be found in [82]. Figure 4.6 shows the experimental and simulated results for steady-state operation conditions. Two variables characterize the performance of the RO system: the recovery rate RR, cf. Figure 4.6a, and the resulting permeate salt mass fraction ξ_{P}, cf. Figure 4.6b. Comparing the calculated and measured values, it can be seen that the predicted recovery rates for different pressures are qualitatively and quantitatively in good agreement, whereas the deviations are higher for lower pressures. The permeate salinity shows a larger discrepancy between the experimental and simulated results, especially for higher temperatures, cf. Figure 4.6b. This can result from scattered measurements in the salt permeability B_{mem}, cf. Figure F.1b, or simplifications in the model approach. Although the absolute values slightly differ, the qualitative trend can be reproduced. Given the reasonable qualitative and quantitative agreement, it can be concluded that the assumptions and simplifications used in the modeling of the RO module are acceptable. The presented model is therefore used for the further considerations.

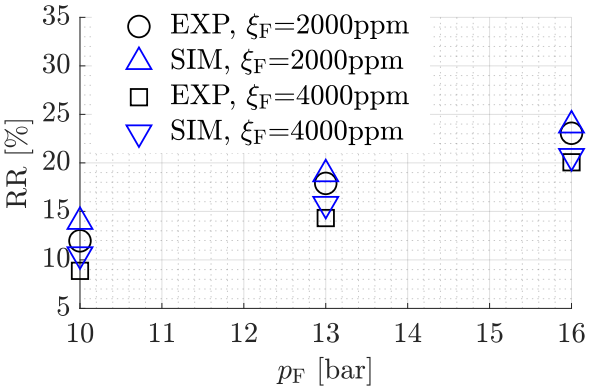

(a) Comparison of the recovery rate RR at steady state for a feed temperature of $T_F = 295$ K.

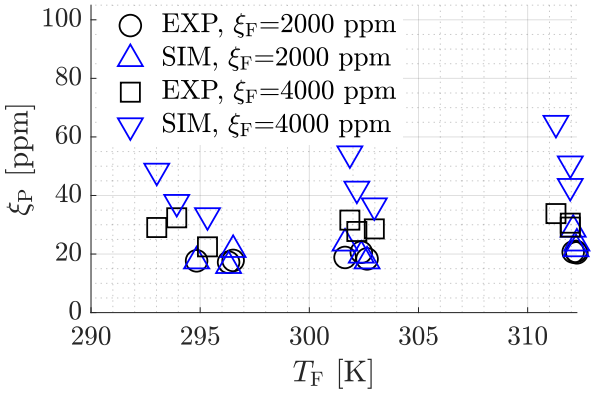

(b) Comparison of the permeate mass fraction ξ_P at steady-state for feed temperatures of $T_F = 295$ K, 302 K and 312 K.

Figure 4.6: Comparison of steady-state experiments with simulations for a feed volume flow rate of $\dot{V}_F = 950\,\mathrm{l\,h^{-1}}$.

4.2.4 Coupling with Pulsating Flows

As described before, the quasi-2D model calculates the steady-state performance of the RO process within the spiral-wound module. In this subsection, the strategy to calculate the time-averaged performance applying pulsating flows is described. As the model does not temporally resolve the equations, it allows for the determination of only time-averaged performance.

The strategy is graphically shown in Figure 4.7. As written before, the model need four input parameters to calculate the performance, cf. Table 4.3. A_{mem} and B_{mem} to calculate the water flux j_w and salt flux j_s across the membrane are determined with experimental steady-state data of the RO module test rig, cf. Section 3.1. These values do not change for the operation with pulsating flows. To calculate the time-averaged permeate flux and salt concentration applying pulsating flows, the additional pressure loss and the Sherwood number has to be provided to the model. The basic idea is to determine the ratio of the steady-state and time-averaged pulsating values, multiply it with the needed input variables and provide them to the model. The Sherwood num-

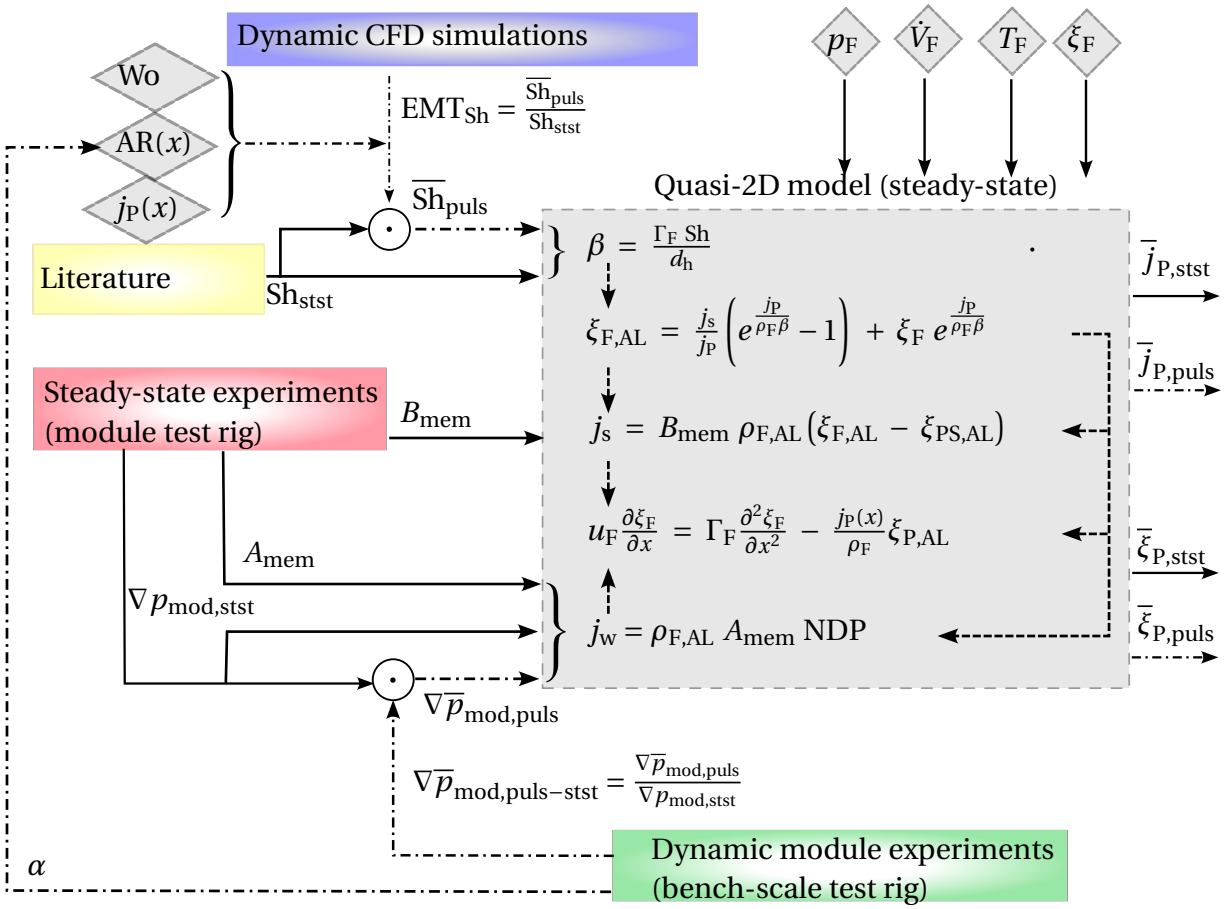

Figure 4.7: Approach to calculate the performance of RO systems applying steady-state and pulsating flows.

ber is needed to calculate the mass transfer coefficient β and the additional pressure loss is needed to calculate the local permeate flux along the module. The ratio of the pressure loss gradient $\nabla \overline{p}_{mod,puls-stst}$ is determined with dynamic RO module experiments. The ratio of Sherwood number EMT_{Sh} is calculated with the CFD simulations, cf. Section 4.1. The Sherwood number for pulsating flows depends on Wo, AR(x) and j_P. AR(x) in turn depends on the damping rate α of pulsating flows within the module. α has also to be determined with dynamic RO module experiments. To generate the input variables, pulsating flows have to be analyzed for a wide range of different boundary conditions, which is described in Chapter 5.

4.3 Summary of the Numerical Methods

In the present chapter, the numerical methods have been presented. The findings can be summarized as follows:

- First, the CFD model to simulate laminar, pulsating flows has been introduced. For this purpose, the salt transport equation and a time-dependent velocity source term were implemented in `OpenFOAM`. The unit cell including two spacer filaments with periodic boundary conditions is used as a representative computational domain. The flow and salt transport equations are solved decoupled from each other. This allowed to efficiently calculate the problem in the hydrodynamically and thermodynamically developed region.
- The CFD solution approach including the salt mass transport through the membrane was verified with steady-state literature data. The average error for BW conditions was $\overline{\eta}_{\mathrm{rel,sim-exp}}$ =5.5 % and for SW conditions $\overline{\eta}_{\mathrm{rel,sim-exp}}$ =10.2%.
- The second part of the chapter focused on the quasi-2D simulation model for spiral-wound module. The model was implemented in MATLAB [72] and verified with experimental data from the test rig described in Subsection 3.1. It could be shown that the simulation predict the permeate flux and the permeate salinity with an average error of around $\overline{\eta}_{\mathrm{rel,sim-exp}}$ =5-15 %, depending on the temperature.
- To evaluate pulsating flows in a complete RO module using the simulation model described, the Sherwood number for pulsating flows has to be determined. This Sherwood number is dependent on AR, Wo, j_{P} and $\overline{\mathrm{Re}}$. Additionally, the damping and increasing pressure drop has to be evaluated to have a complete picture of the problem.

The next chapter will present the determination of the needed input parameters in an experimental and numerical way.

5 Mass Transfer Enhancement due to Pulsating Flows in Spacer-Filled Channels

In the present chapter, the influence of pulsating flows on the mass transfer across the membrane will be analyzed. First, the mass transfer enhancement will be experimentally evaluated in Section 5.1. The simulations will be verified against experimental data obtained from the Forward Osmosis (FO) test rig and Particle Image Velocimetry (PIV) experiments, cf. Section 5.2. In Section 5.3 the flow fields and the interaction between the flow and salt mass fraction field in terms of dynamic modes will be discussed. Additionally, the local mass transfer between two filaments will be analyzed.

5.1 Experimental Evaluation of the Mass Transfer Enhancement due to Pulsating Flows

In the present section, the experimental investigations with the FO test rig described in Section 3.2 are presented. Based on the literature study (c.f. Section 1.1.2) and fundamental considerations (c.f. Section 2.6.2), mainly the frequency and amplitude determine the mass transfer enhancement due to pulsating flows. The experiments were performed with the following boundary conditions: The frequency is adjusted via the frequency converter of the motor driving the Pulsation Generation Device (PGD). The amplitude depends on the frequency and volume flow rate, but could be additionally adjusted with the needle valve in the bypass (c.f. Figure C.2, $NV_{d,1}$). To ensure that deviations in a specific membrane sample did not influence the results, the experiments were reproduced with different membrane sheets. The complete measurement procedure is described in Subsection 3.2.

Table 5.1: Boundary conditions for the experiments of the FO test rig.

Short	Description	Range	Unit
$p_{D,F}$	Pressure draw and feed	1 ... 4	bar
$T_{D,F}$	Temperature draw and feed	293.15	K
ξ_{D}	Salt mass fraction draw	0.17	-
ξ_{F}	Salt mass fraction feed	< 0.005	-
j_{w}	Water flux	2.5 ... 6	$\mathrm{kg\,m^{-2}\,h^{-1}}$
$\dot{V}_{\mathrm{D}}$	Volume flow rate draw	40 ... 44	$\mathrm{l\,h^{-1}}$
AR	Amplitude ratio	0.7 ... 1.4	-
Wo	Womersley number	5 ... 12	-
$\overline{\mathrm{Re}}$	Averaged Reynolds number	138.6 ... 148.5	-

Instead of analyzing the flux enhancement EMT used in preliminary studies [8] on the basis of the water fluxes under steady-state and pulsating flow conditions,

$$\mathrm{EMT} = \frac{\overline{j}_{\mathrm{w,puls}}}{j_{\mathrm{w,stst}}} = \frac{\Delta\overline{p}_{\mathrm{AL,puls}} - \Delta\overline{\pi}_{\mathrm{AL,puls}}}{\Delta p_{\mathrm{AL,stst}} - \Delta\pi_{\mathrm{AL,stst}}}, \tag{5.1}$$

the ratio of the osmotic pressure difference across the membrane $EMT_{\Delta\pi}$ is used,

$$\mathrm{EMT}_{\Delta\pi} = \frac{\Delta\overline{\pi}_{\mathrm{AL,puls}}}{\Delta\pi_{\mathrm{AL,stst}}} = \frac{\Delta\overline{p}_{\mathrm{AL,puls}} - \frac{\overline{j}_{\mathrm{w,puls}}}{A_{\mathrm{mem}}}}{\Delta p_{\mathrm{AL,stst}} - \frac{j_{\mathrm{w,stst}}}{A_{\mathrm{mem}}}}. \tag{5.2}$$

The salt flux is neglected, since $j_{\mathrm{s}} << j_{\mathrm{w}}$. $\mathrm{EMT}_{\Delta\pi}$ indirectly measures the increase or decrease of the concentration at the membrane compared to steady-state conditions captured by the osmotic pressure. Thus, the change in mass transfer can be directly compared. $\mathrm{EMT}_{\Delta\pi}$ could also be calculated using the salt flux. But this would lead to a larger measurement error since the salt flux is smaller than the water flux ($j_{\mathrm{s}} < 1\cdot10^{-3}\ \mathrm{kg\,m^{-2}\,h^{-1}}$). Therefore, the water flux was used as reference. $\mathrm{EMT}_{\Delta\pi} > 1$ corresponds in the FO case to a mass transfer enhancement since the solution is diluted towards the membrane within the concentration boundary layer, cf. Figure 2.2b. A larger enhancement leads therefore to a higher concentration at the AL. For an accurate comparison, the feed concentration needs to be the same, which could be ensured by renewing the feed before each experiment.

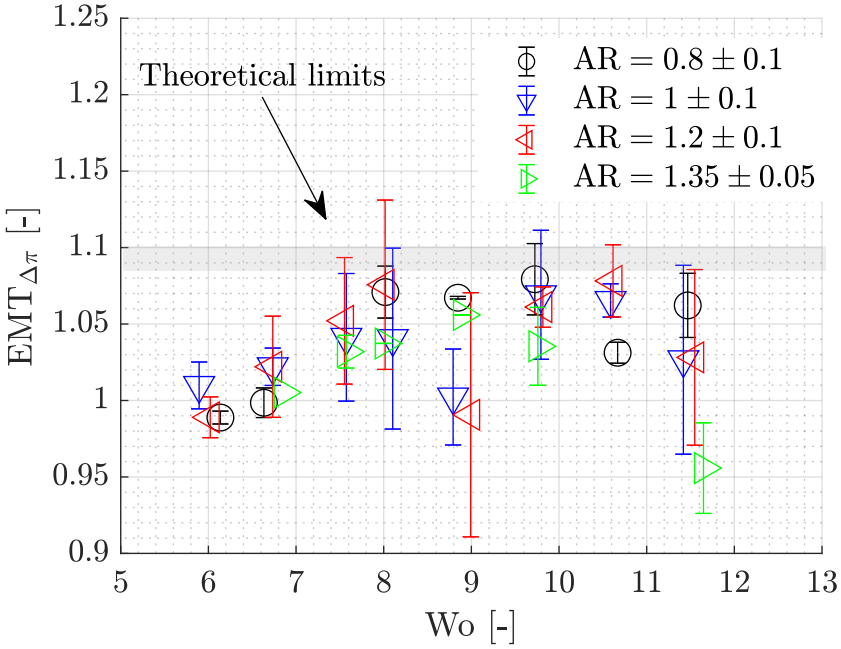

Figure 5.1: EMT$_{\Delta\pi}$ plotted over Wo for different AR.

Figure 5.1 shows EMT$_{\Delta\pi}$ plotted over Wo for amplitude ratios between 0.8 < AR < 1.35. The averaged values with error bars are plotted. The grey shaded area represents the range of the theoretical maximum enhancement factors, calculated by using Equation (2.10) and a water flux in the range of $j_w = 2.5 \ldots 6\ \mathrm{kg\,m^{-2}\,h^{-1}}$.

Despite a significant scatter, a trend towards larger EMT$_{\Delta\pi}$ for increasing Wo up to Wo = 11.8 can be observed when considering the averaged values. For Wo ≥ 6.8, this enhancement is significant compared to the theoretical limit, which also corresponds to the findings in preliminary simulation studies [8]. The enhancement already reaches EMT$_{\Delta\pi}$ = 1.075 and stagnates there close to the theoretical maximum of EMT$_{\Delta\pi} = 1.09 \pm 0.05$ for Wo ≥ 9.8. A slightly decreasing trend for Wo ≥ 11.4 can be noted. A clear trend for different amplitude ratios can not be observed.

As already described before, the scatter is large. It is therefore assumed that the few averaged enhancement values below one result from the averaging of these strongly scattering values. The reason for the large measurement scatter

is inherent with the measurement error of the amplitude ratio, cf. Section 3.4, and the low water flux across the membrane. Thus, already small variations in the measurement of the time integrated flux by the mass balance lead to a relative large scattering. In FO processes, the water flux is strongly decreased compared to RO processes due to the strong influence of the internal concentration polarization (ICP) described in Section 2.3. The low water fluxes of $j_w = 2.5 \ldots 6\,\mathrm{kg\,m^{-2}\,h^{-1}}$ result in a low external concentration polarization (ECP) at the draw side, which only leads to a small enhancement potential when applying pulsating flows. Therefore, the enhancement potential is not as high as for larger fluxes, which are commonly reached for example in industrial RO applications [49]. For these applications, an even larger enhancement for a wider range of Wo is presumed.

5.2 Verification of the CFD simulation approach

Before a comprehensive numerical analysis of the pulsating flow in spacer-filled channels will be performed, the CFD simulation will be validated against experimental results. First, the simulation approach will be verified in terms of flow dynamics using PIV experiments in Subsection 5.2.1. Second, the mass transfer enhancement will be compared to the experimental results obtained from experiments of the FO test rig in Subsection 5.2.2.

5.2.1 Comparison of the CFD Approach with PIV Results

In the present subsection, CFD simulations are compared with PIV measurements described in Section 3.3. Results gained with the PIV setup can also be found in preliminary studies [59]. The aim of this comparison is to verify the needed mesh density and the choice of the laminar CFD simulation approach to capture all occurring flow dynamics for pulsating flows in spacer-filled channels.

To avoid meshing and simulation of the entire test cell, 2D simulations of the specific observation region, cf. Figure 3.2, with periodic boundary con-

ditions at the inlet and outlet of the simulation region were performed. The meshes for the zig-zag spacer contain a number of cells of $4.6 \cdot 10^5$ and $5.2 \cdot 10^5$ for the submerged spacer with specific refinements at walls and spacer filaments analogously to the description in Subsection 4.1.2. The input volume flow rates for the simulations were calculated using the PIV measurements. They were rebuilt to a continuous signal using a Fourier series to set up the mean pressure gradient according to Subsection 4.1.3. Two experimental cases are considered here: the experiment using the zig-zag test cell was performed at an average Reynolds number of $\overline{\mathrm{Re}} = 100$, an excitation frequency of $f_{\mathrm{ex}} = 8.9$ Hz and an amplitude ratio of AR = 0.8. The experiment with the submerged configuration was performed at an averaged Reynolds number of $\overline{\mathrm{Re}} = 100$, an excitation frequency of $f_{\mathrm{ex}} = 12$ Hz and an amplitude ratio of AR = 0.7.

To verify the simulations, the velocity profiles of the time-averaged velocity profiles $\overline{u}$, the amplitude $\overline{\omega}_{\tilde{u}}$ of the periodic fluctuations and the amplitude of the aperiodic, broadband fluctuations $\overline{\omega}_{u'}$ of simulation and experiment are compared. The aperiodic fluctuation amplitudes are calculated by subtraction of the periodic fluctuations calculated using a Fourier series from the measured velocity. In the simulation, no aperiodic fluctuations occur, why it is only shown for the experiments. The velocity profiles over the height are compared at four distances from the upstream filament ($x = 1, 10, 20, 25$ mm).

Figure 5.2 shows the local profiles of the mentioned values for the submerged configuration plotted over the height of the channel. It can be seen that the time-averaged velocity profiles agree with only small deviations. This holds true for all positions considered between the filaments. The amplitude $\omega_{\tilde{u}}$ is also similar comparing simulation and experiment. Moreover, it is in the range of $\overline{\omega}_{\tilde{u}} = 2 \cdot 10^{-3} \ldots 3 \cdot 10^{-3}$ m s^{-1} and is almost constant over the height for all positions considered. It can be observed that the time-averaged amplitude of these fluctuations is very small compared to the averaged velocity. It lies in the range of $\overline{\omega}_{u'} = 1 \cdot 10^{-5} \ldots 2 \cdot 10^{-4}$ m s^{-1}.

Figure 5.3 shows the time-averaged velocity profiles $\overline{u}$, the local amplitude $\overline{\omega}_{\tilde{u}}$ of the periodic fluctuations and the amplitude of the aperiodic, broadband fluctuations $\overline{\omega}_{u'}$ of simulation and experiment for the zig-zag spacer

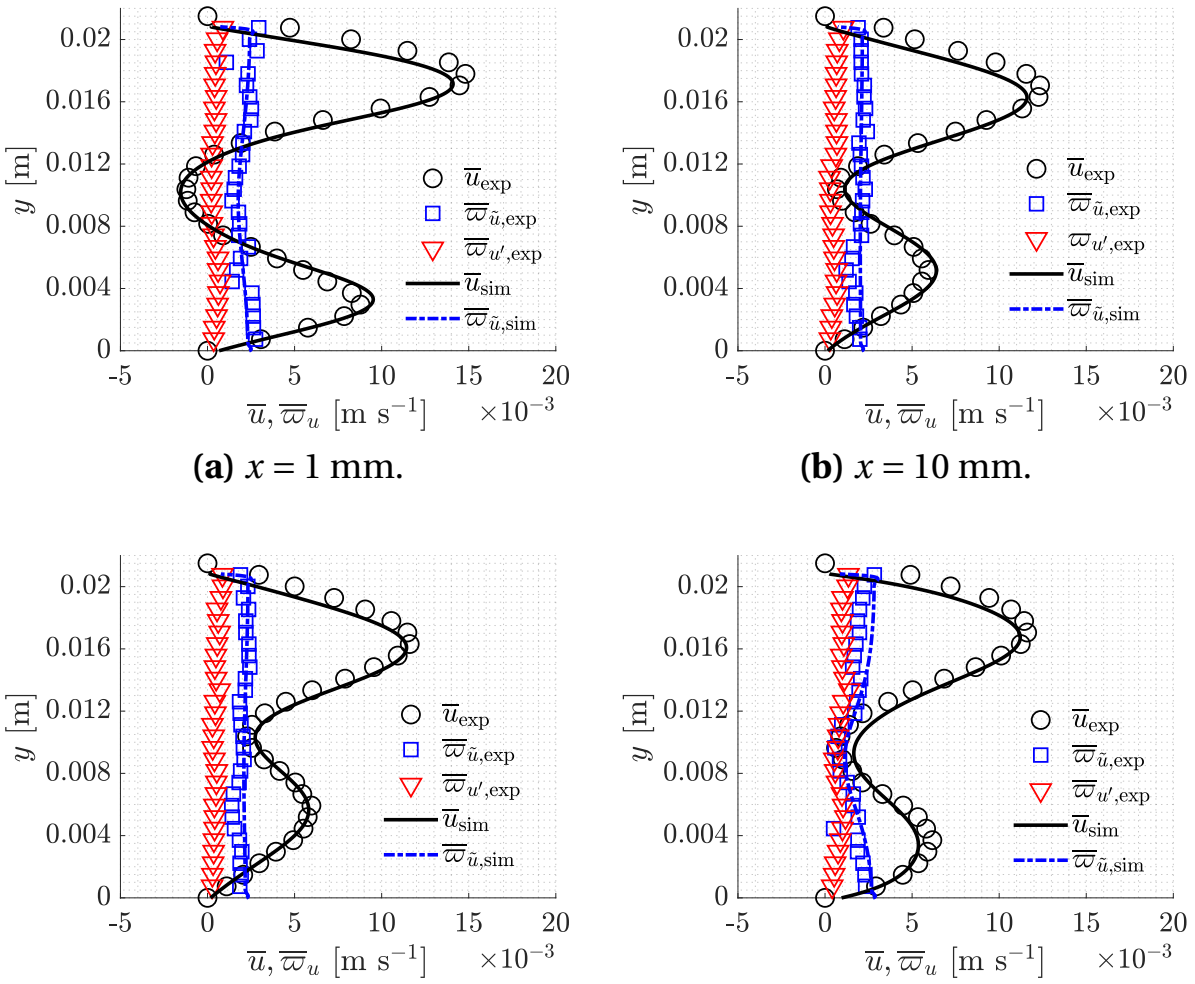

(a) $x = 1$ mm. **(b)** $x = 10$ mm.

(c) $x = 20$ mm. **(d)** $x = 28$ mm.

Figure 5.2: Submerged configuration: Comparison of the time-averaged velocity profiles $\overline{u}$, the local amplitude of the periodic fluctuations $\overline{\omega}_{\tilde{u}}$ and the amplitude of the aperiodic, broadband fluctuations $\overline{\omega}_{u'}$ at four distances x from the spacer filament downstream; simulation: dotted lines, experiments: circles; adapted from preliminary studies [59].

configuration at the described four positions plotted over the height of the channel. Analogous to the submerged configuration, it can be seen that the averaged velocity is well represented. A small vertical shift of the CFD velocity profiles can be identified. This can be caused by small uncertainties

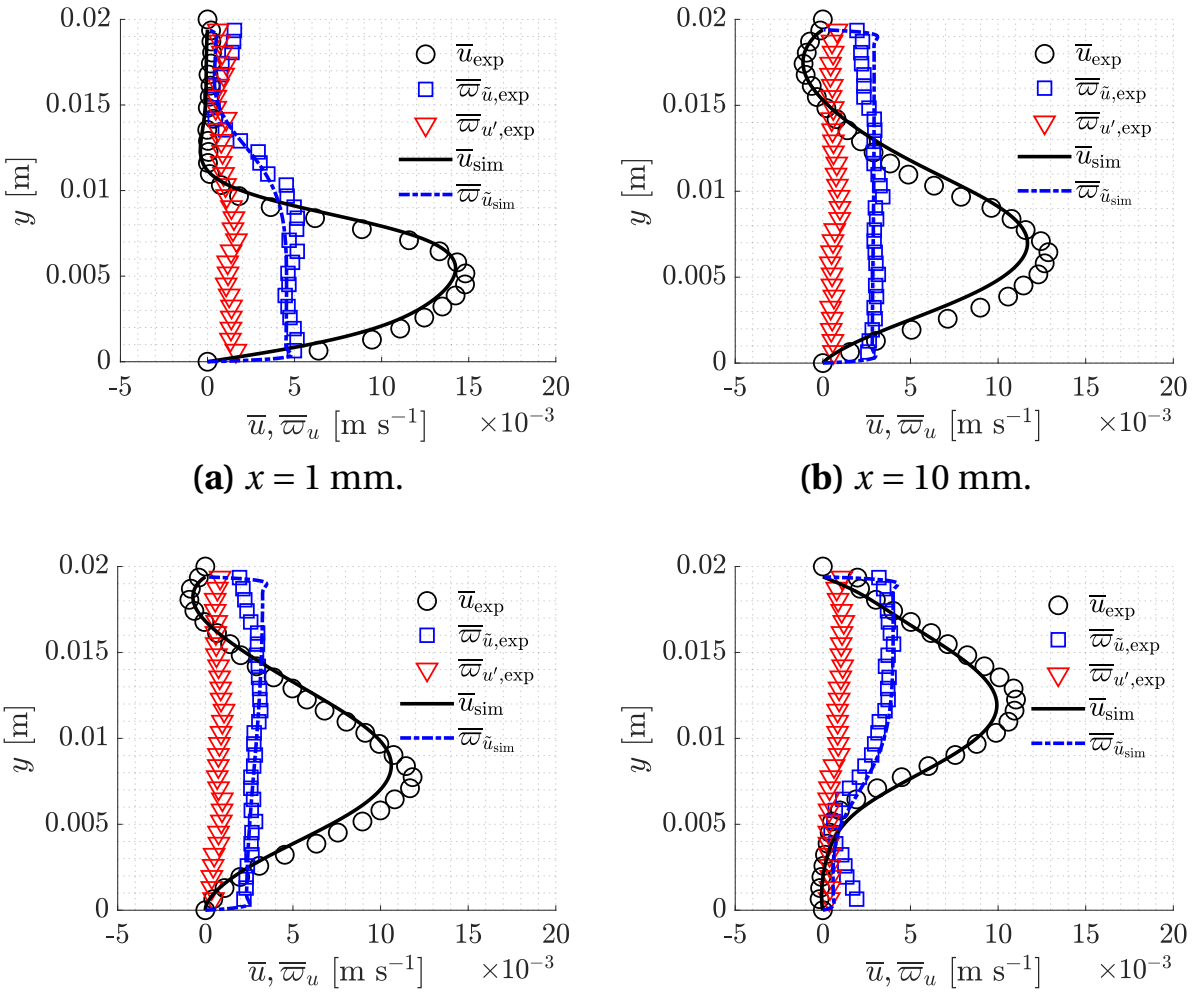

(a) $x = 1$ mm. **(b)** $x = 10$ mm.

(c) $x = 20$ mm. **(d)** $x = 28$ mm.

Figure 5.3: Zig-zag spacer configuration: Comparison of the time-averaged velocity profiles $\overline{u}$, the local amplitude of the periodic fluctuations $\overline{\omega}_{\tilde{u}}$ and the amplitude of the aperiodic, broadband fluctuations $\overline{\omega}_{u'}$ at four distances x from the spacer filament downstream; simulation: dotted lines, experiments: circles.

of rebuilding the geometry. Comparing the amplitudes of the periodic fluctuation $\overline{\omega}_{\tilde{u}}$, simulation and experiment only minimally differ. The amplitude of the aperiodic fluctuations is very small and lies in the range between $\overline{\omega}_{u'} = 1 \cdot 10^{-4}$ ... $1 \cdot 10^{-3}$ m s^{-1}. On average, they are negligible.

Summarizing the results, it can be stated that the velocities can be predicted with a small relative error. Therefore, the fully laminar approach is valid.

5.2.2 Comparison of the Mass Transfer Enhancement from CFD Simulations with Data from the Bench-Scale Test Rig

In the present section, the simulated mass transfer enhancement is compared to the experimental data. The results are obtained with the FO test rig described in Section 3.2. The simulations were performed with the CFD configuration for the zig-zag spacer described in Section 4.1 using the unit cell approach with periodic boundary conditions. Only the bottom wall allows mass transport across the membrane. The pulsating draw mass flow rate is determined via measurements with the orifice, cf. Section 3.4. This mass flow rate is used to calculate the mean pressure gradient to adjust the averaged velocity within the computational domain, cf. Section 4.1. To ensure the equal mass transfer conditions, the average water flux $\overline{j}_\mathrm{w}$ is set constant according to the experiment. The average Reynolds number is $\overline{\mathrm{Re}} = 136.8$.

Three representative experiments with different water fluxes j_w, frequencies Wo and amplitude ratios AR are used to verify the CFD simulation approach. The boundary conditions are listed in Table 5.2. To compare the RO approach and the experimental FO bench-scale results, the mass transfer enhancement $\mathrm{EMT}_{\Delta\pi}$ is used, cf. Equation (5.2). As described in Section 2.3, the basic mass transfer principles of RO and FO are identical. Therefore, RO and FO will show the same behavior at the same flux and hydrodynamic conditions for the comparison of the mass transfer enhancement of steady-state and pulsating flows. This was justified in Section 2.4 in detail. In Subsection 4.1.5, it was shown that the simplified modeling approaches are valid for a wide range of boundary conditions. The results can be seen in Figure 5.4. The CFD simulations show a good agreement with the experimental results with a maximum relative error of 18.8 %. Since the experiments show large scattering, cf. Figure 5.1, it can be stated that the CFD simulations predict an enhancement at the same magnitude as observed in the experiments. The deviations can be explained by the relative error determining the amplitude ratio AR using the procedure

Table 5.2: Boundary conditions for the comparison of CFD and FO experiments.

Wo [-]	AR [-]	j_w [kg m^{-2} h^{-1}]
11.8	1	1.2
13.1	1.2	2.5
14.3	0.9	2

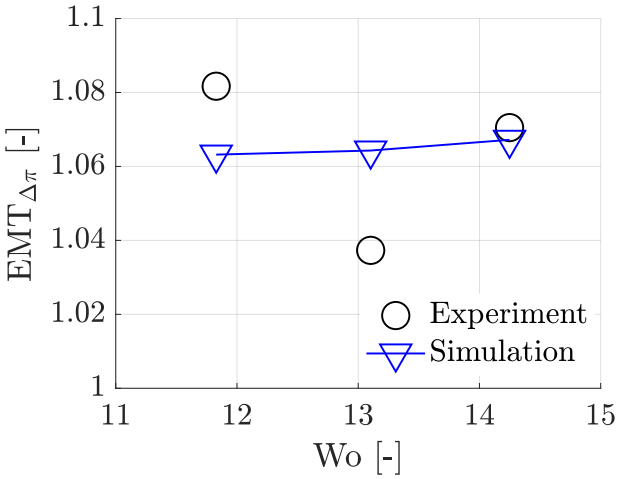

Figure 5.4: Comparison of EMT$_{\Delta\pi}$ of CFD simulations with experiments in the range of Wo = 11.8 ... 14.3 at $\overline{\text{Re}}$ = 136.8.

described in Section 3.4. Deviations in the time-dependent flow rate lead to deviations in the prediction of the mass transfer enhancement EMT$_{\Delta\pi}$. Additionally, the experiments show scattering due to experimental uncertainties, which was already discussed in Section 5.1. Another aspect is the 2D simulation approach, which simplifies the real spacer geometry. Since only a 2D simulation approach is used, this comparison cannot be seen as a full validation. Besides the already considered aspects, the local mass transport in RO modules is also dependent on the hydrodynamic and thermodynamic development length [113]. Nevertheless, the results in combination with the validation using the PIV measurements and verification with literature data show that the 2D CFD simulations can predict the magnitude of the mass transfer enhancement, even within the short length. This in turn demonstrates that the unit-cell approach is a good approximation to characterize the mass transfer enhancement of the entire RO module. With the benefit of less computational effort, the simplified approach is an appropriate tool to analyze the mass transfer enhancement due to pulsating flows in spacer-filled channels.

5.3 Numerical Investigation of Pulsating Flows in Spacer-Filled Channels

After the experimental evaluation and verification of the simulation approach, the underlying mass transfer phenomena will be numerically analyzed in detail. The objective of this analysis is to investigate pulsating flows along the module at various amplitude ratios, permeate fluxes, Reynolds, and Womersley numbers. The analysis will be performed for Womersley numbers between Wo = 10.5 and Wo = 14.9 for the submerged and Wo = 10.5 and Wo = 16.5 for the zig-zag spacer configuration. Various averaged Reynolds numbers will be considered in the range of $\overline{\mathrm{Re}}$ = 68.4 ... 136.8. The amplitude ratios range from AR = 0.2 to AR = 1.2. The simulations were performed with sodium chloride in the feed channel. The average salt mass fraction is set to $\langle\overline{\xi}_{\mathrm{F}}\rangle$=0.035. The simulations are performed with the CFD simulation approach described in Section 4.1.

Initially, the steady-state problem will be analyzed to identify potential areas for improvement in Subsection 5.3.1. Secondly, the dynamic flow and salt mass fraction fields will be analyzed in Subsections 5.3.2, 5.3.3 and 5.3.4. At the end of this Section, the average mass transfer enhancement will be quantified in terms of the local Sherwood number in Subsection 5.3.5.

The flow and salt mass fraction fields for the pulsating flow cases will be evaluated in terms of dynamic modes using the method of Proper Orthogonal Decomposition (POD). An introduction into the method of the snapshot POD method is given in Appendix D. The fundamental idea of this technique is to identify the characteristics of dynamic flow fields by decomposing them into a deterministic function of spatial functions modulated by time coefficients $\psi_{\mathrm{i}}(t)$ [114]. The modes are represented by $\Phi_{\mathrm{i}}(\mathbf{x})$. The order i of the modes is determined by the kinetic energy content of the periodic flow field of each mode. The higher the order, the lower is the energy content. 100 snapshots for each period were used for the analyses. Although the pattern of the different modes cannot be interpreted as actually occurring flow structures, but only as the weighted superposition of them $\psi_{\mathrm{i}}(t)\Phi_{\mathrm{i}}(\mathbf{x})$, the POD method allows to identify the most energetically relevant dynamic modes and possible coher-

ent flow structures [115]. The fewer relevant modes required to describe the flow field, the easier the interpretation [115]. Additionally, the aim of this analysis is to identify a possible interference along the module when decreasing AR and $\overline{\mathrm{Re}}$. The possible interaction would be needed to be considered in the system modeling approach.

5.3.1 Analysis of the Steady-State Salt Mass Fraction and Flow Field within Spacer-Filled Channels

In the present subsection, the steady-state problem of the submerged and zig-zag spacer configuration will be discussed as reference for the pulsating cases. The aim of this analysis is the identification of enhancement potentials for pulsating flows. The analysis is performed for the feed channel.

Figure 5.5a shows the flow pattern within the submerged spacer configuration for steady-state conditions. The velocity $|\mathbf{u}_\mathrm{F}|$ is normalized to the averaged value $\langle|\overline{\mathbf{u}}_\mathrm{F}|\rangle = 0.1$ m s^{-1}, which corresponds to the averaged Reynolds number of $\overline{\mathrm{Re}} = 136.8$, cf. Equation (2.18). It can be seen that the flow is accelerated up to three times compared to the averaged velocity when passing the constrictions by the filaments. A separation zone develops downstream of the filament. The flow is steady, and no vortex shedding occurs, as observed in the free-stream cylinder problem. Figure 5.5b shows the corresponding salt mass fraction field ξ_F normalized by the averaged salt mass fraction $\langle\overline{\xi}_\mathrm{F}\rangle$. In general, it can be seen that the salt mass fraction field is similar to profiles in empty channels, which results from the mainly parallel flow. The height of the concentration boundary layer increases upstream of the filament before subsequently decreasing due to the acceleration along the filament.

Figure 5.6a shows the flow pattern inside the zig-zag spacer configuration for steady-state conditions. It can be seen that the flow is accelerated by the channel constrictions due to the filaments. Flow separation zones develop both upstream and downstream of the filaments. The downstream zone is of larger scale. Figure 5.6b shows the corresponding salt mass fraction field ξ_F normalized by the averaged salt mass fraction $\langle\overline{\xi}_\mathrm{F}\rangle$. It can be observed that the concentration boundary layer is thin at the region where the spacer filament con-

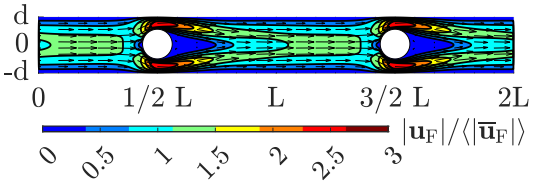

(a) Relative flow pattern at steady-state.

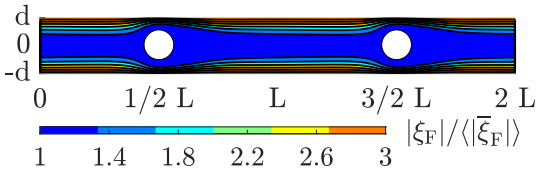

(b) Relative salt mass fraction field at steady-state.

Figure 5.5: Flow and salt mass fraction field for the submerged spacer configuration at steady-state conditions for $\overline{\mathrm{Re}} = 136.8$; the flow field is normalized to the value $\langle|\overline{\mathbf{u}}_F|\rangle = 0.1\ \mathrm{m\,s^{-1}}$ and the salt mass fraction field is normalized to the averaged salt mass fraction $\overline{\xi}_F$ =0.035.

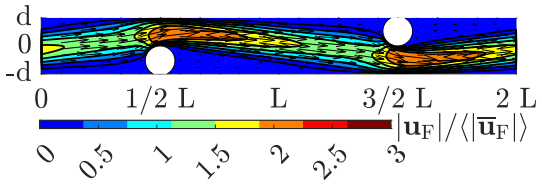

(a) Relative flow pattern at steady-state.

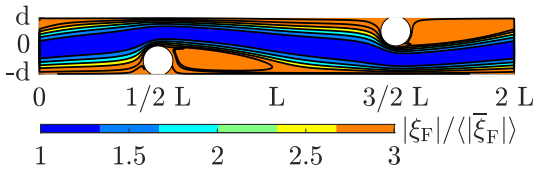

(b) Relative salt mass fraction field at steady-state.

Figure 5.6: Flow and salt mass fraction field for the zig-zag spacer configuration at steady-state flow conditions for $\overline{\mathrm{Re}} = 136.8$; the flow field is normalized to the value $\langle|\overline{\mathbf{u}}_F|\rangle = 0.1\ \mathrm{m\,s^{-1}}$ and the salt mass fraction field is normalized to the averaged mass fraction $\langle\overline{\xi}_F\rangle$ =0.035.

stricts the channel. Up- and downstream of the filaments, the concentration boundary layer strongly increases in the flow separation zones due to the low convective mass transport. Regarding the mass transfer enhancement potential in the stationary field of the submerged spacer, it can be stated that the highest enhancement potential lies in the disturbance of the concentration boundary layer between the filaments. In this region, the largest concentrations occur. Considering the zig-zag spacer configuration, particular attention

has to be given by reducing the concentration especially in the separation zone directly downstream of the filaments. Therefore, to efficiently enhance the mass transfer, mixing especially within these regions has to be increased.

5.3.2 Flow Field Analysis of Pulsating Flows within the Submerged Spacer

After the analysis of the steady-state problem, the dominant dynamic flow structures of pulsating flows for the submerged spacer are analyzed using the method of POD. The POD modes are calculated using the periodic feed flow field $\tilde{\mathbf{u}}_{\mathrm{F}}$. As it is written in Section 5.3, the analysis is performed for different amplitude ratios AR, Womersley numbers Wo and averaged Reynolds numbers $\overline{\mathrm{Re}}$ to characterize the development of the flow dynamics along the spiral-wound module.

Dynamic flow field

Before discussing the POD analysis, the dynamic flow field is analyzed exemplary for AR = 1.0, Wo = 10.5 and $\overline{\mathrm{Re}}$ = 136.8. Figure 5.7 shows the flow field at $\omega t = 0, \pi/2, \pi, 3\pi/2$. It can be seen that the separation zone downstream of the filament first increases during the acceleration phase until $\omega t = \pi/2$ and stays constant until $\omega t = \pi$. During these phases, a backward flow can be observed between the filaments. For $\omega t = 3\pi/2$, the flow is completely perturbed and vortex structures occur between the filaments. Comparing the dynamic to the steady-state flow field in Figure 5.5a, it can be observed that the largest perturbations occur at the location of the steady-state separation zone, cf. Figure 5.5a. To identify the most dominant flow structures for different dynamic boundary conditions and to analyze the dynamics of them, the POD analysis is performed in the following.

Mode energies of the periodic flow field

To efficiently analyze and compare the dynamic flow field for different Wo, AR and $\overline{\mathrm{Re}}$, the most dominant modes have to be identified. According to Holmes et al. [114], for low-order modeling, the number of low-order modes should account for 90 % of the total energy, and no modes with a relative kinetic energy content of $E_{\Phi} > 1$ % should be omitted [116]. Although these limits are empirical values, these empirical limits are also used in this work, since also

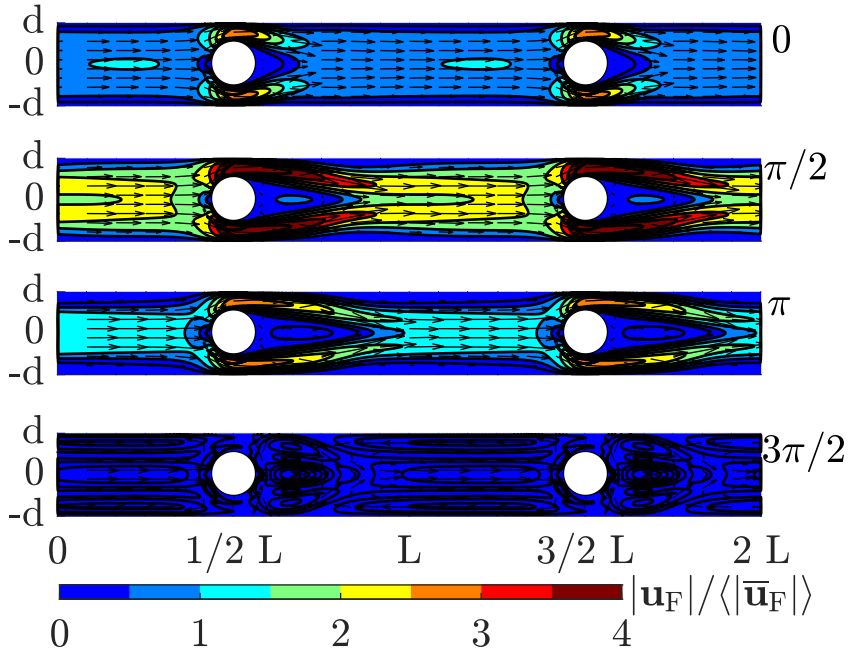

Figure 5.7: Dynamic flow field within the submerged spacer at $\omega t = 0, \pi/2, \pi, 3\pi/2$ for AR= 1.0, Wo = 12.9 and $\overline{\text{Re}} = 136.8$.

the first two modes contain more than 98 % of the relative energy. Therefore, it is assumed that these modes capture the dominant dynamic flow phenomena. Figure 5.8 shows the averaged relative kinetic energy E_Φ of the POD modes. It can be seen that the first mode already contains the highest relative energy of more than $E_\Phi > 90$ % independent of AR, $\overline{\text{Re}}$ and Wo. The higher Wo, the higher is the relative energy of the higher order modes ($i > 2$). For constant Wo, the same behavior can be observed for increasing AR and $\overline{\text{Re}}$. Nevertheless, for higher order mode numbers of $i > 2$, the relative energy content is $E_\Phi < 1\%$.

POD modes and time coefficients for different Womersley numbers

Figures 5.9, 5.10 and 5.11 show the two major POD modes of the periodic velocity field represented by the relative absolute magnitude normalized to the maximum value $|\Phi_i|/|\Phi_{\text{max}}|$. The modes calculated for Wo = 10.8, 12.9, 14.9 at AR = 1.0 and $\overline{\text{Re}}$ = 136.8 are arranged by order from top to bottom. For all Wo considered, the vector field of the first mode represents the averaged flow field at steady-state conditions, cf. Figure 5.5a. The second mode shows

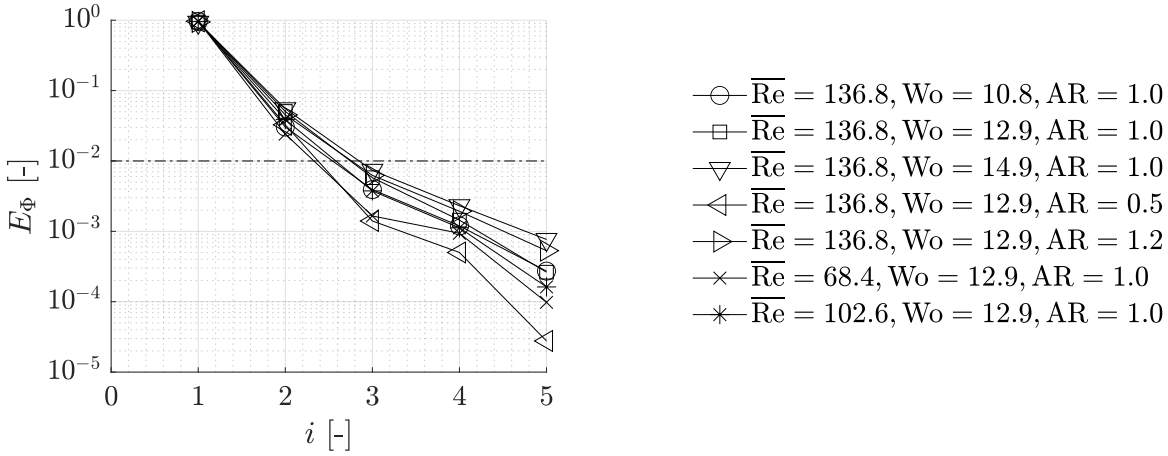

Figure 5.8: Relative kinetic energies of the POD modes for different pulsating cases.

two symmetrical vortex zones directly downstream of the filaments with the highest relative magnitude in the center of the channel. Negative vectors near the membranes can be observed around position x = L. The magnitude is intensified at higher frequencies. The corresponding FFT analysis of the time coefficients can be seen in Figures 5.12a, 5.12b and 5.12c. Analyzing the FFT spectra, it can be seen that all modes have dominant Womersley numbers at Wo = 10.5, 12.9, 14.9.

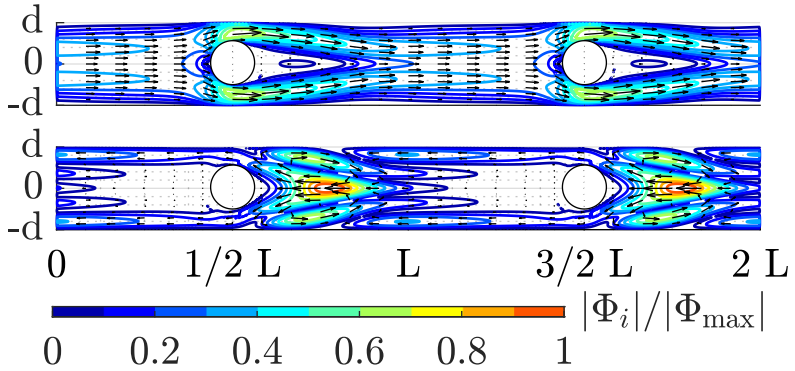

Figure 5.9: POD modes of pulsating flows in the submerged spacer configuration at AR = 1.2, Wo = 10.5 and $\overline{\mathrm{Re}}$ = 136.8.

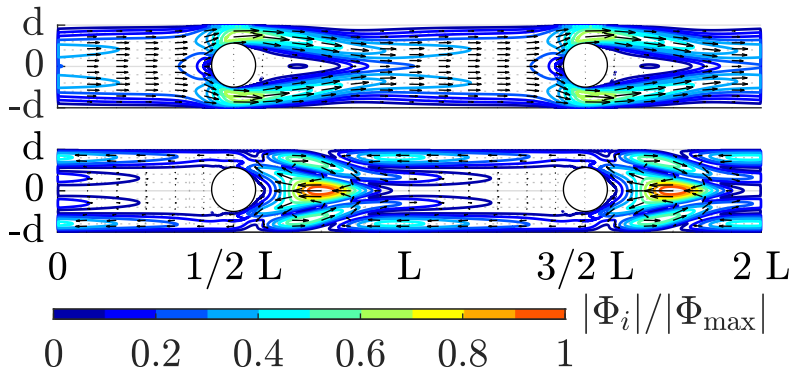

Figure 5.10: POD modes of pulsating flows in the submerged spacer configuration at AR = 1.2, Wo = 12.9 and $\overline{\text{Re}}$ = 136.8.

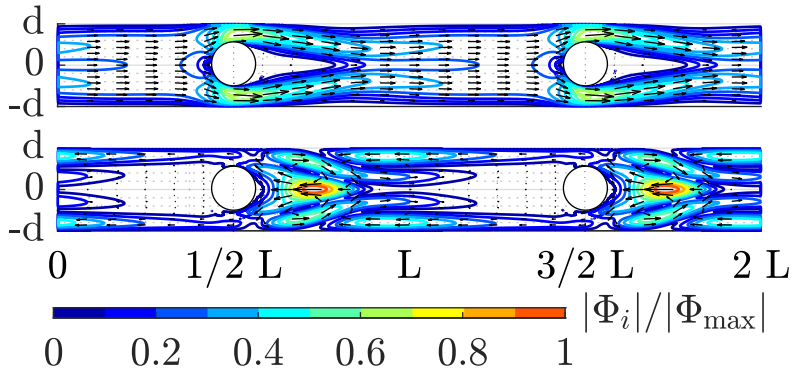

Figure 5.11: POD modes of the submerged spacer configuration at AR = 1.2, Wo = 14.9 and $\overline{\text{Re}}$ = 136.8.

POD modes and time coefficients for different amplitude ratios

Figures 5.13 and 5.14 show analogous to the POD analysis before, the major POD modes for two additional amplitude ratios of AR = 0.5 and AR = 1.0 at Wo = 10.8 and $\overline{\text{Re}}$ = 136.8. Analogous to the considerations for increasing Wo, both modes for each dynamic condition show the same structure and intensity distribution for increasing AR. For larger AR, the negative vectors in the second mode near the membrane becomes stronger. Figures 5.15a and 5.15b show the FFT spectra of the corresponding time coefficients. It can be seen that all time coefficients have their dominant frequency at the corresponding excitation frequency of Wo = 10.8. As AR increases, the time coefficients show a more sinusoidal behavior with a dominant Womersley number of Wo= 10.8.

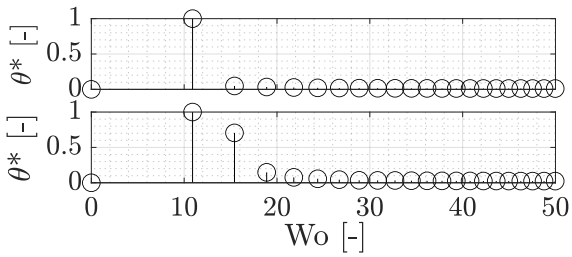

(a) FFT analysis at the dimensionless excitation frequency Wo = 10.5.

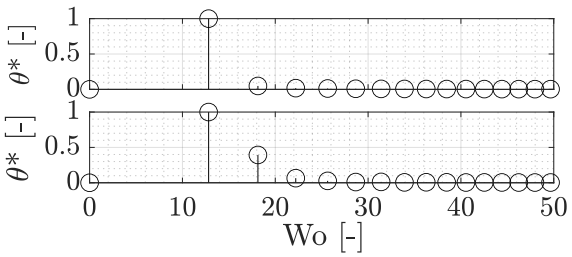

(b) FFT analysis at the dimensionless excitation frequency Wo = 12.9.

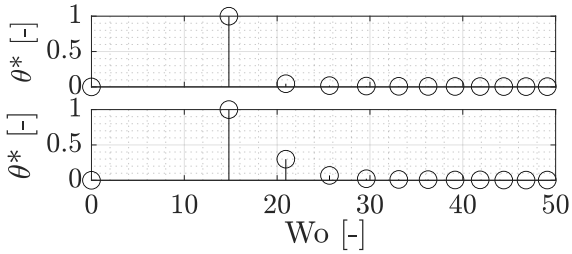

(c) FFT analysis at the dimensionless excitation frequency Wo = 14.9.

Figure 5.12: Submerged spacer: FFT analysis at AR = 1.2 and $\overline{\text{Re}}$ = 136.8.

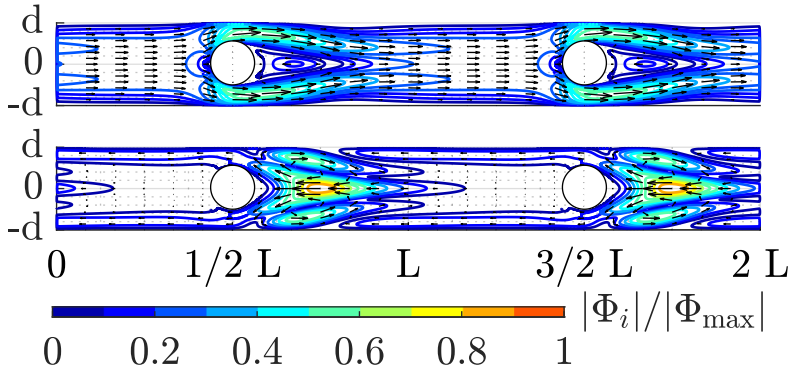

Figure 5.13: POD modes of pulsating flows in the submerged spacer configuration at AR = 0.5, Wo = 10.8 and $\overline{\text{Re}}$ = 136.8.

POD modes and time coefficients for different Reynolds numbers

Figures 5.16 and 5.17 show, again analogously to the POD analysis before, the major POD modes for two additional averaged Reynolds numbers of $\overline{\text{Re}}$ = 68.4 and $\overline{\text{Re}}$ = 102.6 at Wo = 12.9 and AR = 1.0. Also here, similar observations can

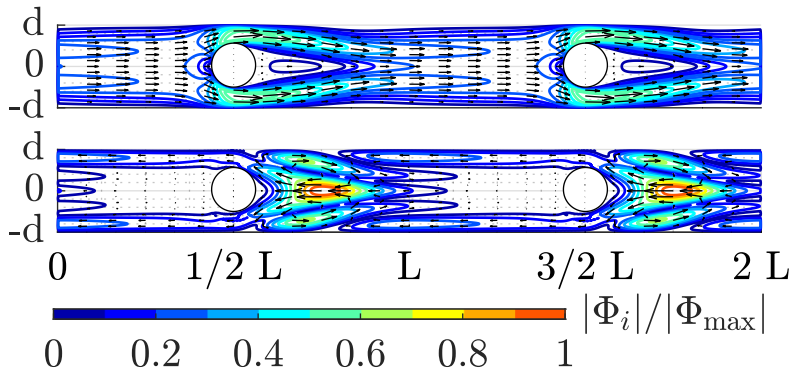

Figure 5.14: POD modes of pulsating flows in the submerged spacer configuration at AR = 1.0, Wo = 10.8 and $\overline{\text{Re}}$ = 136.8.

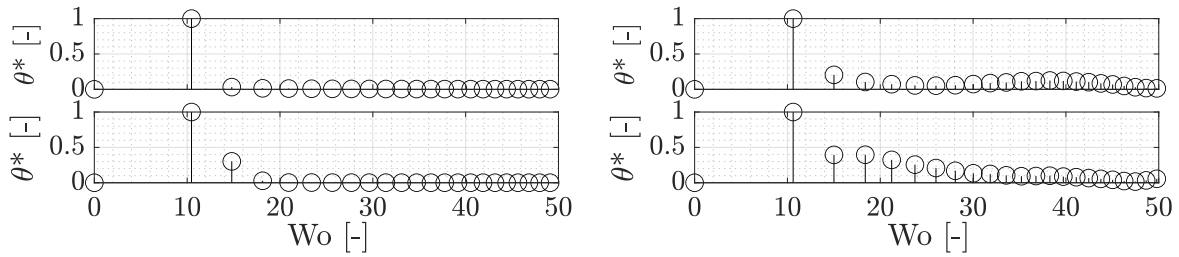

(a) FFT analysis at AR = 0.5.

(b) FFT analysis at AR = 1.0.

Figure 5.15: Submerged spacer: FFT analysis at the dimensionless excitation frequency Wo = 10.8 and $\overline{\text{Re}}$ = 136.8.

be made as for changes in Wo or AR. The dominant flow structures and magnitude distribution remain constant, changing only in level of magnitude. Figures 5.18a and 5.18b show the FFT spectra of the time coefficients. Also here, the same observations can be made as for changes in Wo or AR. The FFT spectra of the corresponding time coefficients have again the dominant frequency at Wo = 12.9 with negligible larger frequencies.

Conclusion

The comparison of the different analyses shows that the dominant POD modes are similar for the considered pulsating cases. The vector fields and the dynamic behavior of the time coefficients of the POD modes do not change significantly. It can be therefore concluded that the dominant flow structures along the spiral-wound module remain the same for decreasing AR (due to

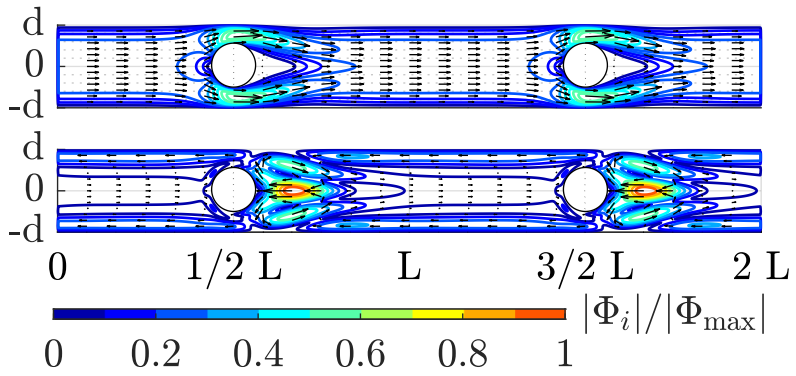

Figure 5.16: POD modes of pulsating flows in the submerged spacer configuration at AR = 1.0, Wo = 12.9 and $\overline{\text{Re}}$ = 68.4.

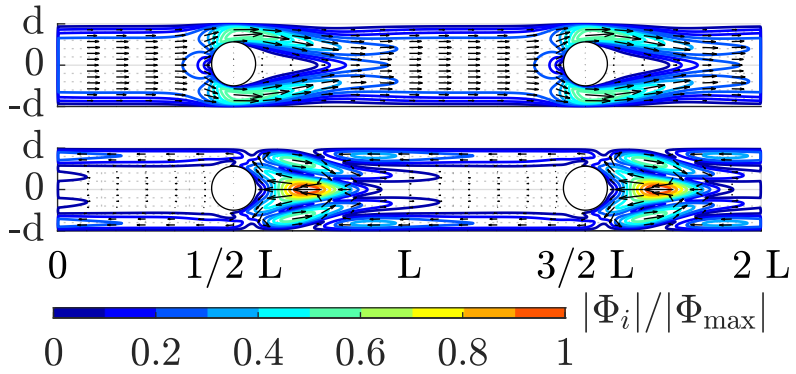

Figure 5.17: POD modes of pulsating flows in the submerged spacer configuration at AR = 1.0, Wo = 12.9 and $\overline{\text{Re}}$ = 102.6.

damping) and Reynolds numbers (due to the permeate flux) when applying pulsating flows. No interference or complex coupling of the modes along the module is expected, which would have to be considered in the quasi-2D simulation model. With regard to the potential for mass transfer enhancement, it can be noted that upstream of the filaments, the pulsations remain primarily axial, and a significant enhancement is not expected. Near the filament, the largest periodic changes in flow and flow direction can be observed in the flow field, characterized by the first mode. The maxima of the POD mode occur directly at the filament. It is anticipated that these periodic perturbations normal to the wall contribute to an enhancement of the mass transfer, cf. Section 2.6.2. An improved mass transfer is also expected due to the vortex structures associated with the second mode. They enhance mixing within the

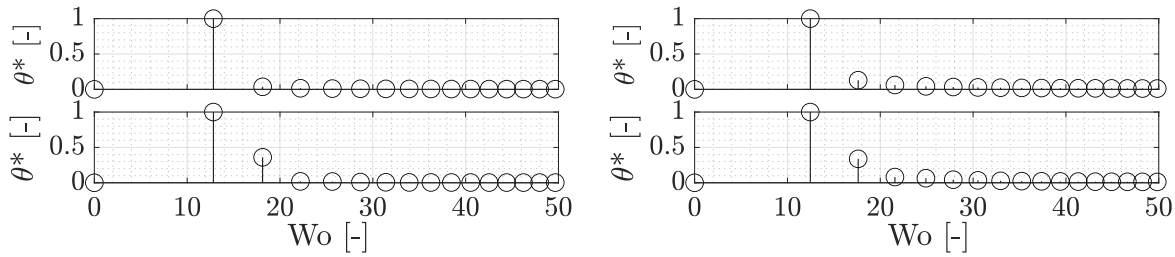

(a) FFT analysis at $\overline{\mathrm{Re}}$ =68.4. **(b)** FFT analysis at $\overline{\mathrm{Re}}$ =102.6.

Figure 5.18: Submerged spacer: FFT analysis at AR = 1.2 and at the dimensionless excitation frequency Wo = 12.9.

channel. When compared to the actual flow field, these structures and maxima correspond to the location of the periodically changing separation zone downstream of the filament.

5.3.3 Flow Field Analysis of Pulsating Flows within the Zig-Zag Spacer

Analogous to the analysis of pulsating flows in the submerged spacer configuration, this subsection examines the dominant flow structures in the zig-zag spacer configuration using the method of POD. This is done for different Womersley numbers Wo, averaged Reynolds numbers $\overline{\mathrm{Re}}$ and amplitude ratios AR, as it was written in Section 5.3.

Dynamic flow field

Prior to the POD analysis, the dynamic flow field of the zig-zag spacer is analyzed for AR = 1.0, Wo = 12.9 and $\overline{\mathrm{Re}}$ = 136.8. Figure 5.7 shows the flow field at $\omega t = 0, \pi/2, \pi, 3\pi/2$. It can be seen that the separation zones downstream of the filaments first increase until $\omega t = \pi/2$ and remain constant until $\omega t = \pi$. At $\omega t = \pi$, the separation zone upstream of the filaments strongly increases and two vortex structures establish down- and upstream of the filament. For $\omega t = 3\pi/2$, the flow is completely perturbed and two vortex structures occur between the filaments.

Mode energies of the periodic flow field

The dominant modes are determined by ordering them according to the av-

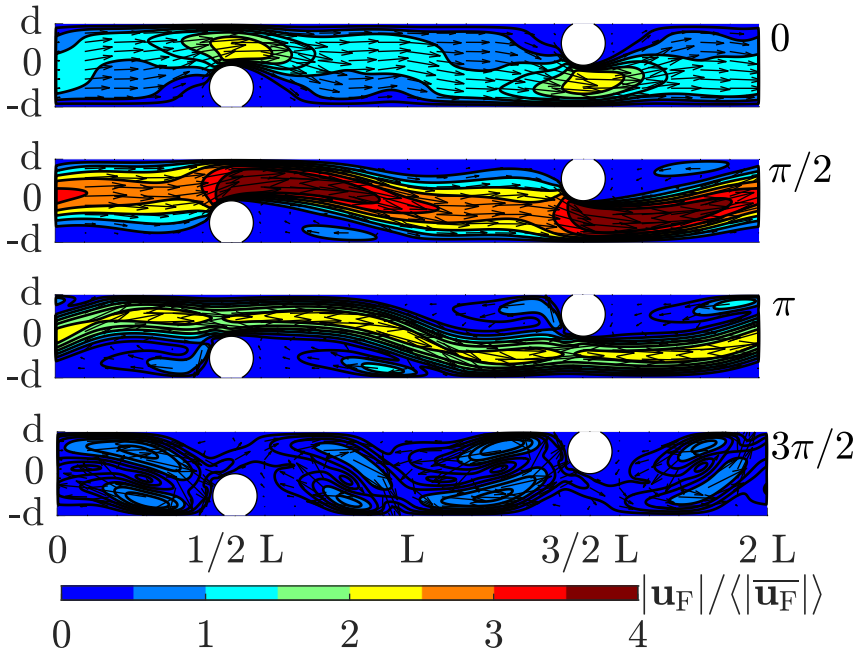

Figure 5.19: Dynamic flow field within the zig-zag spacer at $\omega t = 0, \pi/2, \pi, 3\pi/2$ for AR = 1.0, Wo = 12.9 and $\overline{\text{Re}}$ = 136.8.

eraged relative kinetic energy content of the periodic flow field E_Φ, cf. Figure 5.20. In general, the energy decreases rapidly from the first mode to the fourth mode from $E_\Phi = 80$ % below $E_\Phi = 1$%, except for Wo = 19.8. As already written before, only modes with a relative energy content above $E_\Phi > 1$% are considered, since also the first three to four modes contain more than 96 % of the total energy. For Wo < 19.8, the first three modes are analyzed. For Wo = 19.8, the fourth mode is considered additionally.

POD modes and time coefficients for different Womersley numbers

Figures 5.21, 5.22 and 5.23 show the POD modes of the dynamic velocity field. The POD modes are again represented by the relative magnitude $\Phi_i/\Phi_{\max}$. The modes are arranged by order from top to bottom. Figures 5.24a, 5.24b and 5.24c show the FFT analysis of the corresponding time coefficients. The results are shown for Wo = 10.5, 12.9, 19.8 at AR = 1.0 and $\overline{\text{Re}}$ = 136.8. For Wo = 10.5 and Wo = 12.9, the structure of the first mode is similar to the steady-state velocity field, cf. Figure 5.6a. This mode thus represents in combination with the time coefficient a periodic formation and breakdown of the separation

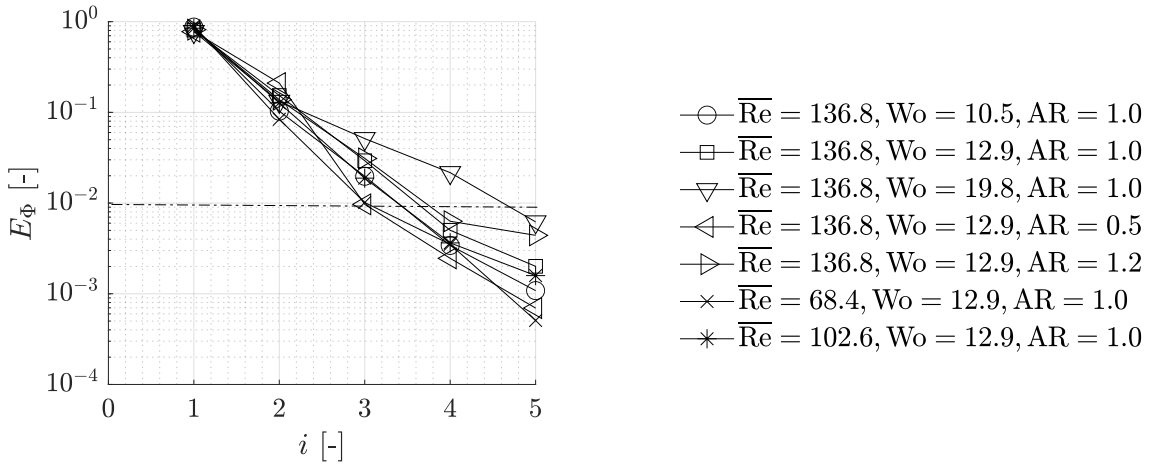

Figure 5.20: Relative kinetic energies of the POD modes plotted sorted by order for the zig-zag spacer configuration.

zone downstream of the filaments, cf. Figure 5.19. That does not apply for Wo = 19.8. Here, the separation zones downstream of the filaments decrease, and a second separation zone establishes between the filaments. In the second mode, two smaller vortex-like structures between the filaments can be identified, which correspond to the location of the establishing vortex structures near the membrane discussed before, cf. Figure 5.19. For Wo = 19.8, these zones are smaller and move upstream. The same behavior can be observed in the third mode for Wo ≤ 12.9. The third mode can be interpreted as an upstream compressed second mode, while for Wo = 19.8, a third vortex structure occur. The fourth mode shows vortex structures between the filaments heterogeneously distributed. Comparing the FFT of the corresponding time coefficients, it can be seen that Wo = 12.9 is the dominant Womersley number for the first two modes. For higher modes of $i \geq 3$, the dominant Womersley number is at the second harmonic of f_{ex}, which corresponds to Wo = 14.9, Wo = 18.2 and Wo = 28.0, respectively.

POD modes and time coefficients for different amplitude ratios

Similar to the previous POD analysis, Figures 5.25 and 5.26 show the major POD modes for two additional amplitude ratios of AR = 0.5 and AR = 1.2 at Wo = 12.9 and $\overline{\mathrm{Re}}$ = 136.8. Comparing the modes for the different AR, the pattern of the first two modes changes only slightly. The largest difference can be

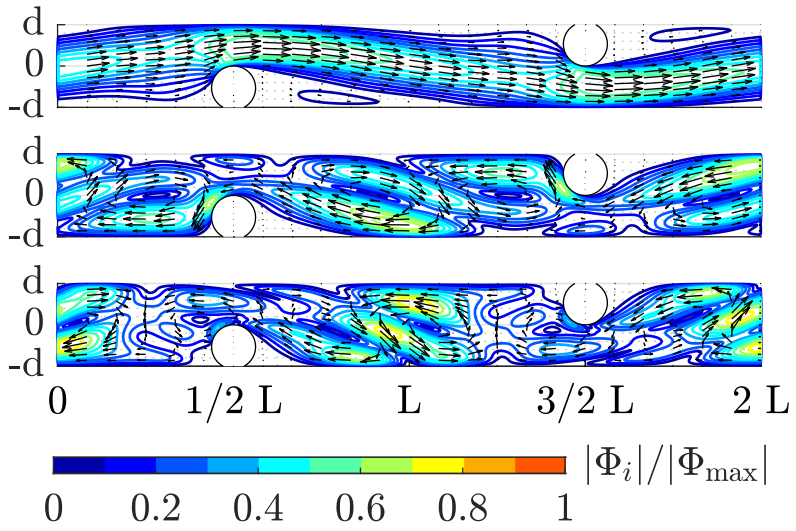

Figure 5.21: POD modes of pulsating flows in the zig-zag spacer configuration at AR = 1.0, Wo = 10.5 and $\overline{\text{Re}}$ = 136.8.

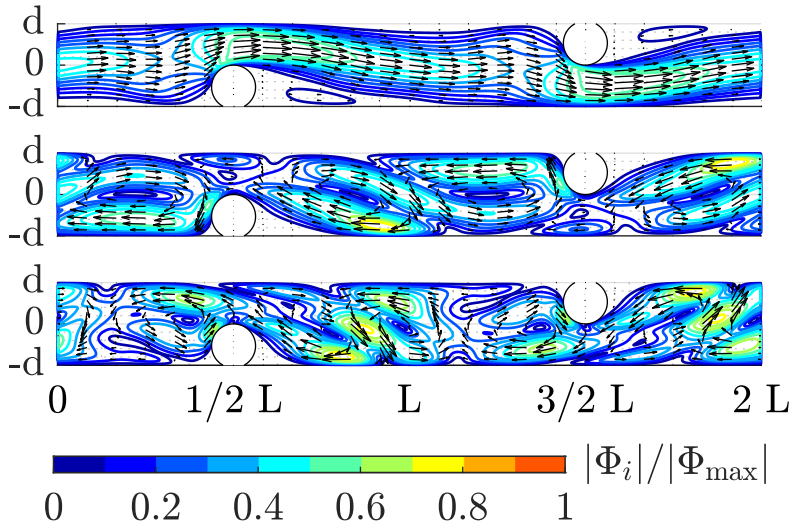

Figure 5.22: POD modes of pulsating flows in the zig-zag spacer configuration at AR = 1.0, Wo = 12.9 and $\overline{\text{Re}}$ = 136.8.

observed for the third mode upstream of the filaments. This mode only contains a low relative energy of E_Φ = 1%. For AR = 0.5, the vortex structures in the third mode can again be considered as an upstream compressed version of the second mode. Figures 5.27a and 5.27b show the FFT analysis of the cor-

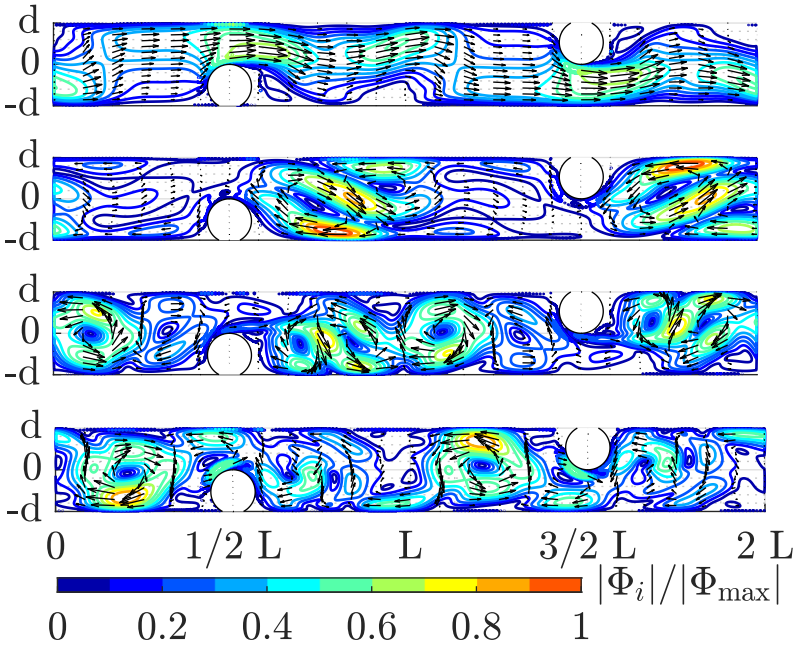

Figure 5.23: POD modes of pulsating flows in the zig-zag spacer configuration at AR = 1.0, Wo = 19.8 and $\overline{\text{Re}}$ = 136.8.

responding time coefficients. It can be seen that the FFT for the different amplitude ratios do not differ from each other. They show an almost sinusoidal profile at the dominant Womersley number Wo = 12.9 for the first two modes and Wo = 18.2 for the third mode.

POD modes and time coefficients for different Reynolds numbers

Finally, Figures 5.28 and 5.29 show the POD modes analogous to the analysis before for two additional averaged Reynolds numbers of $\overline{\text{Re}}$ = 64.2 and $\overline{\text{Re}}$ = 102.6 at Wo = 12.9 and AR = 1.0. Comparing the modes, it can be seen that the modes only slightly change in their pattern. The largest difference can be observed in the intensity of the modes upstream of the filaments. Figures 5.30a and 5.30b show the FFT analysis of the corresponding time coefficients. No significant difference can be identified. The time coefficients behave therefore as already described before.

Conclusion

In summary, the dynamic modes show similar pattern but change their en-

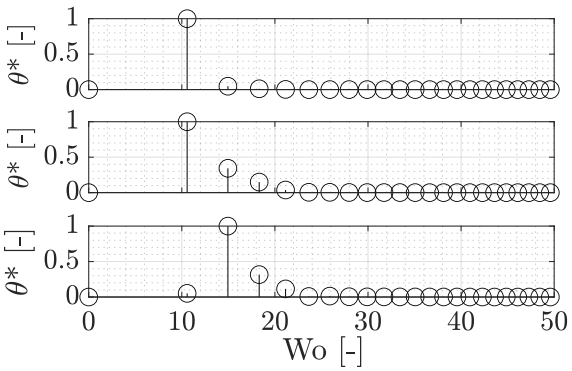

(a) FFT analysis at the dimensionless excitation frequency Wo = 10.5.

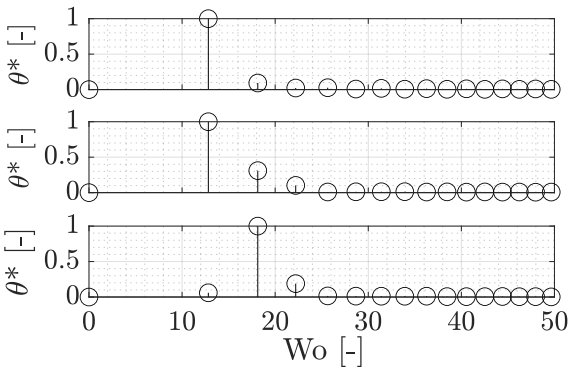

(b) FFT analysis at the dimensionless excitation frequency Wo = 12.9.

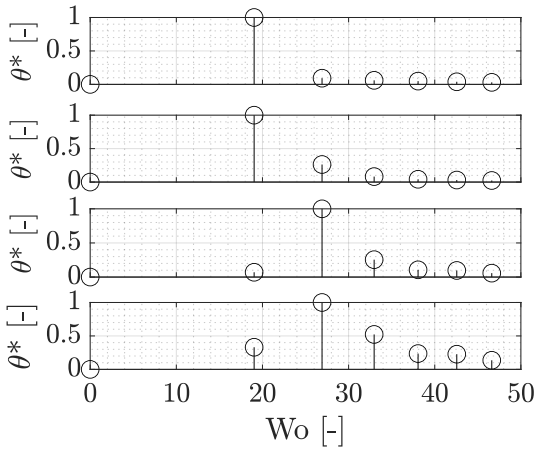

(c) FFT analysis at the dimensionless excitation frequency Wo = 19.8.

Figure 5.24: Zig-zag spacer: FFT analysis at AR = 1.0 and $\overline{\text{Re}}$ = 136.8.

ergy distribution for the considered range at constant Wo. This is widely independent of AR or $\overline{\text{Re}}$. Increasing Wo, the higher order modes become more energetically relevant. All FFT analyses of the time coefficients show a single dominant Womersley number at f_{ex} or the double of it, respectively. The first mode captures in combination with the corresponding time coefficient the periodic change of the steady-state flow field for Wo < 19.8, AR = 0.5 ... 1.2 and $\overline{\text{Re}}$ = 136.8. At Wo = 19.8, the pattern of the first mode significantly changes.

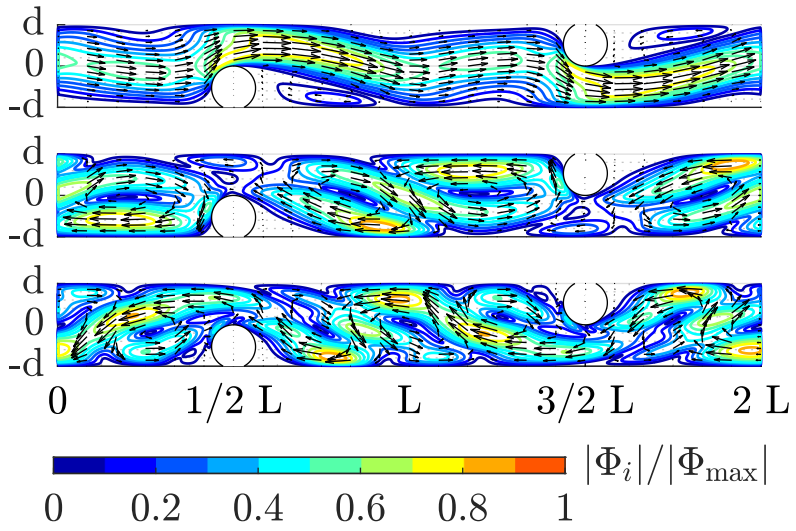

Figure 5.25: POD modes of pulsating flows in the zig-zag spacer configuration at AR = 0.5, Wo = 12.9 and $\overline{\text{Re}}$ = 136.8.

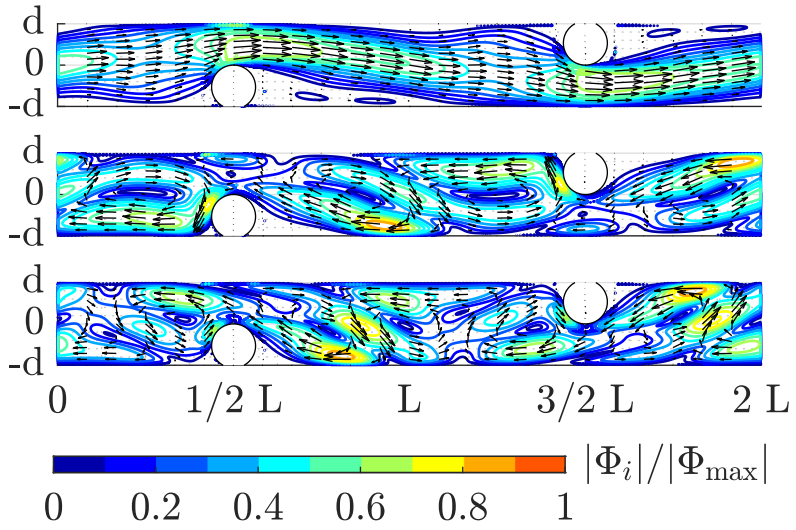

Figure 5.26: POD modes of pulsating flows in the zig-zag spacer configuration at AR = 1.2, Wo = 12.9 and $\overline{\text{Re}}$ = 136.8.

The separation zones are smaller and the maximum intensities are distributed more heterogeneously along the unit cell. This indicates already a stronger disturbance of the flow field near the membranes. For all pulsating conditions considered, the higher order modes have their maximum intensity nearer the

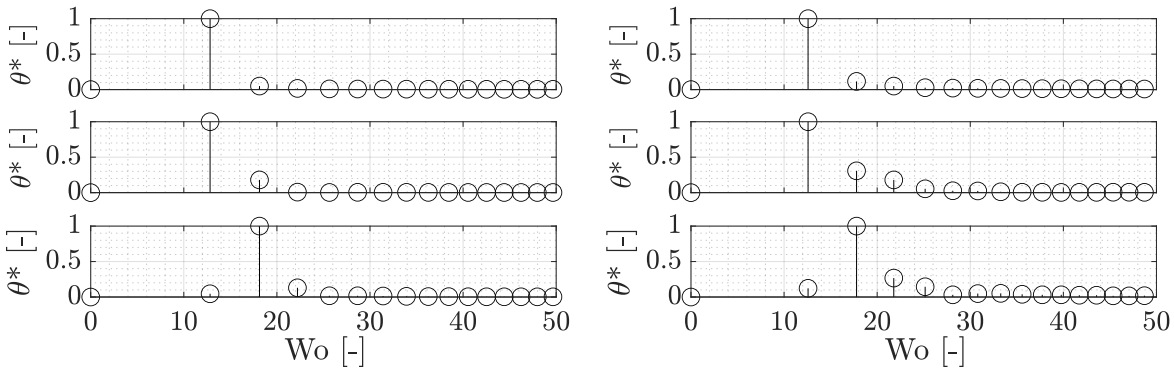

(a) FFT analysis at AR = 0.5.

(b) FFT analysis at AR = 1.2.

Figure 5.27: Zig-zag spacer: FFT analysis at the dimensionless excitation frequency Wo = 12.9 and $\overline{\text{Re}}$ = 136.8.

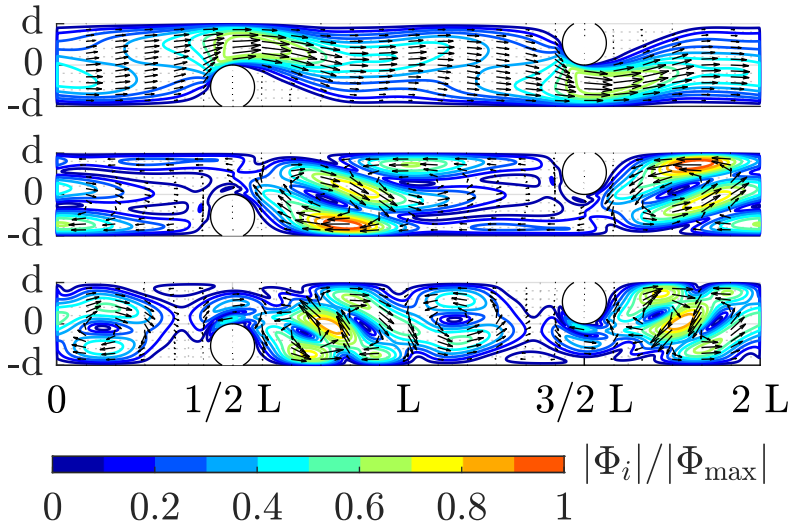

Figure 5.28: POD modes of pulsating flows in the zig-zag spacer configuration at AR = 1.0, Wo = 12.9 and $\overline{\text{Re}}$ = 68.4.

membrane and show vortex-like structures distributed along the unit cell. They contribute to perturbations and mixing within the membrane channel. This especially applies for the region of the separation zones establishing in the steady-state case. For increasing Wo, the vortex structures become smaller and move upstream. Considering the change of the dynamic modes along the module (changing AR and $\overline{\text{Re}}$), it can be observed that the modes and time co-

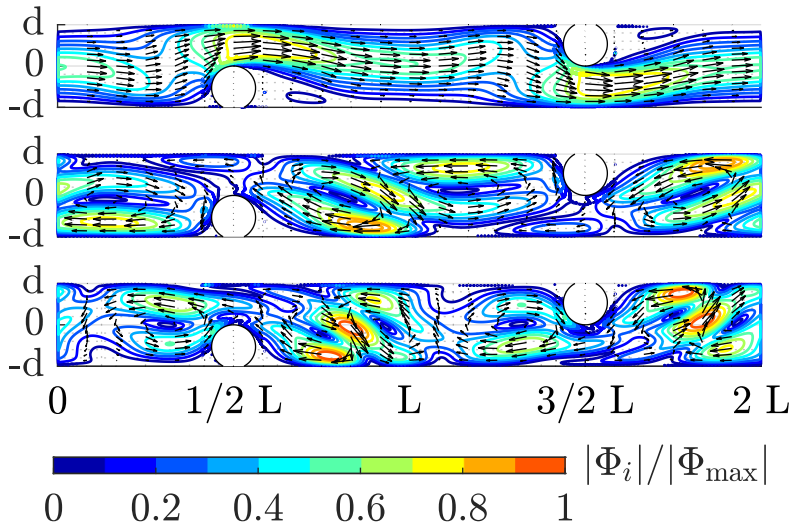

Figure 5.29: POD modes of pulsating flows in the zig-zag spacer configuration at AR = 1.0, Wo = 12.9 and $\overline{\text{Re}}$ = 102.6.

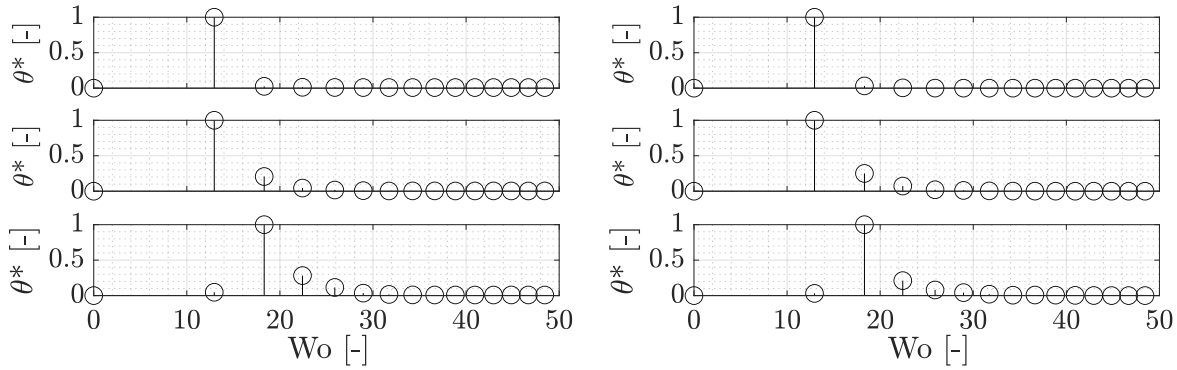

(a) FFT analysis at $\overline{\text{Re}}$ = 68.4. **(b)** FFT analysis at $\overline{\text{Re}}$ = 102.2.

Figure 5.30: Zig-zag spacer: FFT analysis at AR = 1.0 and at the dimensionless excitation frequency Wo = 12.9.

efficients only change slightly in their shape, frequency and magnitude. Moreover, for decreasing AR and $\overline{\text{Re}}$, the third mode becomes less energetically relevant. A complex dynamic behavior or interference of the dominant modes is therefore not expected along the module. This simplifies the system modeling problem.

5.3.4 Salt Mass Fraction Field Analysis for Pulsating Flows within Spacer-Filled Channels

After the analysis of the flow dynamics, the dynamic salt mass fraction field is investigated in this subsection. The averaged Reynolds number is set to $\overline{\mathrm{Re}} = 136.8$.

Dynamic salt mass fraction field

Before analyzing the dynamics using POD, the dynamic salt mass fraction field is discussed using four snapshots during one pulsation cycle at $\omega t = 0, \frac{\pi}{2}, \pi, \frac{3\pi}{2}$, cf. Figure 5.31. The field is analyzed for AR = 1.0, $\overline{\mathrm{Re}}$ = 136.8 and Wo = 12.9. Figure 5.31 shows the salt mass fraction field $|\xi_\mathrm{F}|$ normalized by the averaged salt mass fraction $\langle|\overline{\xi}_\mathrm{F}|\rangle = 0.035$ for the submerged, cf. Figure 5.31a, and zig-zag, cf. Figure 5.31b, spacer configuration. In general, the salt mass fraction field is significantly perturbed and well mixed compared to steady-state operation, especially for the zig-zag spacer configuration. Small perturbations can be identified between the filaments for the submerged spacer configuration. In the case of the zig-zag spacer configuration, minor perturbations induced by vortical velocity structures can be discerned downstream of the filaments.

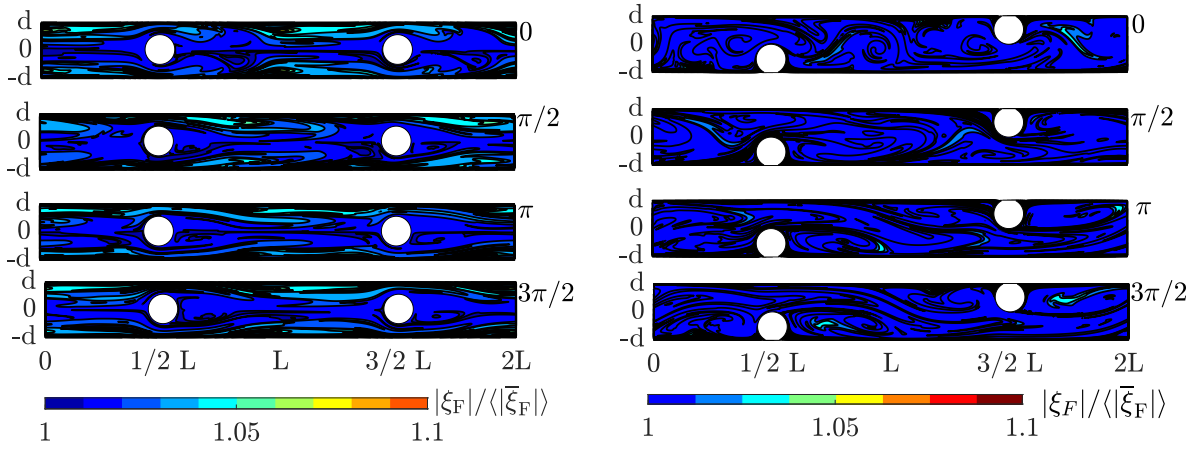

(a) Submerged spacer configuration. **(b)** Zig-zag spacer configuration.

Figure 5.31: Relative salt mass fraction field for both spacer configurations for the pulsating case at $\overline{\mathrm{Re}}$ =136.8, AR = 1.0 and Wo = 12.9 during one pulsation cycle.

Considering the corresponding salt mass fraction at the membrane, which is shown in Figure 5.32, maximum values of $\xi_{F,AL}/\langle\overline{\xi}_F\rangle = 1.21$ for the submerged spacer configuration are reached, which is almost three times lower, than for steady-state operation, cf. Figure 5.5. When examining the dynamic perturbations, it can be observed that the dynamic alteration is modest. For the zig-zag spacer configuration, the highest salt mass fractions are observed precisely at the points of attachment between the filament and the membrane. $\xi_{F,AL}/\langle\overline{\xi}_F\rangle$ reaches maximum values of $\xi_{F,AL}/\langle\overline{\xi}_F\rangle = 1.52$. This is caused by the flow stagnation zone at the attached filament. For the submerged spacer con-

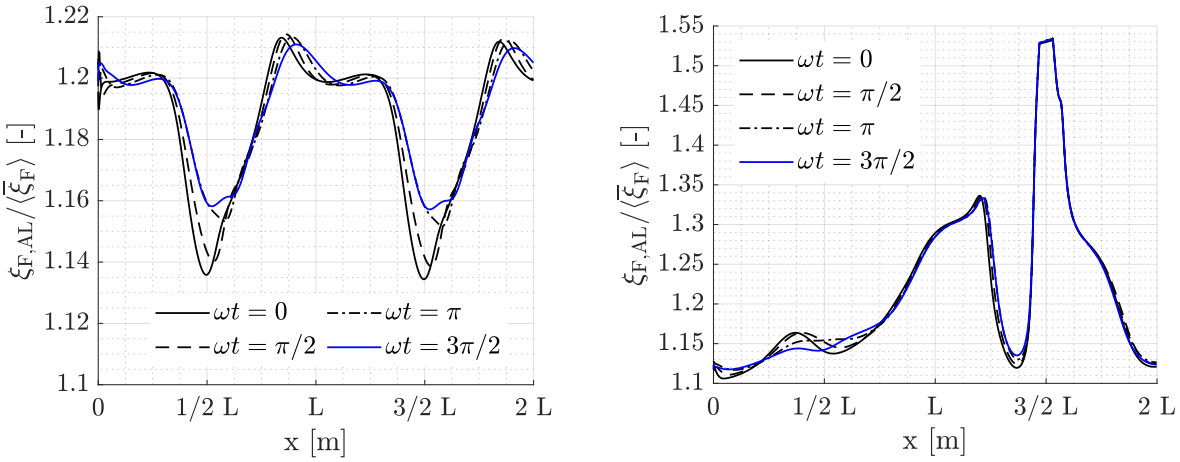

(a) $\xi_{F,AL}/\langle\overline{\xi}_F\rangle$ for the submerged spacer configuration.

(b) $\xi_{F,AL}/\langle\overline{\xi}_F\rangle$ for the zig-zag spacer configuration.

Figure 5.32: Relative salt mass fraction at the membrane $\xi_{F,AL}/\langle\overline{\xi}_F\rangle$ for both spacer configurations for the pulsating case at $\overline{Re}$ =136.8, AR = 1.0 and Wo = 12.9 during one pulsation cycle.

figuration, the largest periodic change of $\xi_{F,AL}/\langle\overline{\xi}_F\rangle$ is observed directly at and downstream of the filament. For the zig-zag spacer configuration, the largest variation is observed at the location of the opposite filament at $x = 1/2L$. Analyzing the periodic change of $\xi_{F,AL}$ for all considered pulsating cases in the work at hand, of which not all of them are shown here, in both spacer configurations reveals a maximum relative amplitude of $AR_{\xi_{F,AL},max} = 6.7$ %. Combining this finding with the results in Subsection 2.6.1, it can be concluded that the quasi-steady-state approach of the mass transport through the membrane

is acceptable.

Since the largest salt mass fraction perturbations occur primarily near the membrane, the POD analysis is performed specifically for the periodic salt mass fraction at the membrane $\tilde{\xi}_{\mathrm{F,AL}}$. This choice is justified by the fact that the dynamic interaction between the flow field and the concentration boundary layer is most important here. As changing AR or $\overline{\mathrm{Re}}$ do not lead to a significant change in flow dynamics, cf. Subsections 5.3.2 and 5.3.3, the POD analysis is only performed for changing Wo at AR = 1.0, $\overline{\mathrm{Re}}$ = 136.8. Due to the vertical symmetry, only the top membrane is considered. The same conclusions can be drawn for the bottom membrane. Instead of arranging the POD modes regarding the relative energy content, the modes are sorted regarding the average of the square magnitude of the volume-averaged periodic salt mass fraction field. For the submerged spacer, the first two and for the zig-zag spacer configuration the first four modes analyzed. These numbers are adapted from the number of dominant modes for the dynamic velocity field, cf. Sections 5.3.2 and 5.3.3.

Submerged spacer: POD modes and time coefficients

Figure 5.33 shows the POD modes of the periodic salt mass fraction field at the top membrane for Womersley numbers of Wo = 10.5, 12.9, 14.9 for the submerged spacer configuration. Figures 5.33b, 5.33d and 5.33f show the FFT analysis of the time coefficients to the corresponding modes shown in Figures 5.33a, 5.33c and 5.33e. It can be observed that the largest magnitudes occur at the position of the filaments at x = 1/2 L and x = 3/2 L. Except for Wo = 10.5, the largest values are reached in the second mode. For Wo = 10.5, different local maxima are distributed along the unit cell. Increasing Wo, the two maxima at the filament position become more pronounced. Considering the time coefficient analysis, the dominant frequency is at the corresponding excitation frequency Wo. When comparing the modes with the velocity POD modes, the two dominant maxima at the filaments correlate to the large magnitudes of the first velocity mode. These maxima also correspond to the location of the largest dynamic changes of the salt mass fraction, cf. Figure 5.32a. The maximum downstream of the filament also corresponds to the large intensity of the second velocity mode.

Zig-zag spacer: POD modes and time coefficients

Figure 5.34 shows the POD modes of the salt mass fraction field at the top membrane for Womersley numbers of Wo = 10.5, 12.9, 19.8 for the zig-zag spacer configuration. Figures 5.34a, 5.34c and 5.34e show the first four POD modes. In Figures 5.34b, 5.34d and 5.34f, the FFT analysis of the corresponding time coefficients can be seen. For Wo = 10.5 and Wo = 12.9, the shapes of the modes are similar. The largest intensities are reached in the first mode and occur upstream of the attached filament at $x = 3/2$ L. Increasing Wo, the maximum moves upstream. The local maxima of the higher order modes can be identified at the position of the opposite filament at $x = 1/2$ L and of the attached filament $x = 3/2$ L. For Wo = 19.8, the dominant maxima are much more concise. Here, the second mode has a dominant maximum downstream of the attached filament. Considering the FFT analysis, all time coefficients oscillate almost harmonically. The time coefficients of the first two modes have their dominant frequency at the excitation frequency at Wo = 10.5, 12.9, 19.8, the third and fourth mode have their peak on the second harmonic at $\sqrt{2}$Wo. Comparing the salt mass fraction modes to the velocity modes, a similar behavior can be observed. For larger Wo, the large intensities near the membrane move upstream. This also applies to the vortices near to the membrane. In general, the local intensity maxima of the velocity modes correspond to the local maxima of the salt mass fraction modes at the membrane.

Conclusion

For both spacer configurations, no direct connection between a single velocity and salt mass fraction mode can be identified but to the combination of them. Regarding the submerged spacer case, maxima of the modes are observed directly around the filaments, where also the largest changes of $\xi_{\mathrm{F,AL}}$ and the maxima of the first velocity mode occur. Considering the zig-zag spacer configuration, the local maxima correspond to the highest intensities of different high order velocity modes and the location of the vortical structures. Comparing the steady-state and dynamic flow and salt mass fractions field, it can be concluded that pulsating flows strongly enhance mixing inside the spacer-filled channel. For the zig-zag case, the periodic perturbation of the separation zones disturbs the formation of the concentration boundary layer up- and downstream of the filaments. For Wo = 19.8, additional vortex-like struc-

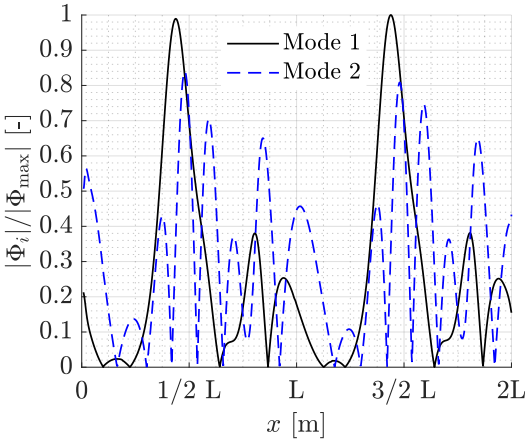

(a) POD modes at Wo=10.5.

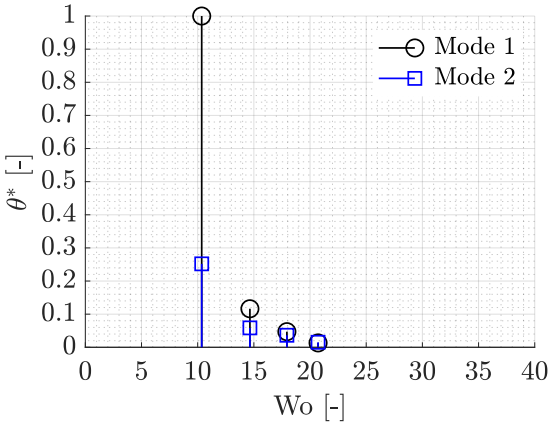

(b) FFT analysis at Wo=10.5.

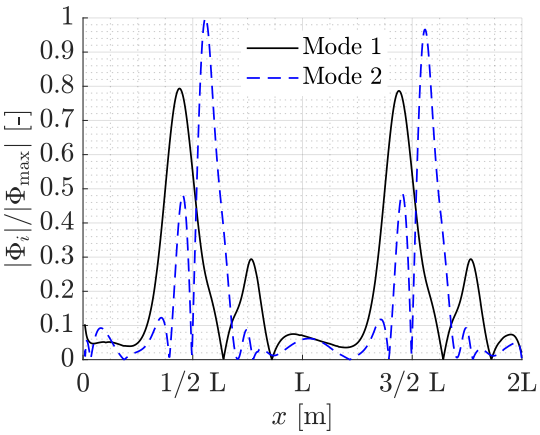

(c) POD modes at Wo=12.9.

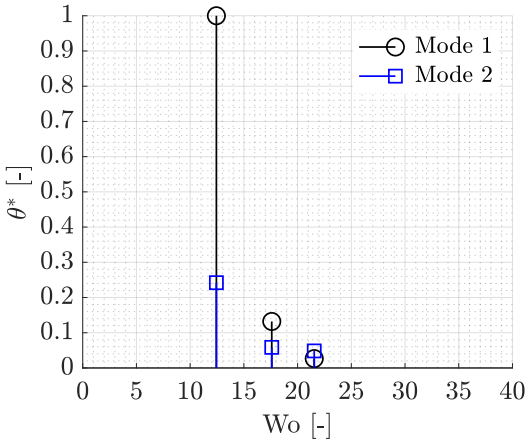

(d) FFT analysis at Wo=12.9.

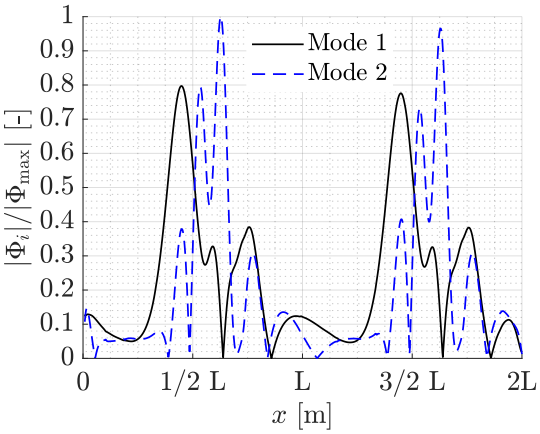

(e) POD modes at Wo=14.9.

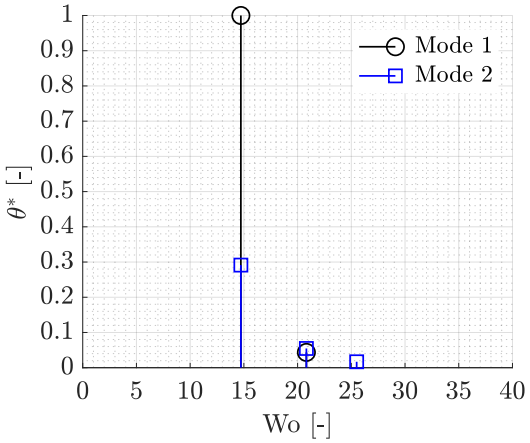

(f) FFT analysis at Wo=14.9.

Figure 5.33: Submerged spacer: POD and FFT analysis of the salt mass fraction field at the membrane at AR = 1.0 and $\overline{\text{Re}}$ = 136.8.

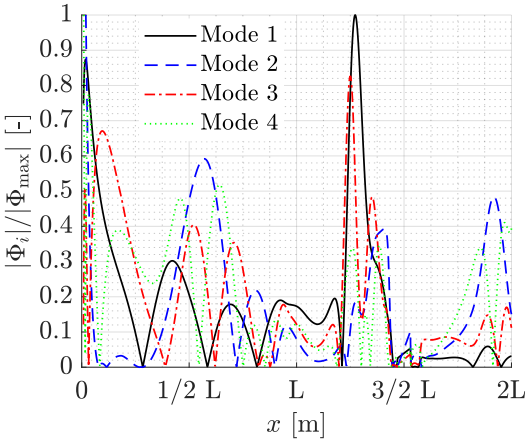

(a) POD modes at Wo=10.5.

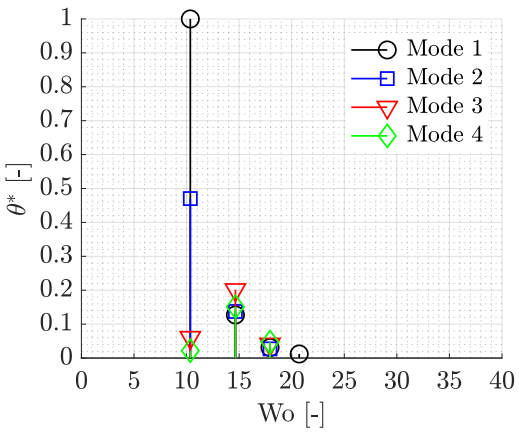

(b) FFT analysis at Wo=10.5.

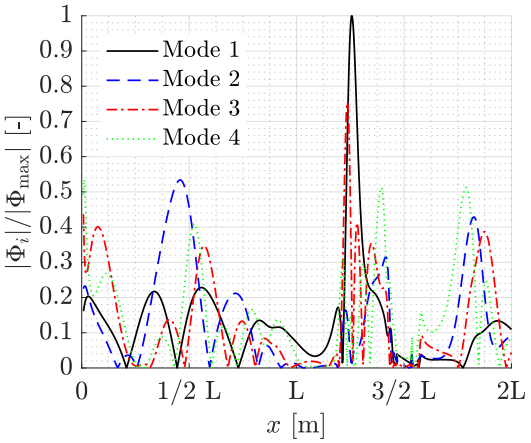

(c) POD modes at Wo=12.9.

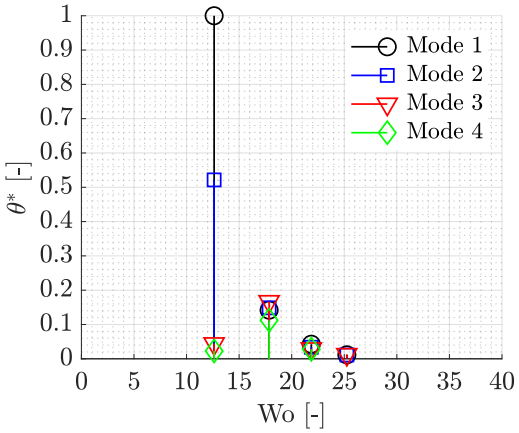

(d) FFT analysis at Wo=12.9.

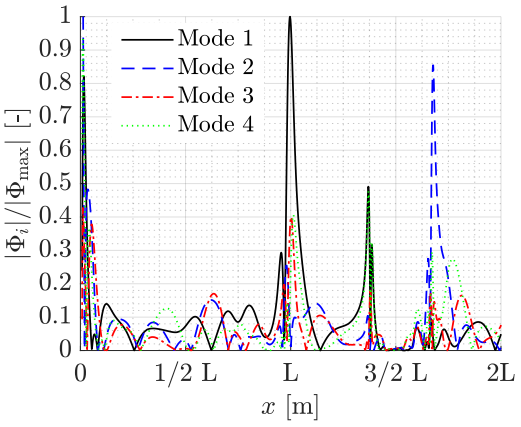

(e) POD modes at Wo=19.8.

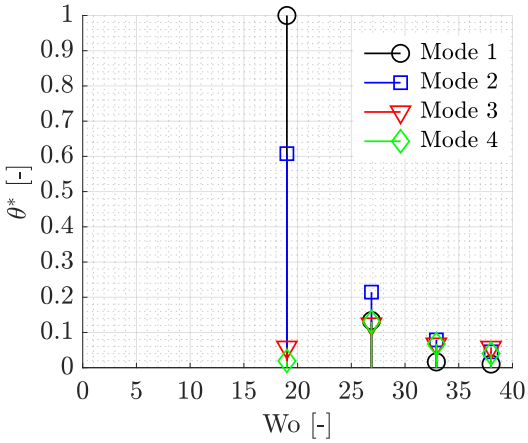

(f) FFT analysis at Wo=19.8.

Figure 5.34: Zig-Zag spacer: POD and FFT analysis of the salt mass fraction field at the membrane at AR = 1.0 and $\overline{\text{Re}}$ = 136.8.

tures in the higher order modes provide a further mixing in the channel and perturbations of the salt mass fraction at the membrane. However, the perturbations at the membrane are not strong. Therefore, potential transient transport effects across the membrane are non-dominant, which is important for the quasi-2D simulation approach. This is also consistent with the analysis in Section 2.6.

5.3.5 Local Sherwood Number between two Filaments

As discussed in Section 5.3.4, mixing in pulsating flows is significantly enhanced for both spacer configurations compared to steady-state conditions. In the present subsection, the corresponding local mass transfer enhancement across the membrane is quantified by comparing the local Sherwood number for the pulsating and steady-state cases $\overline{\mathrm{Sh}}_{\mathrm{puls}}/\overline{\mathrm{Sh}}_{\mathrm{stst}}$. Values of $\overline{\mathrm{Sh}}/\overline{\mathrm{Sh}}_{\mathrm{stst}} > 1$ correspond to a mass transfer enhancement. Additionally, the ratio of the local vorticity flux $\overline{\Omega}_{\mathrm{puls}}/\overline{\Omega}_{\mathrm{stst}}$ and the local amplitude $\varpi_{\mathrm{y,AL}}$ normal to the membrane are evaluated. The local amplitude $\varpi_{\mathrm{y,AL}}$ is calculated using the permeate volume flux v_{P} with

$$\varpi_{\mathrm{y,AL}} = \frac{AR_{v_{\mathrm{P}}} v_{\mathrm{P}}}{f}. \tag{5.3}$$

$\varpi_{\mathrm{y,AL}}$ is used as an indicator of the perturbation of the boundary layer. As discussed in Section 2.6.2, the magnitude of the perturbation depends on the local amplitude along the pulsating flow and Wo. Therefore, the local amplitude normal to the membrane should therefore correlate to a mass transfer enhancement. Again, the analysis is performed for the top membrane only.

Local Sherwood number analysis for the submerged spacer
Figure 5.35 shows the Sherwood number analysis at the top membrane for the submerged case for Womersley numbers of Wo = 12.9, 15.0 at AR = 1.0, 1.2. $\overline{\mathrm{Sh}}_{\mathrm{puls}}/\overline{\mathrm{Sh}}_{\mathrm{stst}}$, cf. Figure 5.35a, is always greater than 1 along the unit cell. The local shape with two maxima at the position of the filaments is similar for all pulsating conditions considered. Increasing AR or Wo leads to a slight increase of $\overline{\mathrm{Sh}}_{\mathrm{puls}}/\overline{\mathrm{Sh}}_{\mathrm{stst}}$.

Figure 5.35b shows the local time-averaged ratio of the vorticity flux $\overline{\Omega}_{\mathrm{puls}}/\overline{\Omega}_{\mathrm{stst}}$. A maximum can be identified between the filaments, where only the magnitude of $\overline{\Omega}_{\mathrm{puls}}/\overline{\Omega}_{\mathrm{stst}}$ changes for the different pulsation conditions. This increase can be attributed to the vortical structures contributed by the second velocity POD mode, cf. Figure 5.12. The magnitude of $\overline{\Omega}_{\mathrm{puls}}/\overline{\Omega}_{\mathrm{stst}}$ increase with increasing Wo.

Figure 5.35c shows the local amplitude $\omega_{\mathrm{y,AL}}$. Two maxima at the position of the filaments can be observed. Increasing Wo and AR, the values of $\omega_{\mathrm{y,AL}}$ decrease. The maxima can be attributed to the fact that the largest perturbations within the boundary layer are induced by pulsations normal to the membrane caused by the flow redirection due to the filament.

The increased vorticity flux results from vortex-like structures in the second mode occurring downstream of the filaments. These vortex-like structures contribute to a better mixing between the filaments. Due to the filament's constriction, pulsations directed normal to the membrane are generated. During the acceleration phase, there is a nonlinear increase in momentum normal to the membrane. Simultaneously, the low bulk salt mass fraction upstream of the filament experiences periodic transport from the bulk to the membrane. The larger AR or Wo, the larger this perturbation. On the one hand, this results in a more pronounced periodic perturbation within the boundary layer, leading to enhanced mass transfer and, consequently, a reduction in the salt mass fraction at the membrane over time. On the other hand, these pulsations induce periodic perturbations in the salt mass fraction within the boundary layer and at the membrane resulting in an increased back diffusion, cf. Section 2.6.2. However, this effect is regarded as minor when compared to the other effects of induced normal pulsations. The maxima of $\omega_{\mathrm{y,AL}}$ and $\overline{\mathrm{Sh}}_{\mathrm{puls}}/\overline{\mathrm{Sh}}_{\mathrm{stst}}$ also correspond to the location of the maxima identified in the salt mass fraction modes, cf. Figure 5.33, which also indicates a large perturbation at these locations. Both phenomena in combination, the better mixing between the filaments and the disturbing by pulsations normal to the membrane, contribute to an increased mass transfer at the membrane along the unit cell.

Local Sherwood number analysis for the zig-zag spacer

Figure 5.36 shows the Sherwood number analysis for the zig-zag spacer con-

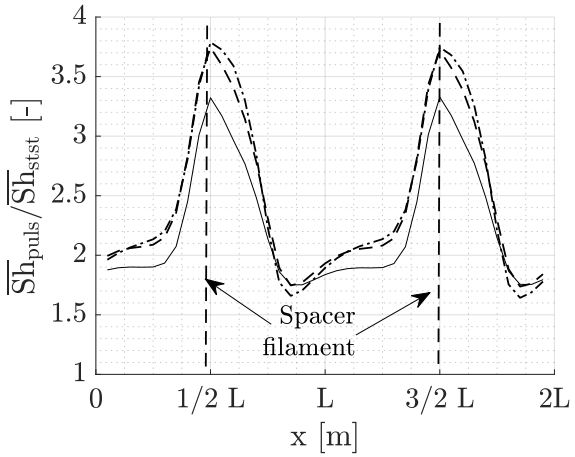

(a) Ratio of Sherwood number $\overline{\mathrm{Sh}}_{\mathrm{puls}}/\overline{\mathrm{Sh}}_{\mathrm{ststst}}$ for the pulsating and steady-state case.

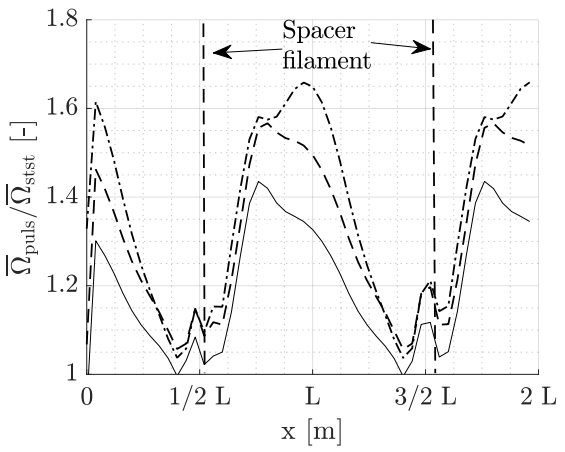

(b) Ratio of vorticity flux $\overline{\Omega}_{\mathrm{puls}}/\overline{\Omega}_{\mathrm{ststst}}$ for the pulsating and steady-state case.

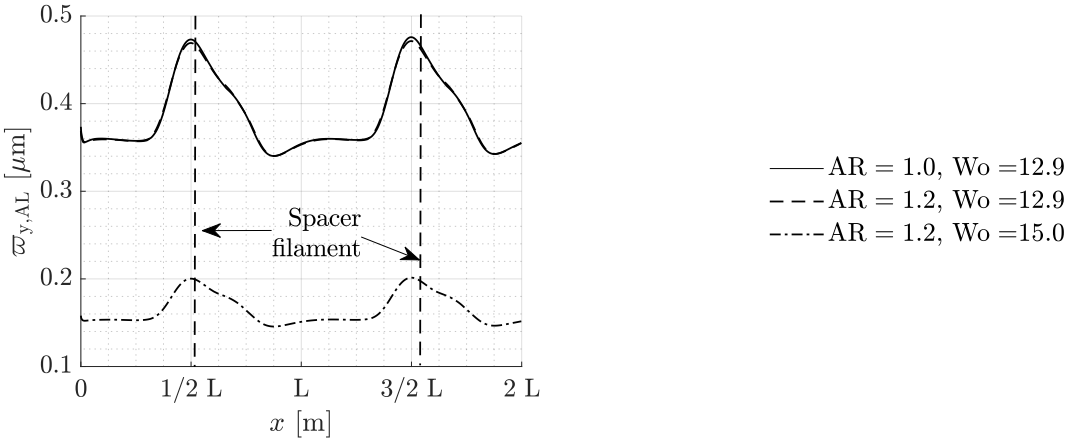

(c) Local amplitude $\varpi_{\mathrm{y,AL}}$.

Figure 5.35: Local Sherwood number analysis in the submerged spacer for pulsating flows.

figuration for Wo = 10.5, 12.9, 19.8, AR = 0.5, 1.0, 1.2 and $\overline{\mathrm{Re}}$ = 136.8. Analogous to the analysis of the submerged spacer, it can be seen that $\overline{\mathrm{Sh}}_{\mathrm{puls}}/\overline{\mathrm{Sh}}_{\mathrm{ststst}}$ is generally greater than 1, except at the position of the attachment point between filament and membrane at x = 3/2 L. Two maxima can be identified upstream and downstream of the attached filament. It can be observed that with increasing AR at Wo = 12.9, the value of the maximum increases. While

the shape remains consistent, the location of the maximum slightly moves upstream. This also applies for increasing Wo at AR = 1.0. For Wo = 19.8, the maximum upstream of the attached filament moves further upstream and is lower. Downstream of x = 3/2 L, the maximum shows the same trend for the different conditions considered, except for that the maximum is larger.

Figure 5.36b shows the local time-averaged vorticity flux $\overline{\Omega}$ for the pulsating case normalized by the steady-state value $\overline{\Omega}_{\mathrm{stst}}$. It can be observed that the shapes for increasing AR at Wo = 12.9 are similar, but the values increase. Increasing Wo, shape and magnitude change significantly. Additionally, an upstream shift of the local maxima can be observed.

Figure 5.36c shows the amplitude $\varpi_{\mathrm{y,AL}}$ along the unit cell. Local maxima can be identified upstream of the attached filament, with the highest values being attained at $x \leq 1/2$ L. For Wo = 19.8, the local maximum is much wider than for lower Wo. Increasing Wo or decreasing AR lead to to a decrease of $\varpi_{\mathrm{y,AL}}$.

The largest enhancement can be identified up- and downstream of the attached filament at x = 3/2 L. The prevention of a stable separation downstream of the filament zone hinders the formation of a large concentration boundary layer. Furthermore, the vorticity flux is significantly amplified along the entire unit cell. From $x = 0$ to $x = L$, the increase of the vorticity flux results from vortical structures contributed by the higher order velocity POD modes at the bottom membrane. For $x >$ L, the maxima are attributed to vortical structures of the higher-order velocity POD modes, located in close proximity to the top membrane. Comparing Figures 5.36a and 5.36b, it can be seen that the local maxima of $\overline{\mathrm{Sh}}_{\mathrm{puls}}/\overline{\mathrm{Sh}}_{\mathrm{stst}}$ correlate to the local maxima of $\overline{\Omega}/\Omega_{\mathrm{stst}}$ for $x >$ L. This implies that the generated longitudinal vortical structures of the higher-order modes near the top membrane contribute to a strong enhancement of the local mass transfer. The vortical structures distributed throughout the entire unit cell also enhance mixing within the entire unit cell. Additionally, analogous to the submerged spacer, pulsations normal to the membrane are induced by the filament and the periodic formation and buildup of the separation zone downstream of the filaments. These phenomena described also cause the augmentation of local perturbations near the membrane, characterized by $\varpi_{j_{\mathrm{p}}}$.

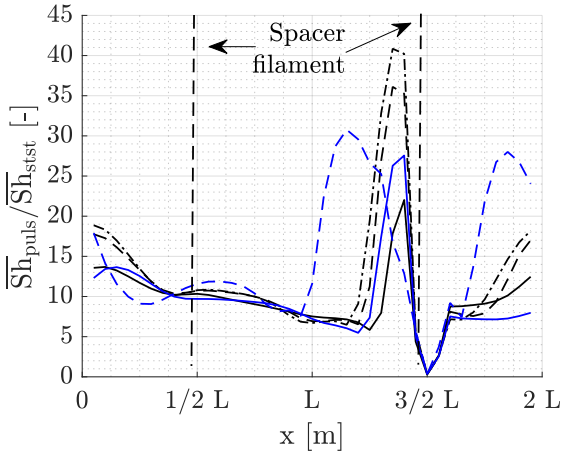

(a) Ratio of Sherwood number $\overline{\mathrm{Sh}}_{\mathrm{puls}}/\overline{\mathrm{Sh}}_{\mathrm{stst}}$ for the pulsating and steady-state case.

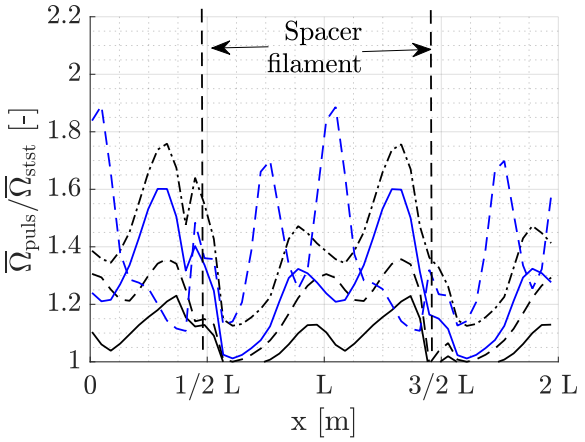

(b) Ratio of vorticity flux $\overline{\Omega}/\Omega_{\mathrm{stst}}$ for the pulsating and steady-state case.

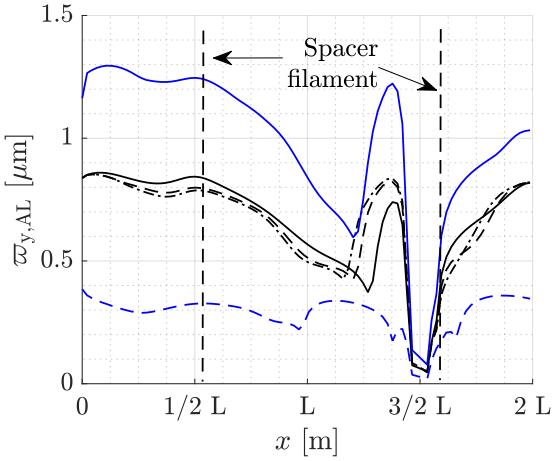

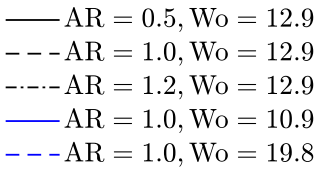

(c) Local amplitude $\varpi_{\mathrm{y,AL}}$.

Figure 5.36: Local Sherwood number analysis in the zig-zag spacer for pulsating flows.

Conclusion

A singular explanation for the mass transfer enhancement in spacer-filled channels cannot be found conclusively. The complex geometry of the spacer-filled channels leads to different local mass transfer enhancement phenomena. The contribution of vortical structures, generation of pulsations normal to the membrane and the prevention of stable separation zones hinder the for-

mation of a large concentration boundary layer and lead to a better mixing as well as local mass transfer along the unit cell. The mass transfer enhancement along the entire unit cell is based on the synergy among these phenomena.

5.4 Summary of the Mass Transfer Enhancement due to Pulsating Flows in Spacer-Filled-Channels

The numerical results can be summarized as follows:

- Different flux measurements with the FO test rig showed that pulsating flows have a positive influence on the mass transfer across the membrane. The enhancement is significant for Wo > 6.8. This is in accordance to preliminary studies [8].
- The CFD simulation model was verified using data from these measurements and PIV data from measurements using Reynolds-similar spacer test cells. It was shown that the CFD model could predict the mass transfer enhancement and velocity profiles with an acceptable relative error.
- The analysis of the steady-state problem revealed that large concentration boundary layers establish in conventionally operated RO systems, especially up- and downstream of the filaments due to the formation of separation zones.
- The POD modes of pulsating flows and the analysis of the local mass transfer showed that for both spacer configurations pulsations normal to the membrane, vortex-like structures and the periodic formation of the averaged flow field lead to an enhanced mixing. The perturbations are intensified for larger AR and Wo.
- No predominant factor contributing to mass transfer enhancement during the application of pulsating flows could be discerned. It is an interplay of the previously described induced flow phenomena.

In addition to improving mass transfer, higher frequencies also result in increased energy demand and a higher damping rate. Therefore, to energetically

benefit from the large mass transfer enhancement, optimal conditions have to be found, where the enhanced mass transfer compensate the additional energy demand for the entire RO system. This is the topic of the next chapter.

6 Pulsating Flows in Small-Scale RO Systems

For an economical application of pulsating flows in RO systems, the improvement of mass transfer has to result in an increased permeate flux with minimal additional energy demand. The findings of the detailed experiments and simulations of this work will be now transferred to the RO system to evaluate the potential reduction in the specific energy consumption (SEC) by applying pulsating flows.

First, the small-scale RO system to be analyzed and the relevant operation window for the application of pulsating flows will be introduced in Section 6.1. In Section 6.2, the needed time-averaged input parameters for the evaluation of applying pulsation flows will be determined with the data gathered with the FO test rig and Computational Fluid Dynamics (CFD) simulations. In Section 6.3, the energy requirement of the application of pulsating flows in small-scaled RO systems will be analyzed and optimal dynamic parameters will be determined.

6.1 Operation Window and Setup of the Small-Scale Reverse Osmosis Plant

The operation constraints for RO systems are represented by the so-called operation window. Figure 6.1a shows three operation windows for three single elements of the type DOW SW-2521 [85] connected in series. The boundaries of each operation window are determined using the manufacturer's data sheet [85] and the simulation approach described in Section 4.2. The following constraints determine the operation window [117]:

- **Constraints due to mechanical stability**: The mechanical stability of the module limits the hydraulic pressure and maximum feed flow rate that can be applied. The maximum feed flow rate is limited by the maximum pressure loss, which would lead to destruction of the module. Both of them can be seen as mandatory limits, which have to be kept to avoid destroying the element.

- **Constraints for stable long-term operation**: The operating conditions for long-term operation to minimize the fouling potential depend on the fouling tendency of the feed. The tendency determines the lower limit of the recommended retentate flow rates due to decreasing wall shear stress with decreasing velocities. This limit must be determined empirically and is given for different feed water compositions by the module manufacturer [85]. The fouling propensity also depends on the concentration polarization and therefore on the permeate flux. A maximum module recovery rate of $RR_{mod} \leq 0.15$ based on the constraints in [85] is used to avoid a strong difference in the flux at the end and beginning of the module.

- **Constraints due to permeate quality**: The needed permeate quality determines the lower pressure limit. The lower the flux, the higher is the concentration at the permeate side. This permeate limit can vary for elements installed in series. A system permeate concentration below $\xi_P < 500$ ppm is recommended.

In order to ensure a long lifetime, these limits must be maintained and are set as boundary conditions in the applied simulation. For elements connected in series, cf. Figure 6.1a, the operation window for each element (Element 1,2 and 3) shifts to higher pressures due to the increasing inlet concentration and the constraint of permeate quality. The inlet concentration for each element depends on RR_{mod} of the element upstream. Thus, the operation window for the elements connected in series shrinks. Therefore, the feed inlet conditions of the first element cannot be chosen arbitrarily for each RO system.

Figure 6.1b shows the needed stages for a maximum module recovery rate at a system recovery rate of $RR_{sys} = 0.3$ for seawater desalination applications using ERD and $RR_{sys} = 0.5$ for brackish water applications, cf. Section 1.1.1.

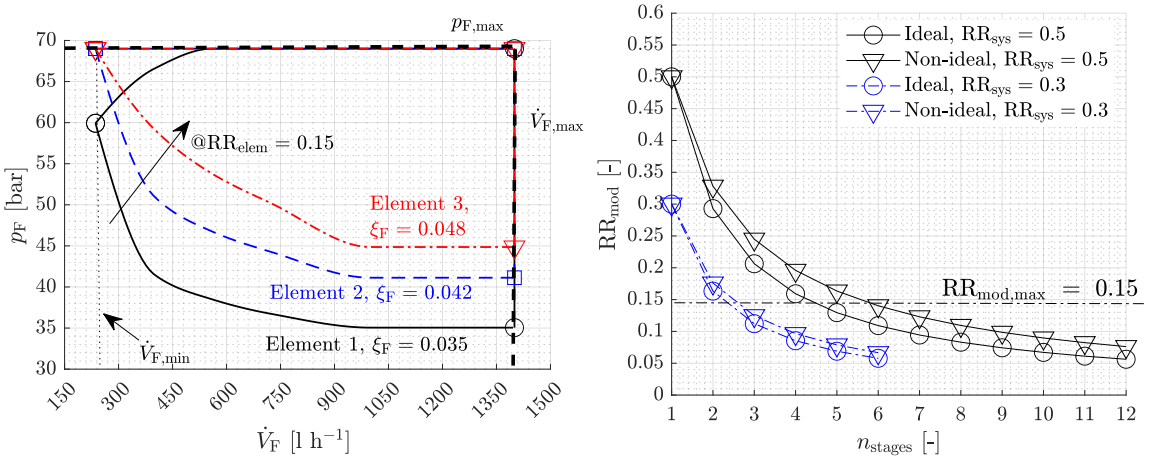

(a) Operation window of a single spiral-wound module at different inlet concentrations.

(b) Needed module recovery rate for ideal and non-ideal systems.

Figure 6.1: Operation window of RO systems and minimum stages needed.

The plot shows the ideal case with booster pumps between each stage and the non-ideal case without them. Additionally, to operate at the lowest energy demand as well as investment cost, each element should be operated at the maximum element recovery rate. For the ideal system, $\mathrm{RR_{mod}}$ equals the maximum element recovery of $\mathrm{RR_{mod}} = 0.15$ in each stage. To calculate the needed elements or stages for an RO system, the maximum system recovery rate $\mathrm{RR_{sys,max}}$ for an ideal system with $n-1$ booster pumps between the n stages can be calculated as follows

$$\mathrm{RR_{sys,max}} = \sum_{a=1}^{n} \mathrm{RR}_a \prod_{b=2}^{a} (1 - \mathrm{RR}_b). \tag{6.1}$$

In a system without booster pumps between the stages, $\mathrm{RR_{mod}}$ decreases with each stage due to increasing osmotic pressure. For system design purposes, $\mathrm{RR_{mod}}$ can be assumed to decrease reciprocally with the increase in concentration for each stage. This holds true, as the osmotic pressure is approximately linearly proportional to the concentration in conventional RO systems [49]. The recovery rate for each stage or element can then be calculated with the

recovery rate of the first stage, which is the maximum recovery rate

$$\mathrm{RR}_b \simeq \mathrm{RR}_1 \prod_{a=2}^{b} (1 - \mathrm{RR}_a). \tag{6.2}$$

It can be seen in Figure 6.1b that the needed recovery rate decreases non-linearly with the stages. The needed maximum recovery rate for BWRO systems only changes slightly for more than 6 elements, for a SWRO system already above 3. If the maximum module recovery rate has to be below $\mathrm{RR}_{\mathrm{mod}} = 15$ % at least 6 elements for the non-ideal configuration (BWRO) are needed. For SWRO systems at least 3 elements are needed to operate within the operational constraints.

6.2 Influence of Pulsating Flows on the RO Performance within Spiral-Wound Modules

As outlined in Section 2.6, a conclusion regarding the performance improvement of pulsating flows in RO systems can only be drawn after analyzing three factors: the increased power consumption, the damping of pulsating flows in spiral-wound modules and the Sherwood number as a function of amplitude ratio AR, Womersley number Wo, average Reynolds number $\overline{\mathrm{Re}}$ and permeate flux $\overline{j}_{\mathrm{P}}$. The determination of these parameters is the aim of this section. The needed input variables and the source of determination are listed in Table 6.1.

Table 6.1: Input parameters (time-averaged) for the quasi-2D simulation model.

Input parameter	Variable	Unit	Source
Damping rate	α	[m $^{-1}$]	FO test rig, cf. Section 6.2.1
Module pressure loss	$\nabla p_{\mathrm{mod,puls-ststst}}$	[-]	FO test rig, cf. Section 6.2.2
Additional pressure	$p_{\mathrm{max,PGD}}$	[Pa]	FO test rig, cf. Section 6.3
Ratio of Sherwood numbers	$\mathrm{EMT}_{\mathrm{Sh}}$	[-]	CFD Simulations, cf. Section 6.2.3

According to Section 5.3.2 and 5.3.3, varying the dynamic flow parameters along the module does not significantly change the dominant dynamic flow structures. This allows a non-coupled modeling approach along the module. The salt and water mass transport within the membrane can be treated as quasi-steady-state, cf. Section 2.6.1.

6.2.1 Propagation of Pulsatile Flows in Spiral-Wound-Modules

Pulsating flows are dampened in spiral-wound modules by loss of kinetic energy due to friction losses or due to interactions with visco-elastic materials [118, 119]. Due to the elasticity of the wall and the periodic pressure changes, an additional transient radial velocity component occurs. Therefore, a wave motion takes place between the fluid and wall, whereas the radial movement can be considered as small. The higher the excitation frequency, the greater is the influence of the visco-elastic material compared to the friction losses. For PA, the material of the membrane, the damping due to the material is dominant for $f_{ex} > 6$ Hz [86]. In a spiral-wound module, the problem is much more complex due to the geometric configuration and material heterogeneity.

To measure the damping characteristics of the pulsation along a module, a FilmTec seawater membrane module (DOW SW30-2521) with a diameter of $d_{mod} = 0.051$ m and a length of $l_{mod} = 0.48$ m was integrated into the FO test rig described in Section 3.2 by replacing the FO test cell (FOTC) with the module. The pressure difference along the module and the absolute pressure at the outlet of the module were measured. Since the test rig operated at ambient pressure, no permeate flux across the membrane was established. This evaluation allowed to estimate the relative damping of the amplitude ratio through the module, while the effect of the recovery rate on damping is excluded. Amplitude ratios in the range of AR = 0.9 ... 1.3 are considered.

The discussion of the damping rate and its calculation is based on the studies of Meissner [118, 119], who analyzed pulsating flows in visco-elastic pipes. This approach is transferred to the spiral-wound module using the hydraulic diameter and the fit of the needed creep function with the experimental data. The aim was to find a semi-empirical approach for the characterization of the

damping. The solution approach for the pressure is

$$p(x,t) = \varpi_p e^{-x(\alpha+i\omega/u_{\text{wave}})} e^{i\omega t} \tag{6.3}$$

and velocity

$$u(x,t) = \varpi_u e^{-x(\alpha+i\omega/u_{\text{wave}})} e^{i\omega t} e^{i\varphi}. \tag{6.4}$$

ϖ_p and ϖ_u are the amplitudes for the pressure and velocity, respectively, at the inlet of the module and φ describes the temporal phase shift angle between pressure and velocity. The local phase shift in relation to the feed inlet is described by the term $e^{-x(i\omega/u_{\text{wave}})}$. α is the damping rate for pressure and velocity pulsations, which defines the damping of the pulsation amplitude while passing the length x. It is calculated for the laminar case with [119]

$$\alpha = \frac{1}{2}\rho\nu u_{\text{wave}} \left(\frac{\text{Wo}}{d_{\text{h}}}\right)^2 \left[\frac{32}{\text{Wo}^2}\left(\frac{1}{El_{\text{f}}} + J'\frac{d_{\text{h}}}{\delta_{\text{mem}}}\right) + J''\frac{d_{\text{h}}}{\delta_{\text{mem}}}\right]. \tag{6.5}$$

δ_{mem} is the wall thickness of the membrane of $\delta_{\text{mem}} = 250\mu\text{m}$. El_{f} is the fluid elasticity. For water, El_{f} is $El_{\text{f}} = 2 \cdot 10^9$ N m^{-2}. u_{wave} is the wave propagation speed, which is calculated for the laminar case with [119]

$$u_{\text{wave}} = \sqrt{\frac{2}{\rho\sqrt{\left[\left(\frac{1}{El_{\text{f}}} + J'\frac{d_{\text{h}}}{\delta_{\text{mem}}}\right)^2\right]\left[1+\left(\frac{32}{\text{Wo}^2}\right)^2\right]} + \frac{1}{El_{\text{f}}} + J'\frac{d_{\text{h}}}{\delta_{\text{mem}}} - \frac{32}{\text{Wo}^2}J''\frac{d_{\text{h}}}{\delta_{\text{mem}}}}}. \tag{6.6}$$

J' and J'' are the real and imaginary part of the complex creep function, which are material dependent constants. Finally, the idea is to fit these variables to the data gained with experiments to get an approximation for the spiral-wound module. The pressure measurements from the experiments were used as input. According to Meissner [118, 119], the damping rate is the same for pressure and velocity. Another important fact is that the damping rate is independent of the amplitude and on the volume flow rate. The same holds true for the creep function [119]. Therefore, the only important variable is Wo, which has to be varied in the experiments. To fit now J' and J'', a MATLAB [72] optimization routine using `fmincon` was implemented with the following minimization problem using a least-square approach

$$\min_{\alpha}\left(\varpi_{\text{p,exp}} e^{-l_{\text{mod}}\alpha} - \varpi_{\text{p,exp}}|_{x=l_{\text{mod}}}\right)^2. \tag{6.7}$$

Using the experimental data gained with the described experiments leads to the solution

$$J' = 1.6 \cdot 10^{-7}\ \mathrm{m^2 N^{-1}} \quad \text{and} \quad J'' = 1.2 \cdot 10^{-7}\ \mathrm{m^2 N^{-1}}. \tag{6.8}$$

Now, the local amplitude ratio AR(x) along the module can be calculated analogously to Equation (6.4) with

$$\mathrm{AR}(x) = \frac{\varpi_u e^{-x\alpha} - \overline{u}(x)}{\overline{u}(x)}, \tag{6.9}$$

neglecting the local phase shift, which is valid since only averaged values are considered in the quasi-2D simulation model. To verify the procedure, the experimental and calculated values of α are compared, cf. Figure 6.2. It can be seen that α increases for increasing Wo. Comparing the calculated and measured value, it can be observed that the calculated values represent the median of the measured values, which shows scattering.

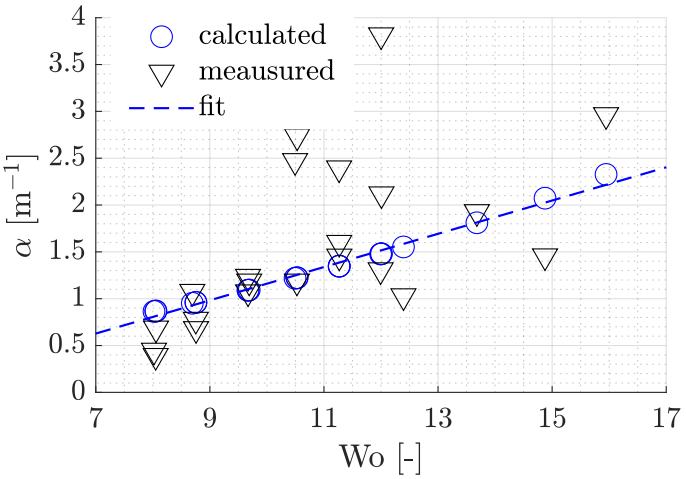

Figure 6.2: Measured and calculated α plotted over Wo.

Although the details of the damping phenomena could not be identified with the performed experiments and calculation procedure, the results allow to estimate the relative propagation of pulsations in spiral-wound modules for different Wo. This is important for the evaluation of the mass transfer enhancement in the RO system. As the presented calculation procedure including the

fitted values shows a good averaged accordance to the measurements, Equation (6.9) is used for calculating the local amplitude ratio in the quasi-2D simulation model.

6.2.2 Additional Pressure Loss in RO Systems applying Pulsating Flows

According to Section 2.6.2, not only the viscous forces but also the inertial forces are responsible for the higher pressure loss of pulsating flows compared to the steady-state operation. The higher the frequency and amplitude ratio applied, the higher the pressure loss. To predict the performance reduction along the module due to the larger pressure drop and the time-averaged energy consumption of the RO systems, two pressures are analyzed in this section: the additional relative pressure loss along the spiral-wound module and the needed maximum absolute pressure, which has to be overcome by the pump to generate pulsating flows. For this purpose, the maximum pressure upstream of the Pulsation Generation Device (PGD) excluding the pressure drop of the orifice is determined. Only the measurements with the needle valve of the bypass closed are taken into consideration. This maximum value multiplied with the average volume flow rate is regarded as the highest amount of additional energy required resulting in the worst-case scenario, as opposed to employing time-averaged pressure. Other pressure losses are not considered, because it is assumed that the pulsations are completely vanished until the end of the RO unit due to the damping. To analyze the pressure drop along the module, the maximum pressure gradient is utilized, which is incorporated into the quasi-2D model to account for the worst-case scenario.

Pressure loss along the spiral-wound module
To evaluate the increased pressure loss along the spiral-wound module, the RO module DOW SW30-2512 was installed in the test rig. Womersley numbers in the range of Wo = 8.5 ... 13.2 were applied. The amplitude ratios varied from AR = 0.8 ... 1.3, measured with the procedure described in Section 3.4. For the comparison, Figure 6.3a shows the measured steady-state pressure gradient plotted over Re and the curve fit. It can be seen that the pressure non-linearly increases with Re. Figure 6.3b shows the ratio of the maximum pressure loss

gradient for pulsating and steady-state conditions

$$\nabla p_{\mathrm{mod,puls-stst}} = \frac{\nabla p_{\mathrm{mod,max,puls}}}{\nabla p_{\mathrm{mod,stst}}} \tag{6.10}$$

plotted over Wo calculated with the hydraulic diameter of the spacer. No significant dependence was found in the measured amplitude ratios and volume flow rate. Therefore, the results are plotted without differentiating between different AR and volume flow rates. Besides, the maximum pressure gradients calculated with the analytical solution for pulsating flows in channels at the corresponding time-averaged Reynolds number for the amplitude ratios of AR = 1.0, AR = 1.3 and AR = 1.7 are shown.

It can be seen that $\nabla p_{\mathrm{mod,puls-stst}}$ increases for increasing Wo. Comparing the pressure loss increase with the analytical solution of pulsating flows in channels, cf. Section 2.6.2, it can be seen that the solution for AR = 1.7 represents the median of the measured data. It is assumed that this similarity can be explained by the fact that for Wo > 3, the pressure loss increase is mainly caused by inertial forces, cf. Figure 2.11b. Therefore, the increasing pressure loss is less dependent on the geometry of the considered section for higher frequencies. To consider the increasing pressure loss in the quasi-2D simulation model, the results gained the with analytical solution are used as input. To account for the difference for the spiral-wound module, the increase of the pressure gradient along the module is calculated with a linear increase factor of 1.72:

$$\nabla p_{\mathrm{mod,puls-stst}}(\mathrm{AR},\mathrm{Wo}) \simeq \nabla p_{\mathrm{max,puls-stst,analyt}}(1.72\cdot\mathrm{AR},\mathrm{Wo}). \tag{6.11}$$

Additional pressure to generate pulsating flows

To calculate the additional energy consumption, the maximum pressure upstream of the PGD, which is periodically released through the PGD, was utilized. This pressure is determined using the maximum pressure upstream of the PGD excluding the pressure drop of the orifice. The results can be seen in Figure 6.4. Additionally to the measurements, the different curve fits using a regression model generated with the function `fitnlm` from MATLAB [72] are plotted. It can be seen that $p_{\mathrm{max,PGD}}$ strongly increases with Wo and $\dot{V}_{\mathrm{D}}$. This is caused by the non-linear increasing inertia forces for Wo > 2, cf. Section 2.6.3. The dependency on the amplitude ratio is only minor for 0.8 < AR < 1.2. The

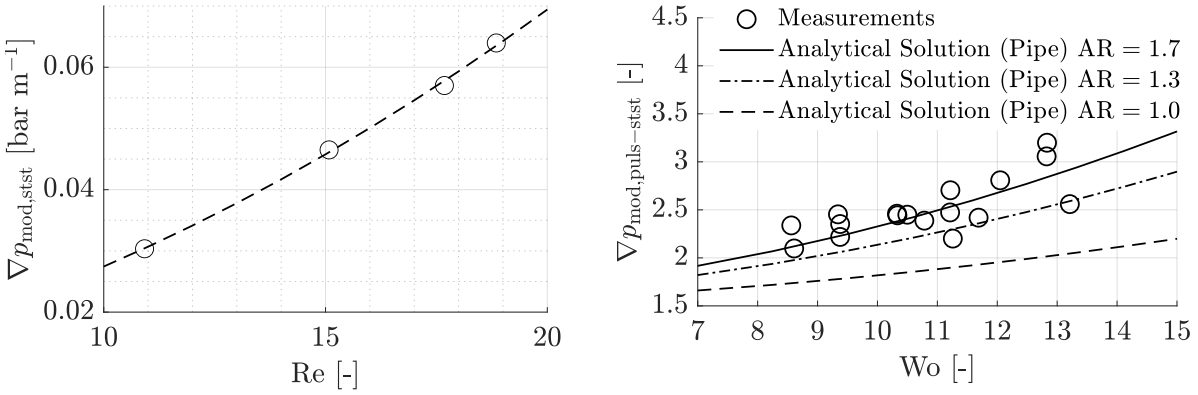

(a) Steady-state pressure gradient. **(b)** Pressure loss increase.

Figure 6.3: Pressure gradients along the module for the steady-state case and pressure loss increase along the module plotted over Wo with an averaged amplitude ratio of the experiments of $\overline{\mathrm{AR}} = 0.99$.

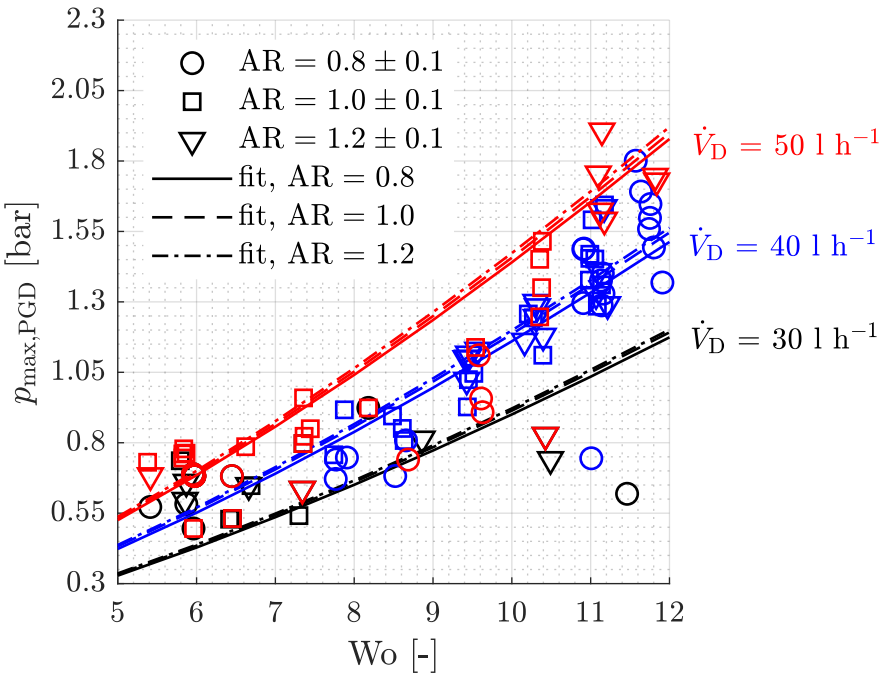

Figure 6.4: Maximum pressure upstream of the PGD for different AR and $\dot{V}_{\mathrm{D}}$ plotted over Wo.

regression model of the measured additional pressure is incorporated to predict the energy demand for the operation of RO systems applying pulsating

flows taking into account AR, $\dot{V}$ and Wo.

6.2.3 Time- and Space-Averaged Sherwood Number Analysis

In addition to the membrane parameters and pressure losses, the quasi-2D RO simulation model, cf. Section 4.2, requires the mass transfer coefficient β as input parameter. For steady-state operation, it can be calculated with the Sherwood number correlation of Shock and Miquel [60], cf. Equation (2.12). To determine the change in β due to pulsating flows, the ratio of the time- and space-averaged Sherwood numbers $\langle\overline{\mathrm{Sh}}_{\mathrm{puls}}\rangle/\langle\overline{\mathrm{Sh}}_{\mathrm{stst}}\rangle$ of the CFD simulations is needed. Therefore, to transfer the results to the RO system, the correlation between the Sherwood number applying pulsating flows $\langle\overline{\mathrm{Sh}}_{\mathrm{puls}}\rangle$ and the Womersley number Wo, amplitude ratio AR, averaged Reynolds number $\overline{\mathrm{Re}}$ and permeate flux $\overline{j}_{\mathrm{P}}$ is required. Except for Wo, these parameters change due to damping effects and the permeate flux across the membrane along the module. Using the simulation model described in Section 4.1, the correlations of $\langle\overline{\mathrm{Sh}}_{\mathrm{puls}}\rangle/\langle\overline{\mathrm{Sh}}_{\mathrm{stst}}\rangle$ and the values mentioned before are determined. The results from the CFD simulation, cf. Section 4.1, are shown in Figure 6.5.

In Figure 6.5a, $\langle\overline{\mathrm{Sh}}_{\mathrm{puls}}\rangle/\langle\overline{\mathrm{Sh}}_{\mathrm{stst}}\rangle$ is plotted over Wo for both spacer configurations applied for different AR. In general, the values almost linearly increase for increasing Wo. Considering the zig-zag spacer, the increase of $\langle\overline{\mathrm{Sh}}_{\mathrm{puls}}\rangle/\langle\overline{\mathrm{Sh}}_{\mathrm{stst}}\rangle$ stagnates at Wo ≥ 12.5 for AR ≥ 1.0 . Looking at the submerged spacer configuration, the increase also stagnates for AR = 1.2 at Wo ≥ 12.5. At Wo ≥ 13.5, the difference for AR ≥ 1.0 is only marginal.

Figure 6.5b shows $\langle\overline{\mathrm{Sh}}_{\mathrm{puls}}\rangle/\langle\overline{\mathrm{Sh}}_{\mathrm{stst}}\rangle$ plotted over AR at different Wo for both spacer configurations. As written before, the values increase with higher amplitude ratios. At AR = 0.2, the Sherwood number for the zig-zag spacer configuration hardly differ from each other for the excitation frequencies applied. For AR ≥ 1.0, the values reach a limiting value. For the submerged spacer, the difference of the values is only marginal at Wo ≥ 13.5.

Considering the dependency of $\langle\overline{\mathrm{Sh}}_{\mathrm{puls}}\rangle/\langle\overline{\mathrm{Sh}}_{\mathrm{stst}}\rangle$ on the averaged Reynolds number $\overline{\mathrm{Re}}$, cf. Figure 6.5c, a similar tendency can be identified.

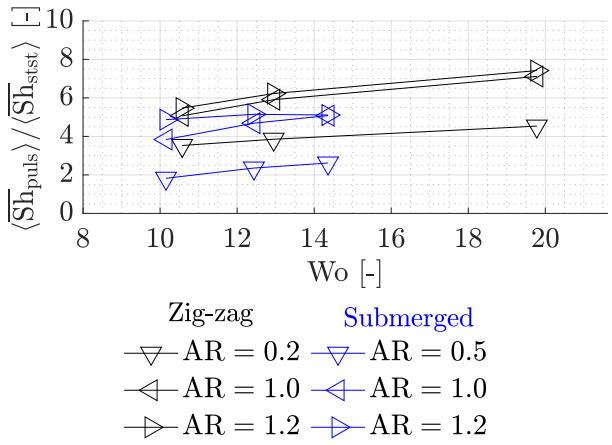

(a) Dependency of $\langle\overline{Sh}_{puls}\rangle/\langle\overline{Sh}_{stst}\rangle$ on Wo at $\overline{Re} = 136.8$.

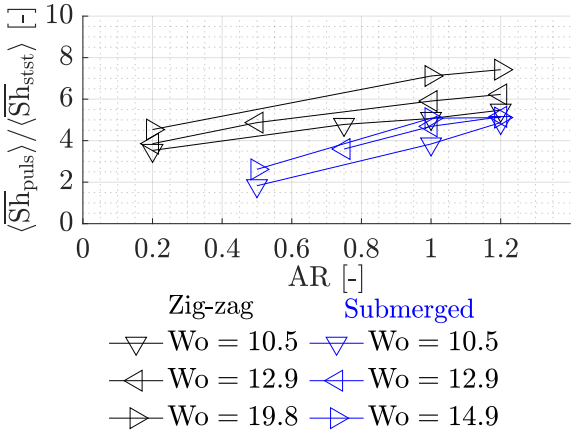

(b) Dependency of $\langle\overline{Sh}_{puls}\rangle/\langle\overline{Sh}_{stst}\rangle$ on AR at $\overline{Re} = 136.8$.

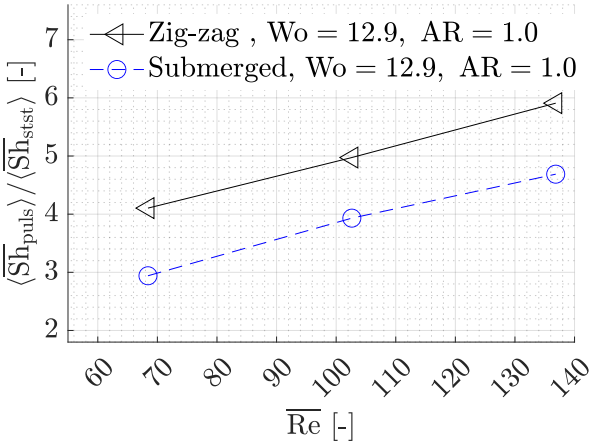

(c) Dependency of $\langle\overline{Sh}_{puls}\rangle/\langle\overline{Sh}_{stst}\rangle$ on $\overline{Re}$.

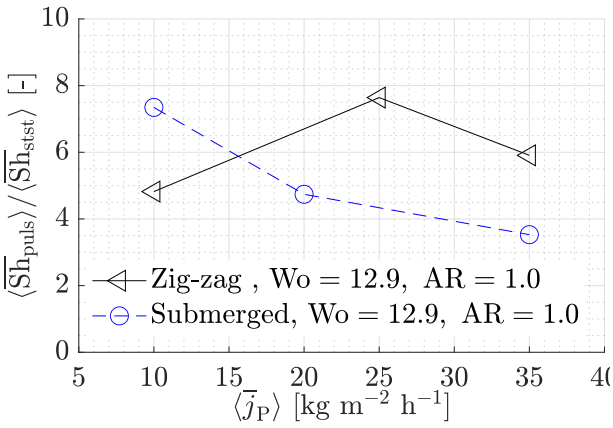

(d) Dependency of $\langle\overline{Sh}_{puls}\rangle/\langle\overline{Sh}_{stst}\rangle$ on $\langle\overline{j}_P\rangle$ at AR = 1.0.

Figure 6.5: Dependencies of $\langle\overline{Sh}_{puls}\rangle/\langle\overline{Sh}_{stst}\rangle$ on Wo, AR, $\overline{Re}$ and $\langle\overline{j}_P\rangle$.

$\langle\overline{Sh}_{puls}\rangle/\langle\overline{Sh}_{stst}\rangle$ linearly increases for higher averaged Reynolds numbers $\overline{Re}$ for both spacer configurations. Figure 6.5d shows the correlation between $\langle\overline{Sh}_{puls}\rangle/\langle\overline{Sh}_{stst}\rangle$ and $\langle\overline{j}_P\rangle$. Considering the submerged spacer configuration, the ratio decreases for increasing $\langle\overline{j}_P\rangle$. The increase of the steady-state Sherwood number $\overline{Sh}_{stst}$ due to the flux is more pronounced. For the zig-zag spacer, the ratio shows a maximum at $\langle\overline{j}_P\rangle = 25$ kg m^{-2} h^{-1}. This is based on the fact that $\langle\overline{Sh}\rangle$ for pulsating flows remains almost constant for $\langle\overline{j}_P\rangle \geq 25$ kg m^{-2} h^{-1},

whereas for the steady-state case, $\langle\overline{\mathrm{Sh}}_{\mathrm{ststst}}\rangle$ increases further.

Taking a comprehensive look at the values, it can be concluded that the enhancement increases with higher Wo, AR and $\overline{\mathrm{Re}}$ due to a stronger perturbation. However, the enhancement approaches a limiting value and only marginally changes for AR > 1. Considering decreasing AR, $\overline{\mathrm{Re}}$ and $\overline{j}_{\mathrm{P}}$, it can be expected that the mass transfer enhancement decreases along the module.

6.3 Energetic Evaluation of Pulsating Flows in Small-Scale RO Systems

The findings of the present work are now integrated into the quasi-2D simulation model described in Section 4.2. Two different simulation scenarios are considered, the BWRO case with 6 modules and the SWRO case with 3 modules connected in series, according to the design requirements, cf. Figure 6.1. The pulsations are generated directly upstream of the RO unit. Both systems work at the energetically optimal system recovery rate. The BWRO system operates at $\mathrm{RR}_{\mathrm{sys}} = 0.5$ and the SWRO system at $\mathrm{RR}_{\mathrm{sys}} = 0.3$, cf. Section 1.1.1. The inlet flow rate is $\dot{V}_{\mathrm{F}} = 620\,\mathrm{l\,h^{-1}}$. The feed pressure is set according to the operation window, cf. Figure 6.1a, to reach a permeate concentration of $\xi_{\mathrm{P}} < 500$ ppm.

For the pulsating cases, the enhancement represented by the increase of the Sherwood number is considered as a function of different amplitude ratios AR, frequencies Wo, Reynolds numbers $\overline{\mathrm{Re}}$, permeate fluxes $\overline{j}_{\mathrm{P}}$, cf. Section 6.2.3. The calculation of the enhancement is integrated into the iterative subroutine of the quasi-2D simulation tool, cf. Section 4.2. The obtained value is used as a pre-factor

$$\overline{\mathrm{Sh}}_{\mathrm{puls}} = \mathrm{EMT}_{\mathrm{Sh}}\,\mathrm{Sh}_{\mathrm{ststst}}. \tag{6.12}$$

$\mathrm{Sh}_{\mathrm{ststst}}$ is calculated using of the correlation from Equation (2.17). The enhancement factor $\mathrm{EMT}_{\mathrm{Sh}}$ is calculated using the CFD simulations and the arithmetic mean of the averaged Sherwood numbers of zig-zag and the submerged con-

figurations with

$$\mathrm{EMT_{Sh}} = \frac{1}{2}\left(\frac{\langle\overline{\mathrm{Sh}}_{\mathrm{zig-zag,puls}}(\mathrm{AR},\mathrm{Wo},\overline{\mathrm{Re}},\overline{j}_{\mathrm{P}})\rangle}{\langle\mathrm{Sh}_{\mathrm{zig-zag,stst}}(\overline{\mathrm{Re}},j_{\mathrm{P}})\rangle} + \frac{\langle\overline{\mathrm{Sh}}_{\mathrm{submerged,puls}}(\mathrm{AR},\mathrm{Wo},\overline{\mathrm{Re}},\overline{j}_{\mathrm{P}})\rangle}{\langle\mathrm{Sh}_{\mathrm{submerged,stst}}(\overline{\mathrm{Re}},j_{\mathrm{P}})\rangle}\right). \tag{6.13}$$

The ratios of the Sherwood numbers are calculated using the results from the CFD simulations, cf. Figure 6.5, based on a regression model generated using the function `fitnlm` from MATLAB [72]. The arithmetic average is used to account for both spacer configurations equally. Besides this correlation, as written before, the correlation of the damping rate α and the increased pressure gradient $\Delta p_{\mathrm{mod,puls-stst}}$ are integrated into the quasi-2D simulation model, cf. Figure 4.7.

To evaluate the benefit of pulsating flows, the relative specific energy requirement and the permeate quality are compared. $\Delta\mathrm{SEC}_{\mathrm{rel,puls-stst}}$ is the ratio of the needed specific energy demand for the steady-state and pulsating case and is defined as

$$\Delta\mathrm{SEC}_{\mathrm{rel,puls-stst}} = \frac{\overline{\mathrm{SEC}}_{\mathrm{puls}} - \overline{\mathrm{SEC}}_{\mathrm{stst}}}{\overline{\mathrm{SEC}}_{\mathrm{stst}}}. \tag{6.14}$$

To account for the needed additional energy demand to generate pulsating feed flow rates, $\overline{\mathrm{SEC}}_{\mathrm{puls}}$ is calculated using Equation (1.1) and additional pressure loss across the PGD adjusted for the applied amplitude ratio, excitation frequency and volume flow rate:

$$\overline{\mathrm{SEC}}_{\mathrm{puls}} = \overline{\mathrm{SEC}} + \frac{p_{\mathrm{max,PGD}}(\mathrm{AR},\mathrm{Wo},\dot{V}_{\mathrm{F}})\,\dot{V}_{\mathrm{F}}}{\dot{V}_{\mathrm{P}}}. \tag{6.15}$$

The relative permeate salt mass fraction $\Delta\xi_{\mathrm{P,rel,puls-stst}}$,

$$\Delta\xi_{\mathrm{P,rel,puls-stst}} = \frac{\overline{\xi}_{\mathrm{P,puls}} - \overline{\xi}_{\mathrm{P,stst}}}{\overline{\xi}_{\mathrm{P,stst}}}, \tag{6.16}$$

is used to compare the permeate quality for the steady-state and pulsating case. Figures 6.6 and 6.7 show the impact of pulsating flows for the BWRO and SWRO scenario.

BWRO system

Figure 6.6 shows $\Delta SEC_{rel,puls-stst}$ and $\Delta\xi_{P,rel,puls-stst}$ for the BWRO system. It can be seen that the energy demand strongly increases for increasing Wo. The demand increases for increasing AR. In all examined scenarios, the energy demand of RO systems is larger for pulsatile feed flows than for steady-state operation. However, the permeate salt concentration significantly decreases, cf. Figure 6.6b. This results from the average reduced salt concentration at the membrane due to the enhanced mass transfer at the membrane.

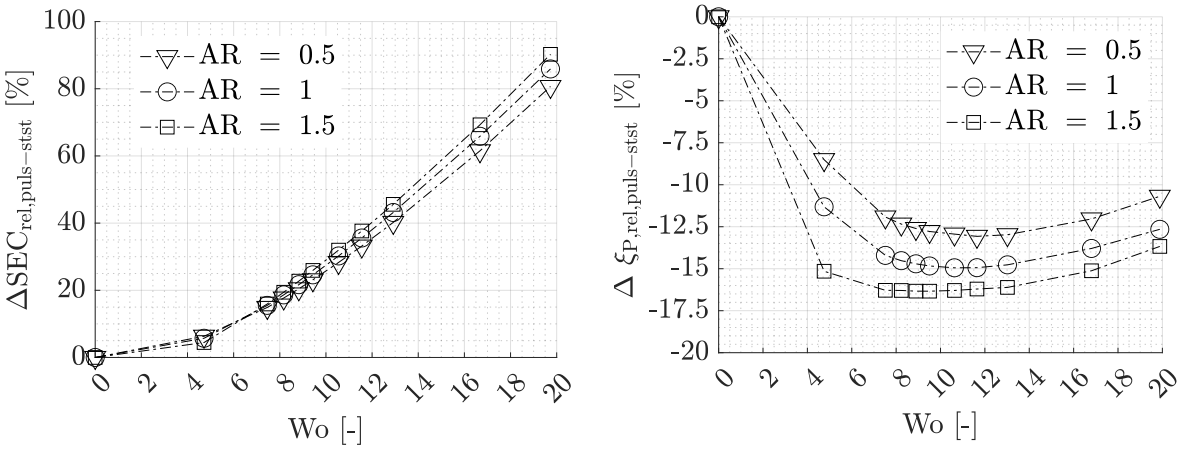

(a) Energy requirement. **(b)** Permeate quality.

Figure 6.6: BW scenario at $RR_{sys} = 0.5$; comparison of the energy requirement and permeate quality of the steady-state and pulsating case for different amplitude ratios and Womersley numbers.

SWRO system

Figure 6.7 shows $\Delta SEC_{rel,puls-stst}$ and $\Delta\xi_{rel,puls-stst}$ for the SWRO system. In Figure 6.7a, it can be seen that the energy demand for the operation with pulsating flows is lower than for the steady-state case Wo < 12. The minima for all cases are between $\Delta SEC_{rel,puls-stst} = -5$ % to $\Delta SEC_{rel,puls-stst} = -9$ % at Wo = 7 depending on the amplitude ratio. For Wo > 12, the energy demand for pulsating flows is larger than for the steady-state operation. Figure 6.7b shows the comparison of the permeate concentration for the steady-state and pulsating case. It can be seen that the permeate concentration is lower for all pulsating scenarios considered. The minima are between $\Delta\xi_{rel,puls-stst} = -17$ % to

$\Delta\xi_{\mathrm{rel,puls-stst}} = -23$ % for Wo between 9.2 and 13, depending on the amplitude ratio.

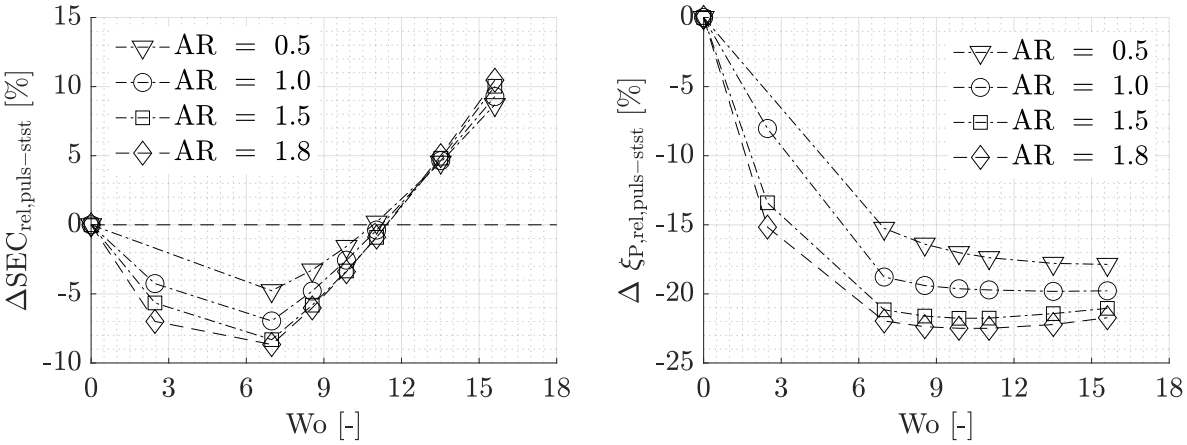

(a) Energy requirement. **(b)** Permeate quality.

Figure 6.7: SW scenario at $\mathrm{RR_{sys}} = 0.3$; comparison of the energy requirement and permeate quality of the steady-state and pulsating case for different amplitude ratios and Womersley numbers.

Conclusion

For the BWRO system, the strong increase of the energy demand can be explained by the strong pressure loss increase and the low absolute pressure, which is needed for the BWRO system. The enhanced mass transfer cannot compensate the additional energy demand. Moreover, due to the damping, the pulsating flow is already completely vanished in the third module, so more than 50 % of the modules are operated completely at steady-state conditions. For the SWRO system, the energy demand and the permeate salt mass fraction is reduced for Womersley numbers below 12. Increasing the amplitude ratio above AR > 1.5, the energy demand only decreases marginally. For Wo > 12, the increased mass transfer cannot compensate the larger additional energy demand. Considering the permeate quality, the permeate salt concentration is strongly reduced for both systems. The occurring minima can be explained by the contrary trends of damping rate and increasing mass transfer enhancement for increasing Wo. For larger Wo, the increasing mass transfer enhancement does not compensate the higher damping rates anymore.

6.4 Summary of Pulsating Flows in Small-Scale RO Systems

This chapter can be summarized as follows:

- For the BWRO system, a minimum of six modules was required, and for the SWRO system, a minimum of three modules was necessary to meet the operational constraints of the considered RO modules.
- A semi-empirical approach was developed to calculate the damping of pulsations along the module. The damping is considered as independent of AR. The higher Wo, the higher is the damping along the module.
- The increased pressure drop over the module and the additional maximum pressure required to generate pulsating feed flows were evaluated. For increasing Wo and AR, both variables increase non-linearly.
- The correlation between the enhancement over a wide range of AR and Wo was developed. Comparing the zig-zag with the submerged spacer configuration, it can be observed that the averaged mass transfer enhancement is larger for the zig-zag spacer configuration in general. For the zig-zag spacer configuration, the values of $\langle\overline{\mathrm{Sh}}_{\mathrm{puls}}\rangle/\langle\overline{\mathrm{Sh}}_{\mathrm{stst}}\rangle$ between 3.8 and 7.8, for the submerged spacer configuration values between 1.9 and 5.0 were achieved.
- The quasi-2D model from Section 4.2 was used to predict the time-average performance of RO systems operated with pulsating and steady-state feed flows.
- For the BWRO system, the SEC strongly increases for increasing Wo compared to the steady-state operation. For the SWRO system, the SEC is lower than that of the steady-state operated system, for Womersley number below 12. A minimum of -9 % for Wo = 7 and AR = 1.5 was predicted. Increasing Wo leads to a strong increase of the energy demand. Increasing AR further, the improvement is only marginal.
- For both systems, the permeate salt concentration could be significantly decreased. The minima, which occur due to contrary trends of increasing mass transfer and increasing damping rate for increasing Womersley

numbers, are between Wo = 9 and Wo = 12. A reduction of the salt concentration of -16 % could be predicted for the BWRO system and -22 % for the SWRO system.

In summary, pulsating flows have the potential to substantially enhance the performance by improving the permeate quality and reducing the SEC. However, the extent of the performance enhancement is highly contingent upon the specific characteristics of the RO system. For BWRO systems, pulsating flows are only recommended, if the permeate quality is critical. The beneficial increase of the mass transfer enhancement cannot compensate the strong pressure loss increase and therefore the strong decrease of the flux across the membrane along the module. If the energy demand should be reduced, it is recommended to use an energy recovery device (ERD) instead of operation with pulsating flows. For SWRO systems, it is recommended to use pulsating flows with Womersley numbers at Wo = 7 and AR $\leq$ 1.5 to significantly decrease the energy demand at a significant enhancement of the permeate quality. For AR > 1.5, no significant performance enhancement could be observed. Since also the mechanical stress increases for increasing AR, AR should not be arbitrarily increased. As a result of the decreased permeate salt mass fraction, there is also the potential to expand the operational window to encompass larger module recovery rates and reduced feed pressures, cf. Section 6.1. Furthermore, the increased wall shear stress, particularly at the module's inlet, can reduce the fouling potential and thereby allow larger module recovery rates. Both could lead to lower energy and investment costs.

7 Summary and Conclusion

The large energy demand of Reverse Osmosis (RO) systems remains one of the major drawbacks of this technology. Its reduction is therefore subject of current research. The large amount of energy is required to overcome the osmotic pressure by the hydraulic pressure to drive the diffusion process of the permeate across the membrane. The formation of a concentration boundary layer at the membrane leads to an increased osmotic pressure and thus to a higher specific energy consumption (SEC) per cubic meter of permeate. The objective of the present work was to use pulsating flows to actively disturb the concentration boundary layer and reduce the SEC. Based on detailed investigations of the flow phenomena and their interaction with the concentration boundary layer, the benefits of applying pulsating flows compared to steady-state operation of RO systems were evaluated. For this purpose, three main parameters needed to be determined: damping rate, pressure loss and mass transfer.

To meet the objectives, different simulation tools and experimental methods were developed. With these methods, different analyses were conducted. The following conclusions can be drawn:

For the investigation of the mass transfer in pulsating flows, RO and Forward Osmosis (FO) test rigs were used. Contrary to the RO system, the FO system works under atmospheric pressure, which simplified the measurements. Fundamental theoretical investigations showed that due to the similarity of the mass transfer in FO and RO processes, it is legitimate to directly transfer the results from FO experiments regarding the mass transfer enhancement to RO processes and vice versa at the same permeate flux, pH value and flow conditions.

Additional theoretical investigations of the mass transport through the exter-

nal (at the membrane) and internal (within the membrane) concentration polarization layers were performed to identify the dominating mass transport resistances for RO processes. This analysis revealed that the mass transport in the concentration boundary layer at the feed side is the dominant and limiting dynamic mass transport process. For the investigation of the interaction of axial pulsating flows and the concentration boundary layer, an analytical solution for the salt mass transport in empty channels was developed. Pulsations parallel to the membrane result in a decrease of the Sherwood number, while even small pulsations normal to the membrane reduce the concentration at the membrane compared to steady-state operation. This is attributed to the enhanced diffusivity along the primary pulsation direction.

A FO lab-scale test rig was used for dynamic experiments. To determine the amplitude ratio, measurements of the pressure drop over an orifice were used. The evaluation procedure was calibrated with PIV measurement data. The newly developed evaluation procedure enabled the measurement of the amplitude ratio with a mean relative error below 50 % for the dynamic conditions considered in the work at hand. Different water flux measurements with the FO test rig showed that pulsating flows have a positive influence on the mass transfer across the membrane. The enhancement is significant for Womersley numbers of $Wo > 6.8$.

A Particle Image Velocimetry (PIV) measurement setup to investigate pulsating flows in Reynolds-similar spacer-filled channels was developed. To study details of the salt mass transport in laminar, pulsating flows within a submerged and zig-zag spacer, a 2D Computations Fluid Dynamics (CFD) model was developed. The CFD model was verified with the data of the flux measurements of the FO test-rig and PIV measurements. The CFD simulations of pulsating flows within the spacer-filled channels were analyzed using the Proper Orthogonal Decomposition (POD) method. Changing time-averaged Reynolds numbers or amplitude ratios did not lead to a significant change of the dominant POD modes. An examination of the POD modes and the local Sherwood number between the filaments showed that pulsations normal to the membrane, vortex-like structures and the periodic formation and breakdown of separation zones lead to a strongly increased mass transfer. A

predominant reason for the mass transfer enhancement could not be determined. It is an interplay among the flow phenomena described before, which are induced by pulsating flows. The perturbations are intensified for larger AR and Wo.

However, increasing Womersley numbers are associated with higher damping rates. These damping rates were determined using a semi-empirical approach and module experiments with the FO bench-scale test rig. The energy requirement also increases with increasing AR and Wo. Using the FO test rig, the increased pressure drop over the module and the additional pump energy requirement were evaluated. For increasing Womersley numbers and amplitude ratios, both pressures increased non-linearly, reaching up to three times the steady-state value. An analysis of the time- and volume-averaged Sherwood number revealed that the improvement increases with increasing amplitude ratios, Womersley and Reynolds numbers. On average, the Sherwood number under pulsating flows increased by 1.9 to 5.0 times compared to steady-state for Womersley numbers between $9.5 < Wo < 14.0$ and amplitude ratios of $0.5 < AR < 1.2$. For Womersley numbers of $Wo > 13.5$ and amplitude ratios of $AR > 1.0$, the increase becomes smaller.

To transfer the findings to an entire RO system, a quasi-2D simulation tool for RO modules was developed. This model was used to predict the time-averaged performance of RO systems operated with steady-state and pulsating flow rates based on the findings of this work. A regression model of the experimental and simulation data was integrated into the quasi-2D simulation model. Utilizing these correlations, it could be demonstrated that pulsating flows can effectively reduce the energy demand and permeate concentration for small-scale seawater RO systems. For brackish water RO systems, the energy demand was increased from 8% to 90 % for Womersley numbers between $4 < Wo < 20$. For seawater RO applications, an optimum Womersley number of $Wo = 7.0$ at an amplitude ratio of $AR = 1.5$ was determined. Here, the SEC could be reduced by 9%. As the amplitude ratios increase, the energy requirement decreased, while the effect is minimal at amplitude ratios above 1.5. The permeate salinity could be reduced for both RO systems by 16 % for the brackish water and 22 % for the seawater system, respectively.

In short, it has been demonstrated that pulsating flows have the potential for the performance improvement, not only in terms of mass transfer but also in reducing the energy demand for an entire RO system. However, several unresolved questions persist, necessitating attention in future research. 3D simulations should be performed to identify the flow phenomena in real spacer geometries. This could improve new spacer designs suitable for dynamic operation. Having a look on the measurements, the determination of the amplitude ratio has to be improved. In addition, the mechanical stresses in the entire RO system need to be investigated to evaluate the practicality of pulsating flows. Moreover, the long-time performance has to be investigated, especially with a focus on bio-fouling. As also the wall-shear stress increases with pulsating flows, this could reduce bio-fouling. Combined with the mass transfer enhancement and the potential for higher recovery rates, a long-term reduction in fouling would lead to higher productivity while also reducing operational and maintenance costs. Together with the development of ultra-permeable membranes, pulsating flows can pave the way to highly efficient RO systems with lower environmental impact.

A Appendix: Analytical Solution of Hydrodynamics of Pulsating Flows in Simple Channels and Pipes

In this section, the derivation of the solution of the velocity for pulsating flows in channels, developed by Haddad et al. [23] is presented. Their study is based on the work of Uchida [76], Ray et al. [74] and Ünsal et al. [75]. The configuration is given in Figure A.1.

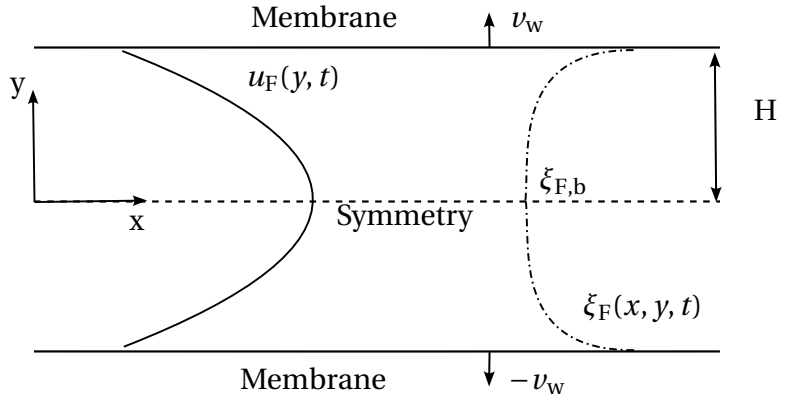

Figure A.1: Channel Configuration.

Using the assumptions declared in Section 2.6.2 and the assumption of an incompressible flow,

$$\frac{\partial u_F}{\partial x} = 0, \tag{A.1}$$

leads to the 1D flow problem

$$\frac{\partial u_F}{\partial t} = -\frac{1}{\rho_F}\frac{\partial p_F}{\partial x} + \nu_F \frac{\partial^2 u_F}{\partial y^2}. \tag{A.2}$$

Using the decomposition for periodic laminar flows,

$$u_{\mathrm{F}}(y,t) \;=\; \overline{u}_{\mathrm{F}}(y) \;+\; \tilde{u}_{\mathrm{F}}(y,t), \tag{A.3}$$

Equation (A.2) can be represented by the steady-state part

$$\nu_{\mathrm{F}}\frac{\partial^2\overline{u}_{\mathrm{F}}}{\partial y^2} \;+\; \frac{\overline{p}_{\mathrm{F}}}{\rho_{\mathrm{F}}} \;=\; 0 \tag{A.4}$$

and the periodic part

$$\frac{\partial\tilde{u}_{\mathrm{F}}}{\partial t} \;+\; \nu_{\mathrm{F}}\frac{\partial^2\tilde{u}_{\mathrm{F}}}{\partial y^2} \;+\; \frac{\tilde{p}_{\mathrm{F}}}{\rho_{\mathrm{F}}} \;=\; 0. \tag{A.5}$$

Equation (A.4) can be solved analytically with the following solution

$$\overline{u}_{\mathrm{F}} \;=\; \left(1-\frac{y^2}{H^2}\right)\frac{\partial\overline{p}_{\mathrm{F}}}{\partial x}\frac{H^2}{3\rho_{\mathrm{F}}\nu_{\mathrm{F}}}. \tag{A.6}$$

The solutions for pulsating flows with fluctuating velocities $\tilde{u}_{\mathrm{F}}$,

$$\tilde{u}_{\mathrm{F}}(y,t) \;=\; \sum_{n\,=\,1}^{\infty} u_{\mathrm{F,n}}e^{i\omega nt} \tag{A.7}$$

and specific pressure gradients

$$\tilde{P}_{\mathrm{F}}(t) \;=\; -\frac{1}{\rho_{\mathrm{F}}}\left(\frac{\mathrm{d}\tilde{p}_{\mathrm{F}}}{\mathrm{d}x}\right) \;=\; \sum_{n\,=\,1}^{\infty} P_{\mathrm{F,n}}e^{i\omega nt}, \tag{A.8}$$

which can be represented by a Fourier series, were found by Ünsal et al. [75].

Inserting Equations (A.7) and (A.8) into Equation (A.5) results in the following equation

$$\frac{\partial^2 u_{\mathrm{F,n}}}{\partial y^2} \;+\; \frac{-i\omega n}{\nu_{\mathrm{F}}}u_{\mathrm{F,n}} \;+\; \frac{P_{\mathrm{F,n}}}{\nu_{\mathrm{F}}} \;=\; 0. \tag{A.9}$$

Equation (A.9) is a Bessel differential equation and has the following solution for the channel [75]

$$u_{\mathrm{F,n}}(y,t) = c_0 \cosh\left(y\sqrt{\frac{i\omega n}{\nu_{\mathrm{F}}}}\right) + c_1 \sinh\left(y\sqrt{\frac{i\omega n}{\nu_{\mathrm{F}}}}\right) + \frac{P_{\mathrm{F,n}}}{i\omega n}. \tag{A.10}$$

Using the no-slip boundary condition at $y = H$ at the wall of the channel

$$u_{\mathrm{F}} = 0 \tag{A.11}$$

and the symmetry boundary condition at $y = 0$

$$\frac{\partial u_{\mathrm{F}}}{\partial y} = 0, \tag{A.12}$$

the constants c_0 and c_1 can be determined as

$$c_1 = 0 \tag{A.13}$$

and

$$c_0 = -\frac{p_{\mathrm{F,n}}}{i\omega n}\frac{1}{\cosh\left(H\sqrt{\frac{i\omega n}{\nu_{\mathrm{F}}}}\right)}. \tag{A.14}$$

This results in following solution [23]:

$$\begin{aligned} u_{\mathrm{F}}(y,t) = \frac{3}{2}\overline{u}_{\mathrm{F}}\Bigg(&\left(1-\frac{y^2}{H^2}\right) \\ &- \Re\left\{\sum_{n=1}^{\infty} i\frac{P_{\mathrm{F,n}}\nu_{\mathrm{F}}}{\overline{P}_{\mathrm{F}}\omega n H^2}\left(1-\frac{\cosh\left(y\sqrt{\frac{i\omega n}{\nu_{\mathrm{F}}}}\right)}{\cosh\left(\mathrm{H}\sqrt{\frac{i\omega n}{\nu_{\mathrm{F}}}}\right)}\right)e^{i\omega n t}\right\}\Bigg). \end{aligned} \tag{A.15}$$

Without derivation, the solution for pipe flows with coordinates x and r is given by [23]

$$\begin{aligned} u_{\mathrm{F}}(r,t) \;=\; 2\overline{u}_{\mathrm{F}} \Bigg(& \left(1-\frac{r^2}{R^2}\right) \\ & - \Re \left\{ \sum_{n\,=\,1}^{\infty} i \frac{2P_{\mathrm{F,n}}\nu_{\mathrm{F}}}{\overline{P}_{\mathrm{F}}\omega R^2 n} \left(1 - \frac{\mathrm{J}_0\left(r\sqrt{\frac{i\omega n}{\nu_{\mathrm{F}}}}\right)}{\mathrm{J}_0\left(R\sqrt{\frac{i\omega n}{\nu_{\mathrm{F}}}}\right)}\right) e^{i\omega n t} \right\} \Bigg). \end{aligned} \tag{A.16}$$

B Appendix: Derivation of the Analytical Solution of the Mass Transport in Empty Channels

This section includes the derivation of the analytical solution presented in Section 2.6.2. The derivation of the solution is based on [73, 77, 78].

The solution needs to be developed for $\xi_F = \overline{\xi}_F + \tilde{\xi}_F$. Using this decomposition as well as the assumptions described in Section 2.6.2, results in two equations for the steady state part

$$\overline{u}_F \frac{\partial \overline{\xi}_F}{\partial x} = \Gamma \frac{\partial^2 \overline{\xi}_F}{\partial y^2}, \tag{B.1}$$

and the dynamic part

$$\frac{\partial \tilde{\xi}_F}{\partial t} + \tilde{u}_F \frac{\partial \overline{\xi}_F}{\partial x} + \tilde{u}_F \frac{\partial \tilde{\xi}_F}{\partial x} = \Gamma \frac{\partial^2 \tilde{\xi}_F}{\partial y^2}. \tag{B.2}$$

A solution of the form [73]

$$\xi_F(x,y,t) = \xi_F(x,y) + \sum_{n=1}^{\infty} \Re \left\{ \frac{\partial \overline{\xi}_F}{\partial x} \Psi_{F,n}(y) e^{2i\omega n t} \right\} \tag{B.3}$$

can be found for Fourier series type fluctuations using the assumption that the time-dependent gradient is small than the general gradient $\left|\frac{\partial \tilde{\xi}_F}{\partial x}\right| << \left|\frac{\partial \overline{\xi}_F}{\partial x}\right|$ [22]. Based on the studies of Zhang and Kurzweg [120], Kim et al. [121] and Blythman et al. [78], this fluctuating gradient can be assumed as negligible.

The n-th part of the Fourier series of the time dependent part of Equation (B.2) can be formulated as

$$\Gamma \frac{\partial^2 \Psi_{\mathrm{F,n}}(y)}{\partial x^2} + u_{\mathrm{F,n}}(y) - i\omega n \Psi_{\mathrm{F,n}}(y) \;=\; 0. \tag{B.4}$$

This equation is a Bessel differential equation and has a solution of the form [73]

$$\begin{aligned} \Psi_{\mathrm{F,n}}(y) \;= c_2 \sinh\left(y\sqrt{\frac{i\omega n}{\Gamma}}\right) + \; c_3 \cosh\left(y\sqrt{\frac{i\omega n}{\Gamma}}\right) \\ + \; \frac{p_{\mathrm{F,n}}}{i^2\omega^2 n^2}\left(\frac{\mathrm{Sc}}{\mathrm{Sc}-1}\frac{\cosh\left(y\sqrt{\frac{i\omega n}{\nu_{\mathrm{F}}}}\right)}{\cosh\left(H\sqrt{\frac{i\omega n}{\nu_{\mathrm{F}}}}\right)} - 1\right). \end{aligned} \tag{B.5}$$

Using the symmetry of the channel at $y \;=\; 0$,

$$\frac{\partial \Psi_{\mathrm{F}}}{\partial y} \;=\; 0, \tag{B.6}$$

results in

$$c_2 \;=\; 0. \tag{B.7}$$

The boundary conditions at the membrane ($y \;=\; H$) using the assumption of an ideal membrane is

$$-\xi_{\mathrm{F,AL}}(j_{\mathrm{p}}) \;+\; \rho_{\mathrm{F}} A_{\mathrm{mem}} \Gamma_{\mathrm{F}} \frac{\partial \xi_{\mathrm{F,AL}}}{\partial y} \;=\; 0. \tag{B.8}$$

The permeate flux j_{p} can be calculated using the solution-diffusion model

$$j_{\mathrm{P}} \;=\; \rho_{\mathrm{F}} A_{\mathrm{mem}}(p_{\mathrm{F}} - p_{\mathrm{P}} - \pi_{\mathrm{AL}}) + \rho_{\mathrm{F}} A_{\mathrm{mem}}(\tilde{p}_{\mathrm{F}} - \tilde{\pi}_{\mathrm{F,AL}}). \tag{B.9}$$

Using the assumption that the fluctuating pressure resulting from the pulsating flows is negligible ($\tilde{p}_\mathrm{F} << \overline{p}_\mathrm{F}$) and a linearization of the osmotic pressure

$$\pi_\mathrm{F} \cong C_\pi \xi_\mathrm{F}, \tag{B.10}$$

which is valid for the concentrations occurring in RO systems, the flux can be calculated with $\Delta p = (p_\mathrm{F} - p_\mathrm{P})$

$$j_\mathrm{P} = \overline{j}_\mathrm{P} + \tilde{j}_\mathrm{P} = \rho_\mathrm{F} A_\mathrm{mem}(\Delta p - \pi_\mathrm{AL}) - \rho_\mathrm{F} A_\mathrm{mem} C_\pi \tilde{\xi}_\mathrm{F,AL} = 0. \tag{B.11}$$

Using the decomposition of Equation (B.11), the boundary condition (B.8) results in

$$-\overline{\xi}_\mathrm{F,AL}\overline{j}_\mathrm{P} - \tilde{\xi}_\mathrm{F,AL}\overline{j}_\mathrm{P} - \overline{\xi}_\mathrm{F,AL}\tilde{j}_\mathrm{P} - \tilde{\xi}_\mathrm{F,AL}\tilde{j}_\mathrm{P} + \rho\Gamma\frac{\partial\overline{\xi}_\mathrm{F,AL}}{\partial y} + \rho_\mathrm{F}\Gamma_\mathrm{F}\frac{\partial\tilde{\xi}_\mathrm{F,AL}}{\partial y} = 0. \tag{B.12}$$

Different researchers showed that the fluctuations of temperature or concentration are small in pulsating flows in pipes or channels [22, 71, 73, 77, 78]. Therefore it can be assumed that the nonlinear term $\tilde{\xi}_\mathrm{F,AL}\tilde{j}_\mathrm{P} \propto \left(\tilde{\xi}_\mathrm{F,AL}\right)^2$ is small compared to the linear terms. Using this linearization and inserting Equation (B.11) into the boundary condition (B.8), the constant c_3 can be calculated after some algebra as

$$\begin{aligned} c_3 = & \frac{-p_\mathrm{F,n}}{i^2\omega^2 n^2(\mathrm{Sc}-1)\cosh\left(R\sqrt{\frac{i\omega n}{\Gamma_\mathrm{F}}}\right)} \\ & \frac{\left(\rho_\mathrm{F}\overline{\xi}_\mathrm{F}A_\mathrm{mem}C_\pi - \overline{j}_\mathrm{P} + \rho\sqrt{i\omega n\nu_\mathrm{F}}\tanh\left(R\sqrt{\frac{i\omega n}{\nu_\mathrm{F}}}\right)\right)}{\left(\rho\overline{\xi}_\mathrm{F}A_\mathrm{mem}C_\pi - \overline{j}_\mathrm{P} + \rho_\mathrm{F}\sqrt{i\omega n\Gamma_\mathrm{F}}\tanh\left(R\sqrt{\frac{i\omega n}{\Gamma_\mathrm{F}}}\right)\right)}. \end{aligned} \tag{B.13}$$

Inserting c_3 in Equation (B.5) leads to the solution of the time dependent mass fraction for pulsating flows in empty RO membrane channels.

C Appendix: Experimental Setups and Experiments

C.1 Technical Details of the Small-Scale Reverse Osmosis System

Figure C.1 shows the P & ID of the module test rig, adapted from [59]. The feed water was pumped from the feed tank (FT) to the HPP via the low pressure feed pump (LPP_F). It was pressurized up to around 2 bar. Before entering the HPP, the feed was filtered with two pre-filters for particles of 50 microns ($F_{F,1}$) and 5 microns ($F_{F,2}$). A buffer tank (BT) with a volume of $V_{BT} = 5$ l was installed between both pumps. A flush tank (FLT) with a volume of $V_{FLT} = 40$ l filled with permeate was installed to clean the spiral-wound module periodically. Downstream of the flush tank, the feed flowed through the spiral-wound module, where it was desalinated. The permeate was filtered with an active carbon filter (ACF). The system was cleaned after each experiment. The feed was pressurized up to a maximum of $p_F = 16$ bar, which allowed to desalinate brackish water with a salt mass fraction of $\xi_F = 4000$ ppm with a recovery rate of RR = 21 %. The retentate and permeate were returned to the FT to keep the inlet concentration constant.

Control and Measurement Devices
The RO unit was controlled via the National Instruments software tool LabView and two Arduino micro-controllers for temperature and pressure control. The original system was modified in two ways to simulate different dynamic situations during a common operation: integration of a puls-width modulation (PWM) unit for power control and a pressure relief valve (PRV) controlled by an Arduino micro-controller and electric motor. This allowed to apply dynamic changes in pressure and volume flow rate separately.

To evaluate the performance of the system and to compare it with the system simulation model, temperature, pressure, conductivity and volume flow rates of feed (index F), retentate (index R) and permeate (index P) were measured continuously up- and downstream of the module. The power consumption of the system including the high pressure pump and the feed pump were measured separately. System and module specifications are given in Tables C.1, C.2 and C.3.

Table C.1: Specifications of the TRUNZ TBL10D unit.

Specification	**Unit**	**Value**
Supplier	-	TRUNZ Water Systems AG,Steinach, Swiss
Year of production	-	2011
Membrane type	-	Toray TLM10D
Feed pump	-	Lorentz Solar Pump
High pressure pump	-	Procon 207mm Expresso Mag
Electrical heater power	kW	9

Table C.2: Membrane module specifications [81].

Specification	**Unit**	**Value**
Vendor	-	Toray
Product type	-	TML10D
Active layer material	-	PA-6
Spacer thickness	mil	34
Pressure range	bar	<40

Table C.3: Operation window for the small-scale RO test rig.

Parameter	**Range**	**Unit**
Feed volume flow rates	600 – 1000	$l\,h^{-1}$
Pressure	0 – 20	bar
Temperature	20 – 40	°C
Salinity	0 – 4	$g\,kg^{-1}$

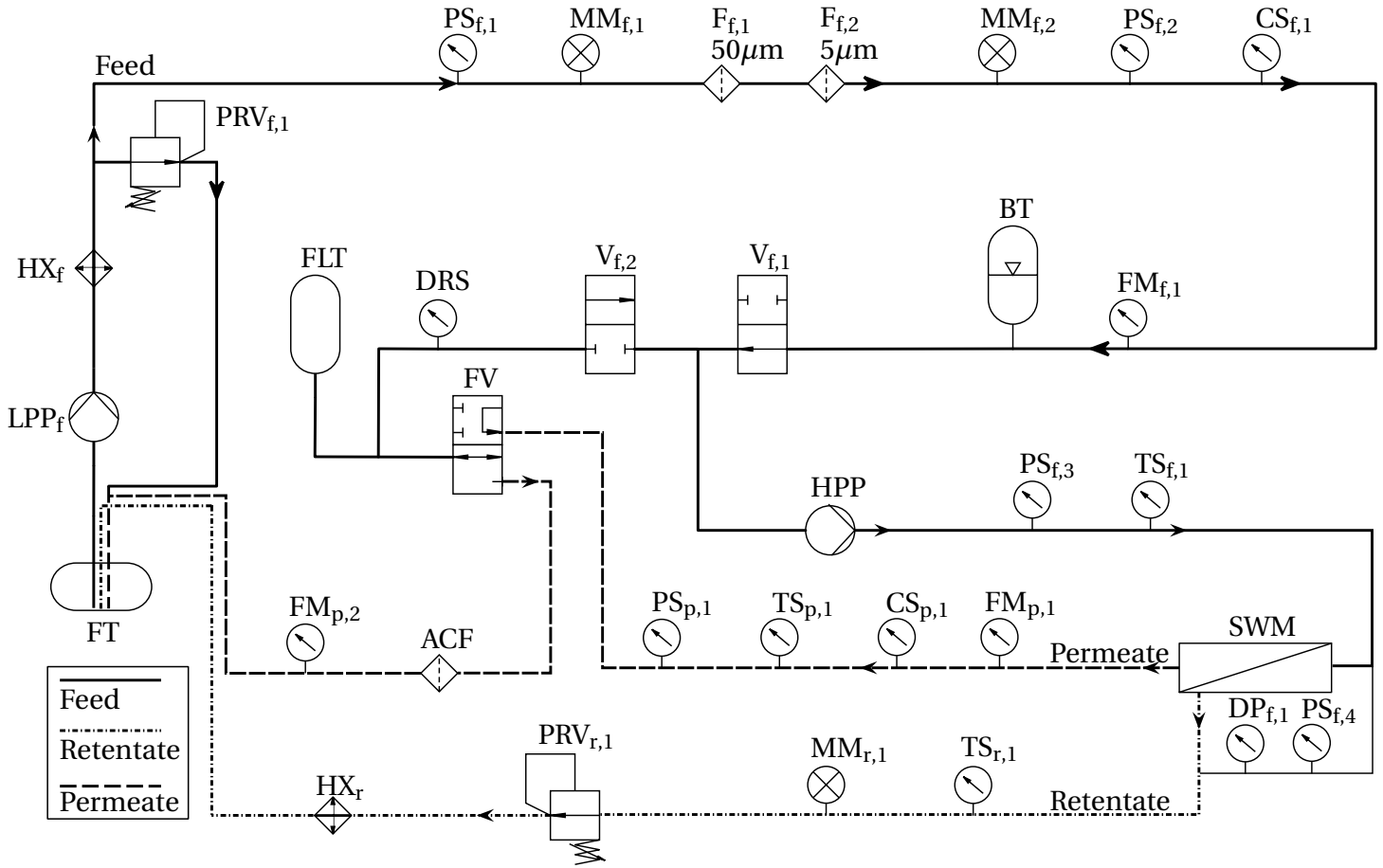

Figure C.1: P & ID of the small-scale RO module test rig adapted from [82];
ACF: Active carbon filter - **BT**: Buffer tank - **CS**: Conductivity sensor - **DRS**: Dry run sensor - **F**: Filter - **FLT**: Flush tank - **FM**: Flow meter - **FT**: Feed tank - **FV**: Flotation valve - **HPP**: High pressure pump - **HX**: Heat exchanger - **LPP**: Low pressure pump - **MM**: Manometer - **PRV**: Pressure relieve valve - **PS**: Pressure sensor - **SWM**: Spiral-wound module - **TS**: Temperature sensor - **V**: Valve.

C.2 Technical Details of the Bench-Scale Forward Osmosis System

The system consists of two hydraulic circuits, as shown in Figure C.2, adapted from [59]: the draw (high concentration) and feed (low concentration) circuit, whereas pulsations were applied only on the draw side. Each circuit was equipped with a gear pump (GP) to provide stable and constant average volume flow rates between $\dot{V}_D = 20\ \mathrm{l\ h^{-1}}$ and $\dot{V}_D = 80\ \mathrm{l\ h^{-1}}$. These volume flow rates correspond to Reynolds numbers from Re = 68.4 to Re = 273.6 inside the draw channel of the Forward Osmosis test cell (FOTC) shown in Figure 3.1. Relative pressures of up to 4 bar could be established by the pumps.

The draw solution was pumped from the draw tank (DT) through the system by the draw gear pump (GP_D). Downstream of the pump three different paths could be chosen

- the pulsation path through the pulsation dampener $PD_{D,1}$, pulsation generation device (PGD) and measurement section,
- the steady-state path or
- the bypass steady-state path with the two pulsation dampeners $PD_{D,3}$ and $PD_{D,4}$.

The steady-state path could be opened or closed by the solenoid valve $SV_{D,1}$. The bypass volume flow rate could be set with the needle valve $NV_{D,1}$. This bypass was used to adjust the volume flow rate, which was measured by the magnetic-inductive flowmeter $FM_{D,1}$. The pulsation dampeners $PD_{D,1}$, $PD_{D,3}$ and $PD_{D,4}$ were used to protect the pump from pressure fluctuations produced by the PGD. A second pulsation dampener $PD_{D,2}$ was installed to minimize the pressure pulsations in the PGD and was connected to the compressed air supply line. This allowed to keep the air volume constant inside the pulsation dampener $PD_{D,2}$. The pressure sensor $PS_{D,2}$ measured the pressure inside the PGD.

Downstream of the PGD, the draw solution flowed through the orifice. Here, the differential pressure sensor $DPS_{D,1}$ was used to determine the amplitude ratio (cf. Section 3.4). The draw solution entered the FOTC downstream of the PGD. The differential pressure sensor $DPS_{D,2}$ measured the differential pressure over the FOTC inside the draw channel.

To eliminate pulsations downstream of the FOTC the pulsation dampener $PD_{D,5}$ was installed. The temperature ($TS_{D,1}$), the conductivity ($CS_{D,1}$) and average volume flow rate ($FM_{D,2}$) were measured in this non-fluctuating part downstream of $PD_{D,5}$. Before entering the draw tank again, the solution was filtered by a 5 micron filter ($F_{D,1}$) to avoid accumulation of particles. The feed was pumped from the feed tank FT by the gear pump GP_f through the FOTC and back to the FT again. The relative pressure, temperature, conductivity and volume flow rate were measured with $PS_{f,1}$, $PS_{f,2}$, $TS_{f,1}$, $CS_{f,1}$ and $FM_{f,1}$, respectively. The flux of the draw and feed solution was determined using the scales B_F and B_D. Test rig and module specifications are given in Tables C.4 and C.5. A detailed description of the measurement setup can also be found in [122].

Table C.4: Measurement equipment of bench scale test rig.

Symbol	Description	Range (calib.)	Error
T	PT1000 4-wire RTD	20-100 °C	0.1 K
$\dot{V}$	Magnetic flow meter Krohne Optiflux 5100C, DN6	0-200 l/h	0.4%+1 mm/s
$\dot{V}$	Magnetic flow meter Krohne Optiflux 5100C, DN4	0-200 l/h	0.4%+1 mm/s
P	Pressure sensors Wika S20	0-4 bar, abs	0.25% BFSL
MB	Scales Kern KMB-TM	0-6 kg	0.2 g
MB	Scales Sartorius Combics 1	0-30 kg	1 g
Δp	High frequent differential pressure sensor (Krohne PD)	-200-200 mbar	0.1 %FS

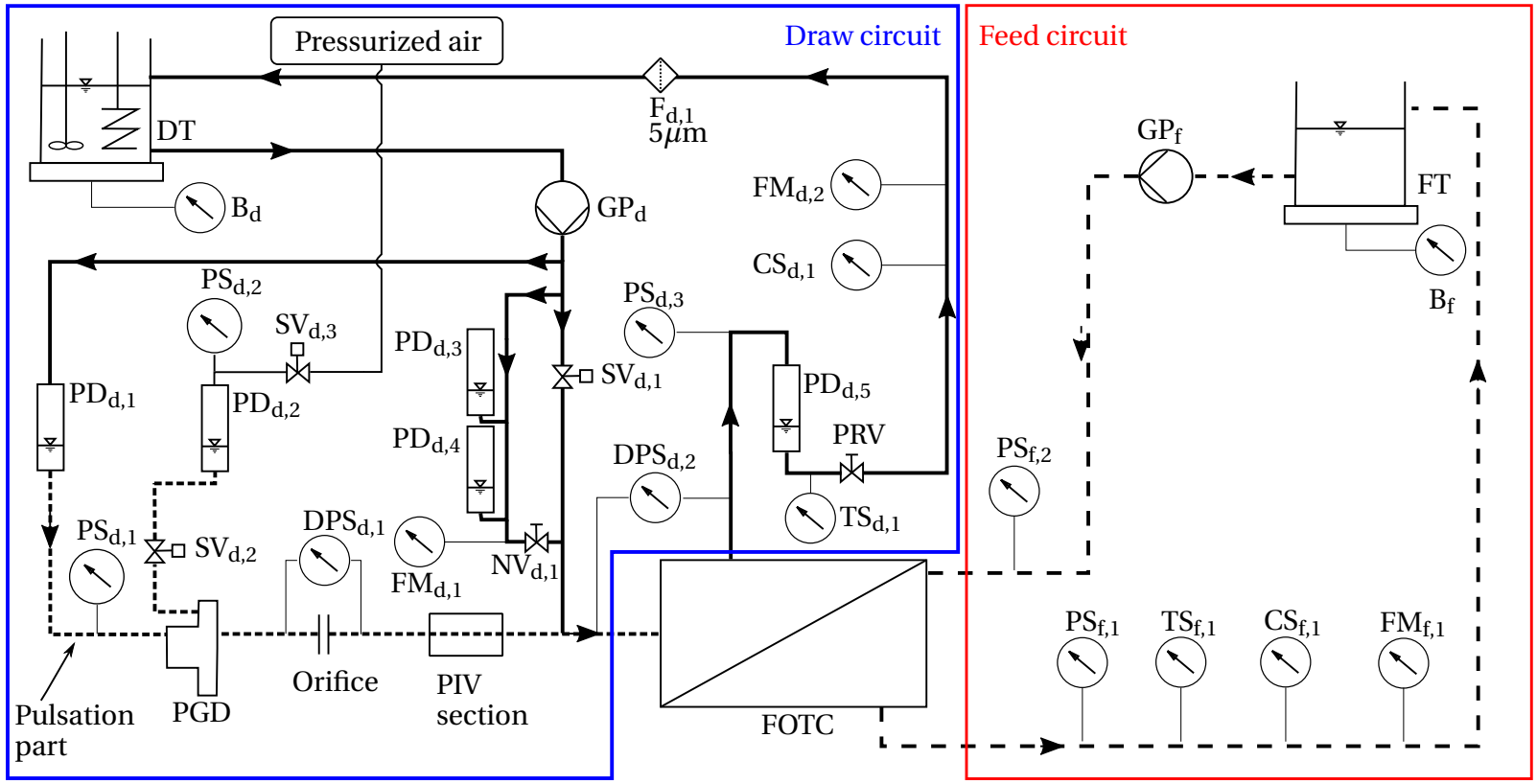

Figure C.2: P & ID of the bench-scale FO test rig adapted from [20, 59];
B: Balance - **DPS**: Differential pressure sensor - **DT**: Draw tank - **CS**: Conductivity sensor - **F**: Filter - **FM**: Flow meter - **FOTC**: Forward Osmosis test cell - **FT**: Feed tank - **GP**: Gear pump - **NV**: Needle valve - **PD**: Pressure dampener - **PGD**: Pulsation generation device - **PRV**: Pressure relieve valve - **PS**: Pressure sensor - **SV**: Solenoid valve.

Table C.5: Operation Window of the FO Test Rig.

Parameter	**Range**	**Unit**
Draw volume flow rates	20 – 60	$l\,h^{-1}$
Feed volume flow rates	20 – 40	$l\,h^{-1}$
Maximum pressure	4	bar
Pulsation frequency range	1 – 18	Hz
Amplitude ratio range	0 – 1.4	-
Water flux brackish water membrane	3 – 6	$l\,m^{-2}\,h^{-1}$
Water flux seawater membrane	2 – 3	$l\,m^{-2}\,h^{-1}$

C.3 Technical Details of the Pulsation Generation Device

Figure C.3 shows the dependence of the parameter A_{orif} on the volume flow rate. It can be seen that the parameter strongly increases and stagnates at around $\dot{V} > 60\,\text{l}\,\text{h}^{-1}$.

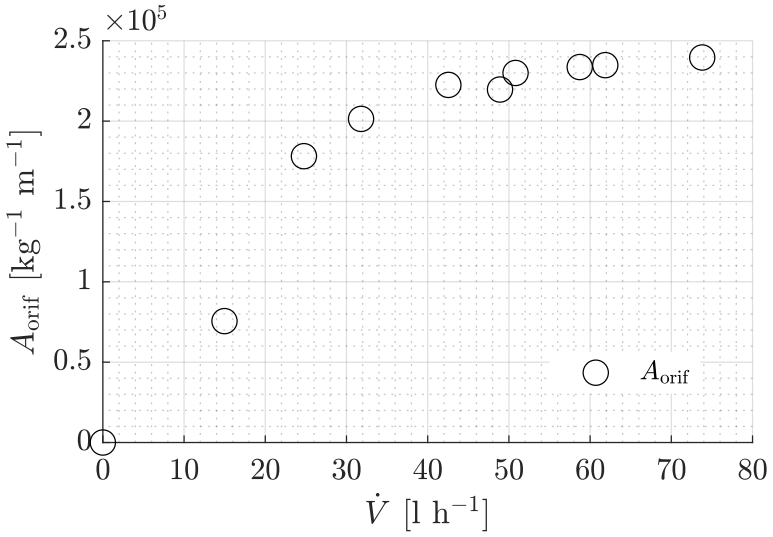

Figure C.3: Variation of parameter A_{orif} for different volume flow rates; adapted from [86].

In Table C.6, the specifications of the Pulsation Generation Device (PGD) are given.

Table C.6: Specification of the PGD.

Specification	Unit	Value
Shaft		Stainless steel 1.4501
Ball bearing		SKF 6403
Taper roller bearing		SKF NU 205 ECP
Disks		Polyoxymethylene
Shaft seal		Type 32x47x8 BA
Casing		Stainless steel 1.4501

D Appendix: Postprocessing with Proper Orthogonal Decomposition

Proper Orthogonal Decomposition (POD) is a valuable tool for investigation of the dominant modes of dynamic systems. The classical snapshot approach, presented by Sirovich [123], is used in this work to identify the dynamic characteristics of pulsating flows in spacer filled channels. It is introduced in the following based on [114, 124].

The laminar periodic flow field $\tilde{\mathbf{u}}$, mass fraction field $\tilde{\xi}$ and vorticity field $\tilde{\Omega}$ is decomposed into spatial modes $\Phi(\mathbf{x})$ and time coefficients ψ_i

$$\mathbf{u}(\mathbf{x},t) \;=\; \overline{\mathbf{u}}(\mathbf{x}) \;+\; \tilde{\mathbf{u}}(\mathbf{x},t) \;=\; \overline{\mathbf{u}}(\mathbf{x}) \;+\; \sum_{i=1}^{N} \psi_i(t)\Phi_i(\mathbf{x}), \tag{D.1}$$

$$\xi(\mathbf{x},t) \;=\; \overline{\xi}(\mathbf{x}) \;+\; \tilde{\xi}(\mathbf{x},t) \;=\; \overline{\xi}(\mathbf{x}) \;+\; \sum_{i=1}^{N} \psi_i(t)\Phi_i(\mathbf{x}). \tag{D.2}$$

Usually, a set of M spatial points over N time steps is considered with $M >> N$, which is the usually the case for PIV or CFD data [114]. For calculation of the POD the correlation matrix $\mathbf{R}$ between two snapshots is needed. It is defined as the L^2 inner product of the flow field fluctuations of two snapshots $\tilde{\mathbf{m}}$ and $\tilde{\mathbf{n}}$

$$\langle \tilde{\mathbf{m}}(\mathbf{x}), \tilde{\mathbf{n}}(\mathbf{x}) \rangle \;=\; \int_V \tilde{\mathbf{m}}(\mathbf{x}), \tilde{\mathbf{n}}(\mathbf{x}) dV, \tag{D.3}$$

where m and n represent the fluctuations of the considered variables. The elements of the correlation matrix are given by

$$R_{\mathrm{i,j}} \;=\; \frac{1}{N} \langle \tilde{m}(\mathbf{x}, t_{\mathrm{i}}), \tilde{n}(\mathbf{x}, t_{\mathrm{j}}) \rangle. \tag{D.4}$$

The temporal coefficients ψ and the mode energies are obtained from the Eigenvalue problem

$$\mathbf{R}\psi_{\mathrm{i}} = \lambda_{\mathrm{i}}\psi_{\mathrm{i}} \text{ with } \lambda_1 \geq \lambda_2 \geq ...\lambda_{\mathrm{N}} \geq 0. \tag{D.5}$$

The entries of the correlation matrix are scaled with the kinetic energy of the single modes.

Finally, the spatial modes can be obtained from the projection of the snapshots

$$\Phi_{\mathrm{i}}(\mathbf{x}) = \frac{1}{N\lambda_{\mathrm{i}}} \sum_{j=1}^{N} \psi_{\mathrm{i}}(t_{\mathrm{j}})\, \tilde{m}(\mathbf{x}, t_{\mathrm{j}}). \tag{D.6}$$

This formulation is the classical snapshot POD [114].

E Appendix: Mesh Study

A detailed mesh study was performed. The grid convergence index (GCI) [55] is calculated for every mesh at an averaged Reynolds number of $\overline{\mathrm{Re}}$=136.8, a Womersley number of Wo = 19.5 and an amplitude ratio of $AR = 1.2$. For the convergence study, the permeate mass flux j_P, the average salt mass fraction at the membrane $\overline{\xi}_\mathrm{F,AL}$ and the maximum and minimum mass fraction $\overline{\xi}_\mathrm{F,AL,min/max}$ are considered. The GCI is based on a generalization of Richardson's extrapolation which goes back to Roache [125]. The GCI for fine and coarse grids can be calculated by

$$\mathrm{GCI}_\mathrm{fine} = \frac{|\eta_\mathrm{GCI}|}{\mathbb{R}^\Pi - 1} \tag{E.1}$$

and

$$\mathrm{GCI}_\mathrm{coarse} = \frac{3|\eta_\mathrm{GCI}|\mathbb{R}^\Pi}{\mathbb{R}^\lambda - 1}. \tag{E.2}$$

$|\eta_\mathrm{GCI}|$ is the relative error for the calculations of the considered integral function, Π is the number of dimension and $\mathbb{R}$ is the ratio between the number of cells of the fine and coarse grid. Verification can be carried out if the GCI for the fine mesh falls below an acceptable error level below 1 % [55]. For the calculations in the present work a GCI below 1% was taken. Figure E.1 shows the convergence for the zig-zag configuration described in Section 4.1.2. At a cell-number of around $n_\mathrm{Cells} = 480,000$ the GCI for the important values values is below 1%. Figure E.2 shows the convergence for the submerged configuration described in Section 4.1.2. At a cell-number of around $n_\mathrm{Cells} = 610,000$ the GCI for the important values values is below 1%.

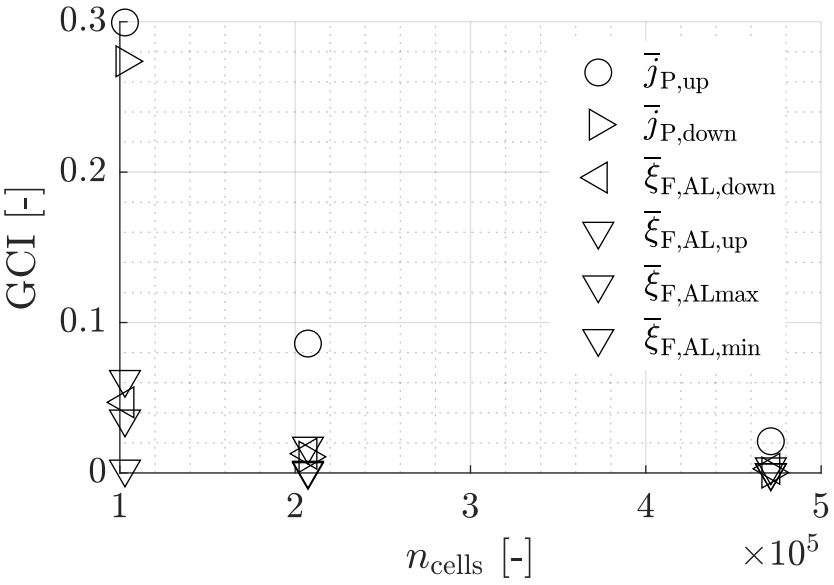

Figure E.1: Convergence study for the zig-zag configuration.

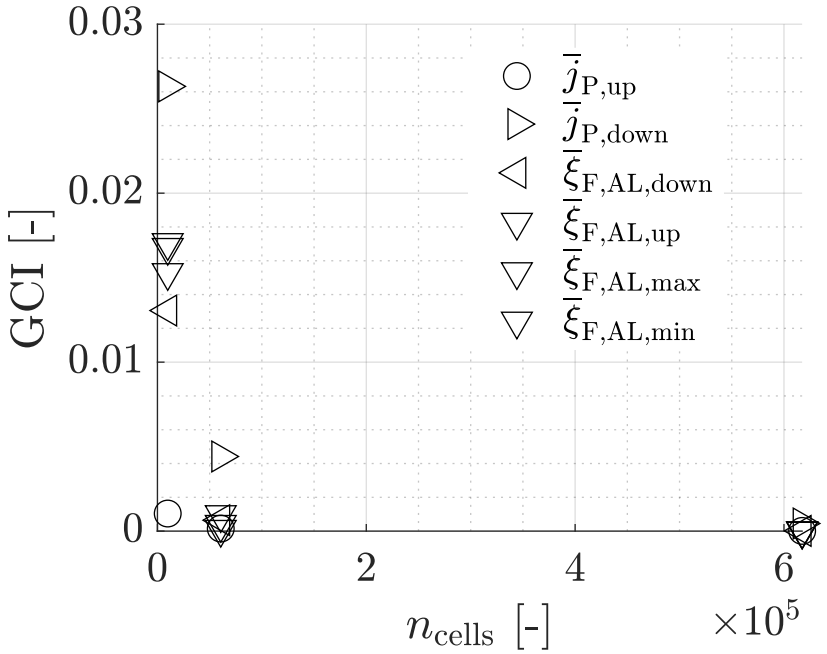

Figure E.2: Convergence study for the submerged configuration.

F Appendix: Calibration of the System Simulation Model

In the present section, the calibration and verification of the quasi-2D RO simulation model is presented. For this purpose, the data obtained with the module test rig are used, cf. Section 3.1. To determine the membrane parameter A_{mem}, RO experiments with pure water (permeate) were performed aiming to exclude concentration polarization. These measurements were made in the studies of Drexler, Thun and Theobald [82, 83, 84] and are also reported in [59]. To calculate the membrane permeability A_{mem}, Equation (2.5) is used in the form of

$$A_{\mathrm{mem}} = \frac{j_{\mathrm{w}}}{\rho_{\mathrm{F}} A_{\mathrm{m}} (p_{\mathrm{F}} - p_{\mathrm{P}})}. \tag{F.1}$$

Each experiment was repeated at different temperatures and pressures to identify any dependencies. The results are presented in Figure F.1a. Depending on the inlet temperature and pressure applied, A_{mem} ranges from $A_{\mathrm{mem}} = 6.8 \cdot 10^{-7} \ldots 11.2 \cdot 10^{-7}$ m s^{-1} bar^{-1}. It can be seen that the parameters increase with temperature and decrease with applied hydraulic pressure. The higher the temperature, the stronger is the dependence on the pressure. The data gained are used to determine the membrane parameter A_{mem} by (adapted from [126] and [82])

$$A_{\mathrm{mem}} = A_{\mathrm{mem,ref}} \exp\left(\alpha_{\mathrm{mem,T}} \frac{T_{\mathrm{F}} - T_{\mathrm{F,ref}}}{T_{\mathrm{F,ref}}}\right) \exp\left(\alpha_{\mathrm{mem,p}} \frac{p_{\mathrm{F}} - p_{\mathrm{F,ref}}}{p_{\mathrm{F,ref}}}\right), \tag{F.2}$$

with the reference temperature $T_{\mathrm{F,ref}} = 293.15$ K and pressure $p_{\mathrm{ref}} = 1$ bar. The parameters $\alpha_{\mathrm{mem,T}}$ and $\alpha_{\mathrm{mem,p}}$ were determined within an optimization routine using `fmincon` from Matlab [72, 82]. Using this routine, $A_{\mathrm{mem,ref}}$ was determined at as $A_{\mathrm{mem,ref}} = 7.865 \cdot 10^{-7}$ ms^{-1}bar^{-1}, $\alpha_{\mathrm{mem,T}}$ as $\alpha_{\mathrm{mem,T}} = 8.03$ and $\alpha_{\mathrm{mem,p}}$ as $\alpha_{\mathrm{mem,p}} = -4.894 \cdot 10^{-8}$ at $T_{\mathrm{F}} = 293.15$. The salt permeability is determined using the Sherwood number correlation of Schock and Michael [60]

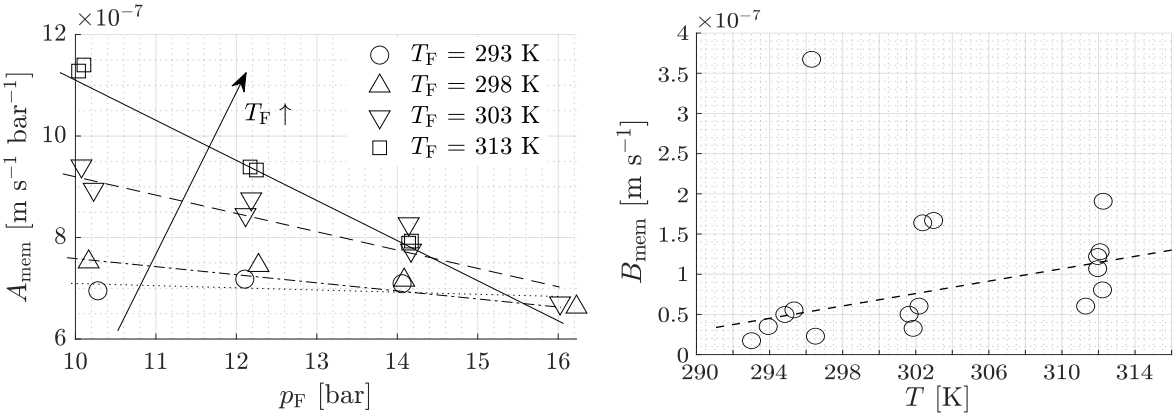

(a) Determination of membrane parameter A_{mem} adapted from [59].

(b) Determination of membrane parameter B_{mem}, adapted from [82].

Figure F.1: Determination of membrane parameters.

and Equation (2.6) to approximate the membrane concentration at the feed side. Pressure or concentration dependencies are neglected, which is feasible for BWRO and SWRO processes [50]. Figure F.1b shows the measured salt permeability B_{mem} over the temperature. It can be seen that the salt permeability scatters, but the values show an increasing trend (dashed line) with increasing temperatures, which is in accordance to the theory [126]. The averaged values range from $B_{\text{mem}} = 3.0 \cdot 10^{-8}\,\text{m s}^{-1}$ at around $T_{\text{F}} = 293.15\,\text{K}$ to $B_{\text{mem}} = 1.1 \cdot 10^{-7}\,\text{m s}^{-1}$ at around $T_{\text{F}} = 312\,\text{K}$. B_{mem} can be represented by [126]

$$B_{\text{mem}} = B_{\text{mem,ref}} \exp\left(\alpha_{\text{mem,B,T}} \frac{T - T_{\text{ref}}}{T_{\text{ref}}}\right). \tag{F.3}$$

The parameter $\alpha_{\text{mem,B,T}}$ is again determined within an optimization routine using `fmincon` from Matlab. Applying this routine, $B_{\text{mem,ref}}$ was determined as $B_{\text{mem,ref}} = 4.343 \cdot 10^{-8}\,\text{ms}^{-1}$ and $\alpha_{\text{mem,B,T}}$ as $\alpha_{\text{mem,B,T}} = 12.53$ [82].

Previous Publications

Teile dieser Dissertation wurden vom Autor bereits standardmäßig vorab als Konferenz- und Zeitschriftenbeiträge sowie Projektabschlussberichte veröffentlicht [8, 20, 59]. Alle Vorveröffentlichungen sind entsprechend der gültigen Promotionsordnung ordnungsgemäßgemeldet.

Parts of this Ph.D. thesis were published by the author beforehand in conference proceedings, journal papers, and reports [8, 20, 59]. All of these prior printed publications are registered according to the valid doctoral regulations.

Supervised Student Theses

Associated with this Ph.D. thesis, a number of student theses were supervised by the author of the present work. These theses were prepared at the Lehrstuhl für Thermodynamik, Technische Universität München in the years 2013 to 2017 under the close supervision of the present author. Parts of these supervised theses may be incorporated into the present thesis. The author would like to express his sincere gratitude to all formerly supervised students for their commitment and support of this research project.

Alexander Präbst

Student	Thesis
M. Hauck	Modeling of an Ultrafiltration Process for Pretreatment of a Photovoltaic Thermal driven Reverse Osmosis Plant, Bachelor's Thesis, 2014.
F. Theobald	Potential analysis of solar sea water desalination by electrodialysis powered by Photovoltaic/Thermal collectors, Semesterarbeit, 2015.
C. Drexler	Setup of a Reverse Osmosis system and analysis of different membrane parameters, Bachelor's Thesis, 2015.
J. Kammerer	Konstruktion eines Drehpulsators zur Erzeugung instationärer Strömungen, Bachelor's Thesis, 2015.
N. Borgmann	Operation and Control of a Small Stand-Alone Reverse Osmosis Desalination Plant Powered by Photovoltaic/Thermal Collectors, Master's Thesis, 2015
G. Bauer	Experimentelle Evaluierung des erhöhten Stoffübergangs in Kanälen mit Turbulenzpromotoren unter laminar pulsierendenStrömungen - Anwendung in Membranprozessen, Semesterarbeit, 2016.
C. Thun	Second Law Efficiency of Solar Powered Desalination Systems, Semesterarbeit, 2016.
J. Czarny	Control and Energy Storage Strategies of PV/T Driven Reverse Osmosis Plants, Master's Thesis, 2016.
M. Usman	Numerical and Experimental Investigations of Colloidal Fouling, Master's Thesis, 2016.
J. Sporrer	Development of Design and Operation Strategies for Reverse Osmosis Systems powered by Renewable Energies, Master's Thesis, 2016.
P. Bürger	Theoretische und experimentelle Untersuchung zu Impuls- und Stofftransport pulsierender Strömungen in Hydrauliksystemen mit besonderem Bezug auf Membranmodule zur Meerwasserentsalzung, Master's Thesis, 2017.

Bibliography

[1] J. H. Lienhard V, K. H. Mistry, M. H. Sharqawy, G. P. Thiel, *Chapter 4 - Thermodynamics, exergy, and energy efficiency in desalination systems*, Desalination Sustainability, pp. 127 – 206, 2017.

[2] R. Semiat, *Energy issues in desalination processes*, Environmental Science & Technology **42**, pp. 8193 – 8201, 2008.

[3] G. Amy, N. Ghaffour, Z. Li, L. Francis, R. V. Linares, T. Missimer, S. Lattemann, *Membrane-based seawater desalination: Present and future prospects*, Desalination **401**, pp. 16 – 21, 2017.

[4] A.G. Fane, *A grand challenge for membrane desalination: More water, less carbon*, Desalination **426**, pp. 155 – 163, 2018.

[5] J. R. Werber, A. Deshmukh, M. Elimelech, *The critical need for increased selectivity, not increased water permeability, for desalination membranes*, Environmental Science & Technology Letters **3**, pp. 112 – 120, 2016.

[6] R. K. McGovern, J. H. Lienhard, *On the asymptotic flux of ultrapermeable seawater reverse osmosis membranes due to concentration polarisation*, Journal of Membrane Science **520**, pp. 560 – 565, 2016.

[7] A. G. Fane, R. Wang, M. X. Hu, *Synthetic membranes for water purification: Status and future*, Angewandte Chemie International Edition **54**, pp. 3368 – 3386, 2014.

[8] A. Präbst, F. Kiefer, A. Kroiß, M. Spinnler, T. Sattelmayer, *Influence of dynamic operation of reverse osmosis systems on fluid dynamics and mass*

transfer by investigation of 2-D spacer filled channels, Desalination and Water Treatment **73**, pp. 30 – 45, 2017.

[9] T. Manth, M. Gabor, *Minimizing RO energy consumption under variable conditions of operation*, Desalination **157**, pp. 9 – 21, 2003.

[10] M. Li, *Energy consumption in spiral-wound seawater reverse osmosis at the thermodynamic limit*, Industrial & Engineering Chemistry Research **53**, pp. 3293 – 3299, 2014.

[11] A. Zhu, Panagiotis, D. Christofides, Y. Cohen, *Effect of thermodynamic restriction on energy cost optimization of RO membrane water desalination*, Industrial & Engineering Chemistry Research **48**, pp. 6010 – 6021, 2009.

[12] S. K. Saha, M. Tiwari, B. Sunden, Z. Wu, *Advances in heat transfer enhancement*, Springer, 2016.

[13] E. M. Benavides, *Heat transfer enhancement by using pulsating flows*, Journal of Applied Physics **105**, 094907, 2009.

[14] A. Sorin, F. Bouloc, B. Bourouga, P. Anthoine, *Experimental study of periodic heat transfer coefficient in the entrance zone of an exhaust pipe*, International Journal of Thermal Sciences **47**, pp. 1665 – 1675, 2008.

[15] H. N. Hemida, M.N. Sabry, A. Abdel-Rahim, H. Mansour, *Theoretical analysis of heat transfer in laminar pulsating flow*, International Journal of Heat and Mass Transfer **45**, pp. 1767 – 1780, 2002.

[16] M. Faghri, K. Javdani, A. Faghri, *Heat transfer with laminar pulsating flow in a pipe*, Letters in Heat and Mass Transfer **6**, pp. 259 – 270, 1979.

[17] M.R. Mackley, P. Stonestreet, *Heat transfer and associated energy dissipation for oscillatory flow in baffled tubes*, Chemical Engineering Science **50**, pp. 2211 – 2224, 1995.

[18] J. C. Yu, Z. X. Li, T.S. Zhao, *An analytical study of pulsating laminar heat convection in a circular tube with constant heat flux*, International Journal of Heat and Mass Transfer **47**, pp. 5297 – 5301, 2004.

[19] M. A. Habib, A. M. Attya, A. I. Eid, A. Z. Aly, *Convective heat transfer characteristics of laminar pulsating pipe air flow*, Heat and Mass Transfer **38**, pp. 221 – 232, 2002.

[20] A. Kastl, A. Praebst, F. Kiefer, M. Spinnler, T. Sattelmayer, *Colloidal fouling mitigation using pulsating flows in osmotic membrane processes*, Desalination and Water Treatment **157**, pp. 228 – 241, 2019.

[21] R. Smith, *Contaminant dispersion in oscillatory flows*, Journal of Fluid Mechanics **114**, pp. 379 – 398, 1982.

[22] P. C. Chatwin, *On the longitudinal dispersion of passive contaminant in oscillatory flows in tubes*, Journal of Fluid Mechanics **71**, pp. 513 – 527, 1975.

[23] K. Haddad, Özgür Ertunç, M. Mishra, A. Delgado, *Pulsating laminar fully developed channel and pipe flows*, Phys. Rev. E **81**, 016303, 2010.

[24] F. Zamani, J. Wei Chew, E. Akhondi, W. B. Krantz, A. G. Fane, *Unsteady-state shear strategies to enhance mass transfer for the implementation of ultrapermeable membranes in reverse osmosis: A review*, Desalination **356**, pp. 328 – 348, 2015.

[25] T. J. Kennedy, R.L. Merson, B.J. McCoy, *Improving permeation flux by pulsed reverse osmosis*, Chemical Engineering Science **29**, pp. 1927 – 1931, 1974.

[26] S. Ilias, R. Govind, *Potential applications of pulsed flow for minimizing concentration polarization in ultrafiltration*, Separation Science and Technology **25**, pp. 1307 – 1324, 1990.

[27] V. I. Baikov, P. K. Znovets, *Membrane processes of separation of solutions in a pulsating flow*, Journal of Engineering Physics and Thermophysics **77**, pp. 802 – 807, 2004.

[28] M. Al haj Ali, A. Ajbar, Emad Ali, and K. Alhumaizi, *Optimization-based periodic forcing of reverse osmosis desalination process for improved performance*, Desalination and Water Treatment **51**, pp. 6961 – 6969, 2013.

[29] A. M. Thomas, A. Jain, *The effect of pulsatile flows on the transport across membranes: An analytical and experimental study*, Separation Science and Technology **42**, pp. 1931-1944, 2007.

[30] M. Y. Jaffrin, L.H. Ding, B.B. Gupta, *Rationale of filtration enhancement in membrane plasmapheresis by pulsatile blood flow*, Life Support Systems: The Journal of the European Society for Artificial Organs **5**, pp. 267 – 271, 1987.

[31] C. D. Bertram, M.R. Hoogland, H. Li, R.A. Odell, A.G. Fane, *Flux enhancement in crossflow microfiltration using a collapsible-tube pulsation generator*, Journal of Membrane Science **84**, pp. 279 – 292, 1993.

[32] B. B. Gupta, P. Blanpain, M.Y. Jaffrin, *Permeate flux enhancement by pressure and flow pulsations in microfiltration with mineral membranes*, Journal of Membrane Science **70**, pp. 257 – 266, 1992.

[33] Y. Y. Liang, G.A. Fimbres Weihs, D.E. Wiley, *Comparison of oscillating flow and slip velocity mass transfer enhancement in spacer-filled membrane channels: CFD analysis and validation*, Journal of Membrane Science **593**, 117433, 2020.

[34] F. J. García-Picazo, D. F. Fletcher, G. A. Fimbres Weihs, *Mass transfer enhancement in spacer-filled membrane channels by flow oscillation induced vortex shedding: Numerical study of the effect of amplitude*, International Journal of Heat and Mass Transfer **209**, 124054, 2023.

[35] A. Abbas and N. Al-Bastaki, *Flux enhancement of reverse osmosis desalination processes*, Desalination **132**, pp. 21 – 27, 2000.

[36] C. Rodrigues, M. Rodrigues, V. Semiao, V. Geraldes, *Enhancement of mass transfer in spacer-filled channels under laminar regime by pulsatile flow*, Chemical Engineering Science **123**, pp. 536 – 541, 2015.

[37] X. Ni, M.R. Mackley, A.P. Harvey, P. Stonestreet, M. H. I. Baird, N.V. Rama Rao, *Mixing through oscillations and pulsations - A guide to achieving process enhancements in the chemical and process industries*, Trans IChemE **81**, Part A, pp. 373 – 383, 2003.

[38] P. Atkins, J. de Paula, *Physikalische Chemie*, Wiley-VCH, 2013.

[39] M. Luckas, J. Krissmann, *Thermodynamik der Elektrolytlösungen - eine einheitliche Darstellung der Berechnung komplexer Gleichgewichte*, Springer Verlag, 2001.

[40] E. C. W. Clarke, D. N. Glew, *Evaluation of thermodynamic functions from equilibrium constants*, Trans. Faraday Soc. **62**, pp. 539 – 547, 1966.

[41] F. Kiefer, *Multi-effect vacuum membrane distillation for high-recovery desalination*, Technische Universität München, 2020.

[42] V. Pipich, M. Dickmann, H. Frielinghaus, R. Kasher, C. Hugenschmidt, W. Petry, Y. Oren, D. Schwahn, *Morphology of thin film composite membranes explored by small-angle neutron scattering and positron-annihilation lifetime spectroscopy*, Membranes **10**, 2020.

[43] E. M. Vrijenhoek, S. Hong, M. Elimelech, *Influence of membrane surface properties on initial rate of colloidal fouling of reverse osmosis and nanofiltration membranes*, Journal of Membrane Science **188**, pp. 115 – 128, 2001.

[44] G. M. Geise, *Water and salt transport structure/property relationships in polymer membranes for desalination and power generation applications*, PhD Thesis, The University of Texas at Austin, 2012.

[45] A. E. Yaroshchuk, *Dielectric exclusion of ions from membranes*, Advances in Colloid and Interface Science **85**, pp. 193 – 230, 2000.

[46] M. Elimelech, A.E. Childress, *Zeta potential of reverse osmosis membranes: Implications for membrane performance*, Technical Report, U.S. Department of the Interior, 1996.

[47] T. Fujioka, N. Oshima, R. Suzuki, W. E. Price, L. D. Nghiem, *Probing the internal structure of reverse osmosis membranes by positron annihilation spectroscopy: Gaining more insight into the transport of water and small solutes*, Journal of Membrane Science **486**, pp. 106 – 118, 2015.

[48] A. Präbst, *A bench-scale reverse osmosis plant - Experimental setup and numerical modeling*, Technische Universität München, Diploma Thesis, 2013.

[49] T. Melin, R. Rautenbach, *Membranverfahren - Grundlagen der Modul- und Anlagenauslegung*, Springer-Verlag, 2007.

[50] D. R. Paul, *Reformulation of the solution-diffusion theory of reverse osmosis*, Journal of Membrane Science **241**, 371-386, 2004.

[51] J. R. McCutcheon, M. Elimelech, *Influence of concentrative and dilutive internal concentration polarization on flux behavior in forward osmosis*, Journal of Membrane Science **284**, pp. 237 – 247, 2006.

[52] J. G. A. Bitter, *Transport mechanisms in membrane separation processes*, The Plenum Chemical Engineering Series, Plenum Press, New York, 1991.

[53] H. D. Baehr, K. Stephan, *Wärme- und Stoffübertragung*, Springer Vieweg, Berlin, Heidelberg, 2019.

[54] A. D'Haese, *Mechanistic modeling of mass transport phenomena in Forward Osmosis*, PhD Thesis, Ghent University, 2017.

[55] G. A. Fimbres-Weihs, D. E. Wiley, *Review of 3D CFD modeling of flow and mass transfer in narrow spacer-filled channels in membrane modules*, Chemical Engineering and Processing **49**, pp. 759 – 781, 2010.

[56] N. Horstmeyer, T. Lippt, D. Schön, F. Schlederer, C. Picioreanu, K. Achterhold, F. Pfeiffer, J. E. Drewes, *CT scanning of membrane feed spacers: Impact of spacer model accuracy on hydrodynamic and solute transport modeling in membrane feed channels*, Journal of Membrane Science **564**, pp. 133 – 145, 2018.

[57] G. Srivathsan, E. M. Sparrow, J. M. Gorman, *Reverse osmosis issues relating to pressure drop, mass transfer, turbulence, and unsteadiness*, Desalination **341**, pp. 83 – 86, 2014.

[58] C. P. Koutsou, S. G. Yiansios, A. J. Karabelas, *Direct numerical simulation of flow in spacer-filled channels: Effect of spacer geometrical characteristics,* Journal of Membrane Science **291**, pp. 53-69, 2007.

[59] A. Präbst, M. Spinnler, T. Sattelmayer, *PV/T betriebene Umkehrosmoseanlagen - Reverse osmosis desalination powered by hybrid photovoltaic/thermal solar systems (PV/T-RO)*, Fachlicher Schlussbericht zum BMBF Förderkennzeichen 02WA1299, Technische Universität München, 2016.

[60] A. Miquel, G. Schock, *Mass transfer and pressure loss in spiral-wound modules*, Desalination **64**, pp. 339-352, 1987.

[61] A. M. Jacobi, R.K. Shah, *Heat transfer surface enhancement through the use of longitudinal vortices: A review of recent progress*, Experimental Thermal and Fluid Science **11**, pp. 295 – 309, 1995.

[62] L.-M. Chang, L.-B. Wang, K.-W. Song, D.-L. Sun, J.-F. Fan, *Numerical study of the relationship between heat transfer enhancement and absolute vorticity flux along main flow direction in a channel formed by a flat tube bank fin with vortex generators*, International Journal of Heat and Mass Transfer **52**, pp. 1794 – 1801, 2009.

[63] C. Habchi, T. Lemenand, H. Peerhossaini, *Turbulence behavior of artificially generated vorticity*, Journal of Turbulence **11**, pp. 1-28, 2010.

[64] T. Lemenand, C. Habchi, D. Della Valle, H. Peerhossaini, *Vorticity and convective heat transfer downstream of a vortex generator*, International Journal of Thermal Sciences **125**, pp. 342-349, 2018.

[65] R. Mathie, H. Nakamura, C. N. Markides, *Heat transfer augmentation in unsteady conjugate thermal systems, part II: Applications*, International Journal of Heat and Mass Transfer **56**, pp. 819 – 833, 2013.

[66] R. Mathie, C.N. Markides, *Heat transfer augmentation in unsteady conjugate thermal systems, part I: Semianalytical 1-D framework*, International Journal of Heat and Mass Transfer **56**, pp. 802 – 818, 2013.

[67] D. P. Telionis, *Unsteady viscous flows*, Springer Berlin, Heidelberg, 1981.

[68] A. Cardenas, *Influence of enhanced heat transfer in pulsating flow on the damping characteristics of resonator rings*, Dissertation, Professur für Thermofluiddynamik, Technische Universität München, 2014.

[69] M. Manna, A. Vacca, R. Verzicco, *Pulsating pipe flow with large-amplitude oscillations in the very high frequency regime. Part 1. Time-average analysis*, J. Fluid. Mech. **700**, pp. 246 – 282, 2012.

[70] R. Blythman, *Hydrodynamics and heat transfer of laminar pulsating flow in a rectangular channel*, Ph.D thesis, Department of Mechanical and Manufacturing Engineering, University of Dublin, 2017.

[71] U. H. Kurzweg, *Enhanced heat conduction in oscillating viscous flows within parallel-plate channels*, Journal of Fluid Mechanics **156**, pp. 291 – 300, 1985.

[72] The MathWorks Inc., *MATLAB version: 9.13.0 (R2022b)*, Natick, Massachusetts, United States, https://www.mathworks.com, 2022.

[73] E. J. Watson, *Diffusion in oscillatory pipe flow*, Journal of Fluid Mechanics **133**, pp. 233 – 244, 1983.

[74] S. Ray, B. Ünsal, F. Durst, Ö. Ertunc, O. A. Bayoumi, *Mass flow rate controlled fully developed laminar pulsating pipe flows*, Journal of Fluids Engineering **127**, pp. 405 – 418, 2005.

[75] B. Ünsal, S. Ray, F. Durst, Ö. Ertunç, *Pulsating laminar pipe flows with sinusoidal mass flux variations*, Fluid Dynamics Research **37**, pp. 317 – 3333, 2005.

[76] S. Uchida, *The pulsating viscous flow superposed on the steady laminar motion of incompressible fluid in a circular pipe*, Zeitschrift für angewandte Mathematik und Physik ZAMP **7**, pp. 403 – 422, 1956.

[77] G. J. Brereton, S. M. Jalil, *Diffusive heat and mass transfer in oscillatory pipe flow*, Physics of Fluids **29**, 073601, 2017.

[78] R. Blythman, T. Persoons, N. Jeffers, D.B. Murray, *Heat transfer of laminar pulsating flow in a rectangular channel*, International Journal of Heat and Mass Transfer **128**, pp. 279 – 289, 2019.

[79] A. P. Reverberi, V. P. Meshalkin, C. Cerrato, Yu. O. Savina, *Dynamics of a reverse osmosis unit with application to pulsating regimes for process optimization*, Theoretical Foundations of Chemical Engineering **45**, pp. 190 – 197, 2011.

[80] R. Blythman, S. Alimohammadi, T. Persoons, N. Jeffers, D. B. Murray, *Parametric analysis of laminar pulsating flow in a rectangular channel*, Heat and Mass Transfer **54**, pp. 2177 – 2186, 2018.

[81] Inc. Toray Industries, *Product data sheet for membrane module TML10d*, http://www.toraywater.com/products/ro/pdf/TML(D).pdf, Accessed: 2018-08-20.

[82] C. Drexler, *Setup of a reverse osmosis system and analysis of different membrane properties*, Bachelor's Thesis, Lehrstuhl für Thermodynamik, Technische Universität München, 2015.

[83] C. Thun, *Second law efficiency of solar powered desalination systems*, Technische Universität München, Semesterarbeit, 2016.

[84] C. Theobald, *Setup of a reverse osmosis system and analysis of different membrane properties*, Technische Universität München, Semesterarbeit, 2016.

[85] Inc. DuPont Water Solution, *Product data sheet for membrane module Filmtec SW30-2521*, https://www.dupont.com/content/dam/dupont/amer/us/en/water-solutions/public/documents/en/45-D01519-en.pdf, Accessed: 2020-01-20.

[86] P. Bürger, *Theoretische und experimentelle Untersuchung zu Impuls- und Stofftransport pulsierender Strömungen in Hydrauliksystemen mit besonderem Bezug auf Membranmodule zur Meerwasserentsalzung*, Master's Thesis, Lehrstuhl für Thermodynamik, Technische Universität München, 2017.

[87] M. Raffel, C. E. Willert, F. Scarano, C. J. Kähler, S. T. Wereley, J. Kompenhans, *Particle Image Velocimetry*, Springer International Publishing, 2018.

[88] W. Thielicke, E.J Stamhuis, *PIVlab towards user-friendly, affordable and accurate digital Particle Image Velocimetry in MATLAB*, Journal of Open Research Software **2**, pp. 1 – 10, 2014.

[89] M. Nabavi, K. Siddiqui, *A critical review on advanced velocity measurement techniques in pulsating flows*, Measurement Science and Technology **21**, 042002, 2010.

[90] K. Doblhoff-Dier, K. Kudlaty, M. Wiesinger, M. Gröschl, *Time resolved measurement of pulsating flow using orifices*, Flow Measurement and Instrumentation **22**, pp. 97 – 103, 2011.

[91] *Measurement of fluid flow in closed conduits - Guidelines on the effects of flow pulsations on flow-measurement instruments*, Norm, ISO/TR 3313.

[92] B. Dobrowolski, Z. Kabza, J. Pospolita, *Theoretische und experimentelle Untersuchungen des Einflusses der Pulsationsströmung auf die Charakteristiken der Drosselgeräte*, VDI-Verlag, Düsseldorf, 1991.

[93] A. Schlenkhoff, *Druckverlust an Blenden in einer oszillierenden Rohrströmung*, Dissertation, Fachbereich Bautechnik, Universität Wuppertal, 1991.

[94] A. Svete, J. Kutin, I. Bajsic, J. Slavic, *Development of a liquid-flow pulsator*, Flow Measurement and Instrumentation **23**, pp. 1 – 8, 2012.

[95] J. A. Miller, A. A. Fejer, *Transition phenomena in oscillating boundary-layer flows*, Journal of Fluid Mechanics **18**, pp. 438 – 448, 1964.

[96] M. Hino, M. Sawamoto, S. Takasu, *Experiments on transition to turbulence in oscillatory pipe flow*, Journal of Fluid Mechanics **75**, pp. 139 – 207, 1974.

[97] M. A. Carpinlioclu, M. Y. Gundodu, *A critical review on pulsatile pipe flow studies directing towards future research topics*, Flow Measurement and Instrumentation **12**, pp. 163 – 174, 2001.

[98] F. Durst, U. Heim, B. Ünsal, G. Kullik, *Mass flow rate control system for time-dependent laminar and turbulent flow investigations*, Measurement Science and Technology **14**, pp. 893 – 902, 2003.

[99] F. Durst, B. Ünsal, S. Ray, D. Trimis, *Method for defined mass flow variations in time and its application to test a mass flow rate meter for pulsating flows*, Measurement Science and Technology **18**, pp. 790 – 802, 2007.

[100] F. Durst, K. Haddad, A. Al-Salaymeh, Shadi Eid, and B. Ünsal, *Mass flow-rate control unit to calibrate hot-wire sensors*, Experiments in Fluids **44**, pp. 189 – 197, 2007.

[101] P. Eichinger, *Untersuchung des Reibungsverhaltens bei instationären Strömungsvorgängen in Rohrleitungen*, Thesis, Universität Stuttgart,1992.

[102] E. Spiazzi, J. Lenoir, A. Grangeon, *A new generator of unsteady-state flow regime in tubular membranes as an anti-fouling technique: A hydrodynamic approach*, Journal of Membrane Science **80**, pp. 49 – 57, 1993.

[103] J. Kammerer, *Konstruktion eines Drehpulsators zur Erzeugung instationärer Strömungen*, Bachelor Thesis, Lehrstuhl für Thermodynamik, Technische Universität München, Bachelor Thesis - 2015.

[104] R. Kathan, *Verlustmechanismen in Raketenbrennkammern*, Dissertation, Lehrstuhl für Thermodynamik, Technische Universität München, 2013.

[105] S. Ray, B. Ünsal, F. Durst, *Development length of sinusoidally pulsating laminar pipe flows in moderate and high Reynolds number regimes*, International Journal of Heat and Fluid Flow **37**, pp. 167 – 176, 2012.

[106] I. Bajsic, J. Kutin, T. Zagar, *Response time of a pressure measurement system with a connecting tube*, Instrumentation Science & Technology **35**, pp. 399 – 409, 2007.

[107] K. Foerner, *Nonlinear aeroacoustic characterization of resonators*, Dissertation, Professur für Thermofluiddynamik, Technische Universität München, 2017.

[108] M. Zamir, *The physics of pulsatile flow*, Springer New York, 2000.

[109] W. Malalasekera, H.K. Versteeg, *An introduction to Computational Fluid Dynamics - The Finite Volume Method - Second Editions*, Pearson Verlag, 2007.

[110] A. Alexiadis, D.E. Wiley, A. Vishnoi, R.H.K. Lee, D.F. Fletcher, J.Bao, *CFD modeling of reverse osmosis membrane flow and validation with experimental results*, Desalination **217**, pp. 242 – 250, 2007.

[111] P. Xie, L. C. Murdoch, D. A. Ladner, *Hydrodynamics of sinusoidal spacers for improved reverse osmosis performance*, Journal of Membrane Science **453**, pp. 92 – 99, 2014.

[112] N. Borgmann, *Operation and control of small stand-alone reverse osmosis, desalination plants powered by a photovoltaic-thermal-collector*, Master's Thesis, Technische Universität München, 2015.

[113] W. Rohlfs, J. Lienhard, *Entrance length effects on Graetz number scaling in laminar duct flows with periodic obstructions: Transport number correlations for spacer-filled membrane channel flows*, International Journal of Heat and Mass Transfer **97**, pp. 842 – 852, 2016.

[114] P. Holmes, J. L. Lumley, G. Berkooz, C. W. Rowley, *Turbulence, coherent structures, dynamical systems and symmetry*, Cambridge Monographs on Mechanics, Cambridge University Press, 2012.

[115] J. Weiss, *A tutorial on the proper orthogonal decomposition*, AIAA Aviation Forum, 2019.

[116] H. Chen, D. L. Reuss, V. Sick, *On the use and interpretation of proper orthogonal decomposition of in-cylinder engine flows*, Measurement Science and Technology **23**, 085302, 2012.

[117] B. S. Richards, G. L. Park, T. Pietysch, A. Schäfer, *Renewable energy powered membrane technology: Safe operating window of a brackish water desalination system*, Journal of Membrane Science **468**, pp. 400 – 409, 2014.

[118] E. Meissner, *Fortpflanzungsgeschwindigkeit und Abbau einer harmonischen Druckschwingung in visko-elastischen Leitungen*, Forschung im Ingenieurwesen A **41**, pp. 80 – 84, 1975.

[119] E. Meissner, *Berechnung pulsierender Strömung in Systemen aus Kunststoffleitungen mit Berücksichtigung von Reibungsverlusten*, Forschung im Ingenieurwesen A **41**, pp. 53 – 63, 1977.

[120] J. G. Zhang, U. H. Kurzweg, *Numerical simulation of time-dependent heat transfer in oscillating pipe flow*, Journal of Thermophysics and Heat Transfer **5**, pp. 401 – 406, 1991.

[121] S. Y. Kim, B. H. Kang, J. M. Hyun, *Heat transfer in the thermally developing region of a pulsating channel flow*, International Journal of Heat and Mass Transfer **36**, pp. 4257 – 4266, 1993.

[122] G. Bauer, *Experimentelle Evaluatierung des erhöhten Stoffübergangs in Kanälen mit Turbulenzpromotoren unter laminar pulsierenden Strömungen - Anwendung in Membranprozessen*, Semester Thesis, Lehrstuhl für Thermodynamik, Technische Universität München, 2016.

[123] L. Sirovich, *Turbulence and the dynamics of coherent structures. I. Coherent structures*, Quarterly of Applied Mathematics **45**, pp. 561 – 571, 1987.

[124] M. Sieber, C. Oliver Paschereit, K. Oberleithner, *Spectral proper orthogonal decomposition*, Journal of Fluid Mechanics **792**, pp. 798 – 828, 2016.

[125] P. J. Roache, *Quantification of uncertainty in Computational Fluid Dynamics*, Annu. Rev. Fluid. Mech. **29**, pp. 123 – 160, 1997.

[126] R. Rautenbach, R. Albrecht, *Membrane processes*, John Wiley and Sons Ltd., 1989.